Lukas Grabenwarter, BSc

Investigation of Impact Ionization for Spinless Fermions in One Dimension with Matrix Product States

MASTER'S THESIS

to achieve the university degree of

Diplom-Ingenieur

Master's degree programme: Technical Physics

submitted to

Graz University of Technology

Supervisor

Hans Gerd Evertz, Ao.Univ.-Prof. Dipl.-Phys. Dr.rer.nat.

Institute of Theoretical and Computational Physics

Graz, November 2020

AFFIDAVIT

I declare that I have authored this thesis independently, that I have not used other than the declared sources/resources, and that I have explicitly indicated all material which has been quoted either literally or by content from the sources used. The text document uploaded to TUGRAZonline is identical to the present master's thesis.

_____

Date, Signature

Abstract

Impact ionization refers to the generation of multiple charge excitations from a single photon shining on a material. Unlike in conventional semiconductors, in strongly correlated materials like Mott insulators this can happen on faster time scales than electron-phonon scattering. Because of the potential applications in solar cells, impact ionization in such materials has generated considerable interest. In one dimension, matrix product states have proved to be a valuable tool for precise ground state calculations as well as for non-equilibrium time evolution of strongly correlated systems.

In this thesis, impact ionization is studied for spinless fermions in one dimension with MPS-based time-evolution methods. Time-dependent expectation values of relevant observables during and after a light pulse are calculated and analyzed, showing impact ionization for the first time in a purely one-dimensional system. The interpretation of the results is supported with spectral functions for the same system, which are also calculated using MPS.

An additional focus lies on the analysis and comparison of the methods used, particularly the transverse contraction method, which allows to calculate time-dependent expectation values in the thermodynamic limit with matrix product states.

Kurzfassung

Als Stoßionisation (*impact ionization*) wird die Erzeugung mehrerer Ladungsträger durch ein einzelnes eingestrahltes Photon bezeichnet. Anders als in herkömmlichen Halbleitern kann dies in stark korrelierten Materialien wie beispielsweise Mott-Isolatoren auf kürzeren Zeitskalen als Elektron-Phonon Streuprozesse stattfinden. Aufgrund der möglichen Anwendung in Solarzellen hat Stoßionisation in solchen Materialien großes Interesse hervorgerufen. Matrixproduktzustände (*matrix product states, MPS*) als wertvolles Hilfsmittel sowohl für präzise Grundzustandsberechnungen als auch für Zeitentwicklungen eindimensionaler stark korrelierter Systeme erwiesen.

In dieser Arbeit wird Stoßionisation für eindimensionale Ketten spinloser Fermionen mit MPS-basierten Zeitentwicklungsmethoden untersucht. Zeitabhängige Erwartungswerte relevanter Observablen während und nach einem Lichtpuls werden berechnet und analysiert, wobei zum ersten Mal in einer Dimension Stoßionisation gezeigt wird. Die Interpretation der Ergebnisse wird durch Spektralfunktionen für dasselbe System unterstützt, welche ebenso unter Verwendung von MPS berechnet werden.

Ein weiterer Fokus liegt auf der Analyse und dem Vergleich der verwendeten Methoden, insbesondere der Methode der transversalen Kontraktion (*transverse contraction*), die die Berechnung zeitabhängiger Erwartungswerte im thermodynamischen Limes mit Matrixproduktzuständen ermöglicht.

Acknowledgements

Contents

1. Introduction

The efficient conversion of solar energy to electrical energy is one of the major challenges in the field of sustainable energy production. For conventional semiconductor-based photovoltaic cells consisting of a single p-n junction, the efficiency is bounded by the Shockley-Queisser limit [1]. This is due to the fact that electrons which are excited beyond the bottom of the conduction band by high-energy photons typically lose their excess energy through scattering with phonons. In strongly correlated materials like Mott insulators, however, electron-electron interactions happen on a shorter time scale than in conventional semiconductors, allowing the high-energy electrons to scatter other electrons into the conduction band [2, 3, 4]. This process is referred to as *impact ionization* and leads to the generation of multiple charge carriers from a single incident photon.

A very successful theoretical model for the description of strongly correlated electrons is the Hubbard model. In this model, impact ionization has been observed in theoretical calculations for various lattice geometries, including small two-dimensional square and triangular lattices [5, 6] as well as an infinite-dimensional hypercubic lattice [3], but it is absent in one-dimensional chains [5].

Despite its formal simplicity, a numerical treatment of the Hubbard model with the methods used in the present thesis is computationally expensive and would be restricted to short time scales or very small systems. Therefore, the simpler model of spinless fermions, often referred to as the t-V model [7], is used. This model still captures some key features of a Mott insulator and has been used for instance for the investigation of Mott insulator junctions [8] and systems exposed to a periodic drive [9].

For the numerical simulation of strongly correlated electrons, a class of states known as matrix product states (MPS) has proved to be a valuable tool, particularly in one dimension [10]. Various algorithms for precise ground state calculations of both finite and infinite systems as well as non-equilibrium time evolutions have been developed over the last decades. Apart from the standard methods DMRG for ground state calculations [11, 12, 13] and TEBD for time evolution [14], many alternative approaches have been proposed, one of which is the *transverse contraction* method that allows to calculate time-dependent expectation values in the thermodynamic limit [15, 16].

In this thesis, MPS-based time-evolution methods are used to study impact ionization in one-dimensional spinless fermion models with nearest and next-nearest neighbor interactions. The purpose is to gain insights on whether impact ionization occurs in one dimension and how it depends on the interactions in the model. A second essential goal is the analysis and comparison of the methods used and in particular the examination of the applicability of the transverse contraction method to such problems.

The first chapter (Chapter 2) is a review of the quantum mechanical basics of lattice

models, Green's functions and entanglement. In Chapter 3, various models for correlated electrons are presented, along with a brief discussion of quantum integrability and the process of impact ionization.

Chapter 4 contains an overview of the basics of matrix product states and descriptions of all MPS-based methods used within this thesis, including a detailed discussion of the transverse contraction method.

In Chapter 5, the TEBD method is applied to small spinless fermion chains. First, the density of states and spectral functions for several observables are calculated to obtain insights on the frequency-dependent response of the system. Then, incident electromagnetic radiation is simulated during the time-evolution and the time-dependent observables which are relevant for impact ionization are measured, followed by a discussion of the results. Besides, the limits of the TEBD approach are discussed.

Chapter 6 deals with the transverse contraction method which is applied to the same problem as treated in the previous chapter. The influence of various settings and parameters on the quality of the results is investigated as well as the limits of the transverse approach and its advantages and drawbacks compared to TEBD.

2. Theoretical Background

2.1. Many-Body Hilbert Spaces

Many-body problems are usually treated in the language of second quantization, where states and operators are represented in terms of creation and annihilation operators on a Fock space. Here the formalism is introduced mainly following the books by Nolting ([17] and [18, chapter 8]).

2.1.1. Second Quantization for Fermions

The quantum mechanical state of a single particle can be described by a vector $|\psi\rangle$ in a Hilbert space $\mathcal{H}_1$. If two identical, but distinguishable particles are considered, of which one is in the state $|\psi_1\rangle \in \mathcal{H}_1$ and the other in the state $|\psi_2\rangle \in \mathcal{H}_1$, then their joint state is represented by the tensor product of the individual states $|\psi_1\rangle \otimes |\psi_2\rangle$ and is an element of the *product space*

$$\mathcal{H}_2 = \mathcal{H}_1 \otimes \mathcal{H}_1,$$

which is by definition a Hilbert space with the scalar product

$$(\langle\phi_1| \otimes \langle\phi_2|) \cdot (|\psi_1\rangle \otimes |\psi_2\rangle) := \langle\phi_1|\psi_1\rangle \langle\phi_2|\psi_2\rangle \ .$$

Since identical quantum mechanical particles are indistinguishable, the state of two identical particles must be either symmetric or antisymmetric under exchange of the particles. Therefore, it can not simply be given by $|\psi_1\rangle \otimes |\psi_2\rangle$, but rather

$$|\Psi\rangle = \frac{1}{2} \left(|\psi_1\rangle \otimes |\psi_2\rangle + \zeta |\psi_2\rangle \otimes |\psi_1\rangle \right), \tag{2.1}$$

where $\zeta = +1$ for bosons and $\zeta = -1$ for fermions. Since this thesis only deals with electrons, the discussion here is restricted to fermions.

The above description can easily be generalized to N particles, where the Hilbert space is

$$\mathcal{H}_N = \mathcal{H}_1 \otimes \mathcal{H}_1 \otimes \ldots \otimes \mathcal{H}_1 =: \mathcal{H}_1^N.$$

Using an arbitrary basis $\{|\chi_j\rangle\}$ of $\mathcal{H}_1$ we can construct a basis of $\mathcal{H}_N$ by defining

$$|\chi_{i_1 i_2 \ldots i_N}^{(N)}\rangle = |\chi_{i_1}\rangle \otimes |\chi_{i_2}\rangle \otimes \ldots \otimes |\chi_{i_N}\rangle \,.$$

All *allowed* (antisymmetric) N-particle states are spanned by the antisymmetrized basis states

$$\hat{\mathcal{A}} |\chi_{i_1 i_2 \ldots i_N}^{(N)}\rangle := \frac{1}{\sqrt{N!}} \sum_{\mathcal{P}} \text{sign}(\mathcal{P}) |\chi_{i_{\mathcal{P}(1)}}\rangle \otimes |\chi_{i_{\mathcal{P}(2)}}\rangle \otimes \ldots \otimes |\chi_{i_{\mathcal{P}(N)}}\rangle, \tag{2.2}$$

where the sum is taken over all permutations $\mathcal{P}$ of the numbers $1 \ldots N$. These objects seem complicated, but the information which particle is in which single-particle state is not required, because the particles are indistinguishable. In fact, since the sum in (2.2) runs over all permutations anyway, it is sufficient to assign to each single-particle state the number of particles occupying it to uniquely determine the many-particle basis state. Thus, we can equivalently write the state (2.2) as

$$|n_1, n_2, \ldots, n_M\rangle \tag{2.3}$$

where $n_j = 1$ if $j \in \{i_1, \ldots, i_N\}$ and 0 otherwise and M is the dimension of the single-particle Hilbert space. This is the *occupation number representation* and the set of states of the form (2.3) with $n_j \in \{0, 1\}$ for fermions (due to the Pauli exclusion principle) and $\sum_j n_j = N$ is a basis for the space $\mathcal{F}_N := \hat{A} \mathcal{H}_N$ of all antisymmetric states in $\mathcal{H}_N$. As a finite-dimensional subspace of a Hilbert space, $\mathcal{F}_N$ is a Hilbert space itself [19, thm 13.7]. Note that together with the occupation numbers, the basis of single-particle states must be specified to determine the many-particle state.

Within $\mathcal{F}_N$, the total number of particles is fixed to N. For systems with variable particle numbers Fock [20] introduced what is now called the (fermionic) *Fock space*, which is (the completion of) the direct sum of all antisymmetrized N-particle Hilbert spaces,

$$\mathcal{F} = \bigoplus_{N=0}^{\infty} \mathcal{F}_N.$$

with the scalar product $\langle n_1 n_2 \ldots n_M | n_1' n_2' \ldots n_M' \rangle := \delta_{n_1 n_1'} \delta_{n_2 n_2'} \ldots \delta_{n_M n_M'}$. The Hilbert space $\mathcal{F}_0 \equiv \mathbb{C}$ is spanned by one single element, the *vacuum state* $|0\rangle$ without any particles in any state.

Apart from operators acting on one of the subspaces $\mathcal{H}_N$, on a Fock space operators can be defined which map from $\mathcal{H}_N$ to $\mathcal{H}_{N-1}$ or $\mathcal{H}_{N+1}$, i.e. add or remove particles. These operators are called *creation* and *annihilation operators* and for fermions are defined by

$$c_j |n_1, n_2, \ldots, n_j, \ldots, n_M\rangle = (-1)^{\sum_{i<j} n_i} (1 - n_j) |n_1, n_2, \ldots, n_j - 1, \ldots, n_M\rangle, \tag{2.4}$$

$$c_j^\dagger |n_1, n_2, \ldots, n_j, \ldots, n_M\rangle = (-1)^{\sum_{i<j} n_i} n_j |n_1, n_2, \ldots, n_j + 1, \ldots, n_M\rangle. \tag{2.5}$$

It can be shown that indeed $(c_j)^\dagger = c_j^\dagger$ [17, p.12f]. From the definitions (2.4) and (2.5) follow the anticommutation relations (in accordance with the required antisymmetry properties)

$$\{c_i, c_j\} = \{c_i^\dagger, c_j^\dagger\} = 0, \quad \{c_i, c_j^\dagger\} = \delta_{ij}. \tag{2.6}$$

This implies in particular $(c_j)^2 = (c_j^\dagger)^2 = 0$, which is Pauli's exclusion principle, meaning that each single-particle state j can be occupied by at most one particle. In the notation here spin is implicitly included in the label j.

Each basis state $|n_1, n_2, \ldots, n_M\rangle$ can be expressed in terms of creation operators and the vacuum state $|0\rangle$ only, because

$$|n_1, n_2, \ldots, n_M\rangle = (c_1^\dagger)^{n_1} (c_2^\dagger)^{n_2} \ldots (c_M^\dagger)^{n_M} |0\rangle. \tag{2.7}$$

Since the order of the creation operators makes a difference, a "natural" order of the states $1, \ldots, M$ must be defined. Throughout this thesis, the operators are ordered as in (2.7) with ascending indices.

From the definitions (2.4) and (2.5), it is evident that the operator $\hat{n}_j := c_j^\dagger c_j$ counts the particles in the state j,

$$\hat{n}_j \left| n_1, n_2, \ldots, n_j, \ldots, n_M \right\rangle = n_j \left| n_1, n_2, \ldots, n_j, \ldots, n_M \right\rangle.$$

It is therefore called the *(occupation-)number operator*.

2.1.2. Operators in Second Quantization

In many-body systems, single particle operators usually appear in the form of sums over all particles, $\hat{O} = \sum_{l=1}^{N} O(\hat{\boldsymbol{q}}_l, \hat{\boldsymbol{p}}_l)$, which is expressed in second quantization in a basis $\{|\chi_j\rangle\}$ as

$$\hat{O} = \sum_{ij} \langle \chi_i | O(\hat{\boldsymbol{q}}, \hat{\boldsymbol{p}}) | \chi_j \rangle \, c_i^\dagger c_j. \tag{2.8}$$

Two-particle interaction operators of the form $\hat{V} = \sum_{l \neq m} V(\hat{\boldsymbol{q}}_l, \hat{\boldsymbol{q}}_m)$ become

$$\hat{V} = \sum_{ijkl} \langle \chi_i \chi_j | V(\hat{\boldsymbol{q}}_1, \hat{\boldsymbol{q}}_2) | \chi_l \chi_k \rangle \, c_i^\dagger c_j^\dagger c_k c_l. \tag{2.9}$$

These results are derived e.g. in [17].

2.1.3. Basis Transformations

Consider a basis transformation of the form $|\tilde{\chi}_i\rangle = \sum_j U_{ij} |\chi_j\rangle$ with a unitary matrix U (which is the matrix representation of a unitary operator). The Fock states for N particles in the basis $\{|\tilde{\chi}_j\rangle\}$ read

$$\tilde{c}_{i_1}^\dagger \ldots \tilde{c}_{i_N}^\dagger \left| 0 \right\rangle = \hat{\mathcal{A}} \left| \tilde{\chi}_{i_1} \ldots \tilde{\chi}_{i_N} \right\rangle$$

and expressing this in the basis $\{|\chi_j\rangle\}$ we obtain

$$\tilde{c}_{i_1}^\dagger \ldots \tilde{c}_{i_N}^\dagger \left| 0 \right\rangle = \sum_{j_1, \ldots, j_N} U_{i_1 j_1} \ldots U_{i_N j_N} \hat{\mathcal{A}} \left| \chi_{j_1} \ldots \chi_{j_N} \right\rangle = \sum_{j_1, \ldots, j_N} U_{i_1 j_1} \ldots U_{i_N j_N} c_{j_1}^\dagger \ldots c_{j_N}^\dagger \left| 0 \right\rangle.$$

Hence, the creation operators are transformed like the basis functions, while the annihilation operators are transformed inversely:

$$\tilde{c}_i^\dagger = \sum_j U_{ij} c_j^\dagger, \quad \tilde{c}_i = \sum_j U_{ij}^\dagger c_j. \tag{2.10}$$

Transforming the Hamiltonian according to (2.10) is sufficient if the basis transformation is time-independent. If, however, the basis transformation is time-dependent, an additional term arises in the time-dependent Schrödinger equation [21].

The time evolution of the new basis states is then given by

$$\mathrm{i}\partial_t \tilde{c}_{i_1}^\dagger \dots \tilde{c}_{i_N}^\dagger \ket{0} = \sum_{j_1,\dots,j_N} \left[\mathrm{i}\partial_t (U_{i_1 j_1} \dots U_{i_N j_N}) c_{j_1}^\dagger \dots c_{j_N}^\dagger \ket{0} + U_{i_1 j_1} \dots U_{i_N j_N} \mathrm{i}\partial_t c_{j_1}^\dagger \dots c_{j_N}^\dagger \ket{0} \right].$$

Assuming that the old basis states obey the time-dependent Schrödinger equation

$$\mathrm{i}\partial_t c_{j_1}^\dagger \dots c_{j_N}^\dagger \ket{0} = \hat{H} c_{j_1}^\dagger \dots c_{j_N}^\dagger \ket{0}$$

and using the linearity of $\hat{H}$, the second term can be simplified, yielding

$$\mathrm{i}\partial_t \tilde{c}_{i_1}^\dagger \dots \tilde{c}_{i_N}^\dagger \ket{0} = \sum_{j_1,\dots,j_N} \mathrm{i}\partial_t (U_{i_1 j_1} \dots U_{i_N j_N}) c_{j_1}^\dagger \dots c_{j_N}^\dagger \ket{0} + \hat{H} \tilde{c}_{i_1}^\dagger \dots \tilde{c}_{i_N}^\dagger \ket{0}. \tag{2.11}$$

Applying the product rule to the first term and inserting $\mathbb{1} = U^\dagger U$ gives

$$\sum_{j_1,\dots,j_N} \mathrm{i}\partial_t (U_{i_1 j_1} \dots U_{i_N j_N}) c_{j_1}^\dagger \dots c_{j_N}^\dagger \ket{0} =$$

$$= \sum_{j_1,\dots,j_N} \sum_{l=1}^N \sum_{\alpha_l,\beta_l} \mathrm{i}\dot{U}_{i_l \alpha_l} U_{\alpha_l \beta_l}^\dagger U_{\beta_l j_l} \left(\prod_{m\neq l} U_{i_m j_m} \right) c_{j_1}^\dagger \dots c_{j_N}^\dagger \ket{0}$$

$$= \sum_{l=1}^N \sum_{\alpha_l,\beta_l} \mathrm{i}\dot{U}_{i_l \alpha_l} U_{\alpha_l \beta_l}^\dagger (-1)^l \tilde{c}_{\beta_l}^\dagger \prod_{m\neq l} \tilde{c}_{i_m}^\dagger \ket{0}.$$

Since the state i_l does not appear in the product, we can safely create and then annihilate a particle in this state without changing anything:

$$\sum_{j_1,\dots,j_N} \mathrm{i}\partial_t (U_{i_1 j_1} \dots U_{i_N j_N}) c_{j_1}^\dagger \dots c_{j_N}^\dagger \ket{0} = \sum_{l=1}^N \sum_{\alpha_l,\beta_l} \mathrm{i}\dot{U}_{i_l \alpha_l} U_{\alpha_l \beta_l}^\dagger (-1)^l \tilde{c}_{\beta_l}^\dagger \tilde{c}_{i_l} \tilde{c}_{i_l}^\dagger \prod_{m\neq l} \tilde{c}_{i_m}^\dagger \ket{0}$$

$$= \sum_{l=1}^N \sum_{\alpha_l,\beta_l} \mathrm{i}\dot{U}_{i_l \alpha_l} U_{\alpha_l \beta_l}^\dagger \tilde{c}_{\beta_l}^\dagger \tilde{c}_{i_l} \tilde{c}_{i_1}^\dagger \dots \tilde{c}_{i_N}^\dagger \ket{0}.$$

Plugging this into (2.11) results in

$$\mathrm{i}\partial_t \tilde{c}_{i_1}^\dagger \dots \tilde{c}_{i_N}^\dagger \ket{0} = \left(\hat{H} + \mathrm{i}\sum_{l=1}^N \sum_{\alpha_l,\beta_l} \dot{U}_{i_l \alpha_l} U_{\alpha_l \beta_l}^\dagger \tilde{c}_{\beta_l}^\dagger \tilde{c}_{i_l} \right) \tilde{c}_{i_1}^\dagger \dots \tilde{c}_{i_N}^\dagger \ket{0}.$$

Without explicitly using the particle number N this can be written as

$$\mathrm{i}\partial_t \prod_{i=1}^M \left(\tilde{c}_i^\dagger \right)^{n_i} \ket{0} = \left(\hat{H} + \mathrm{i}\sum_{i,j,m=1}^M \dot{U}_{jm} U_{mi}^\dagger \tilde{c}_i^\dagger \tilde{c}_j \right) \prod_{i=1}^M \left(\tilde{c}_i^\dagger \right)^{n_i} \ket{0}.$$

Hence, the dynamics of the system in the new basis are governed by the time-dependent Schrödinger equation with the Hamiltonian

$$\hat{H}' = \hat{H} + \mathrm{i}\sum_{i,j=1}^M \left(\sum_{m=1}^M \dot{U}_{jm} U_{mi}^\dagger \right) \tilde{c}_i^\dagger \tilde{c}_j. \tag{2.12}$$

To show that $\hat{H}'$ is hermitian, we must prove that $(\mathrm{i}\dot{U}U^\dagger)_{ji} = (\mathrm{i}\dot{U}U^\dagger)_{ij}^*$. By differentiating $UU^\dagger = \mathbb{1}$ (which is valid for every unitary matrix) with respect to time, we find $\dot{U}U^\dagger = -U\dot{U}^\dagger$ and therefore $(\mathrm{i}\dot{U}U^\dagger)_{ij}^* = -(\mathrm{i}U\dot{U}^\dagger)_{ij}^* = \mathrm{i}(U^*\dot{U}^\top)_{ij} = (\mathrm{i}\dot{U}U^\dagger)_{ji}$.

2.1.4. Electrons in Periodic Crystals

Bloch [22] showed that the solutions of the Schrödinger equation for every periodic system with $V(\boldsymbol{r}) = V(\boldsymbol{r} + l\boldsymbol{a} + m\boldsymbol{b} + n\boldsymbol{c})$ for all integers l, m, n have a real-space basis of the form

$$\psi_{\boldsymbol{k}}(\boldsymbol{r}) = \mathrm{e}^{\mathrm{i}\boldsymbol{k}\cdot\boldsymbol{r}}\, u_{\boldsymbol{k}}(\boldsymbol{r}), \tag{2.13}$$

where the functions $u_{\boldsymbol{k}}(\boldsymbol{r})$ have the same periodicity as the lattice. If the length of the crystal in a certain direction is L_i then, assuming periodic boundary conditions, the components of $\boldsymbol{k}$ in this direction can take the values $2\pi n_i/L_i$ with arbitrary integers n_i. Since $n_i = L_i$ is equivalent to $n_i = 0$, the plane wave part of (2.13) repeats outside the first Brioullin zone, which gives rise to multiple bands. They are often denoted separately with a *band index n*,

$$\psi_{n\boldsymbol{k}}(\boldsymbol{r}) = \mathrm{e}^{\mathrm{i}\boldsymbol{k}\cdot\boldsymbol{r}}\, u_{n\boldsymbol{k}}(\boldsymbol{r}),$$

where $\boldsymbol{k}$ now only takes values inside the first Brioullin zone. In the present thesis, we focus on single band models, where one isolated band is considered.

The Bloch waves described by (2.13) are delocalized over the whole crystal. In situations where electrons are tightly bound to their respective atom it may be more natural to use a basis of localized states. While atomic orbitals would be an obvious choice, they have the drawback of not being orthogonal (if belonging to different atoms). For this reason, Wannier [23] suggested using the functions

$$w_j(\boldsymbol{r}) = \frac{1}{\sqrt{L}} \sum_{\boldsymbol{k}}^{1\mathrm{BZ}} \mathrm{e}^{-\mathrm{i}\boldsymbol{k}\cdot\boldsymbol{R}_j}\, \psi_{\boldsymbol{k}}(\boldsymbol{r}) \tag{2.14}$$

as a basis. These *Wannier functions* are localized around the lattice site $\boldsymbol{R}_j$, only depend on $\boldsymbol{r} - \boldsymbol{R}_j$ and form an orthonormal basis of the space of all solutions of the Schrödinger equation [23]. If the sum over $\boldsymbol{k}$ in (2.14) is taken over all values in the first Brioullin zone, we obtain one orbital (Wannier function) per unit cell, which corresponds to a single Bloch band. Additional Wannier functions at the same site would be constructed from Bloch waves corresponding to higher Brioullin zones (i.e. other bands) [24].

Interacting non-relativistic electrons in a crystal are described by the Hamiltonian (using units where $m_e = 1$)

$$\hat{H} = \sum_{i=1}^{N} \left(\frac{\hat{\boldsymbol{p}}_i^2}{2} + V_0(\hat{\boldsymbol{q}}_i) \right) + \sum_{i \neq j} V(\hat{\boldsymbol{q}}_i, \hat{\boldsymbol{q}}_j) =: \sum_{i=1}^{N} h(\hat{\boldsymbol{q}}_i, \hat{\boldsymbol{p}}_i) + \sum_{i \neq j} V(\hat{\boldsymbol{q}}_i, \hat{\boldsymbol{q}}_j), \tag{2.15}$$

where V_0 is the periodic lattice potential and V is the Coulomb interaction potential. According to (2.8) and (2.9) the Hamiltonian in second quantization reads

$$\hat{H} = \sum_{ij\sigma} \langle w_i | h(\hat{\boldsymbol{q}}, \hat{\boldsymbol{p}}) | w_j \rangle\, c_{i\sigma}^{\dagger} c_{j\sigma} + \sum_{ijkl\sigma\sigma'} \langle w_i w_j | V(\hat{\boldsymbol{q}}_1, \hat{\boldsymbol{q}}_2) | w_l w_k \rangle\, c_{i\sigma}^{\dagger} c_{j\sigma'}^{\dagger} c_{k\sigma'} c_{l\sigma}$$

$$=: -\sum_{ij\sigma} T_{ij} c_{i\sigma}^{\dagger} c_{j\sigma} + \sum_{ijkl\sigma\sigma'} U_{ijkl} c_{i\sigma}^{\dagger} c_{j\sigma'}^{\dagger} c_{k\sigma'} c_{l\sigma} \tag{2.16}$$

where $c_{j\sigma}$ ($c_{j\sigma}^{\dagger}$) annihilates (creates) an electron with spin σ in the Wannier state $|w_j\rangle$ and the sums run over all lattice sites i, j, k, l. Note that neither the Wannier functions nor

the Hamiltonian depend on spin. Therefore, the total state of a single particle is given by $|w_j\rangle \otimes |\sigma_j\rangle$ and in the matrix elements the spin parts simply give Kronecker deltas, reducing the number of spin sums.

Since (2.16) represents the full non-relativistic many-particle Hamiltonian, it is the most generic form of a single-band Hamiltonian on a periodic lattice. The terms in the first sum can be interpreted as an electron "hopping" from site j to site i and therefore the matrix elements T_{ij} are called *hopping integrals*. Notwithstanding the conventional notation, a capital T is used throughout the present thesis to avoid confusion with time t.

Due to the localization of the Wannier functions, the hopping integrals fall off rapidly with increasing distance between the sites i and j. Neglecting the Coulomb interaction for now, this leads to the common approximation known as the *tight binding model*, where the matrix elements T_{ij} are only taken into account if i and j are nearest neighbors. For a homogeneous and isotropic crystal, the Hamiltonian then reads

$$\hat{H}_{\mathrm{TB}} = -\sum_{\langle ij \rangle \sigma} \left(T c_{i\sigma}^\dagger c_{j\sigma} + T^* c_{j\sigma}^\dagger c_{i\sigma} \right) + \sum_{i\sigma} \varepsilon c_{i\sigma}^\dagger c_{i\sigma}, \qquad (2.17)$$

where $\langle ij \rangle$ denotes all ordered pairs of nearest neighbors in the crystal lattice, T is the hopping integral T_{ij} for nearest neighbors i and j and $\varepsilon = T_{ii}$ is the on-site matrix element. The second sum in (2.17) is often dropped, because it is proportional to the total particle number $\hat{N} = \sum_{i\sigma} \hat{n}_{i\sigma}$, which commutes with the Hamiltonian and is therefore a conserved quantity (i.e. it only shifts the spectrum of the Hamiltonian).

2.2. Electromagnetic Fields - The Peierls Substitution

In the presence of classical electromagnetic fields described by a vector potential $\boldsymbol{A}(\boldsymbol{r}, t)$ and a scalar potential $\phi(\boldsymbol{r}, t)$, the Hamiltonian for a single electron reads[1]

$$\hat{H} = \frac{1}{2} \left(\hat{\boldsymbol{p}} - \boldsymbol{A}(\hat{\boldsymbol{q}}, t) \right)^2 + V_0(\hat{\boldsymbol{q}}) + \phi(\hat{\boldsymbol{q}}, t). \qquad (2.18)$$

Here, relativistic corrections such as spin-orbit coupling are neglected, and we assumed that the fields are sufficiently weak so that the crystal potential V_0 retains its equilibrium value. The interaction of the spin with the magnetic field is not relevant for the following discussion and is therefore also neglected.

Since the Hamiltonian is different for each value of the electromagnetic potentials, in principle the matrix elements in (2.16) must be reevaluated for each value to obtain a second quantization expression. However, there is an approximation tracing back to Peierls [25], which recovers the single-particle term from (2.16) with only a modification of the matrix elements T_{ij}.

The derivation given here in large parts follows the one by Luttinger [26]. Instead of the

---

[1]Throughout this thesis we use units where $\hbar = c = e = m_e = 1$.

original Wannier functions (2.14), we use the set

$$\tilde{w}_j(\boldsymbol{r}, t) = \exp\big(\mathrm{i}\varphi_j(\boldsymbol{r}, t)\big) w_j(\boldsymbol{r}) \quad \text{with} \quad \varphi_j(\boldsymbol{r}, t) := \int_{\boldsymbol{R}_j}^{\boldsymbol{r}} \boldsymbol{A}(\boldsymbol{r}', t) \cdot \mathrm{d}\boldsymbol{r}' \qquad (2.19)$$

as a basis. The integration is carried out along a straight line between $\boldsymbol{R}_j$ and $\boldsymbol{r}$. Since the prefactor is only a phase, these functions share the localization properties of the Wannier functions and therefore are an equally useful basis for the tight binding Hamiltonian. However, in general the $\tilde{w}_j$ are strictly speaking not orthogonal, because

$$\tilde{w}_i^*(\boldsymbol{r}, t)\tilde{w}_j(\boldsymbol{r}, t) = \exp\big(\mathrm{i}[\varphi_i(\boldsymbol{r}, t) - \varphi_j(\boldsymbol{r}, t)]\big) w_i^*(\boldsymbol{r})w_j(\boldsymbol{r})$$

$$= \exp\left(\mathrm{i}\oint_{\mathcal{C}} \boldsymbol{A}(\boldsymbol{r}', t) \cdot \mathrm{d}\boldsymbol{r}' - \mathrm{i}\int_{\boldsymbol{R}_i}^{\boldsymbol{R}_j} \boldsymbol{A}(\boldsymbol{r}', t) \cdot \mathrm{d}\boldsymbol{r}'\right) w_i^*(\boldsymbol{r})w_j(\boldsymbol{r}) \qquad (2.20)$$

where $\mathcal{C}$ is the path connecting the points $\boldsymbol{R}_i \to \boldsymbol{r} \to \boldsymbol{R}_j \to \boldsymbol{R}_i$ in straight lines. To obtain an orthonormal basis, the integral along the closed contour must be neglected, because then

$$\int_{\mathbb{R}^d} \tilde{w}_i^*(\boldsymbol{r}, t)\tilde{w}_j(\boldsymbol{r}, t)\,\mathrm{d}^d\boldsymbol{r} \approx \exp\left(-\mathrm{i}\int_{\boldsymbol{R}_i}^{\boldsymbol{R}_j} \boldsymbol{A}(\boldsymbol{r}', t) \cdot \mathrm{d}\boldsymbol{r}'\right) \int_{\mathbb{R}^d} w_i^*(\boldsymbol{r})w_j(\boldsymbol{r})\,\mathrm{d}^d\boldsymbol{r} = \delta_{ij}.$$

The neglected term, which is simply the magnetic flux through the triangle spanned by the three points $\boldsymbol{R}_i$, $\boldsymbol{r}$ and $\boldsymbol{R}_j$, vanishes exactly if the vector potential is uniform inside this triangle. But even if this is not the case the strong localization of the Wannier functions around a single point in space will make the expression (2.20) very small unless $\boldsymbol{r}$ is very close to $\boldsymbol{R}_i$ *and* $\boldsymbol{R}_j$. Therefore, neglecting the flux integral for $i \neq j$ is certainly justified, given that the Wannier functions are sufficiently localized, and for $i = j$ it vanishes anyway.

Using the temporal gauge with $\phi = 0$, the action of the Hamiltonian (2.18) on the new basis functions is given by

$$H\tilde{w}_j(\boldsymbol{r}, t) = \left[\frac{1}{2}\big(-\mathrm{i}\boldsymbol{\nabla} - \boldsymbol{A}(\boldsymbol{r}, t)\big)^2 + V_0(\boldsymbol{r})\right] \exp\big(\mathrm{i}\varphi_j(\boldsymbol{r}, t)\big) w_j(\boldsymbol{r}). \qquad (2.21)$$

The only part of H which does not commute with $\exp\big(\mathrm{i}\varphi_j(\boldsymbol{r}, t)\big)$ is the differential operator $\boldsymbol{\nabla}$. Since

$$\boldsymbol{\nabla}\exp(\mathrm{i}\varphi_j)w_j(\boldsymbol{r}) = \exp\big(\mathrm{i}\varphi_j\big)\big(\boldsymbol{\nabla} + \mathrm{i}(\boldsymbol{\nabla}\varphi_j)\big)w_j(\boldsymbol{r})$$

we can shift the operator H past the exponential upon replacing $\boldsymbol{\nabla} \to \boldsymbol{\nabla} + \mathrm{i}(\boldsymbol{\nabla}\varphi_j)$ in (2.21), resulting in

$$H\tilde{w}_j(\boldsymbol{r}, t) = \exp\big(\mathrm{i}\varphi_j(\boldsymbol{r}, t)\big)\left[\frac{1}{2}\big(-\mathrm{i}\boldsymbol{\nabla} + \big(\boldsymbol{\nabla}\varphi_j(\boldsymbol{r}, t)\big) - \boldsymbol{A}(\boldsymbol{r}, t)\big)^2 + V(\boldsymbol{r}, t)\right]w_j(\boldsymbol{r}). \quad (2.22)$$

The gradient of φ_j can be written in the form (see Appendix A)

$$\boldsymbol{\nabla}\varphi_j(\boldsymbol{r}, t) = \boldsymbol{A}(\boldsymbol{r}, t) + \int_0^1 \lambda(\boldsymbol{r} - \boldsymbol{R}_j) \times \boldsymbol{B}\big(\boldsymbol{R}_j + \lambda(\boldsymbol{r} - \boldsymbol{R}_j), t\big)\,\mathrm{d}\lambda\,,$$

where $\boldsymbol{B} = \boldsymbol{\nabla} \times \boldsymbol{A}$ is the magnetic field. Inserting this result into (2.22) gives

$$H\tilde{w}_j(\boldsymbol{r},t) = \exp\left(\mathrm{i}\varphi_j(\boldsymbol{r},t)\right)\left[\frac{1}{2}\left(-\mathrm{i}\boldsymbol{\nabla} + \int\limits_0^1 \lambda(\boldsymbol{r}-\boldsymbol{R}_j)\times\boldsymbol{B}\big(\boldsymbol{R}_j+\lambda(\boldsymbol{r}-\boldsymbol{R}_j),t\big)\,\mathrm{d}\lambda\right)^2 \right.$$
$$\left. + V(\boldsymbol{r},t)\right]w_j(\boldsymbol{r}). \quad (2.23)$$

Luttinger now argues that the integral can be neglected because the term $\boldsymbol{r} - \boldsymbol{R}_j$ is small in the vicinity of the lattice point $\boldsymbol{R}_j$ around which the Wannier function w_j is strongly localized. However, at the same time he admits that this approximation is difficult to justify and several other authors have also questioned its validity in general cases [27, 28]. Fortunately, as described below, the situation is much clearer in one dimensional systems which are treated in this thesis.

Within this approximation we can thus write

$$H\tilde{w}_j(\boldsymbol{r},t) = \exp\left(\mathrm{i}\varphi_j(\boldsymbol{r},t)\right)\left(-\frac{1}{2}\boldsymbol{\nabla}^2 + V(\boldsymbol{r},t)\right)w_j(\boldsymbol{r}) = \exp\left(\mathrm{i}\varphi_j(\boldsymbol{r},t)\right)H_0 w_j(\boldsymbol{r}) \quad (2.24)$$

where H_0 is the Hamiltonian of the system without the electromagnetic fields. The matrix elements of the Hamiltonian in the basis spanned by the $\tilde{w}_j$ then become

$$\langle\tilde{w}_i|\hat{H}|\tilde{w}_j\rangle = \int_{\mathbb{R}^d} \tilde{w}_i^*(\boldsymbol{r},t)H\tilde{w}_j(\boldsymbol{r},t)\,\mathrm{d}^d\boldsymbol{r}$$
$$= \int_{\mathbb{R}^d} \exp\left(\mathrm{i}[\varphi_j(\boldsymbol{r},t)-\varphi_i(\boldsymbol{r},t)]\right)w_i(\boldsymbol{r})H_0 w_j(\boldsymbol{r})\,\mathrm{d}^d\boldsymbol{r}. \quad (2.25)$$

Here, a similar argument as in the orthogonality considerations holds. Again, the phase difference can be split into an integral around the triangle spanned by $\boldsymbol{R}_i$, $\boldsymbol{r}$ and $\boldsymbol{R}_j$ and an integral straight from $\boldsymbol{R}_i$ to $\boldsymbol{R}_j$, exactly as in (2.20). Since the exponential is multiplied by w_i, it will only significantly contribute to (2.25) if $\boldsymbol{r} \approx \boldsymbol{R}_i$. Then the triangle has a small area and we can neglect the flux through it if the vector potential does not vary too much inside. There is no simple way of estimating the error of this approximation, but again, this has no consequences for the cases treated in the present thesis, because in a linear one-dimensional chain, the closed integration path is empty anyway.

After neglecting the flux integral, we are left with

$$\langle\tilde{w}_i|\hat{H}|\tilde{w}_j\rangle = \exp\left(-\mathrm{i}\int\limits_{\boldsymbol{R}_i}^{\boldsymbol{R}_j} \boldsymbol{A}(\boldsymbol{r}',t)\cdot\mathrm{d}\boldsymbol{r}'\right)\langle w_i|\hat{H}_0|w_j\rangle. \quad (2.26)$$

All approximations applied so far are exact if the vector potential is spatially uniform. Then the magnetic field $\boldsymbol{B} = \boldsymbol{\nabla}\times\boldsymbol{A}$ vanishes in (2.23) and the integration along the closed path $\mathcal{C}$ in (2.20) and (2.25) yields exactly zero. Hence, we can assume that the result (2.26) is a good approximation as long as the vector potential is close to uniform on the scale of the system. For an electromagnetic wave this means that the wavelength must be much larger than the system under consideration.

Substituting the matrix elements according to (2.26) is called the *Peierls substitution*. Since the integral vanishes for $i = j$, it does not affect on-site terms, while hopping-like terms are modified with a phase depending on the positions of the lattice sites involved:

$$T_{ij} \to T_{ij} \exp\left(-\mathrm{i}\int_{\boldsymbol{R}_i}^{\boldsymbol{R}_j} \boldsymbol{A}(\boldsymbol{r}', t) \cdot \mathrm{d}\boldsymbol{r}'\right). \tag{2.27}$$

If the vector potential is assumed spatially uniform, the Peierls substitution has a particularly simple form in momentum space. In the basis of Bloch functions, the hopping part of the Hamiltonian is diagonal and the diagonal elements are given by [17]

$$\varepsilon(\boldsymbol{k}) = \frac{1}{L}\sum_{ij} T_{ij}\, \mathrm{e}^{-\mathrm{i}\boldsymbol{k}\cdot(\boldsymbol{R}_i - \boldsymbol{R}_j)}\,.$$

Modifying the hopping elements according to (2.27) results in

$$\varepsilon'(\boldsymbol{k}) = \frac{1}{L}\sum_{ij} T_{ij}\, \mathrm{e}^{-\mathrm{i}\boldsymbol{k}\cdot(\boldsymbol{R}_i - \boldsymbol{R}_j)}\, \mathrm{e}^{\mathrm{i}\boldsymbol{A}(t)\cdot(\boldsymbol{R}_i - \boldsymbol{R}_j)} = \frac{1}{L}\sum_{ij} T_{ij}\, \mathrm{e}^{-\mathrm{i}(\boldsymbol{k} - \boldsymbol{A}(t))\cdot(\boldsymbol{R}_i - \boldsymbol{R}_j)}$$

if $\boldsymbol{A}$ does not depend on $\boldsymbol{r}$. Hence, in momentum space the Peierls substitution for a spatially homogeneous vector potential is simply given by

$$\varepsilon(\boldsymbol{k}) \to \varepsilon(\boldsymbol{k} - \boldsymbol{A}(t)).$$

2.2.1. Peculiarities in one dimension

In one-dimensional systems, the considerations in the previous section become much simpler. The integration path $\mathcal{C}$ in (2.20) is then empty, meaning that the basis functions $\tilde{w}_j$ are exactly orthogonal and that the expressions (2.25) and (2.26) are exactly equal. Besides, for a one-dimensional system the calculation of $\boldsymbol{\nabla}\varphi_j(\boldsymbol{r}, t)$ simply gives $\partial\varphi_j/\partial x = A(x, t)$. Therefore, also (2.24) and hence finally the whole Peierls substitution is exact (for a single-band model with only hopping and density interactions).

Assuming that the vector potential is constant across the system, the hopping terms take the simple form

$$T_{ij} \to T_{ij}\, \mathrm{e}^{-\mathrm{i}(j - i)A(t)},$$

if we use the lattice constant as the unit of length.

For open boundary conditions, the Peierls substitution is in fact equivalent to the application of an electrostatic potential. To see this, we perform a time dependent basis transformation $\tilde{c}_j = \exp\{-\mathrm{i}jA(t)\}c_j$. This transformation removes the Peierls phases, but according to Section 2.1.3, we must then modify the Hamiltonian, resulting in

$$\hat{H}' = \hat{H} + \sum_{j=1}^{L} j\frac{\mathrm{d}A}{\mathrm{d}t}\hat{n}_j = \hat{H} - E(t)\sum_{j=1}^{L} j\hat{n}_j. \tag{2.28}$$

The additional term describes a position-dependent chemical potential $\mu_j = -jE(t)$, which is equal to the electrostatic potential that creates the field $E(t)$. Hence, the transformation carried out is equivalent to a classical gauge transformation (in one dimension) $A \to 0$, $\phi \to \phi + \int \partial_t A\,\mathrm{d}x$.

2.3. Green's Functions

This section is intended to give a brief overview of the results relevant for the present thesis and is mainly based on the book by Nolting [17].

In the context of many-particle physics, Green's functions are an important tool in linear response theory. The *retarded Green's function* for an arbitrary pair of operators $\hat{A}$, $\hat{B}$ is defined as

$$G_{AB}^r(t - t') \equiv \langle\langle \hat{A}, \hat{B} \rangle\rangle^r = -\mathrm{i}\Theta(t - t') \left\langle [\hat{A}(t), \hat{B}(t')]_{-\zeta} \right\rangle, \tag{2.29}$$

where the time-dependence of the operators is to be understood in the sense of the Heisenberg representation, $\Theta(t - t')$ is the Heavyside step function and $[\cdot, \cdot]_{-\zeta}$ denotes the commutator for bosonic operators and the anticommutator for fermionic ones. It describes the response of the system in terms of the expectation value of $\hat{A}$ when a perturbation is applied that couples to $\hat{B}$.

If a system is initially (for $t \to -\infty$) described by a Hamiltonian $\hat{H}_0$ and at some later time the Hamiltonian changes to

$$\hat{H}_0 + \hat{B}f(t)$$

with an arbitrary complex-valued function $f(t)$, then the perturbed expectation value of the observable $\hat{A}$ can be expressed in terms of the unperturbed expectation value $\langle \hat{A} \rangle_0$ and the retarded Green's function as

$$\langle \hat{A} \rangle (t) = \langle \hat{A} \rangle_0 + \int_{-\infty}^{\infty} f(t') \, G_{AB}^r(t - t') \, \mathrm{d}t'.$$

This is, however, only true if the commutator is used in the definition (2.29).

A closely related object is the *spectral function*

$$S_{AB}(t - t') := \frac{1}{2\pi} \left\langle [\hat{A}(t), \hat{B}(t')]_{-\zeta} \right\rangle, \tag{2.30}$$

the Fourier transform of which is connected to the retarded Green's function by the relation

$$S_{AB}(\omega) = -\frac{1}{\pi} \operatorname{Im} G_{AB}^r(\omega). \tag{2.31}$$

In principle, the expectation values in (2.29) and (2.30) involve a thermal average, but in the present thesis we will only work at zero temperature and therefore in the following, all expectation values are taken in the ground state. The spectral function can then be expanded to

$$S_{AB}(t - t') = \sum_n \langle 0|\hat{A}|n \rangle \, \langle n|\hat{B}|0 \rangle \, \mathrm{e}^{-\mathrm{i}(E_n - E_0)(t - t')} + \langle 0|\hat{B}|n \rangle \, \langle n|\hat{A}|0 \rangle \, \mathrm{e}^{\mathrm{i}(E_n - E_0)(t - t')}, \tag{2.32}$$

where $|n\rangle$ are the eigenstates of the Hamiltonian with energies E_n. Note that $|0\rangle$ here denotes the ground state and not the vacuum state! The Fourier transform of (2.32) is

$$S_{AB}(\omega) = \sum_n \langle 0|\hat{A}|n \rangle \, \langle n|\hat{B}|0 \rangle \, \delta\big(\omega - (E_n - E_0)\big) + \langle 0|\hat{B}|n \rangle \, \langle n|\hat{A}|0 \rangle \, \delta\big(\omega + (E_n - E_0)\big),$$

and in particular for $\hat{B} = \hat{A}^\dagger$ we obtain

$$S_{A^\dagger A}(\omega) = \sum_n |\langle n|\hat{A}|0\rangle|^2 \delta\big(\omega - (E_n - E_0)\big) + |\langle 0|\hat{A}|n\rangle|^2 \delta\big(\omega + (E_n - E_0)\big). \qquad (2.33)$$

Hence, $S_{A^\dagger A}$ has a peak at each energy that corresponds to a possible excitation of the system from the ground state to a level E_n and the intensity of this peak is proportional to the probability of finding the system in the eigenstate $|n\rangle$ after applying the operator $\hat{A}$. Peaks at negative energies correspond to transitions from the eigenstate $|n\rangle$ to the ground state in the same way.

For a real-valued harmonic perturbation $\hat{H} = \hat{H}_0 + (f_0\,\mathrm{e}^{\mathrm{i}\omega t} + f_0^*\,\mathrm{e}^{-\mathrm{i}\omega t})\hat{A}$ which couples to a *hermitian* operator $\hat{A}$, the average dissipation rate Q (net energy absorbed by the system per unit time) can be expressed in terms of the spectral function S_{AA} as [29, p. 540][1]

$$Q(\omega) = -2\omega|f_0|^2\,\mathrm{Im}\,G^r_{AA}(\omega) = 2\pi\omega|f_0|^2 S_{AA}(\omega). \qquad (2.34)$$

A special role is played by the one-particle spectral function $S_{\boldsymbol{k}\sigma}$, where the operators $\hat{A}$ and $\hat{B}$ are the annihilation and creation operators $c_{\boldsymbol{k}\sigma}$ and $c^\dagger_{\boldsymbol{k}\sigma}$, respectively. In the case of non-interacting fermions, its Fourier transform is equal to the density of states of the system:

$$D(\omega) = \sum_{\boldsymbol{k}\sigma} S_{\boldsymbol{k}\sigma}(\omega). \qquad (2.35)$$

For interacting electrons, this quantity can still be identified with the quasiparticle density of states.

Denoting by $S_{ij\sigma}$ the spectral function associated to the operators $c_{i\sigma}$ and $c^\dagger_{j\sigma}$, the density of states (2.35) can equivalently be expressed in the real space basis,

$$D(\omega) = \sum_{i\sigma} S_{ii\sigma}(\omega) = \sum_i D_i(\omega), \qquad (2.36)$$

where $D_i(\omega)$ is the contribution of site i to the density of states, i.e. the local density of states at this site.

2.4. Singular Value Decomposition and Schmidt Decomposition

The singular value decomposition (SVD) is a matrix decomposition of an arbitrary complex matrix into a product of three matrices. It plays an important role in most MPS-based algorithms, because it allows for efficient truncation of the matrices and ensures unitarity [10].

---

[1]According to the definitions, the function χ_{AA} in [29] corresponds to $-G^r_{AA}$ in this thesis.

Theorem 1: Singular value decomposition

For every complex matrix $A \in \mathbb{C}^{m \times n}$ with rank r there are unitary matrices $U \in \mathbb{C}^{m \times m}$ and $V \in \mathbb{C}^{n \times n}$ and a square diagonal matrix $D \in \mathbb{R}^{\min(m,n) \times \min(m,n)}$ such that

$$A = U \Lambda V^{\dagger} \tag{2.37}$$

where

$$\Lambda = \begin{pmatrix} D \\ 0 \end{pmatrix} \ \ if \ m > n \quad or \quad \Lambda = \begin{pmatrix} D & 0 \end{pmatrix} \ \ if \ m < n \ .$$

The diagonal elements λ_i of D are called singular values *and can always be chosen to be real, and ordered $\lambda_1 \geq \lambda_2 \geq \ldots \geq \lambda_r > 0$ and $\lambda_{r+1} = \ldots = \lambda_{\min(m,n)} = 0$* [30].

Proof. For the proof the reader is referred to [30, p.150f]. $\qquad \square$

Since the part of Λ that contains only zeros does not contribute to the product, the decomposition can equivalently be represented with the square matrix D and accordingly truncated rectangular U or $V^{\dagger}$. The relations $U^{\dagger}U = V^{\dagger}V = \mathbb{1}$ then still hold true (but in general $UU^{\dagger} \neq \mathbb{1}$ and $VV^{\dagger} \neq \mathbb{1}$).

The numerical computation of an SVD with standard algorithms requires $\mathcal{O}(mn^2)$ floating point operations, where $m > n$ are the dimensions of the matrix [31].

Related to the SVD is the Schmidt decomposition of quantum mechanical states, which introduces the SVD as an important tool into the theory of matrix product states.

Theorem 2: Schmidt decomposition

Every pure state $|\psi\rangle$ of a system, which is composed of two subsystems A and B, can be written in the form

$$|\psi\rangle = \sum_{i=1}^{r} \lambda_i |A_i\rangle |B_i\rangle \ , \tag{2.38}$$

where $\{|A_i\rangle\}$ and $\{|B_i\rangle\}$ are orthonormal bases of the subsystems A and B, respectively, and λ_i are real, positive numbers with $\sum_i \lambda_i^2 = 1$. This decomposition is called the Schmidt decomposition *and the coefficients λ_i are called* Schmidt coefficients [32].

Proof. Let $\mathcal{H}_A$ be the n_A-dimensional Hilbert space of subsystem A and $\mathcal{H}_B$ the n_B-dimensional Hilbert space of subsystem B. Then the Hilbert space of the composite system $\mathcal{H}_{AB}$ is the tensor product of the Hilbert spaces of the subsystems, $\mathcal{H}_{AB} = \mathcal{H}_A \otimes \mathcal{H}_B$, and an arbitrary pure state of the composite system is given in terms of orthonormal bases $\{|\alpha_i\rangle\}$ and $\{|\beta_i\rangle\}$ of the subsystems by

$$|\psi\rangle = \sum_{j=1}^{n_A} \sum_{k=1}^{n_B} c_{jk} |\alpha_j\rangle |\beta_k\rangle \ . \tag{2.39}$$

The coefficients c_{jk} form an $n_A \times n_B$ matrix, which can be singular value decomposed

into

$$c_{jk} = \sum_{i=1}^{r} U_{ji} \lambda_i \left(V^\dagger\right)_{ik}$$

with unitary matrices U and V and χ the number of non-zero singular values, resulting in

$$|\psi\rangle = \sum_{j=1}^{n_A} \sum_{k=1}^{n_B} \sum_{i=1}^{r} U_{ji} \lambda_i \left(V^\dagger\right)_{ik} |\alpha_j\rangle |\beta_k\rangle = \sum_{i=1}^{r} \left(\sum_{j=1}^{n_A} U_{ji} |\alpha_j\rangle \right) \lambda_i \left(\sum_{k=1}^{n_B} \left(V^\dagger\right)_{ik} |\beta_k\rangle \right).$$

Since U and V are unitary, the sets

$$|A_i\rangle := \sum_{j=1}^{n_A} U_{ji} |\alpha_j\rangle \quad \text{and} \quad |B_i\rangle := \sum_{k=1}^{n_B} \left(V^\dagger\right)_{ik} |\beta_k\rangle$$

are also orthonormal bases of the subsystems A and B and the state $|\psi\rangle$ can be written in the form (2.38). The additional properties of the λ_i follow from the fact that they are singular values. $\qquad\square$

Hence, the Schmidt decomposition of a state $|\psi\rangle$ is equivalent to the SVD of its coefficient matrix as defined in (2.39) and the Schmidt values are simply the singular values of that matrix. The number of non-zero singular values r is the rank of the coefficient matrix and in this context is also called *Schmidt rank*.

An important application of the SVD is the approximation of matrices by matrices with lower rank, which is justified by the Eckart-Young-Mirsky theorem [33].

Theorem 3: Eckart-Young-Mirsky theorem

Let $A \in \mathbb{C}^{m \times n}$ have the singular value decomposition $A = U\Lambda V^\dagger$ with the singular values ordered by descending absolute value. Furthermore, let $A_k := U\Lambda_k V^\dagger$ where in Λ_k the singular values $\lambda_{k+1}, \ldots, \lambda_{\min(m,n)}$ are replaced by 0. Then

$$\|A - A_k\| \leq \|A - B\| \quad \forall\, B \in \mathbb{C}^{m \times n} \text{ with } \mathrm{rank}(B) = k \qquad (2.40)$$

for any unitarily invariant norm $\|\cdot\|$.

Proof. A proof for a general unitarily invariant norm is given in [33]. $\qquad\square$

The significance of this theorem for quantum mechanics and in particular for MPS is given by relating it to the Schmidt decomposition. If a state $|\psi\rangle$ is given in the form (2.39) in terms of orthogonal bases of two subsystems, then its norm

$$\||\psi\rangle\| = \left\| \sum_{jk} c_{jk} |\alpha_j\rangle |\beta_k\rangle \right\| = \sum_{jk} |c_{jk}|^2 \qquad (2.41)$$

is the Frobenius norm of the matrix defined by the coefficients c_{jk}. Since the Frobenius norm is unitarily invariant, we can apply the Eckart-Young-Mirsky theorem, stating that

the best (in the sense of the Frobenius norm) lower-rank approximation is given by truncating the singular values. Translating this result to the quantum states means that the best (in the sense of the usual Hilbert space norm) approximation to the state with lower Schmidt rank for the respective bipartition is obtained by simply truncating the Schmidt coefficients to the desired rank.

2.5. Subsystems and Entanglement

A system in a pure state $|\psi\rangle$ can equivalently be described by its density matrix [32]

$$\hat{\rho} = |\psi\rangle\langle\psi| , \tag{2.42}$$

and expectation values can be expressed as $\langle\hat{O}\rangle = \mathrm{tr}(\hat{\rho}\hat{O})$. If the system is composed of two subsystems A and B, meaning that its Hilbert space is $\mathcal{H} = \mathcal{H}_A \otimes \mathcal{H}_B$, then for observables only acting on subsystem A, the expectation value can be calculated with the *reduced density matrix*

$$\hat{\rho}_A = \mathrm{tr}_B(\hat{\rho}), \tag{2.43}$$

where tr_B denotes the partial trace over subsystem B (i.e. the trace is only carried out in $\mathcal{H}_B$) [32].

The entanglement between the two subsystems can be quantified with the help of the *von Neumann entropy* [34]. For a generic system in a state specified by the density operator $\hat{\rho}$, the von Neumann entropy is defined as

$$S(\hat{\rho}) = -\mathrm{tr}(\hat{\rho}\log\hat{\rho}) , \tag{2.44}$$

where the basis of the logarithm does not matter as long as it is used consistently. Throughout this thesis we will use the natural logarithm.

For a bipartition AB of a quantum system in a pure state, the von Neumann entropy of the reduced density matrix of either A or B (both yield the same value, as shown below) is a measure for the entanglement between the subsystems. It is therefore called *entanglement entropy* [34]

$$S_{AB} = S(\hat{\rho}_A) = S(\hat{\rho}_B) . \tag{2.45}$$

Theorem 4: Bipartite entanglement

Let a composite system AB be in an arbitrary pure state. The bipartite entanglement entropy between the subsystems A and B is given by

$$S_{AB} = -\sum_{\gamma=1}^{\chi} \lambda_\gamma^2 \log \lambda_\gamma^2,$$

where λ_γ are the Schmidt coefficients of the bipartition AB and χ is the corresponding Schmidt rank.

Proof. According to Theorem 2, a pure state $|\psi\rangle$ can be Schmidt-decomposed into

$$|\psi\rangle = \sum_i \lambda_i |A_i\rangle |B_i\rangle$$

The density matrix of the system is given by $\hat{\rho} = |\psi\rangle\langle\psi|$, which becomes

$$\hat{\rho} = \sum_{ij} \lambda_i \lambda_j |A_i\rangle |B_i\rangle \langle A_j| \langle B_j|$$

in the Schmidt basis. Using the fact that the $|B_i\rangle$ form an orthonormal basis of subsystem B, the reduced density matrix of subsystem A can be written as

$$\hat{\rho}_A \equiv \text{tr}_B\, \hat{\rho} = \sum_\gamma \langle B_\gamma| \left(\sum_{ij} \lambda_i \lambda_j |A_i\rangle |B_i\rangle \langle A_j| \langle B_j| \right) |B_\gamma\rangle = \sum_\gamma \lambda_\gamma^2 |A_\gamma\rangle\langle A_\gamma|$$

and, analogously, the reduced density matrix of subsystem B reads

$$\hat{\rho}_B \equiv \text{tr}_A\, \hat{\rho} = \sum_\gamma \lambda_\gamma^2 |B_\gamma\rangle\langle B_\gamma| \ .$$

The von Neumann entropies as defined in (2.44) for these density matrices can be easily calculated, because they are already written in terms of their eigenbases. One obtains the same result for both subsystems,

$$S(\hat{\rho}_A) = S(\hat{\rho}_B) = -\sum_\gamma \lambda_\gamma^2 \log \lambda_\gamma^2 \ .$$

$\square$

2.5.1. Area Laws

In the ground states of gapped[1] systems with local interactions, the bipartite entanglement satisfies an *area law* [34]. This means that the entanglement entropy has an upper bound that is not proportional to the volume of the system (as for a random state), but rather to the area of the boundary between the two subsystems.

In one dimension, the boundary between any two complementary subsystems is a single point (or two for periodic boundary conditions). Therefore, in this case the area law implies that the entanglement entropy is bounded by a constant independent of the system size.

For critical one-dimensional systems, the entanglement scales as $\log(L)$ [35].

---

[1]Gapped means that there is a finite energy gap between the ground state and the first excited state in the thermodynamic limit.

2.6. Loschmidt Amplitude and Eigenstate Spectrum

The Loschmidt amplitude

$$L(t) = \langle\psi|e^{-i\hat{H}t}|\psi\rangle \tag{2.46}$$

and the related Loschmidt echo are usually used in the context of quantum chaos [36, 37] and work done by quenches [38, 39], but the Loschmidt amplitude has recently proved as a powerful tool to numerically determine the eigenstate spectrum of an arbitrary state [6, 40].

Expanding the state $|\psi\rangle$ in the orthonormal eigenstates $|n\rangle$ of the Hamiltonian, $|\psi\rangle = \sum_n c_n |n\rangle$, the Loschmidt amplitude (2.46) reads

$$L(t) = \sum_{nn'} c_n^* c_{n'} \langle n|e^{-i\hat{H}t}|n'\rangle = \sum_{nn'} c_n^* c_{n'} e^{-iE_n t} \langle n|n'\rangle = \sum_n |c_n|^2 e^{-iE_n t}. \tag{2.47}$$

We can therefore extract the overlaps with the eigenstates $|c_n|^2 = |\langle n|\psi\rangle|^2$ by Fourier transforming the Loschmidt amplitude:

$$\int_{-\infty}^{\infty} L(t) e^{i\omega t} \, dt = \sum_n |c_n|^2 \int_{-\infty}^{\infty} e^{i(\omega - E_n)t} \, dt = 2\pi \sum_n |c_n|^2 \delta(\omega - E_n). \tag{2.48}$$

To obtain the Loschmidt amplitude numerically, the initial state $|\psi\rangle$ is time evolved with a method of choice and the overlap with the initial state is measured in regular intervals, which yields a time series $\langle\psi|\psi(t_i)\rangle = \langle\psi|e^{-i\hat{H}t_i}|\psi\rangle = L(t_i)$. Due to the finite time evolution it is advisable to use a window function for the Fourier transformation, which we choose to be a half Gaussian $\Theta(t) e^{-\eta t^2}$ ($\Theta(t)$ is the Heavyside step function). The eigenstate spectrum is then obtained by evaluating the integral

$$\int_0^{\infty} L(t) e^{i\omega t - \eta t^2} \, dt = \sum_n |c_n|^2 \int_0^{\infty} e^{i(\omega - E_n)t - \eta t^2} \, dt, \tag{2.49}$$

which in practice is cut off at a certain value $t_{\max}$ where the window function $e^{-\eta t^2}$ is already close to zero. The remaining integral in (2.49) can be rewritten as

$$\int_0^{\infty} e^{i(\omega - E_n)t - \eta t^2} \, dt = \frac{e^{-\alpha^2}}{\sqrt{\eta}} \int_{0-i\alpha}^{\infty-i\alpha} e^{-z^2} \, dz \qquad \text{with } \alpha := \frac{\omega - E_n}{2\sqrt{\eta}},$$

which by Cauchy's theorem is equal to

$$\frac{e^{-\alpha^2}}{\sqrt{\eta}} \left(\int_0^{\infty} e^{-z^2} \, dz - \int_0^{-i\alpha} e^{-z^2} \, dz \right).$$

Since on the path in the second integral, z is purely imaginary, $z =: ix$, the integrand e^{x^2} is real and $dz = i \, dx$ is imaginary. Therefore, the whole integral is purely imaginary, while the first integral is obviously purely real and evaluates to $\sqrt{\pi}/2$.

Thus, by taking the real part of (2.49) we obtain

$$\mathcal{L}(\omega) := \mathrm{Re}\left(\int_0^\infty L(t)\, \mathrm{e}^{\mathrm{i}\omega t - \eta t^2}\, \mathrm{d}t\right) = \sqrt{\frac{\pi}{4\eta}} \sum_n |c_n|^2 \exp\left(-\frac{(\omega - E_n)^2}{4\eta}\right), \qquad (2.50)$$

which is the eigenstate spectrum of the state $|\psi\rangle$ with a Gaussian broadening of width $\sigma = \sqrt{2\eta}$.

3. Correlated Electron Models

3.1. Heisenberg Models

Heisenberg noticed that ferromagnetism originates from the interaction of electrons in a many-electron system and can be described with the spins of electrons on a fixed lattice [41]. The Hamiltonian corresponding to the Heisenberg model reads

$$\hat{H}_{\text{Heis}} = -J \sum_{\langle ij \rangle} \hat{\boldsymbol{S}}_i \cdot \hat{\boldsymbol{S}}_j \,, \tag{3.1}$$

where J is the exchange coupling and $\langle ij \rangle$ denotes all ordered pairs of nearest neighbors in the crystal lattice. The operators $\hat{\boldsymbol{S}}_i$ are the usual spin-1/2 operators (which are represented by the Pauli matrices in the z-basis) with the commutation relations

$$[\hat{S}_i^\alpha, \hat{S}_j^\beta] = \mathrm{i} \sum_\gamma \varepsilon_{\alpha\beta\gamma} \hat{S}_i^\gamma \delta_{ij}, \quad \alpha, \beta, \gamma \in \{x, y, z\}. \tag{3.2}$$

For $J > 0$, the energy is lower if the spins are aligned, hence the model describes a ferromagnetic interaction. If $J < 0$, antiparallel alignment of the spins is favored and in this case, (3.1) describes an antiferromagnet [42].

The Hamiltonian (3.1) describes the special case of a system with homogeneous and isotropic exchange coupling. For a generic system of spins fixed in space with nearest neighbor interactions (sometimes called *XYZ model*) the Hamiltonian is given by

$$\hat{H}_{\text{XYZ}} = - \sum_{\langle ij \rangle} \left(J_{ij}^x \hat{S}_i^x \hat{S}_j^x + J_{ij}^y \hat{S}_i^y \hat{S}_j^y + J_{ij}^z \hat{S}_i^z \hat{S}_j^z \right)$$

with different couplings in each direction and on each site.

Apart from the isotropic Heisenberg model (3.1) another frequently used special case is the *XXZ model*, where the coupling is assumed to be the same in two directions and different in the third. Expressing the $\hat{S}^x$ and $\hat{S}^y$ operators in terms of the ladder operators

$$\hat{S}^\pm = \hat{S}^x \pm \mathrm{i} \hat{S}^y$$

and assuming a homogeneous system leads to the Hamiltonian

$$\hat{H}_{\text{XXZ}} = - \sum_{\langle ij \rangle} \left[\tfrac{1}{2} J^{xy} \left(\hat{S}_i^+ \hat{S}_j^- + \hat{S}_i^- \hat{S}_j^+ \right) + J^z \hat{S}_i^z \hat{S}_j^z \right]. \tag{3.3}$$

By the transformation $\hat{S}_i^x \to (-1)^i \hat{S}_i^x$, $\hat{S}_i^y \to (-1)^i \hat{S}_i^y$, $\hat{S}_i^z \to \hat{S}_i^z$ (which leaves the commutation relations (3.2) unchanged) one can see that the model for J^{xy} and $-J^{xy}$ is equivalent

on a bipartite lattice. Hence, we can restrict J^{xy} to positive values and the character of the model can only depend on the sign of J^z. Comparison with the isotropic case (3.1) shows that the model describes a ferromagnet for $J^z = J^{xy}$ (and also for $J^z > J^{xy}$) and an antiferromagnet for $J^z = -J^{xy}$ (and also for $J^z < -J^{xy}$) [42].

In the limit of very large anisotropy $J^z/J^{xy} \to \pm\infty$, the XXZ model becomes equal to the Ising model.

3.1.1. Ground State of the XXZ Model in 1D

Being an integrable model (see Section 3.4), the XXZ model can be solved exactly by the Bethe ansatz in one dimension [43]. Often, Bethe ansatz calculations are rather cumbersome and still involve a numerical solution in the end, but for the ground state energy of the XXZ model with $\sum_i \left\langle \hat{S}_i^z \right\rangle = 0$ and $\Delta := J^z/J^{xy} < -1$ in the thermodynamic limit, Yang and Yang [44, 45] have found the explicit formula

$$\lim_{L \to \infty} \frac{E_0}{J^{xy}L} = -\frac{\Delta}{4} - \sqrt{\Delta^2 - 1} \left(\frac{1}{2} + 2\sum_{n=1}^{\infty} \left[1 + e^{2n\lambda} \right]^{-1} \right), \tag{3.4}$$

where $\cosh(\lambda) = -\Delta$ and $\lambda > 0$.

In the antiferromagnetic phase at $\Delta < -1$, the model is known to have a two-fold degenerate ground state with a gap to the first excited state in the thermodynamic limit [46]. Assuming a finite even number of sites with open boundary conditions, the ground state is non-degenerate [46] and the energy difference between the two lowest states (which become the degenerate ground state in the thermodynamic limit) vanishes exponentially when $L \to \infty$ [47].

3.1.2. Symmetries and Conserved Quantities in the XXZ Model

Due to the isotropy in the x-y plane, the XXZ Hamiltonian (3.3) has a rotational symmetry around the z-axis. Global rotation of spins around the z-axis is generated by the z-component of the total spin $\hat{\mathcal{S}}^z := \sum_i \hat{S}_i^z$, which is thus the conserved quantity corresponding to this continuous symmetry [48],

$$[\hat{H}_{\mathrm{XXZ}}, \hat{\mathcal{S}}^z] = 0. \tag{3.5}$$

Besides, the Hamiltonian is invariant under flipping all spins ($\hat{S}_i^+ \leftrightarrow \hat{S}_i^-$, $\hat{S}_i^z \to -\hat{S}_i^z$ for all i). This corresponds to the particle-hole symmetry of the equivalent fermionic T-V model (Section 3.2).

3.2. Interacting Spinless Fermions (T-V Model)

The T-V model describes spinless fermions with nearest-neighbor interactions [7]. In real materials, spinless electrons do not exist, but this simple model is a good starting point

for the theoretical investigation of strongly correlated electrons. Besides, in one dimension with open boundary conditions it is equivalent to the XXZ model (see Section 3.2.1).

Usually, the hopping integral giving the model its name is denoted by a lowercase t, but to avoid confusion with time, we use a **capital T for the hopping** in this thesis. Therefore, we also refer to this model as the T-V model, whereas in the literature it is commonly known as t-V model.

The model is obtained from the tight-binding model by adding nearest-neighbor Coulomb interactions, i.e.

$$\hat{H}_{\mathrm{TV}} = \sum_{\langle ij \rangle} \left(-T c_i^\dagger c_j - T^* c_j^\dagger c_i + V \hat{n}_i \hat{n}_j \right). \tag{3.6}$$

It is easy to check that the Hamiltonian commutes with the operator of the total particle number $\hat{N} = \sum_i \hat{n}_i$ and therefore the particle number is conserved.

Throughout this thesis, we use the particle-hole symmetric version of the Hamiltonian. In one dimension with open boundary conditions, it reads

$$\hat{H}_{\mathrm{TV}} = \sum_{i=1}^{L-1} \left(-T c_i^\dagger c_{i+1} - T^* c_{i+1}^\dagger c_i + V \left(\hat{n}_i - \tfrac{1}{2} \right) \left(\hat{n}_{i+1} - \tfrac{1}{2} \right) \right), \tag{3.7}$$

and thus differs from (3.6) by the terms

$$V \sum_{i=1}^{L-1} \left(-\tfrac{1}{2} \hat{n}_i - \tfrac{1}{2} \hat{n}_{i+1} + \tfrac{1}{4} \right) = -V \hat{N} + V \frac{L-1}{4} + \frac{1}{2} (\hat{n}_1 + \hat{n}_L).$$

The first term, which is proportional to the total particle number, is either constant or can be absorbed into the chemical potential in a grand-canonical description, and the second term is constant anyway. Hence, the two Hamiltonians are equivalent except for the boundary term. A proof that (3.7) is particle-hole symmetric is given in Appendix B.

3.2.1. Equivalence to the XXZ Model in 1D

On a local single-particle Hilbert space, the action of spin operators on a spin-1/2 particle is identical to the action of creation and annihilation operators on the isomorphic local Hilbert space of a spinless fermionic orbital. In terms of their action on basis states, these operators are defined by

$$\begin{aligned} c \,|0\rangle = c^\dagger |1\rangle &= 0\,, & \hat{S}^- |\downarrow\rangle = \hat{S}^+ |\uparrow\rangle &= 0\,, \\ c^\dagger |0\rangle &= |1\rangle\,, & \hat{S}^+ |\downarrow\rangle &= |\uparrow\rangle\,, \\ c \,|1\rangle &= |0\rangle\,, & \hat{S}^- |\uparrow\rangle &= |\downarrow\rangle\,. \end{aligned}$$

For a single particle we thus have the analogies

$$|0\rangle \leftrightarrow |\downarrow\rangle\,, \quad |1\rangle \leftrightarrow |\uparrow\rangle\,, \quad c \leftrightarrow \hat{S}^-\,, \quad c^\dagger \leftrightarrow \hat{S}^+\,, \quad \hat{n} = c^\dagger c \leftrightarrow \hat{S}^z + \tfrac{1}{2}\,.$$

However, on a Fock space comprising multiple local Hilbert spaces (e.g. a lattice with multiple sites), the action of fermionic and spin operators differs due to the commutation rules. While fermionic operators acting on different sites anticommute, spin operators commute. To map these operators onto each other, we make use of the Jordan-Wigner transformation [49].

Let $b_j^\dagger, b_j$ be creation and annihilation operators, which obey the commutation rules of the spin operators, i.e.

$$[\hat{S}_i^-, \hat{S}_j^-] = 0 \qquad \leftrightarrow \qquad [b_i, b_j] = 0,$$
$$[\hat{S}_i^+, \hat{S}_j^-] = 2\hat{S}_i^z \delta_{ij} \qquad \leftrightarrow \qquad [b_i^\dagger, b_j] = (2b_i^\dagger b_i - 1)\delta_{ij}.$$

To obtain the desired fermionic anticommutation rules, we define new operators

$$c_j = \exp\left(\mathrm{i}\pi \sum_{n=1}^{j-1} b_n^\dagger b_n\right) b_j. \tag{3.8}$$

By counting the number of fermions "before" the site j where the operator is applied, this transformation introduces the sign, which originates from shifting the operator past the creation operators in a natural-ordered fermionic basis state

$$(c_1^\dagger)^{n_1} \cdots (c_M^\dagger)^{n_M} |0\rangle.$$

The proof that the operators c_j and $c_j^\dagger$ defined by (3.8) indeed fulfill the fermionic anticommutation relations is given in Appendix C.

Writing the Hamiltonian of the one-dimensional XXZ model with *open boundary conditions* in terms of the operators b and $b^\dagger$ (which corresponds to a simple renaming of states and operators) yields

$$\hat{H}'_{\mathrm{XXZ}} = -\sum_{j=1}^{L-1} \left[\tfrac{1}{2}J^{xy}\left(b_j^\dagger b_{j+1} + h.c.\right) + J^z\left(b_j^\dagger b_j - \tfrac{1}{2}\right)\left(b_{j+1}^\dagger b_{j+1} - \tfrac{1}{2}\right)\right]. \tag{3.9}$$

In the on-site terms like $b_j^\dagger b_j$, the phase factors from the transformation (3.8) cancel out and therefore $b_j^\dagger b_j = c_j^\dagger c_j$. Applying the inverse of the transformation to the term $b_j^\dagger b_{j+1}$ results in

$$b_j^\dagger b_{j+1} = c_j^\dagger \exp\left(-\mathrm{i}\pi c_j^\dagger c_j\right) c_{j+1} = c_j^\dagger c_{j+1},$$

because the creation operator to the left of the exponential forces the site j to be empty before its application. We obtain

$$\hat{H}'_{\mathrm{XXZ}} = -\sum_{j=1}^{L-1} \left[\tfrac{1}{2}J^{xy}\left(c_j^\dagger c_{j+1} + h.c.\right) + J^z\left(\hat{n}_j - \tfrac{1}{2}\right)\left(\hat{n}_{j+1} - \tfrac{1}{2}\right)\right], \tag{3.10}$$

which is exactly the Hamiltonian of the one-dimensional, particle-hole symmetric T-V model with $T = J^{xy}/2$ and $V = -J^z$.

Since the Hamiltonians (3.9) and (3.10), corresponding to the XXZ model and the T-V model in one dimension with open boundary conditions, are formally equivalent, they share the same spectrum and therefore all expectation values are identical. However, $\hat{S}^\pm$ and $c^\dagger, c$ are still different operators and correlation functions such as $\langle \hat{S}_i^+ \hat{S}_j^- \rangle$ and $\langle c_i^\dagger c_j \rangle$ are in general different from each other (except if i and j are nearest neighbors).

3.2.2. Ground State of the T-V Model in 1D

Due to the equivalence to the XXZ model with open boundary conditions via the Jordan-Wigner transformation, the T-V model shares the ground state properties of the XXZ model (see Section 3.1.1). Using (3.4) with the substitutions $J^{xy} = 2T$ and $\Delta = -V/2T$, we obtain for the ground state energy for $V/T > 2$ at half filling in the thermodynamic limit

$$\lim_{L \to \infty} \frac{E_0}{TL} = \frac{V}{4T} - \sqrt{(V/T)^2 - 4} \left(\frac{1}{2} + 2 \sum_{n=1}^{\infty} \left[1 + e^{2n\lambda} \right]^{-1} \right), \tag{3.11}$$

where $\cosh(\lambda) = V/2T$ and $\lambda > 0$. This result furthermore enables us to calculate an exact expression for the ground state nearest-neighbor occupancy

$$\mathcal{N} := \sum_{i=1}^{L-1} \left\langle (n_i - \tfrac{1}{2})(n_{i+1} - \tfrac{1}{2}) \right\rangle \tag{3.12}$$

per site, because

$$E = \left\langle \hat{H}_{\text{TV}} \right\rangle = -T \sum_{i=1}^{L-1} \left\langle c_i^\dagger c_{i+1} + h.c. \right\rangle + V\mathcal{N}$$

and hence $\mathcal{N} = \partial E / \partial V$. Thus, the nearest-neighbor occupancy per site in the ground state is given by the derivative of (3.11) with respect to V,

$$\lim_{L \to \infty} \frac{\mathcal{N}_0}{L} = \frac{1}{4} - \frac{V}{\sqrt{V^2 - 4T^2}} \left(\frac{1}{2} + 2 \sum_{n=1}^{\infty} \left[1 + e^{2n\lambda} \right]^{-1} \right) + 2 \sum_{n=1}^{\infty} n \left[1 + \cosh(2n\lambda) \right]^{-1}. \tag{3.13}$$

When exchanging the order of the limit and the derivative we implicitly assumed that $\mathcal{N}_0/L$ as a function of V converges uniformly on $(2T, \infty)$ as $L \to \infty$ [50, thm 7.17].

3.2.3. Extensions of the T-V Model

Due to the $1/r$-dependence of the Coulomb potential and particularly the exponential screening by other electrons, in real materials the two-body interaction decreases rapidly with distance. This justifies the restriction of the interaction V to nearest neighbors in the T-V model. The hopping integrals are also much smaller for more distant sites because of the strong localization of the Wannier functions. Nevertheless, the most obvious extension of the T-V model is the inclusion of next-nearest neighbor terms, which leads to what we will call the *extended T-V model*. In one dimension, its Hamiltonian is given by

$$\hat{H}_{\text{TVe}} = \hat{H}_{\text{TV}} + \sum_{i=1}^{L-2} \left(-T_2 c_i^\dagger c_{i+2} - T_2^* c_{i+2}^\dagger c_i + V_2 \left(\hat{n}_i - \tfrac{1}{2} \right) \left(\hat{n}_{i+2} - \tfrac{1}{2} \right) \right). \tag{3.14}$$

For $T_2 \neq 0$, the model is no longer particle-hole symmetric, because no bipartition of the system provides opposite signs for both nearest and next-nearest neighbor pairs. Therefore, the change of sign in the hopping part of the Hamiltonian can no longer be compensated by a canonical transformation (see Appendix B).

3.3. Hubbard Model

The Hubbard model was introduced by John Hubbard to describe the correlations of d-electrons in solids [51]. Starting from the generic Hamiltonian of electrons with two-body interaction on a lattice with L sites,

$$\hat{H} = -\sum_{i,j=1}^{L}\sum_{\sigma} T_{ij} c_{i\sigma}^{\dagger} c_{j\sigma} + \sum_{i,j,k,l=1}^{L}\sum_{\sigma\sigma'} U_{ijkl} c_{i\sigma}^{\dagger} c_{j\sigma'}^{\dagger} c_{k\sigma'}^{\dagger} c_{l\sigma} \, ,$$

he argued that the on-site Coulomb interaction U_{iiii} is much larger than the other elements of U_{ijkl} and proposed the approximation $U_{ijkl} \approx \frac{U}{2}\delta_{ij}\delta_{ik}\delta_{il}$. This leads to the Hamiltonian

$$\hat{H} = -\sum_{i,j=1}^{L}\sum_{\sigma} T_{ij} c_{i\sigma}^{\dagger} c_{j\sigma} + \frac{U}{2}\sum_{i=1}^{L}\sum_{\sigma,\sigma'} \hat{n}_{i\sigma}\hat{n}_{i\sigma'}$$

$$= -\sum_{i,j=1}^{L}\sum_{\sigma} T_{ij} c_{i\sigma}^{\dagger} c_{j\sigma} + U\sum_{i=1}^{L} \hat{n}_{i\uparrow}\hat{n}_{i\downarrow} + \frac{U}{2}\sum_{i=1}^{L}(\hat{n}_{i\uparrow} + \hat{n}_{i\downarrow}) \, ,$$

where $\hat{n}_{i\sigma} = c_{i\sigma}^{\dagger} c_{i\sigma}$ is the particle number operator counting the particles with spin σ at site i. The last term is proportional to the total number of electrons and can therefore be dropped, since it is either constant for a fixed particle number or can be absorbed into the chemical potential in a grand-canonical description.

A further commonly applied approximation is to restrict the range of the hopping T_{ij} to nearest neighbors. Assuming homogeneous and isotropic hopping T, we obtain the following simple Hamiltonian, which in this thesis will be referred to as the *Hubbard model*:

$$\hat{H}_{\text{Hub}} = -T\sum_{\langle ij\rangle}\sum_{\sigma} c_{i\sigma}^{\dagger} c_{j\sigma} + U\sum_{i=1}^{L} \hat{n}_{i\uparrow}\hat{n}_{i\downarrow} \, . \tag{3.15}$$

The term with $i = j$ was omitted, because it is again proportional to the total particle number.

In the limit of very strong coupling $U \gg T$, the Hubbard model (3.15) at half filling is equivalent to the isotropic Heisenberg antiferromagnet with $J = -2T^2/U$ [17, 4.1.6].

In one dimension, the Hubbard Hamiltonian simplifies to

$$\hat{H} = -T\sum_{i=1}^{L-1}\sum_{\sigma}(c_{i\sigma}^{\dagger} c_{i+1,\sigma} + c_{i+1,\sigma}^{\dagger} c_{i\sigma}) + U\sum_{i=1}^{L} \hat{n}_{i\uparrow}\hat{n}_{i\downarrow} \, . \tag{3.16}$$

3.4. Integrability

Integrability is a concept that originates from classical mechanics. A classical system with N coordinates (i.e. a $2N$-dimensional phase space) is said to be integrable if N independent constants of motion exist, providing the possibility to integrate the equations of motion from given initial conditions.

Although this concept is not trivially extendible to quantum mechanics for several reasons [48, 52], the term is often used in the context of quantum mechanical models and commonly equated with solvability by the Bethe ansatz (which was introduced by Hans Bethe in 1931 [43] and has since then been used to exactly solve numerous models). Assuming a quantum system on a lattice, a possible definition of integrability that keeps the spirit of the classical definition is, that a system is integrable if one can find an extensive number (i.e. infinitely many in the thermodynamic limit) of *local* operators which commute with each other and with the Hamiltonian [52][1].

All models mentioned above (isotropic Heisenberg model, XXZ model, T-V model and Hubbard model) are integrable in one dimension [52], but only as long as the interaction range does not exceed nearest neighbors [7].[2]

3.5. Impact Ionization

Impact ionization originally refers to ionization by electron-electron scattering in atoms (e.g. in gas discharges) [54] or semiconductors [55]. In the latter case, a high-energy electron in the conduction band creates a second electron-hole pair by lifting another electron from the valence band to the conduction band. A comparable process can also occur in excited states of Mott-Hubbard insulators (insulating phases of the Hubbard model), where a high-energy electron in the upper Hubbard band can excite a second electron from the lower into the upper band. In the Hubbard model, this corresponds to the creation a doublon-hole pair (one doubly occupied and one empty site) [3].

This process can thus create additional charge carriers using excess energy of excited electrons, if it happens on a shorter time scale than electron-phonon scattering (or scattering with other degrees of freedom such as spin). Concerning an application as a solar cell, this would allow to obtain multiple excitons from a single high-energy photon and therefore to overcome the Shockley-Queisser limit [1] which sets an upper bound to the efficiency of photovoltaic cells operated with the sun's blackbody radiation [3, 56]. In conventional semiconductor-based solar cells, impact ionization does not play a significant role because electron-phonon scattering in these materials is faster than electron-electron scattering [57, 58].

Since the total number of doublons in the Hubbard model is proportional to the potential energy (see Section 3.3), impact ionization can as well be viewed as a conversion of kinetic energy into potential energy mediated by electron-electron interactions [5]. Transferring this idea to the T-V model of spinless fermions (Section 3.2), we can equate impact ionization in the Hubbard model with an increase of the nearest-neighbor occupancy $\mathcal{N}$ at the expense of kinetic energy. In the context of the T-V model, we will therefore refer to this process as impact ionization. A more detailed analysis of the phenomena in the T-V model is given in Section 5.2.4.

---

[1]In the reference this is referred to as *linear integrability*.

[2]With next-nearest neighbor density interactions, the model can be made integrable by adding a conserved term to the Hamiltonian [53, sec. 4.3.2].

In the Hubbard model, impact ionization has been observed in various theoretical calculations in many lattice geometries [3, 5, 6]. It has, however, not occurred in the one-dimensional Hubbard model with only nearest-neighbor coupling [5], which is an integrable model. On the other hand, the Hubbard model with a ladder geometry (equivalent to a chain with additional longer-range couplings, not integrable) did show impact ionization [5]. One might therefore conjecture that integrability with its extensive number of conserved quantities is the reason for the absence of impact ionization in the 1D Hubbard model. A closer investigation of the relationship between integrability and impact ionization, using the T-V model as a simple example, is one of the purposes of this thesis and will be done in Section 5.2. It will turn out that non-integrability does not always coincide with the occurrence of impact ionization.

4. Matrix Product States (MPS)

When working with many-particle systems, one always encounters the problem of exponential growth of the Hilbert space with the system size. This makes it impossible to store generic states of large systems on a classical computer. For a certain important class of states, namely ground states of local gapped Hamiltonians in one dimension, matrix product states provide an efficient parametrization for very good approximations to the state [10].

This chapter gives an overview of matrix product states and the related methods used in the present thesis and is mainly based on the review by Schollwöck [10].

4.1. Decomposition of States into Matrix Products

Consider a quantum system on a lattice with L sites and a local Hilbert space $\mathcal{H}_{\text{loc}}$ with dimension d at each site. A general pure state of this system can be written in the form

$$|\psi\rangle = \sum_{s_1,s_2,\ldots,s_L=1}^{d} c_{s_1 s_2 \ldots s_L} |s_1 s_2 \ldots s_L\rangle \tag{4.1}$$

where $|s_j\rangle \in \mathcal{H}_{\text{loc}}$ are the local basis vectors at site j, e.g. $s_j \in \{\uparrow, \downarrow\}$ for the Heisenberg model or $s_j \in \{0, \uparrow, \downarrow, \uparrow\downarrow\}$ for the Hubbard model, and $c_{s_1 s_2 \ldots s_L}$ are the d^L complex coefficients of the basis vectors of the product space $\mathcal{H}_{\text{loc}}^L$. These coefficients can be thought of as a $d \times d^{L-1}$ matrix $c_{s_1(s_2 \ldots s_L)}$ and singular-value decomposed into

$$c_{s_1(s_2 \ldots s_L)} = \sum_{\alpha_1=1}^{d} U_{s_1 \alpha_1}^{(1)} \lambda_{\alpha_1} V_{\alpha_1(s_2 \ldots s_L)}^{\dagger} =: \sum_{\alpha_1=1}^{d} U_{s_1 \alpha_1}^{(1)} c_{\alpha_1 s_2 \ldots s_L}^{(1)}.$$

The new matrix $U_{s_1 \alpha_1}^{(1)}$ is of dimension $d \times d$. Now the indices of $c^{(1)}$ can be regrouped as $c_{(\alpha_1 s_2)(s_3 \ldots s_L)}^{(1)}$ and a singular value decomposition of this matrix leads to

$$c_{s_1 s_2 \ldots s_L} = \sum_{\alpha_1=1}^{d} \sum_{\alpha_2=1}^{d^2} U_{s_1 \alpha_1}^{(1)} U_{(\alpha_1 s_2)\alpha_2}^{(2)} c_{\alpha_2 s_3 \ldots s_L}^{(2)}$$

with a new $d^2 \times d^2$-matrix $U_{(\alpha_1 s_2)\alpha_2}^{(2)}$. Relabeling $U_{s_1 \alpha_1}^{(1)} = A_{\alpha_1}^{[1]s_1}$ and $U_{(\alpha_1 s_2)\alpha_2}^{(2)} = A_{\alpha_1 \alpha_2}^{[2]s_2}$ and repeating the procedure for all indices s_i finally results in

$$c_{s_1 s_2 \ldots s_L} = \sum_{\{\alpha_i\}} A_{\alpha_1}^{[1]s_1} A_{\alpha_1 \alpha_2}^{[2]s_2} A_{\alpha_2 \alpha_3}^{[3]s_3} \ldots A_{\alpha_{L-2}\alpha_{L-1}}^{[L-1]s_{L-1}} A_{\alpha_{L-1}}^{[L]s_L}.$$

The state that was originally described by the coefficients $c_{s_1 s_2 \ldots s_L}$ can then be written in terms of the matrices $A^{[j]s_j}$ as

$$|\psi\rangle = \sum_{\{s_i\}} \sum_{\{\alpha_i\}} A^{[1]s_1}_{\alpha_1} A^{[2]s_2}_{\alpha_1 \alpha_2} A^{[3]s_3}_{\alpha_2 \alpha_3} \ldots A^{[L-1]s_{L-1}}_{\alpha_{L-2}\alpha_{L-1}} A^{[L]s_L}_{\alpha_{L-1}} |s_1 s_2 \ldots s_L\rangle \tag{4.2}$$

with the shorthand notation $\sum_{\{s_i\}}$ for summation over $s_1, \ldots, s_L$ from 1 to d. This form is called *matrix product state* (MPS). Up to here, no approximations have been made and (4.1) and (4.2) are equivalent representations of the same state.

MPS can also be thought of as a generalization of product states. If all matrices are 1-by-1, the form (4.2) falls apart into

$$|\psi\rangle = \left(\sum_{s_1=1}^{d} A^{[1]s_1} |s_1\rangle \right) \otimes \left(\sum_{s_2=1}^{d} A^{[2]s_2} |s_2\rangle \right) \otimes \ldots \otimes \left(\sum_{s_L=1}^{d} A^{[L]s_L} \right) \tag{4.3}$$

with scalars $A^{[j]s_j}$, which is a generic product state. Thus, product states are a subset of MPS, namely those with 1-by-1 matrices.

In terms of memory required to store the state, the exact MPS representation does not have any advantage over the representation (4.1), because the j-th matrices $A^{[j]s_j}$ are of dimension $d^{j-1} \times d^j$, i.e. the required matrix dimensions to describe a generic state grow exponentially with the size of the system. However, many physically relevant states can be very well approximated by MPS with much smaller matrix dimensions. In particular this is true for the ground states of one-dimensional gapped systems [10], which has to do with the area law for the entanglement entropy that they satisfy (see Section 2.5.1).

4.2. Graphical Representation of Tensor Networks

Matrix product states and manipulations on them can be visualized using the graphical notation for tensors proposed by Penrose [59]. A tensor is represented by a geometrical shape with one "leg" for each index, thus the number of legs is equal to the rank of the tensor. As an example for this notation, the graphical representation of a rank 3 tensor is shown in Figure 4.1.
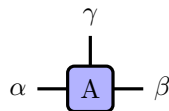

Figure 4.1. Graphical representation of a tensor $A_{\alpha\beta\gamma}$.

Contraction of two tensors is indicated by connecting the corresponding legs and a tensor product by simple juxtaposition (see Figure 4.2).

Concerning MPS, the matrices $A^{[j]s_j}$ can be interpreted as third rank tensors $A^{[j]s_j}_{\alpha_{j-1}\alpha_j}$ and the state (or actually the tensor of coefficients $c_{s_1 s_2 \ldots s_L}$) is given by the contraction of adjacent tensors over the indices α_j, as shown in Figure 4.3.
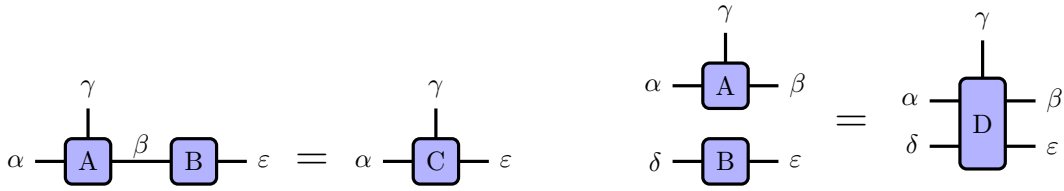
Figure 4.2. Graphical representation of the tensor contraction $A_{\alpha\beta\gamma}B_{\beta\varepsilon} = C_{\alpha\varepsilon\gamma}$ (left) and the tensor product $A_{\alpha\beta\gamma}B_{\delta\varepsilon} = D_{\alpha\beta\gamma\delta\varepsilon}$ (right).
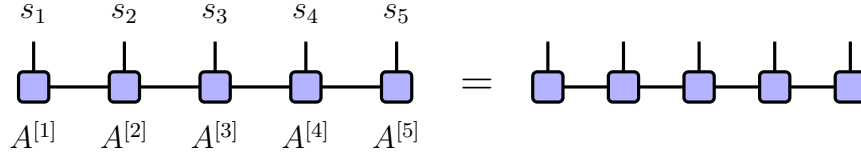

Figure 4.3. Graphical representation of an MPS with 5 sites. The labels of the tensors and indices are often omitted, because they provide no important information.

The up-pointing indices s_i are the indices of the coefficient $c_{s_1 s_2 \ldots s_L}$, which are called *physical indices* or *site indices*, while the (horizontal) matrix indices arise from the decomposition and are called *bond indices* or *auxiliary indices*.

4.3. Canonical Representations

The MPS representation (4.2) is not unique, because any transformation of the form

$$A^{[j]s_j} \to A^{[j]s_j} X, \quad A^{[j+1]s_{j+1}} \to X^{-1} A^{[j+1]s_{j+1}}$$

with an arbitrary invertible matrix X gives a different set of matrices which describe the same state. Hence, MPS have a gauge degree of freedom. This fact allows to demand additional properties of the matrices, which can drastically facilitate manipulations of the MPS. These special gauges are called *canonical forms* [10].

4.3.1. Left- and Right-Canonical Form

By the construction described in Section 4.1 the matrices obey

$$\sum_{s_j=1}^{d} \sum_{\beta=1}^{\chi_{j-1}} A^{[j]s_j\dagger}_{\alpha\beta} A^{[j]s_j}_{\beta\gamma} = \sum_{s_j=1}^{d} \sum_{\beta=1}^{\chi_{j-1}} A^{[j]s_j*}_{\beta\alpha} A^{[j]s_j}_{\beta\gamma} = \sum_{s_j=1}^{d} \sum_{\beta=1}^{\chi_{j-1}} U^{(j)*}_{(\beta s_j)\alpha} \, U^{(j)}_{(\beta s_j)\gamma}$$

$$= \sum_{(\beta s_j)=1}^{d\chi_{j-1}} U^{(j)\dagger}_{\alpha(\beta s_j)} U^{(j)}_{(\beta s_j)\gamma} = \delta_{\alpha\gamma}$$

because $U^{(j)}$ originates from an SVD and is therefore unitary. Here, χ_{j-1} is the dimension of the $(j-1)$-th bond index, called the *bond dimension* at that bond. The above condition

can be written more compactly as

$$\sum_{s_j=1}^{d} A^{[j]s_j\dagger} A^{[j]s_j} = \mathbb{1}, \tag{4.4}$$

and matrices for which (4.4) holds true are called *left-orthogonal*. If all matrices of an MPS satisfy (4.4), it is said to be in *left-canonical form*. In this thesis, left-orthogonal matrices are denoted by A and represented graphically by right-pointing triangles (see Figure 4.4). The condition in general does not hold for the last matrices (or actually vectors) $A^{[L]s_L}$, because they correspond to $\Lambda V^\dagger$ from the last SVD. However, for these vectors the expression in (4.4) yields a scalar and

$$\sum_{s_L=1}^{d} A^{[L]s_L\dagger} A^{[L]s_L} = 1$$

if and only if the state is normalized, i.e. $\langle\psi|\psi\rangle = 1$ (for more details see Section 4.5.2).

The procedure in Section 4.1 could as well have been carried out starting at the last site L, i.e. decomposing

$$c_{(s_1...s_{L-1})s_L} = \sum_{\alpha_{L-1}=1}^{d} U_{(s_1...s_{L-1})\alpha_{L-1}} \lambda_{\alpha_{L-1}} V^{(L)\dagger}_{\alpha_{L-1}s_L} =: \sum_{\alpha_{L-1}=1}^{d} c^{(L-1)}_{s_1...s_{L-1}\alpha_{L-1}} V^{(L)\dagger}_{\alpha_{L-1}s_L}$$

and iterating from right to left. Then, with $B^{[j]s_j}_{\alpha_{j-1}\alpha_j} := V^{(j)\dagger}_{(\alpha_{j-1}s_j)\alpha_j}$ we obtain the MPS in the form

$$c_{s_1s_2...s_L} = \sum_{\{\alpha_i\}} B^{[1]s_1}_{\alpha_1} B^{[2]s_2}_{\alpha_1\alpha_2} \ldots B^{[L]s_L}_{\alpha_{L-1}}$$

and this time the unitarity of the $V^{(j)}$ leads to the condition

$$\sum_{s_j=1}^{d} B^{[j]s_j} B^{[j]s_j\dagger} = \mathbb{1}. \tag{4.5}$$

Matrices which fulfill (4.5) are called *right-orthogonal* and an MPS in which all matrices are right-orthogonal is called *right-canonical*. In this thesis, right-orthogonal matrices are denoted by B and represented graphically by left-pointing triangles (see Figure 4.4).
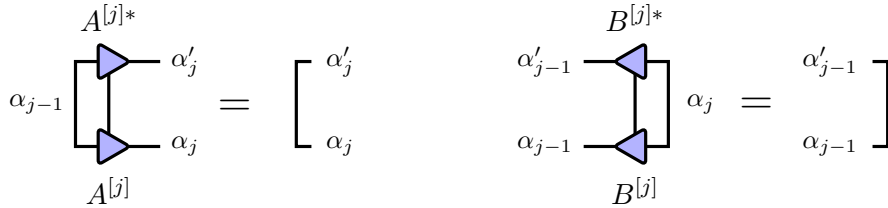

Figure 4.4. Graphical representation of the orthogonality conditions for left- and right-orthogonal MPS matrices.

4.3.2. Mixed-Canonical Form and Schmidt Decomposition

It will turn out that it is often particularly useful to have an MPS in the *mixed-canonical form*, where all matrices up to a certain site $j - 1$ are left-orthogonal and all matrices starting from site $j + 1$ are right-orthogonal. The site j is then called the *orthogonality center* of the MPS and the matrices at this site do not have special orthogonality properties. An example of a mixed-canonical MPS is shown in Figure 4.5.
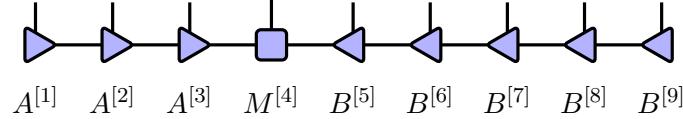

$$A^{[1]} \quad A^{[2]} \quad A^{[3]} \quad M^{[4]} \quad B^{[5]} \quad B^{[6]} \quad B^{[7]} \quad B^{[8]} \quad B^{[9]}$$

Figure 4.5. Graphical representation of a mixed-canonical MPS with the orthogonality center at site 4.

An additional SVD of two adjacent matrices of which one is at the orthogonality center gives an MPS in the form $A^{[1]} \ldots A^{[j]} \Lambda^{[j]} B^{[j+1]} \ldots B^{[L]}$. Defining the vectors

$$|A_\alpha\rangle := \sum_{s_1,\ldots,s_j} \sum_{\alpha_1,\ldots,\alpha_{j-1}} A^{[1]s_1}_{\alpha_1} A^{[2]s_2}_{\alpha_1\alpha_2} \ldots A^{[j]s_j}_{\alpha_{j-1}\alpha},$$

$$|B_\alpha\rangle := \sum_{s_{j+1},\ldots,s_L} \sum_{\alpha_{j+1},\ldots,\alpha_{L-1}} B^{[j+1]s_{j+1}}_{\alpha\alpha_{j+1}} \ldots B^{[L-1]s_{L-1}}_{\alpha_{L-2}\alpha_{L-1}} B^{[L]s_L}_{\alpha_{L-1}},$$

the state of the system can then be written as

$$|\psi\rangle = \sum_\alpha \lambda_\alpha |A_\alpha\rangle |B_\alpha\rangle. \tag{4.6}$$

Since the sets $|A_\alpha\rangle$ and $|B_\alpha\rangle$ are orthonormal due to the orthogonality properties (4.4) and (4.5) of the A and B matrices, this is the Schmidt decomposition with respect to the bipartition $(1,\ldots,j)(j+1,\ldots,L)$. Hence, *the Schmidt decomposition for the bipartition at a certain bond can be read off from an MPS directly only if all matrices to the left of this bond are left-orthogonal and all to the right are right-orthogonal.*

In particular, this means that the calculation of the von Neumann entanglement entropy across the bond between j and $j + 1$ is straightforward if the state is given as a mixed-canonical MPS with the orthogonality center at site j (or $j + 1$): We must simply SV-decompose the matrix $M^{[j]}B^{[j+1]}$ and from the singular values calculate the entanglement entropy according to Theorem 4.

Since the maximum von Neumann entanglement entropy S of a bipartition with bond dimension χ is $\ln \chi$ (which is attained if all singular values are the same), a bond dimension of approximately e^S is required to encode a certain entanglement entropy. For one-dimensional states satisfying an area law (see Section 2.5.1), the entanglement entropy does not grow with the system size and thus these states can be well approximated by MPS even for large systems.

4.3.3. Canonical (ΓΛ-)Form

For certain considerations, it is advantageous to store the Schmidt values in separate matrices. Such a form was introduced by Vidal [60] and can be obtained from the left-canonical form by defining

$$A^{[j]s_j}_{\alpha\beta} = \lambda^{[j-1]}_\alpha \Gamma^{[j]s_j}_{\alpha\beta} \tag{4.7}$$

where $\lambda^{[j-1]}_\alpha$ are the Schmidt values of the bond between sites $j-1$ and j. With the additional definitions $\lambda^{[0]}_\alpha = \lambda^{[L]}_\alpha = 1$, the MPS can then be written as

$$c_{s_1 s_2 \ldots s_L} = \sum_{\alpha_0=1}^{1} \sum_{\alpha_1=1}^{\chi_1} \cdots \sum_{\alpha_L=1}^{1} \lambda^{[0]}_{\alpha_0} \Gamma^{[1]s_1}_{\alpha_0\alpha_1} \lambda^{[1]}_{\alpha_1} \Gamma^{[2]s_2}_{\alpha_1\alpha_2} \ldots \Gamma^{[L]s_L}_{\alpha_{L-1}\alpha_L} \lambda^{[L]}_{\alpha_L} \tag{4.8}$$

which is called the *canonical form*. In this thesis, Γ-matrices are denoted by disks and the diagonal matrices Λ (with the Schmidt values λ_α on the diagonal) by small diamonds, as shown in Figure 4.6. For an MPS given in this form, the Schmidt values of a bipartition of the system at any bond can be directly read off without additional SVDs. How an MPS can be cast into this form is described in Section 4.3.4.

$$\Lambda^{[0]} \quad \Gamma^{[1]} \quad \Lambda^{[1]} \quad \Gamma^{[2]} \quad \Lambda^{[2]} \quad \Gamma^{[3]} \quad \Lambda^{[3]} \quad \Gamma^{[4]} \quad \Lambda^{[4]}$$
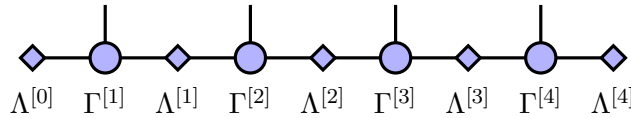
Figure 4.6. Graphical representation of a canonical MPS.

Both left- and right-orthogonal matrices can be constructed straightforwardly from the canonical form: The left- and right-orthogonal matrices A and B for each site are related to each other, because Schmidt decompositions of the state at two adjacent bonds lead to the two equivalent representations

$$c_{s_1 s_2 \ldots s_L} = \sum_{\{\alpha_i\}} A^{[1]s_1}_{\alpha_1} A^{[2]s_2}_{\alpha_1\alpha_2} \ldots A^{[j-1]s_{j-1}}_{\alpha_{j-2}\alpha_{j-1}} A^{[j]s_j}_{\alpha_{j-1}\alpha_j} \lambda^{[j]}_{\alpha_j} B^{[j+1]s_{j+1}}_{\alpha_j\alpha_{j+1}} \ldots B^{[L]s_L}_{\alpha_{L-1}}$$

$$= \sum_{\{\alpha_i\}} A^{[1]s_1}_{\alpha_1} A^{[2]s_2}_{\alpha_1\alpha_2} \ldots A^{[j-1]s_{j-1}}_{\alpha_{j-2}\alpha_{j-1}} \lambda^{[j-1]}_{\alpha_{j-1}} B^{[j]s_j}_{\alpha_{j-1}\alpha_j} B^{[j+1]s_{j+1}}_{\alpha_j\alpha_{j+1}} \ldots B^{[L]s_L}_{\alpha_{L-1}}$$

and hence $A^{[j]s_j}\Lambda^{[j]} = \Lambda^{[j-1]}B^{[j]s_j}$. Together with the definition (4.7), we thus have the following relationships between the matrices A, B, Λ and Γ:

$$A^{[j]s_j} = \Lambda^{[j-1]}\Gamma^{[j]s_j} \;, \tag{4.9}$$

$$B^{[j]s_j} = \Gamma^{[j]s_j}\Lambda^{[j]} \;. \tag{4.10}$$

With the orthogonality conditions (4.4) and (4.5) this implies the conditions

$$\sum_{s_j=1}^{d} \Gamma^{[j]s_j\dagger} \Lambda^{[j-1]\dagger} \Lambda^{[j-1]} \Gamma^{[j]s_j} = \sum_{s_j=1}^{d} \Gamma^{[j]s_j\dagger} \big(\Lambda^{[j-1]}\big)^2 \Gamma^{[j]s_j} = \mathbb{1} \;, \tag{4.11}$$

$$\sum_{s_j=1}^{d} \Gamma^{[j]s_j} \Lambda^{[j]} \Lambda^{[j]\dagger} \Gamma^{[j]s_j\dagger} = \sum_{s_j=1}^{d} \Gamma^{[j]s_j} \big(\Lambda^{[j]}\big)^2 \Gamma^{[j]s_j\dagger} = \mathbb{1} \;, \tag{4.12}$$
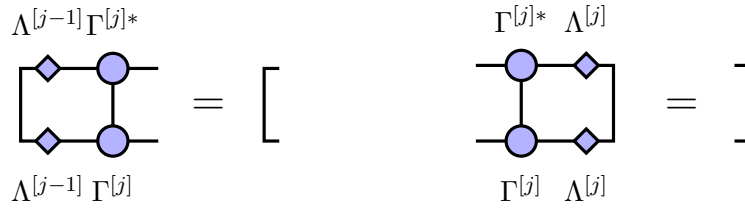
Figure 4.7. Graphical representation of the orthogonality conditions for the Λ- and Γ-matrices of a canonical MPS.

the graphical representation of which is shown in Figure 4.7.

To obtain the canonical $\Gamma\Lambda$-form, we can first bring the MPS into left- or right-canonical form (see Section 4.3.4) and remember the matrix of singular values Λ at each bond. Then (4.9) or (4.10) can be used to obtain the Γ-matrices as

$$\Gamma^{[j]s_j} = \left(\Lambda^{[j-1]}\right)^{-1} A^{[j]s_j} \quad \text{or} \quad \Gamma^{[j]s_j} = B^{[j]s_j} \left(\Lambda^{[j]}\right)^{-1} .$$

In order to avoid numerical problems due to very small singular values, a pseudoinverse should be used where diagonal elements corresponding to singular values below a certain threshold are set to zero in the inverse. Besides, depending on the implementation of the SVD the Λ matrices may contain singular values which are actually zero[1], which is also taken care of by the pseudoinverse. As a consequence of using the pseudoinverse, this procedure does not exactly preserve the orthogonality and norm of the state which can lead to problems in certain algorithms [10]. In the present thesis, the $\Gamma\Lambda$-representation is used merely for conceptual considerations.

4.3.4. Orthogonalization and Normalization

If an MPS is given in an arbitrary gauge with matrices $M^{[j]s_j}_{\alpha_{j-1}\alpha_j}$ (where α_0 and α_L are dummy indices with dimension 1), it can be transformed to a left-canonical form by starting at the left end of the system and subsequently SV-decomposing the matrices

$$\tilde{M}_{(\alpha_{j-1}s_j)(\alpha_{j+1}s_{j+1})} = \sum_{\alpha_j=1}^{\chi_j} M^{[j]s_j}_{\alpha_{j-1}\alpha_j} M^{[j+1]s_{j+1}}_{\alpha_j\alpha_{j+1}} \tag{4.13}$$

into

$$\tilde{M}_{(\alpha_{j-1}s_j)(\alpha_{j+1}s_{j+1})} = \sum_{\gamma=1}^{\chi_j} U_{(\alpha_{j-1}s_j)\gamma}\lambda_\gamma V^\dagger_{\gamma(\alpha_{j+1}s_{j+1})} . \tag{4.14}$$

The resulting matrices are then reshaped as

$$A^{[j]s_j}_{\alpha_{j-1}\alpha_j} = U_{(\alpha_{j-1}s_j)\alpha_j} , \quad M^{[j+1]s_{j+1}}_{\alpha_j\alpha_{j+1}} = \lambda_{\alpha_j} V^\dagger_{\alpha_j(\alpha_{j+1}s_{j+1})} , \tag{4.15}$$

---

[1] These singular values correspond to irrelevant subspaces, because the respective columns of U and rows of $V^\dagger$ are multiplied with 0 anyway, and therefore it does not matter if we also set them to zero in the inverse.

where the summation index γ was renamed to α_j. Again, the unitarity of U implies the left-orthogonality of the newly formed A. Thus, after moving through the system from left to right and applying the described steps for every lattice site, the MPS is in left-canonical form. If the initial MPS was not normalized, then in the last step a constant remains that must be dropped to obtain a normalized state. Figure 4.8 shows the first step of the described procedure graphically.
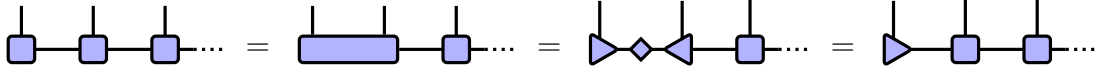

Figure 4.8. Procedure for left-orthogonalizing an arbitrarily gauged MPS.

Analogously, the MPS can be cast into the right-canonical form by moving through the system from right to left, performing the same SVDs and defining

$$M^{[j]s_j}_{\alpha_{j-1}\alpha_j} = U_{(\alpha_{j-1}s_j)\alpha_j}\lambda_{\alpha_j} \ , \quad B^{[j+1]s_{j+1}}_{\alpha_j\alpha_{j+1}} = V^{\dagger}_{\alpha_j(\alpha_{j+1}s_{j+1})} \ . \tag{4.16}$$

For a mixed-canonical MPS, one single step following (4.13), (4.14) and then (4.15) or (4.16) can be used to shift the orthogonality center one site to the right or left.

4.4. Truncation

In order to avoid exponential growth in the matrix dimensions of the MPS with increasing system size, a truncation procedure must be employed. Ideally, this procedure should produce small and controllable errors when truncating the matrices. These requirements are perfectly fulfilled by discarding the smallest Schmidt values at each bond [10].

The Schmidt decomposition of the exact state at a certain bond, which divides the system into two subsystems A and B, reads

$$|\psi\rangle = \sum_{i=1}^{r} \lambda_i |A_i\rangle |B_i\rangle .$$

Here r is the bond dimension at the respective bond, which is simply the Schmidt rank. According to the Eckart-Young-Mirsky theorem (Theorem 3), the best approximation with a given matrix dimension $\chi < r$ at that bond is

$$|\psi'\rangle = \sum_{i=1}^{\chi} \lambda_i |A_i\rangle |B_i\rangle ,$$

assuming that the Schmidt values are given in descending order.

To restore the normalization of the state, the remaining Schmidt values must be rescaled. If the original state is normalized, then

$$\sum_{i=1}^{r} \lambda_i^2 = 1. \tag{4.17}$$

For the truncated state this means

$$\sum_{i=1}^{\chi} \lambda_i^2 = 1 - \sum_{i=\chi+1}^{r} \lambda_i^2 =: 1 - w, \tag{4.18}$$

where w is called the *discarded weight*. Thus, the normalized truncated state is given by

$$|\tilde{\psi}\rangle = \frac{1}{\sqrt{1-w}} |\psi'\rangle .$$

It is important to keep in mind that the SVD of the product of two adjacent matrices is equivalent to the Schmidt decomposition of the state *only if* all matrices to the left are left-orthogonal and all to the right are right-orthogonal. Therefore, for the truncation at a certain bond, the MPS must be given either in the $\Gamma\Lambda$-form or in the mixed-canonical form with the orthogonality center at one of the sites next to the respective bond [61].

As a measure for the truncation error, the distance between the full MPS $|\psi\rangle$ and the truncated MPS $|\tilde{\psi}\rangle$ can be used, which according to Section 2.4 can be written in terms of the Frobenius norm of the matrix containing the Schmidt values:

$$\big\| |\tilde{\psi}\rangle - |\psi\rangle \big\|^2 = \big\| \tilde{\Lambda} - \Lambda \big\|_F^2 = \sum_{i=1}^{r} \big| \tilde{\lambda}_i - \lambda_i \big|^2 = \sum_{i=1}^{r} (\tilde{\lambda}_i^2 + \lambda_i^2 - 2\tilde{\lambda}_i \lambda_i).$$

Since the Schmidt values of the truncated and normalized state are given by $\tilde{\lambda}_i = \lambda_i / \sqrt{1-w}$ for $i \leq \chi$ and $\tilde{\lambda}_i = 0$ otherwise, we obtain with (4.17) and (4.18)

$$\big\| |\tilde{\psi}\rangle - |\psi\rangle \big\|^2 = 1 + \sum_{i=1}^{\chi} \frac{\lambda_i^2}{1-w} - 2 \sum_{i=1}^{\chi} \frac{\lambda_i^2}{\sqrt{1-w}} = 1 + \frac{1-w}{1-w} - 2\frac{1-w}{\sqrt{1-w}} = 2\left(1 - \sqrt{1-w}\right).$$

Since $w \ll 1$, the square root can be expanded into a Taylor series, yielding

$$\big\| |\tilde{\psi}\rangle - |\psi\rangle \big\|^2 = 2\left(1 - \left(1 - \frac{w}{2} + \mathcal{O}(w^2)\right)\right) = w + \mathcal{O}(w^2) .$$

Therefore, the truncation error in terms of the wave functions is given by

$$\big\| |\tilde{\psi}\rangle - |\psi\rangle \big\| \approx \sqrt{w} .$$

This result can be used to give an upper bound of the error in the expectation value of observables. The inequality

$$\big\| \hat{A} |\psi\rangle \big\| \leq \big\| \hat{A} \big\| \, \big\| |\psi\rangle \big\| \tag{4.19}$$

follows directly from the definition of an operator norm. With the triangle inequality, the Cauchy-Schwarz inequality and (4.19) one obtains

$$\begin{aligned}
\varepsilon(\hat{A}) :=& \big| \langle\tilde{\psi}|\hat{A}|\tilde{\psi}\rangle - \langle\psi|\hat{A}|\psi\rangle \big| = \big| \langle\tilde{\psi}|\hat{A}|\tilde{\psi}\rangle - \langle\psi|\hat{A}|\tilde{\psi}\rangle + \langle\psi|\hat{A}|\tilde{\psi}\rangle - \langle\psi|\hat{A}|\psi\rangle \big| \\
\leq& \big| \big(\langle\tilde{\psi}| - \langle\psi| \big)\hat{A} |\tilde{\psi}\rangle \big| + \big| \langle\psi| \hat{A} \big(|\tilde{\psi}\rangle - |\psi\rangle \big) \big| \\
\leq& \big\| |\tilde{\psi}\rangle - |\psi\rangle \big\| \, \big\| \hat{A} |\tilde{\psi}\rangle \big\| + \big\| |\psi\rangle \big\| \, \big\| \hat{A} \big(|\tilde{\psi}\rangle - |\psi\rangle \big) \big\| \\
\leq& \big\| |\tilde{\psi}\rangle - |\psi\rangle \big\| \, \big\| \hat{A} \big\| \, \big\| |\tilde{\psi}\rangle \big\| + \big\| |\psi\rangle \big\| \, \big\| \hat{A} \big\| \, \big\| |\tilde{\psi}\rangle - |\psi\rangle \big\| \\
=& 2 \big\| \hat{A} \big\| \, \big\| |\tilde{\psi}\rangle - |\psi\rangle \big\| \approx 2 \big\| \hat{A} \big\| \sqrt{w} .
\end{aligned}$$

Thus, the error in observables has the same dependence on the discarded weight as the error in the wave function. Therefore, to avoid large errors in measurements, the discarded weight w must be kept very small.

Sequentially discarding singular values at each bond is a simple and efficient way to reduce the matrix dimensions of an MPS, though not necessarily the most accurate one. The Eckart-Young-Mirsky theorem guarantees that the approximation is optimal for the truncation at a single bond, but this does not imply that repeating the procedure at each bond is the optimal way to truncate the whole MPS. In fact, there are variational algorithms which produce better approximations, but are reliant on good initial states and therefore usually implemented in addition to the SVD-based compression [10].

During an algorithm involving MPS, the bond dimension can grow and truncation must in general be employed during or after each step. This can be done either by defining a maximum bond dimension and discarding all Schmidt values beyond this number at each bond, or by specifying a maximum discarded weight and discarding Schmidt values starting from the lowest until the discarded weight reaches this value. A convenient combination of both is to define both a maximum bond dimension and a maximum discarded weight and keep the discarded weight below the threshold until the maximum bond dimension is reached.

4.5. Basic Operations with MPS

4.5.1. Application of Local Operators

Local operators of the form $\hat{O}_j = \hat{\mathbb{1}}_1 \otimes \ldots \otimes \hat{\mathbb{1}}_{j-1} \otimes \hat{O}_j \otimes \hat{\mathbb{1}}_{j+1} \otimes \ldots \otimes \hat{\mathbb{1}}_L$, acting only on one site, can be applied to a state which is represented by an MPS by a reasonably simple procedure. Let the initial state be given as

$$|\psi\rangle = \sum_{\{s_i\}} c_{s_1 \ldots s_L} |s_1 \ldots s_L\rangle = \sum_{\{s_i\}} A^{[1]s_1} \ldots A^{[j-1]s_{j-1}} M^{[j]s_j} B^{[j+1]s_{j+1}} \ldots B^{[L]s_L} |s_1 \ldots s_L\rangle,$$

i.e. in mixed-canonical form with the orthogonality center at site j. Applying the operator $\hat{O}_j$ to this state yields

$$\hat{O}_j |\psi\rangle = \sum_{\{s_i\}} A^{[1]s_1} \ldots A^{[j-1]s_{j-1}} M^{[j]s_j} B^{[j+1]s_{j+1}} \ldots B^{[L]s_L} |s_1\rangle \otimes \ldots \otimes \hat{O}_j |s_j\rangle \otimes \ldots \otimes |s_L\rangle.$$

To restore the MPS form we insert the identity $\sum_{s'_j} |s'_j\rangle\langle s'_j|$ to obtain

$$\hat{O}_j |\psi\rangle = \sum_{\{s_i\},s'_j} A^{[1]s_1} \ldots A^{[j-1]s_{j-1}} M^{[j]s_j} B^{[j+1]s_{j+1}} \ldots B^{[L]s_L} \langle s'_j|\hat{O}_j|s_j\rangle |s_1 \ldots s'_j \ldots s_L\rangle$$

and exchange the names of the summation indices s_j and s'_j, resulting in

$$\hat{O}_j \,|\psi\rangle = \sum_{\{s_i\}} A^{[1]s_1} \dots A^{[j-1]s_{j-1}} \left(\sum_{s'_j} \langle s_j|\hat{O}_j|s'_j\rangle \, M^{[j]s'_j} \right) B^{[j+1]s_{j+1}} \dots B^{[L]s_L} \,|s_1 \dots s_L\rangle$$

$$=: \sum_{\{s_i\}} A^{[1]s_1} \dots A^{[j-1]s_{j-1}} \tilde{M}^{[j]s_j} B^{[j+1]s_{j+1}} \dots B^{[L]s_L} \,|s_1 \dots s_L\rangle .$$

Hence, a local operator is applied to an MPS in mixed-canonical form simply by replacing

$$M^{[j]s_j} \to \sum_{s'_j} \langle s_j|\hat{O}_j|s'_j\rangle \, M^{[j]s'_j}, \tag{4.20}$$

where the site j on which the operator acts is at the same time the orthogonality center of the MPS. This corresponds to a contraction over the local physical index of the MPS tensor and the matrix representation of the operator in the local basis, which is shown graphically in Figure 4.9.
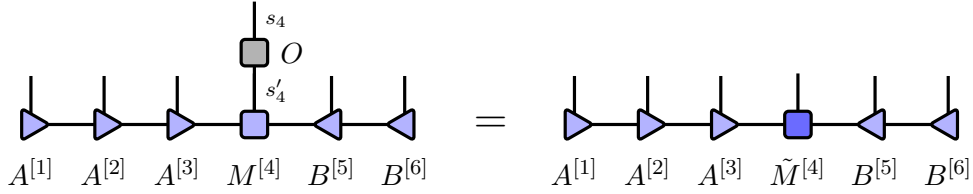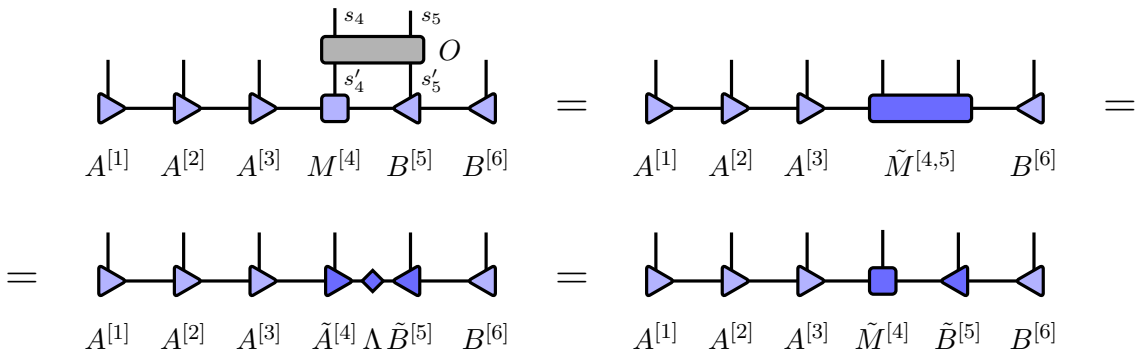

Figure 4.9. Graphical representation of the application of a local operator $\hat{O}_4$ with the matrix representation $O_{s_4 s'_4} = \langle s_4|\hat{O}_4|s'_4\rangle$ to a mixed-canonical MPS with the orthogonality center at site 4.

For a two-site operator $\hat{O}_{j,j+1} = \hat{\mathbb{1}}_1 \otimes \dots \otimes \hat{\mathbb{1}}_{j-1} \otimes \hat{O}_{j,j+1} \otimes \hat{\mathbb{1}}_{j+2} \otimes \dots \otimes \hat{\mathbb{1}}_L$, the procedure becomes slightly more elaborate. Applying $\hat{O}_{j,j+1}$ to the state gives

$$\hat{O}_{j,j+1} \,|\psi\rangle = \sum_{\{s_i\}} A^{[1]s_1} \dots A^{[j-1]s_{j-1}} M^{[j]s_j} B^{[j+1]s_{j+1}} \dots B^{[L]s_L} \,|s_1\rangle \otimes \dots$$

$$\dots \otimes \hat{O}_{j,j+1} \,|s_j s_{j+1}\rangle \otimes \dots \otimes |s_L\rangle .$$

Again inserting an identity $\hat{\mathbb{1}}_{j,j+1} = \sum_{s'_j s'_{j+1}} |s'_j s'_{j+1}\rangle\langle s'_j s'_{j+1}|$ and relabeling the indices as above we obtain

$$\hat{O}_{j,j+1} \,|\psi\rangle = \sum_{\{s_i\}} A^{[1]s_1} \dots A^{[j-1]s_{j-1}} \left(\sum_{s'_j s'_{j+1}} \langle s_j s_{j+1}|\hat{O}_{j,j+1}|s'_j s'_{j+1}\rangle \, M^{[j]s'_j} B^{[j+1]s'_{j+1}} \right) \times$$

$$\times B^{[j+2]s_{j+2}} \dots B^{[L]s_L} \,|s_1 \dots s_L\rangle .$$

The object in parentheses is a set of matrices $\tilde{M}^{[j,j+1]s_j s_{j+1}}$ that can be SV-decomposed into

$$\tilde{M}^{[j,j+1]s_j s_{j+1}}_{\alpha\beta} = \sum_{\gamma} U^{s_j}_{\alpha\gamma} \lambda_\gamma V^{s_{j+1}\dagger}_{\gamma\beta} .$$

Then choosing $\tilde{M}^{[j]s_j} = U^{s_j}\Lambda$ and $\tilde{B}^{[j+1]s_{j+1}} = V^{s_{j+1}\dagger}$ leads to the MPS representation

$$\hat{O}_{j,j+1}\,|\psi\rangle = \sum_{\{s_i\}} A^{[1]s_1}\ldots A^{[j-1]s_{j-1}}\tilde{M}^{[j]s_j}\tilde{B}^{[j+1]s_{j+1}}B^{[j+2]s_{j+2}}\ldots B^{[L]s_L}\,|s_1\ldots s_L\rangle$$

of the new state with the orthogonality center at site j (see Figure 4.10). Alternatively, the matrix Λ containing the singular values could as well be combined with $V^\dagger$, resulting in an MPS with the orthogonality center at site $j+1$. Note that it is not important for the described procedure, whether the orthogonality center of the original MPS is at site j or $j+1$. Therefore, a shift of the orthogonality center can be included in the application of a two-site operator without any additional effort.

Figure 4.10. Graphical representation of the application of a two-site operator $\hat{O}_{4,5}$ with the tensor representation $O_{s_4 s_5 s'_4 s'_5} = \langle s_4 s_5|\hat{O}_{4,5}|s'_4 s'_5\rangle$ to a mixed-canonical MPS with the orthogonality center at site 4.

Since the SVD is performed on a $d\chi \times d\chi$ matrix (assuming same bond dimensions χ left and right for simplicity), we obtain $d\chi$ singular values and thus a bond dimension of $d\chi$ at the new bond between j and $j+1$. Therefore, the matrix of singular values may need to be truncated to remain below the desired maximum bond dimension.

4.5.2. Overlaps and Expectation Values

Let two arbitrary states $|\phi\rangle$ and $|\psi\rangle$ be given in terms of MPS as

$$|\phi\rangle = \sum_{\{s_i\}} P^{[1]s_1}\ldots P^{[L]s_L}\,|s_1\ldots s_L\rangle, \quad |\psi\rangle = \sum_{\{s_i\}} Q^{[1]s_1}\ldots Q^{[L]s_L}\,|s_1\ldots s_L\rangle,$$

where $P^{[j]s_j}$ and $Q^{[j]s_j}$ are matrices which do not need to fulfill any particular orthogonality conditions. The overlap of these two states reads

$$\langle\phi|\psi\rangle = \sum_{\{s_i\}}\sum_{\{s'_i\}} P^{[L]s_L\dagger}\ldots P^{[1]s_1\dagger}Q^{[1]s'_1}\ldots Q^{[L]s'_L}\,\langle s_1\ldots s_L|s'_1\ldots s'_L\rangle$$

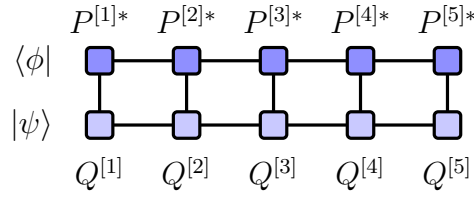$$= \sum_{\{s_i\}} P^{[L]s_L\dagger}\ldots P^{[1]s_1\dagger}Q^{[1]s_1}\ldots Q^{[L]s_L}, \tag{4.21}$$

Figure 4.11. Graphical representation of the overlap $\langle\phi|\psi\rangle$ of two MPS.

which is shown diagrammatically in Figure 4.11. Note that the transposition is taken care of by the arrangement of tensors and thus their elements must only be complex conjugated.

A special case of an overlap is the squared norm of a state $\langle\psi|\psi\rangle$, the evaluation of which is particularly simple if the MPS is given in mixed-canonical form. Then the network collapses due to the orthogonality conditions (4.4) and (4.5) and, assuming the orthogonality center at site j, reduces to

$$
\begin{aligned}
\langle\psi|\psi\rangle &= \sum_{\{s_i\}} \mathrm{tr}\left(B^{[L]s_L\dagger} \ldots B^{[j+1]s_{j+1}\dagger} M^{[j]s_j\dagger} A^{[j-1]s_{j-1}\dagger} \ldots A^{[1]s_1\dagger} \times \right. \\
&\qquad\qquad \left. \times\, A^{[1]s_1} \ldots A^{[j-1]s_{j-1}} M^{[j]s_j} B^{[j+1]s_{j+1}} \ldots B^{[L]s_L} \right) \\
&= \sum_{s_j} \mathrm{tr}\left(M^{[j]s_j\dagger} M^{[j]s_j} \right),
\end{aligned}
\tag{4.22}
$$

where the trace in the first line does not make a difference, because its argument is a scalar. As shown in Figure 4.12, this relation can be directly read off the diagram using Figure 4.4. In particular, this implies that only the matrix at the orthogonality center must be normalized in order to normalize a mixed-canonical MPS.

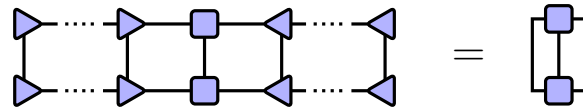**Figure 4.12.** Graphical representation of the squared norm $\langle\psi|\psi\rangle$ of a mixed-canonical MPS.

Expectation values of single-site operators can be calculated similarly. The application of a local operator to an MPS was already treated in Section 4.5.1 and the expectation value can be interpreted as the overlap of $|\psi\rangle$ and $\hat{O}_j|\psi\rangle$. If the orthogonality center of the MPS is at the same site on which the operator acts, then with the rule (4.20) the same considerations as for the norm above lead to

$$
\langle\psi|\hat{O}_j|\psi\rangle = \sum_{s_j s_j'} \mathrm{tr}\left(M^{[j]s_j\dagger} \langle s_j|\hat{O}_j|s_j'\rangle M^{[j]s_j'} \right).
\tag{4.23}
$$

This can be immediately understood diagrammatically by combining Figure 4.9 and Figure 4.12, which is illustrated in Figure 4.13.

The generalization to multiple-site operators is straightforward. If the orthogonality center of the mixed-canonical MPS is between the first and last site affected by the operator,
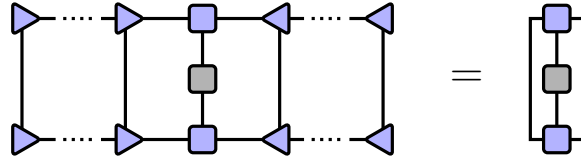
Figure 4.13. Graphical representation of the expectation value $\langle \psi | \hat{O}_j | \psi \rangle$ of a local operator $\hat{O}_j$ in a state represented by a mixed-canonical MPS with the orthogonality center at site j. The elements of the gray matrix are $\langle s_j | \hat{O}_j | s'_j \rangle$.

then the parts of the network to the left and to the right of the operator reduce to identity matrices. The remaining network, comprising all sites between the first and last site where the operator acts non-trivially (no matter if its action is trivial at sites in between), must be explicitly contracted.

4.5.3. Addition of MPS

If two states have the MPS representations

$$|\phi\rangle = \sum_{\{s_i\}} P^{[1]s_1} \ldots P^{[L]s_L} |s_1 \ldots s_L\rangle , \quad |\psi\rangle = \sum_{\{s_i\}} Q^{[1]s_1} \ldots Q^{[L]s_L} |s_1 \ldots s_L\rangle ,$$

then their sum can be represented by [10]

$$|\phi\rangle + |\psi\rangle = \sum_{\{s_i\}} \begin{pmatrix} P^{[1]s_1} & Q^{[1]s_1} \end{pmatrix} \begin{pmatrix} P^{[2]s_2} & 0 \\ 0 & Q^{[2]s_2} \end{pmatrix} \cdots \begin{pmatrix} P^{[L]s_L} \\ Q^{[L]s_L} \end{pmatrix} |s_1 s_2 \ldots s_L\rangle .$$

The bond dimensions of the resulting MPS are the sums of the original bond dimensions. It may therefore be necessary to truncate the MPS after the addition (see Section 4.4), which can be possible without loss of information (i.e. only discarding singular values which are exactly zero, consider for instance the case where both MPS are the same).

4.6. Matrix Product Operators (MPO)

The idea of writing the coefficient of a state as a matrix product can be easily transferred to operators. An arbitrary operator acting on the Hilbert space $\mathcal{H}_{\mathrm{loc}}^L$ of a system on L lattice sites is given by

$$\hat{O} = \sum_{\{s_i\},\{s'_i\}} O_{\{s_i\}\{s'_i\}} |s_1 \ldots s_L\rangle \langle s'_1 \ldots s'_L| . \tag{4.24}$$

Following [62] and [63], we define *matrix product operators* (MPO) by writing the operator coefficients in (4.24) as a matrix product,

$$\hat{O} = \sum_{\{s_i\},\{s'_i\}} W^{[1]s_1 s'_1} \ldots W^{[L]s_L s'_L} |s_1 \ldots s_L\rangle \langle s'_1 \ldots s'_L| . \tag{4.25}$$
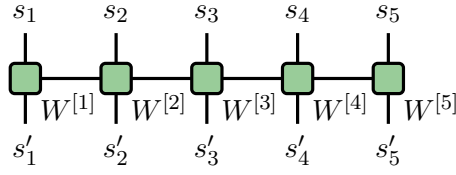
Figure 4.14. Graphical representation of an MPO for 5 sites.

At the bulk sites, the $W^{[i]}$ are matrices with additional indices s_i and s_i' and therefore can be interpreted as tensors of rank four, whereas $W^{[1]}$ and $W^{[L]}$ have rank three. The resulting diagrammatic representation of an MPO is shown in Figure 4.14.

Concerning the notation, instead of writing d^2 matrices (one for each combination of s and s') per site, it is often simpler to think of the MPO as a product of operator-valued matrices, i.e.

$$\hat{O} = \sum_{\{\alpha_i\}} \left(\sum_{s_1 s_1'} W^{[1]s_1 s_1'}_{\alpha_1} |s_1\rangle \langle s_1'| \right) \otimes \left(\sum_{s_2 s_2'} W^{[1]s_2 s_2'}_{\alpha_1 \alpha_2} |s_2\rangle \langle s_2'| \right) \otimes \dots$$

$$= \sum_{\{\alpha_i\}} \hat{W}^{[1]}_{\alpha_1} \otimes \hat{W}^{[2]}_{\alpha_1 \alpha_2} \otimes \dots \otimes \hat{W}^{[L]}_{\alpha_{L-1}}. \tag{4.26}$$

4.6.1. Application of MPOs to MPS

States and operators can both be represented with matrix products, which raises the question how to apply an MPO to an MPS, i.e. obtain $\hat{O} |\psi\rangle$ when $\hat{O}$ is given as an MPO and $|\psi\rangle$ as an MPS.

If we denote the matrices representing $|\psi\rangle$ by M and those representing $\hat{O}$ by W, then the product of both is given by

$$\hat{O} |\psi\rangle = \sum_{\{s_i\},\{s_i'\},\{s_i''\}} W^{[1]s_1 s_1'} \dots W^{[L]s_L s_L'} |s_1 \dots s_L\rangle \langle s_1' \dots s_L'| M^{[1]s_1''} \dots M^{[L]s_L''} |s_1'' \dots s_L''\rangle$$

$$= \sum_{\{\alpha_i\},\{\beta_i\}} \sum_{\{s_i\},\{s_i'\}} W^{[1]s_1 s_1'}_{\beta_1} W^{[2]s_2 s_2'}_{\beta_1 \beta_2} \dots W^{[L]s_L s_L'}_{\beta_{L-1}} M^{[1]s_1'}_{\alpha_1} M^{[2]s_2'}_{\alpha_1 \alpha_2} \dots M^{[L]s_L'}_{\alpha_{L-1}} |s_1 \dots s_L\rangle.$$

Now the MPS form can be restored easily by defining the matrices

$$\tilde{M}^{[j]s_j}_{(\alpha_{j-1}\beta_{j-1})(\alpha_j\beta_j)} := \sum_{s_j'} W^{[j]s_j s_j'}_{\beta_{j-1}\beta_j} M^{[j]s_j'}_{\alpha_{j-1}\alpha_j},$$

resulting in

$$\hat{O} |\psi\rangle = \sum_{\{s_i\}} \tilde{M}^{[1]s_1} \dots \tilde{M}^{[L]s_L} |s_1 \dots s_L\rangle.$$

Hence, the application of an MPO to an MPS is in principle straightforward, which becomes particularly clear in the graphical notation (Figure 4.15). However, the bond

dimensions of the new MPS are the products of the bond dimensions χ of the original MPS and χ_{MPO} of the MPO and thus much larger than before. In general, a truncation will therefore be required after applying the MPO. Since the application of the MPO destroys the orthogonality properties of the matrices, the new MPS must be cast into a canonical form (see Section 4.3) before starting the truncation, which makes the overall procedure costly in terms of floating-point operations.
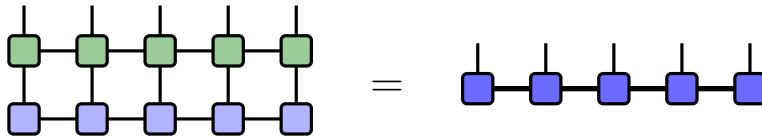

Figure 4.15. Graphical representation of the application of an MPO (green) to an MPS (blue). The contraction leads to larger bond dimensions visualized by the thick lines.

Alternatively, the application of the MPO and the truncation can be carried out in a single sweep over all sites with the zip-up method proposed by Stoudenmire and White [61]. It is based on the assumption that, although the application of the MPO destroys any canonical form of the MPS, the resulting MPS is still sufficiently close to the canonical form to allow for truncation, iteratively at each site, without introducing too large errors. Therefore, the method is expected to give the best results if the MPS and the MPO are both given in right-canonical form (or mixed-canonical with the orthogonality center at site 1 or 2).[1] Starting at the first site, all tensors (from the MPS and the MPO) at the first and second site are contracted into a single matrix,

$$\tilde{M}_{s_1(\alpha_2\beta_2 s_2)} = \sum_{s_1' s_2'} \sum_{\alpha_1 \beta_1} B_{\alpha_1}^{[1]s_1'} B_{\alpha_1\alpha_2}^{[2]s_2'} W_{\beta_1}^{[1]s_1 s_1'} W_{\beta_1\beta_2}^{[2]s_2 s_2'}.$$

This matrix is now SV-decomposed, truncated to the desired bond dimension and reshaped into

$$\tilde{M}_{s_1(\alpha_2\beta_2 s_2)} \rightarrow \sum_{\alpha_1} A_{\alpha_1}^{[1]s_1} M_{\alpha_1\alpha_2\beta_2}^{[2]s_2},$$

where the singular value matrix is multiplied into M. For the second site we define

$$\tilde{M}_{(\alpha_1 s_2)(\alpha_3\beta_3 s_3)} = \sum_{s_3'} \sum_{\alpha_2\beta_2} M_{\alpha_1\alpha_2\beta_2}^{[2]s_2} B_{\alpha_2\alpha_3}^{[3]s_3'} W_{\beta_2\beta_3}^{[3]s_3 s_3'},$$

SV-decompose, truncate and reshape as for the first site. Repeating this procedure for all sites finally yields a new MPS in left-canonical form with truncated bonds. The first step of the zip-up algorithm is depicted graphically in Figure 4.16.

During one bulk step of the zip-up algorithm, the most expensive task is the SVD of a $(d\chi) \times (d\chi\chi_{\mathrm{MPO}})$-matrix (see Figure 4.16, rightmost diagram), which according to Section 2.4 requires $\mathcal{O}(d^3\chi^3\chi_{\mathrm{MPO}})$ operations.

---

[1] The orthogonality conditions for MPOs are defined analogously to those for MPS with sums over both physical indices.
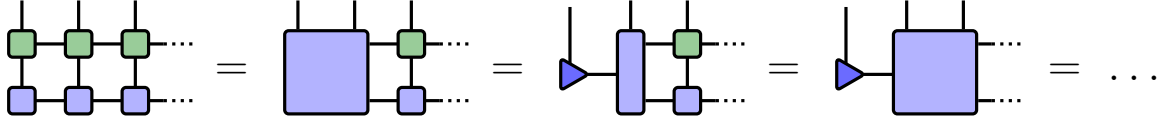
Figure 4.16. Graphical representation of the zip-up algorithm for the application of an MPO (green) to an MPS (blue).

4.7. Density Matrix Renormalization Group (DMRG)

DMRG is a variational algorithm for finding ground states of (at least formally) one-dimensional many-body Hamiltonians. When it was originally invented by Steven White [11], it was formulated without explicitly using matrix product states. However, in the meantime it has become clear that MPS provide an elegant way to express and extend the DMRG algorithm [10, 12, 13]. Therefore, DMRG is presented in the MPS language here, mainly following [10].

The idea behind this formulation of DMRG is to minimize the energy of the MPS with respect to one or two of the matrices while keeping all other matrices fixed. One distinguishes between single-site DMRG, where only one matrix is used as the variational parameter, and two-site DMRG, where the matrices at two adjacent sites are varied simultaneously. We will first explain the single-site algorithm and discuss the differences later.

If we use a Lagrangian multiplier to enforce the normalization of the state, the functional to be minimized is

$$\mathcal{E} = \langle\psi|\hat{H}|\psi\rangle - \lambda\,\langle\psi|\psi\rangle\,,$$

where λ has the meaning of the energy of the state.

Now we assume that $|\psi\rangle$ is given as an MPS in mixed-canonical form and $\hat{H}$ as an MPO, leading to

$$\langle\psi|\psi\rangle = \sum_{\alpha_{j-1}\alpha_j s_j} M^{[j]s_j*}_{\alpha_{j-1}\alpha_j} M^{[j]s_j}_{\alpha_{j-1}\alpha_j},$$

$$\langle\psi|\hat{H}|\psi\rangle = \sum_{\substack{\alpha_{j-1}\alpha'_{j-1}\\ \alpha_j\alpha'_j\\ \{s_i\}\{s'_i\}}} \left(A^{[1]s_1}\dots A^{[j-1]s_{j-1}}\right)^*_{\alpha_{j-1}} M^{[j]s_j*}_{\alpha_{j-1}\alpha_j} \left(B^{[j+1]s_{j+1}}\dots B^{[L]s_L}\right)^*_{\alpha_j}$$
$$\times \left(W^{[1]s_1s'_1}\dots W^{[L]s_Ls'_L}\right)$$
$$\times \left(A^{[1]s'_1}\dots A^{[j-1]s'_{j-1}}\right)_{\alpha'_{j-1}} M^{[j]s'_j}_{\alpha'_{j-1}\alpha'_j} \left(B^{[j+1]s'_{j+1}}\dots B^{[L]s'_L}\right)_{\alpha'_j}.$$

Since for the current step only the matrices at site j are relevant, the notation can be simplified by formally combining all tensors to the left of this site into $L_{\alpha_{j-1}\beta_{j-1}\alpha'_{j-1}}$ and those to the right into $R_{\alpha_j\beta_j\alpha'_j}$. Then $\mathcal{E}$ is given by

$$\mathcal{E} = \sum_{\substack{\alpha_{j-1}\alpha'_{j-1}\beta_{j-1}\\ \alpha_j\alpha'_j\beta_js_js'_j}} L_{\alpha_{j-1}\beta_{j-1}\alpha'_{j-1}} M^{[j]s_j*}_{\alpha_{j-1}\alpha_j} W^{[j]s_js'_j}_{\beta_{j-1}\beta_j} M^{[j]s'_j}_{\alpha'_{j-1}\alpha'_j} R_{\alpha_j\beta_j\alpha'_j} - \lambda \sum_{\alpha_{j-1}\alpha_j s_j} M^{[j]s_j*}_{\alpha_{j-1}\alpha_j} M^{[j]s_j}_{\alpha_{j-1}\alpha_j},$$
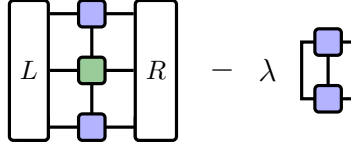
Figure 4.17. Tensor network representing the energy functional to be minimized in single-site DMRG.

the graphical representation of which is shown in Figure 4.17.

To minimize $\mathcal{E}$ by variation of $M^{[j]s_j*}_{\alpha_{j-1}\alpha_j}$, we demand that

$$\frac{\partial \mathcal{E}}{\partial M^{[j]s_j*}_{\alpha_{j-1}\alpha_j}} = \sum_{\substack{\alpha'_{j-1}\beta_{j-1} \\ \alpha'_j\beta_j s'_j}} L_{\alpha_{j-1}\beta_{j-1}\alpha'_{j-1}} W^{[j]s_j s'_j}_{\beta_{j-1}\beta_j} M^{[j]s'_j}_{\alpha'_{j-1}\alpha'_j} R_{\alpha_j\beta_j\alpha'_j} - \lambda M^{[j]s_j}_{\alpha_{j-1}\alpha_j} \overset{!}{=} 0. \qquad (4.27)$$

By simply combining indices, (4.27) can be formulated as an ordinary eigenvalue problem: Defining an *effective Hamiltonian*

$$H^{\text{eff}}_{(\alpha_{j-1}\alpha_j s_j)(\alpha'_{j-1}\alpha'_j s'_j)} = \sum_{\beta_{j-1}\beta_j} L_{\alpha_{j-1}\beta_{j-1}\alpha'_{j-1}} W^{[j]s_j s'_j}_{\beta_{j-1}\beta_j} R_{\alpha_j\beta_j\alpha'_j}, \qquad (4.28)$$

we obtain

$$\sum_{(\alpha'_{j-1}\alpha'_j s'_j)} H^{\text{eff}}_{(\alpha_{j-1}\alpha_j s_j)(\alpha'_{j-1}\alpha'_j s'_j)} M^{[j]}_{(\alpha'_{j-1}\alpha'_j s'_j)} - \lambda M^{[j]}_{(\alpha_{j-1}\alpha_j s_j)} = 0. \qquad (4.29)$$

The matrix H^{eff} is usually too large to diagonalize it exactly, but since we are interested in the ground state, we only need the smallest eigenvalue λ_0 and the corresponding eigenvector, which can be found with an iterative eigensolver. Due to the hermiticity of the Hamiltonian MPO, H^{eff} is also hermitian and therefore a Lanczos [64] or Davidson [65] routine can be employed for this task. Note that for these eigensolvers, the matrices H^{eff} never need to be built explicitly, because they only require a rule how to apply the matrix to a vector and this can be done by contracting over the three tensor indices separately.

Once the eigenvalue problem has been solved for the smallest eigenvalue, the original tensor at the j-th site of the MPS is replaced by the newly found eigentensor.

In order to find the ground state of the system, these local optimizations must be carried out in sweeps, repeating the procedure at each site while moving through the system from left to right and then from right to left. After each step, the orthogonality center of the MPS must be shifted by one site to keep it at the currently considered site. The left tensors $L_{\alpha_{j-1}\beta_{j-1}\alpha'_{j-1}}$ can be built up iteratively during the right-moving part of the sweep and saved for each site to have them ready for the left-moving part, saving computational time. Likewise, all right tensors can be stored while moving left.

Single-Site and Two-Site DMRG

In the original formulation of DMRG without MPS, the wave function is optimized at two sites at once. The steps described above can be easily generalized to this two-site

DMRG by keeping all matrices except for two adjacent ones fixed. The dimension of the eigenvalue problem for the effective Hamiltonian then increases by a factor of the local dimension d and the resulting eigentensor must be SV-decomposed (and possibly truncated) to recover the MPS form. Note that this SVD does not involve any additional expense compared to the single-site algorithm, because it must be done anyway to shift the orthogonality center.

A drawback of the single-site algorithm is that is tends to get stuck in local minima[1] because the bases at each bond are fixed, while in the two-site version new bases are introduced when decomposing the optimized two-site tensor [10].

On the other hand, two-site DMRG can get stuck in a linear combination of the ground state and low-lying excited states if the energy difference is very small, because it favors states with low entanglement [13, 66]. This can lead to differences between even and odd sites that are not present in the true ground state (as a simplified picture, imagine that DMRG only finds $|\dots \uparrow\downarrow\uparrow\downarrow \dots\rangle$ instead of $|\dots \uparrow\downarrow\uparrow\downarrow \dots\rangle + |\dots \downarrow\uparrow\downarrow\uparrow \dots\rangle$ in an antiferromagnetic model). A further discussion thereof in the context of infinite systems can be found in Section 4.10.3.

Initial State and Infinite-System DMRG

Although DMRG can be started with an arbitrary initial state (e.g. a random MPS), faster convergence may be achieved by constructing an initial state with *infinite-system DMRG*. In the formulation without MPS, this algorithm is necessary as an initialization step [11]. It starts with a chain consisting of two sites and iteratively increases the system size.

Let us assume that the ground state for two sites is known exactly and given in the form

$$|\psi_2\rangle = \sum_{s_1 s_2} M^{s_1 s_2} |s_1 s_2\rangle \,,$$

which can be cast into MPS form by singular-value decomposing $M^{s_1 s_2}$, resulting in

$$|\psi_2\rangle = \sum_{s_1 s_2} A^{[1]s_1} \Lambda^{[1]} B^{[2]s_2} |s_1 s_2\rangle \,.$$

For the next step, two additional sites are inserted at the center of the system, yielding a system with four sites, described by the state

$$|\tilde{\psi}_4\rangle = \sum_{s_1 s_3 s_4 s_2} A^{[1]s_1} M^{s_3 s_4} B^{[2]s_2} |s_1 s_3 s_4 s_2\rangle \,.$$

The set of matrices $M^{s_3 s_4}$ can in principle be chosen randomly and only serves as an initial guess for the minimization of the energy with respect to the Hamiltonian of the four-site system, which is done analogously to the finite-size algorithm. After the optimization, the

---

[1]This can happen in the two-site version, too, but less likely.

resulting matrix is again SV-decomposed and, if necessary, truncated to a certain bond dimension. Now, the state of the four-site system is given by

$$|\psi_4\rangle = \sum_{s_1 s_3 s_4 s_2} A^{[1]s_1} A^{[3]s_3} \Lambda^{[3]} B^{[4]s_4} B^{[2]s_2} |s_1 s_3 s_4 s_2\rangle .$$

This procedure is iterated until after n steps an MPS for $2n$ sites is obtained, which can be used as an initial guess for a finite-size DMRG calculation with system size $L = 2n$.

4.8. Time Evolution of MPS

Two commonly used time evolution algorithms in the context of MPS and DMRG are *time-evolving block decimation* (TEBD) and *time-dependent DMRG* (tDMRG) which are similar and were developed at the same time [10, 14, 67]. For the present thesis, TEBD is used and therefore discussed in the following.

An alternative approach to time evolution of MPS is to represent the time evolution operator as an MPO and apply it to the MPS. This method is treated in Section 4.8.2.

A detailed discussion of various time evolution methods for MPS is given in [68].

4.8.1. Time-evolving Block Decimation (TEBD)

The heart of the TEBD algorithm introduced by Vidal [14] is the *Suzuki-Trotter decomposition* [69] of the time evolution operator. Assuming a Hamiltonian on a 1D lattice, which consists of local and nearest-neighbor terms only,

$$\hat{H} = \sum_{j=1}^{L-1} \hat{h}_{j,j+1},$$

it allows splitting the time evolution operator $\exp(-\mathrm{i}\hat{H}\tau)$ into a set of local gates for small time steps τ.

First, the Hamiltonian is split into two parts, each of which consists of mutually commuting terms:

$$\hat{H} = \sum_{j \text{ odd}} \hat{h}_{j,j+1} + \sum_{j \text{ even}} \hat{h}_{j,j+1} = \hat{H}_{\text{odd}} + \hat{H}_{\text{even}}.$$

In the simplest approximation, the first-order Suzuki-Trotter expansion (ST1), the time evolution operator for a small time step τ is then written as

$$\exp(-\mathrm{i}\hat{H}\tau) = \exp\left(-\mathrm{i}\hat{H}_{\text{even}}\tau - \mathrm{i}\hat{H}_{\text{odd}}\tau\right) = \exp\left(-\mathrm{i}\hat{H}_{\text{even}}\tau\right) \exp\left(-\mathrm{i}\hat{H}_{\text{odd}}\tau\right) + \mathcal{O}(\tau^2),$$

where the last step can be verified easily by Taylor expansion of both sides. Since within $\hat{H}_{\text{odd}}$ and $\hat{H}_{\text{even}}$ all terms commute, the exponentials can be split further into

$$\exp(-\mathrm{i}\hat{H}\tau) = \prod_{j \text{ even}} \exp\left(-\mathrm{i}\hat{h}_{j,j+1}\tau\right) \prod_{j \text{ odd}} \exp\left(-\mathrm{i}\hat{h}_{j,j+1}\tau\right) + \mathcal{O}(\tau^2).$$

Thus, up to first order in τ, the time evolution operator is equal to the set of two-site operators (gates)

$$\hat{U}_{\text{ST1}}(\tau) = \prod_{j \text{ even}} \exp\left(-\mathrm{i}\hat{h}_{j,j+1}\tau\right) \prod_{j \text{ odd}} \exp\left(-\mathrm{i}\hat{h}_{j,j+1}\tau\right). \tag{4.30}$$

The time evolution step in TEBD consists in applying these gates to the MPS representing the current state $|\psi(t)\rangle$ to obtain

$$|\psi(t+\tau)\rangle \approx \hat{U}_{\text{ST1}}(\tau)\,|\psi(t)\rangle\,.$$

This operation follows the rules derived in Section 4.5.1 and can be represented graphically as shown in Figure 4.18.

$\exp(-\mathrm{i}\hat{H}_{\text{even}}\tau)$

$\exp(-\mathrm{i}\hat{H}_{\text{odd}}\tau)$

$|\psi\rangle$
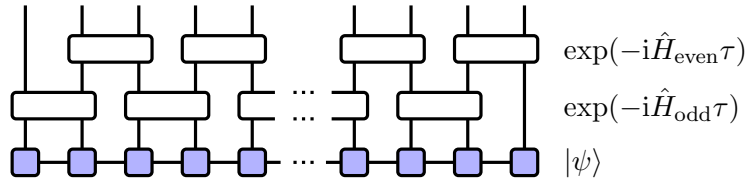
Figure 4.18. Graphical representation of $\hat{U}_{\text{ST1}}(\tau)\,|\psi\rangle$ in the first-order Trotter approximation $\hat{U}_{\text{ST1}}(\tau) = \exp(-\mathrm{i}\hat{H}_{\text{even}}\tau)\exp(-\mathrm{i}\hat{H}_{\text{odd}}\tau)$.

Since each application of a two-site gate involves truncation to keep the MPS below a maximum bond dimension, the overall error of a TEBD time evolution consists of the error due to the Suzuki-Trotter decomposition and the truncation error.

Next-Nearest Neighbor Coupling

If the Hamiltonian contains longer-range terms (e.g. next-nearest neighbor terms), it must be split into more parts to achieve commutativity among the single terms in each of them. The gates then extend over more sites, reducing the efficiency of the algorithm. A Hamiltonian containing next-nearest neighbor terms, for instance, can be decomposed into

$$\hat{H} = \sum_{i=1}^{L-2} \hat{h}_{i,i+1,i+2} = \hat{H}_1 + \hat{H}_2 + \hat{H}_3,$$

where $\hat{H}_1$ contains all terms $\hat{h}_{i,i+1,i+2}$ with $i \bmod 3 = 1$, $\hat{H}_2$ the terms with $i \bmod 3 = 2$ and $\hat{H}_3$ those with $i \bmod 3 = 0$. To obtain mutually commuting terms in the exponent, the exponential must be split twice with an error of order τ^2. A time evolution step with three-site gates is graphically depicted in Figure 4.20 on the right.

When applying a three-site gate, two SVDs are performed. If we assume equal bond dimensions χ at each bond, the first SVD is applied to a $d\chi \times d^2\chi$-matrix and thus scales as $(d^2\chi)(d\chi)^2 = d^4\chi^3$. The matrix on which the second SVD is performed has dimensions $d\chi \times d\chi$, adding another $\mathcal{O}(d^3\chi^3)$ operations. Since the number of three-site gates is $L-2$ per time step, the overall cost of one time step amounts to $\mathcal{O}\big((L-2)(d+1)d^3\chi^3\big)$.

An alternative approach uses so-called *swap gates*, which swap the positions of two sites [61, 70]. The matrix elements of a swap gate for the sites i and j are

$$\langle s_i s_j | \hat{S}_{ij} | s_i' s_j' \rangle = \sigma_{s_i s_j} \delta_{s_i s_j'} \delta_{s_i' s_j},$$

where $\sigma_{s_i s_j} = \pm 1$ accounts for the minus sign that appears when swapping two singly occupied fermionic sites [70]. In the graphical notation, a swap gate corresponds to a crossing of the legs belonging to the indices s_i and s_j. Using these gates, we can apply next-nearest neighbor operators $g_{i,i+2}$ by swapping the sites $i+1$ and $i+2$, then acting onto sites i and $i+1$ with $g_{i,i+1}$ (which is now a simple two-site gate) and then swapping the sites back. This procedure is shown graphically in Figure 4.19.
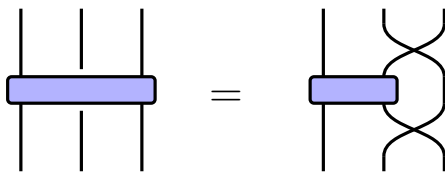
Figure 4.19. A next-nearest neighbor gate replaced by a nearest-neighbor gate and two swap gates.

For the use of swap gates, a Hamiltonian with nearest-neighbor and next-nearest neighbor coupling must be decomposed into even more parts, because each gate can only act on two sites. This can be achieved with

$$\hat{H} = \hat{H}_{\text{odd}}^{(\text{nn})} + \hat{H}_{\text{even}}^{(\text{nn})} + \hat{H}_1^{(\text{nnn})} + \hat{H}_2^{(\text{nnn})} + \hat{H}_3^{(\text{nnn})},$$

where $\hat{H}_{\text{odd}}^{(\text{nn})}$ and $\hat{H}_{\text{even}}^{(\text{nn})}$ contain the nearest-neighbor terms $\hat{h}_{i,i+1}$ with odd and even i, respectively, and $\hat{H}_j^{(\text{nnn})}$ the next-nearest neighbor terms $\hat{h}_{i,i+2}$ with $i = j + 3n$. The exponential must thus be split four times until each exponent consists of mutually commuting terms only, introducing an error of order τ^2 each time.

One time evolution step then involves the application of the nearest-neighbor gates and the next-nearest neighbor gates combined with swap gates, as shown in Figure 4.20 on the left.

Concerning the CPU time, each application of a two-site gate involves an SVD of a $d\chi \times d\chi$-matrix and therefore requires $\mathcal{O}\big((d\chi)^3\big)$ operations (assuming equal bond dimensions for simplicity). Per time step, $L - 1$ nearest-neighbor gates and $L - 2$ next-nearest neighbor gates preceded and followed by a swap gate must be applied, giving a total of $L - 1 + 3(L - 2) = 4L - 7$ gates. Hence, the approximate cost of one time step with swap gates is $\mathcal{O}\big((4L - 7)d^3\chi^3\big)$.

For large systems (such that $4L - 7 \approx 4L$ and $L - 2 \approx L$), one time step thus requires $\mathcal{O}(4Ld^3\chi^3)$ operations with swap gates and $\mathcal{O}(L(d+1)d^3\chi^3)$ operations with three-site gates. The respective values for the typical physical dimensions $d = 2$ (e.g. XXZ model, T-V model) and $d = 4$ (Hubbard model) are listed in Table 4.1. Although the differences are not too large, the algorithm with three-site gates scales slightly better for $d = 2$, whereas for $d = 4$ the swap gates have the lower cost. Therefore, we will use three-site gates for the T-V model and the swap gate approach for the Hubbard model.
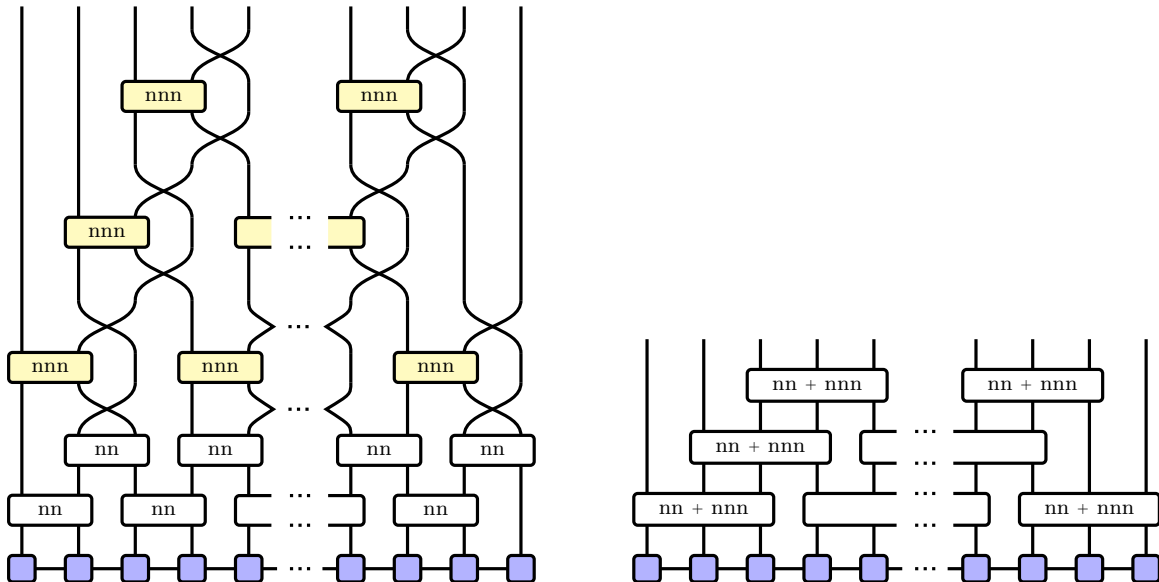
Figure 4.20. Graphical representation of $\hat{U}_{\mathrm{ST1}}(\tau)\,|\psi\rangle$ in the first-order Trotter approximation for a Hamiltonian containing nearest-neighbor and next-nearest neighbor terms with swap gates (left, nearest-neighbor gates in white and next-nearest neighbor gates in beige) and three-site gates (right).

Table 4.1. Comparison of swap gates and three-site gates for the time evolution of a Hamiltonian containing nearest-neighbor and next-nearest-neighbor couplings: Approximate scaling of the operations during one time evolution step with the bond dimension χ for large system sizes L and different values of the physical dimension d.

d	swap	three-site
2	$\mathcal{O}(32L\chi^3)$	$\mathcal{O}(24L\chi^3)$
4	$\mathcal{O}(256L\chi^3)$	$\mathcal{O}(320L\chi^3)$

Second-Order Decomposition

A version of the Suzuki-Trotter decomposition which is accurate up to second order in the time step τ is obtained by the simple modification

$$\exp(-\mathrm{i}\hat{H}\tau) = \exp\left(-\mathrm{i}\hat{H}_{\mathrm{odd}}\tfrac{\tau}{2}\right)\exp\left(-\mathrm{i}\hat{H}_{\mathrm{even}}\tau\right)\exp\left(-\mathrm{i}\hat{H}_{\mathrm{odd}}\tfrac{\tau}{2}\right) + \mathcal{O}(\tau^3), \qquad (4.31)$$

which can again be verified by Taylor expansion of both sides. This increases the number of gates per time step, but in return allows for larger time steps because the error is one order higher in τ.

If the state is not explicitly required (e.g. for measurements) after every time step, then the half-step gates of consecutive time steps can even be combined into

$$\exp\left(-\mathrm{i}\hat{H}_{\mathrm{odd}}\tfrac{\tau}{2}\right)\exp\left(-\mathrm{i}\hat{H}_{\mathrm{odd}}\tfrac{\tau}{2}\right) = \exp\left(-\mathrm{i}\hat{H}_{\mathrm{odd}}\tau\right),$$

eliminating the additional effort for all time steps without measurements.

For three-site gates, the same considerations yield the decomposition

$$\mathrm{e}^{-\mathrm{i}\hat{H}\tau} = \mathrm{e}^{-\mathrm{i}\hat{H}_1\tau/2}\,\mathrm{e}^{-\mathrm{i}\hat{H}_2\tau/2}\,\mathrm{e}^{-\mathrm{i}\hat{H}_3\tau}\,\mathrm{e}^{-\mathrm{i}\hat{H}_2\tau/2}\,\mathrm{e}^{-\mathrm{i}\hat{H}_1\tau/2} + \mathcal{O}(\tau^3). \qquad (4.32)$$

White and Feiguin [71] suggested a different second-order accurate decomposition of nearest-neighbor Hamiltonians, which is more convenient when working with mixed-canonical MPS. Applying first all odd-site gates and then all even-site gates to an MPS in mixed-canonical form requires an additional SVD after each gate to shift the orthogonality center to the site where the next gate is applied. This can be avoided by using the decomposition

$$\mathrm{e}^{-\mathrm{i}\hat{H}\tau} = \mathrm{e}^{-\mathrm{i}\hat{h}_{1,2}\tau/2}\ldots\mathrm{e}^{-\mathrm{i}\hat{h}_{L-2,L-1}\tau/2}\,\mathrm{e}^{-\mathrm{i}\hat{h}_{L-1,L}\tau}\,\mathrm{e}^{-\mathrm{i}\hat{h}_{L-2,L-1}\tau/2}\ldots\mathrm{e}^{-\mathrm{i}\hat{h}_{1,2}\tau/2} + \mathcal{O}(\tau^3), \quad (4.33)$$

with the drawback of a larger number of gates per time step. Throughout the present thesis, the decompositions (4.31) and (4.32) are used and referred to as *second-order Trotter approximation* $\hat{U}_{\mathrm{ST2}}$.

4.8.2. Time Evolution with MPOs

An alternative way of time-evolving an MPS is representing the time-evolution operator as an MPO and applying it to the MPS. Exact MPO representations exist for certain models [72], but in most cases one must rely on approximations.

MPOs from Trotter Gates

One possibility is to build MPOs directly from Trotter gates [16]. For this purpose, the Trotter gates are singular-value decomposed to split them into separate matrices for each site,

$$G^{[i]}_{(s_i s_i')(s_{i+1} s_{i+1}')} := \left\langle s_i s_{i+1}\middle|\exp(-\mathrm{i}\hat{h}_{i,i+1}\tau)\middle|s_i' s_{i+1}'\right\rangle = \sum_\alpha U^{[i]}_{(s_i s_i')\alpha_i}\lambda^{[i]}_{\alpha_i}V^{[i]\dagger}_{\alpha_i(s_{i+1} s_{i+1}')}. \qquad (4.34)$$

To obtain an MPO form, these matrices can then be combined as follows:

$$W^{[i]s_i s_i'}_{\alpha_{i-1}\alpha_i} = \sum_{s_i''} V^{[i-1]\dagger}_{\alpha_{i-1}(s_i'' s_i')} U^{[i]}_{(s_i s_i'')\alpha_i} \lambda^{[i]}_{\alpha_i} \qquad \text{for } i \text{ even,}$$

$$W^{[i]s_i s_i'}_{\alpha_{i-1}\alpha_i} = \sum_{s_i''} U^{[i]}_{(s_i'' s_i')\alpha_i} \lambda^{[i]}_{\alpha_i} V^{[i-1]\dagger}_{\alpha_{i-1}(s_i s_i'')} \qquad \text{for } i \text{ odd.} \tag{4.35}$$

At the edges of the system ($i = 1$ and $i = L$), the MPO tensors consist only of the contribution by one gate ($U\Lambda$ on the first site and $V^\dagger$ on the last site). The above steps are illustrated in Figure 4.21 (first two diagrams). If the Hamiltonian is translationally invariant, such that each term $\hat{h}_{i,i+1}$ has the same form, then (except for the edges) the MPO is composed of only two different tensors $W^{[A]}$ and $W^{[B]}$ (Figure 4.21, second and third diagram). Since the matrices which are decomposed (corresponding to the reshaped gates) have dimensions $d^2 \times d^2$, the resulting MPO has a bond dimension of at most d^2.
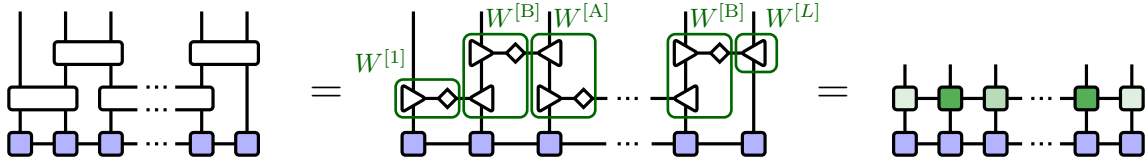
Figure 4.21. Formation of an MPO from Trotter gates by SVD. The MPO tensors are constructed from the SV-decomposed gates as indicated by the green boxes in the middle. If the Trotter gates are the same at each site, the bulk MPO is invariant under translation by two sites.

For some applications[1], it may be advantageous to use a more symmetric gauge of the MPO. This can be achieved by symmetrically distributing the singular value matrix Λ when decomposing the Trotter gates in the sense that, instead of using $(U\Lambda)$ and $V^\dagger$ as in (4.35), we use $(U\sqrt{\Lambda})$ and $(\sqrt{\Lambda}V^\dagger)$ as shown in Figure 4.22.
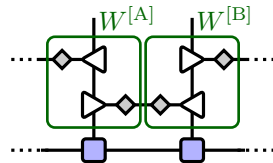

Figure 4.22. Symmetric formation of an MPO from SV-decomposed Trotter gates. Each diamond-shaped tensor corresponds to $\sqrt{\Lambda}$ from the respective SVD and the green boxes indicate the MPO tensors.

The same procedure can be applied to three-site gates by decomposing them into three matrices, but the resulting MPO will have a higher bond dimension. In cases where more two-site gates per time step are involved, e.g. when using swap gates or second-order approximations, multiple MPOs per time step can be formed to avoid large bond dimensions.

---

[1]One of them is the transverse contraction method described in Section 4.11. The influence of the gauge of the MPO on this particular algorithm is investigated in Section 6.1.2.

When using a second-order Suzuki-Trotter decomposition (see Section 4.8.1, page 52), we can simply view the time step

$$e^{-i\hat{H}_{\text{odd}}\tau/2}\, e^{-i\hat{H}_{\text{even}}\tau}\, e^{-i\hat{H}_{\text{odd}}\tau/2}$$

as two half time steps

$$\left(e^{-i\hat{H}_{\text{odd}}\tau/2}\, e^{-i\hat{H}_{\text{even}}\tau/2}\right)\left(e^{-i\hat{H}_{\text{even}}\tau/2}\, e^{-i\hat{H}_{\text{odd}}\tau/2}\right).$$

The decomposition described above can then be done for both half steps, yielding two MPOs per time step. Since the sets of gates for even and odd sites are applied in reversed order in the second half step, the two MPOs are not equal, but if the gates are the same at every site (i.e. the Hamiltonian is translationally invariant) the MPO for the second half step can be obtained from the first by swapping the $W^{[A]}$ and $W^{[B]}$ matrices.

Since MPOs obtained in this way are an exact MPO representation of the underlying Trotter gates, they preserve the unitarity of the time-evolution operator.

The W$^{\text{I}}$-Approximation

A different approach to obtain MPOs via a series expansion of the time evolution operator has been proposed by Zaletel et al. [73]. If the Hamiltonian is given by an MPO with matrices

$$\hat{\mathcal{W}}^{[i]} = \begin{pmatrix} \hat{\mathbb{1}}_i & \hat{C}_i & \hat{D}_i \\ 0 & \hat{A}_i & \hat{B}_i \\ 0 & 0 & \hat{\mathbb{1}}_i \end{pmatrix}, \tag{4.36}$$

where $\hat{C}$ is a 1-by-m matrix and $\hat{B}$ is a n-by-1 matrix, then the MPO with matrices

$$\hat{W}^{\text{I}[i]}(\tau) = \begin{pmatrix} \hat{\mathbb{1}}_i - i\tau\hat{D}_i & \sqrt{-i\tau}\hat{C}_i \\ \sqrt{-i\tau}\hat{B}_i & \hat{A}_i \end{pmatrix}, \tag{4.37}$$

where τ is the time step[1], is a first-order accurate approximation for the time evolution operator. This is called the W$^{\text{I}}$-approximation and is an exact MPO representation of

$$\hat{U}^{\text{I}}(\tau) = \hat{\mathbb{1}} - i\tau\sum_i \hat{h}_i - \tau^2 \sum_{i<j}\hat{h}_i\hat{h}_j + i\tau^3 \sum_{i<j<k}\hat{h}_i\hat{h}_j\hat{h}_k + \ldots, \tag{4.38}$$

where $\hat{h}_i$ are the single terms of the Hamiltonian and by $i < j$ we mean that all sites affected by $\hat{h}_i$ are to the left of those affected by $\hat{h}_j$ [73].

At the first and last site, the matrices of the Hamiltonian MPO (4.36) are vectors and thus $\hat{A}_1$, $\hat{B}_1$, $\hat{A}_L$ and $\hat{C}_L$ are empty, leading to

$$\hat{W}^{\text{I}[1]}(\tau) = \begin{pmatrix} \hat{\mathbb{1}}_1 - i\tau\hat{D}_1 & \sqrt{-i\tau}\hat{C}_1 \end{pmatrix}, \qquad \hat{W}^{\text{I}[L]}(\tau) = \begin{pmatrix} \hat{\mathbb{1}}_L - i\tau\hat{D}_L \\ \sqrt{-i\tau}\hat{B}_L \end{pmatrix} \tag{4.39}$$

for the edge matrices of the W$^{\text{I}}$-MPO.

---

[1]Note that in [73] the symbol t does not denote real time but the exponent in $\exp(t\hat{H})$.

If instead of the real time step τ, two complex time steps $\tau_1 = \frac{1+\mathrm{i}}{2}\tau$ and $\tau_2 = \frac{1-\mathrm{i}}{2}\tau$ are performed, then the error of the W$^{\mathrm{I}}$-approximation is of order τ^3 [73]. We will refer to this version as the *second-order W$^{\mathrm{I}}$-approximation*. In this case, two different MPOs have to be applied for one real time step.

Unlike the MPOs formed from Trotter gates, those obtained from the W$^{\mathrm{I}}$-approximation are *not* unitary. Assuming that all $\hat{h}_i$ are hermitian, the hermitian conjugate of (4.38) is given by

$$\hat{U}^{\mathrm{I}\dagger}(\tau) = \hat{\mathbb{1}} + \mathrm{i}\tau^* \sum_i \hat{h}_i - (\tau^*)^2 \sum_{i<j} \hat{h}_i \hat{h}_j - \mathrm{i}(\tau^*)^3 \sum_{i<j<k} \hat{h}_i \hat{h}_j \hat{h}_k + \dots$$

and for the product $\hat{U}^\dagger \hat{U}$ we obtain

$$\hat{U}^{\mathrm{I}\dagger}(\tau)\hat{U}^{\mathrm{I}}(\tau) = \hat{\mathbb{1}} + \mathrm{i}(\tau^* - \tau)\sum_i \hat{h}_i - \left(\tau^2 + (\tau^*)^2\right)\sum_{i<j}\hat{h}_i\hat{h}_j + \tau\tau^*\sum_{ij}\hat{h}_i\hat{h}_j + \mathcal{O}\left(\tau^3\right).$$

For an ordinary real time step τ, the approximation is thus unitary to the order τ, while for the complex time steps in the second-order approximation, deviations from unitarity already occur at the order τ.

4.9. Conserved Quantities in MPS

A considerable speedup as well as memory savings for many algorithms can be achieved by making use of good quantum numbers. We will only treat the simplest case of additive quantum numbers such as spin (S^z in a spin-1/2 system, to be precise) and particle number.

To understand how conservation laws can be exploited in MPS, first note that each MPS matrix $M^{[j]s_j}$ maps a set of states of the subsystem comprising sites 1 to $j-1$ onto a set of states of the subsystem additionally including the j-th site [74],

$$|a_{\alpha_j}^{(j)}\rangle = \sum_{\alpha_{j-1}} \sum_{s_j} M_{\alpha_{j-1}\alpha_j}^{[j]s_j} |a_{\alpha_{j-1}}^{(j-1)}\rangle |s_j\rangle. \tag{4.40}$$

Let us consider the specific example of conserved particle number N and choose the local basis states $|s_i\rangle$ to be eigenstates of the local particle number operator $\hat{n}_i$ with eigenvalues $n(s_i)$. Then we can restrict the state of the system to the eigenspace of the total particle number operator with eigenvalue N and each of the states $|a_{\alpha_{j-1}}^{(j-1)}\rangle$ must be an eigenstate of the particle number in the respective left subsystem, $\sum_{i=1}^{j-1}\hat{n}_i$ (otherwise combining it with a state of the remaining subsystem would never lead to an eigenstate of the total particle number). The corresponding eigenvalue is in general different for different values of α_{j-1} and denoted by $n^{(j-1)}(\alpha_{j-1})$. Likewise, the states $|a_{\alpha_j}^{(j)}\rangle$ must be eigenstates of $\sum_{i=1}^{j}\hat{n}_i$ with eigenvalues $n^{(j)}(\alpha_j)$.

Since for each value of s_j, the state $|s_j\rangle$ contributes a well-defined number of particles $n(s_j)$, only those elements of $M_{\alpha_{j-1}\alpha_j}^{[j]s_j}$ can be non-zero where

$$n^{(j-1)}(\alpha_{j-1}) + n(s_j) = n^{(j)}(\alpha_j). \tag{4.41}$$

This restriction gives the matrices a block form that saves memory as well as computation time when performing operations such as contractions and SVDs.

If we assign a *direction* to each index (which is indicated by an arrow in the graphical notation) to specify whether it belongs to the domain or codomain of the map (4.40), then the rule (4.41) can be formulated more generally as follows:

> *For each non-zero element of a tensor, the sum of the quantum numbers of ingoing indices must be equal to the sum of the quantum numbers of outgoing indices.*

In the example (4.40), α_{j-1} and s_j are ingoing indices and α_j is an outgoing index, resulting in (4.41) for each MPS tensor (see Figure 4.23 for an example of an MPS with directed indices). But the general rule does not only apply to the MPS tensors, but also to the matrix representations of operators and to MPO tensors. More details are given e.g. in [10, 74, 75] and references therein.
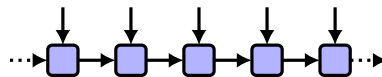
Figure 4.23. Graphical representation of an MPS using good quantum numbers. The arrows indicate the directions assigned to the indices to distinguish ingoing and outgoing indices. For the dummy indices on the first and last tensors, the values of the quantum numbers must be chosen to match the global quantum number value (see also [10]).

4.10. MPS for infinite systems (iMPS)

For a translationally invariant state in the thermodynamic limit, the matrices constituting the MPS can be chosen site-independent [76]. For a unit cell comprising more than one site, a corresponding set of matrices is required. With these iMPS, ground state calculations and time evolutions can be done in the thermodynamic limit without the need for extrapolation [77, 78].

4.10.1. iDMRG

Originally, the infinite-size version of DMRG (see Section 4.7) was used merely as an initialization step for the actual finite-size DMRG algorithm [11]. McCulloch [78] found a modification that makes iDMRG a valuable tool for the determination of ground states in the thermodynamic limit.

In this thesis, we will use a two-site version of iDMRG. The algorithm is in most parts equal to the infinite-system DMRG described in Section 4.7 (page 47), where after n steps we have an approximation of the ground state of a system with $2n$ sites in the form

$$|\psi_{2n}\rangle = \sum_{\substack{s_1,\ldots,s_n \\ s_1',\ldots,s_n'}} A^{[1]s_1} \ldots A^{[n]s_n} \Lambda^{[n]} B^{[n]s_n'} \ldots B^{[1]s_1'} |s_1 \ldots s_n s_n' \ldots s_1'\rangle . \qquad (4.42)$$

The only difference between the original infinite-system algorithm and the method introduced by McCulloch is the initial prediction of the state for the next step. First we use SVDs to transform $A^{[n]s_n}\Lambda^{[n]} \to \Lambda_L^{[n]}B^{[n+1]s_n}$ and $\Lambda^{[n]}B^{[n]s'_n} \to A^{[n+1]s'_n}\Lambda_R^{[n]}$, where the new A and B have the usual orthogonality properties. As the initial guess for the state of the system with two sites added in the center, we then use

$$|\tilde{\psi}_{2n+2}\rangle = \sum_{\substack{s_1,\ldots,s_{n+1} \\ s'_1,\ldots,s'_{n+1}}} A^{[1]s_1}\ldots A^{[n]s_n}A^{[n+1]s_{n+1}}\Lambda_R^{[n]}\left(\Lambda^{[n-1]}\right)^{-1}\Lambda_L^{[n]}B^{[n+1]s'_{n+1}}B^{[n]s'_n}\ldots$$
$$\ldots B^{[1]s'_1}\left|s_1\ldots s_{n+1}s'_{n+1}\ldots s'_1\right\rangle. \quad (4.43)$$

With increasing system size, the central unit cell will converge to the ground state in the thermodynamic limit. The convergence can be checked in terms of the ground state energy or by measuring the orthogonality fidelity [78].

To obtain an iMPS from the calculation, we must pick out a portion of the final state that can be infinitely repeated. This can be achieved by using the central part of (4.42)

$$A^{[n]s_n}\Lambda^{[n]}B^{[n]s'_n} = \Lambda^{[n-1]}\Gamma^{A[n]s_n}\Lambda^{[n]}\Gamma^{B[n]s'_n}\Lambda^{[n-1]}$$

and removing one of the $\Lambda^{[n-1]}$ (for details on the $\Gamma\Lambda$-form see Section 4.3.3). A possible unit cell is thus given by

$$\Lambda^{[n-1]}\Gamma^{A[n]s_n}\Lambda^{[n]}\Gamma^{B[n]s'_n} = A^{[n]s_n}\Lambda^{[n]}B^{[n]s'_n}\left(\Lambda^{[n-1]}\right)^{-1}$$

and if we perform the same SVD as for the prediction of the next state, this can be written as

$$A^{[n]s_n}A^{[n+1]s'_n}\Lambda_R^{[n]}\left(\Lambda^{[n-1]}\right)^{-1}. \quad (4.44)$$

Note that the iMPS defined by the unit cell (4.44) is not in left-canonical form due to the additional matrix $\Lambda_R^{[n]}\left(\Lambda^{[n-1]}\right)^{-1}$.

4.10.2. Orthogonalization and Normalization of iMPS

An iMPS as obtained from iDMRG in the form (4.44) does in general neither obey any orthogonality conditions nor is it normalized. McCulloch [78] also provides a procedure for orthogonalizing the resulting iMPS that was originally introduced by Orús and Vidal [79]. First, it is important to note that the left orthogonality relations (4.4) are equivalent to the *transfer matrix*

$$\mathcal{T}^A_{(\alpha_{j-1}\alpha'_{j-1})(\alpha_j\alpha'_j)} = \sum_{s_j} A^{[j]s_j}_{\alpha_{j-1}\alpha_j}A^{[j]s_j*}_{\alpha'_{j-1}\alpha'_j} \quad (4.45)$$

having the identity matrix $\delta_{\alpha_{j-1}\alpha'_{j-1}}$ as a left eigenvector with eigenvalue 1. Analogously, the right orthogonality relations (4.5) are equivalent to the corresponding transfer matrix having the identity as a right eigenvector with eigenvalue 1.

We can therefore employ as a left-orthogonality condition for the iMPS that the transfer matrix of the unit cell,

$$\mathcal{T}^A_{(\alpha_L\alpha'_L)(\alpha_R\alpha'_R)} = \sum_{s_1s_2} M^{s_1s_2}_{\alpha_L\alpha_R}M^{s_1s_2*}_{\alpha'_L\alpha'_R}, \quad (4.46)$$

has the identity as a left eigenvector with eigenvalue 1. Thus, we demand

$$\sum_{\alpha_L \alpha'_L} \delta_{\alpha_L \alpha'_L} \sum_{s_1 s_2} M^{s_1 s_2}_{\alpha_L \alpha_R} M^{s_1 s_2 *}_{\alpha'_L \alpha'_R} = \delta_{\alpha_R \alpha'_R}.$$

For the unit cell given by (4.44), however, we have

$$\sum_{\substack{\alpha_L \alpha'_L}} \delta_{\alpha_L \alpha'_L} \sum_{\substack{s_1 s_2 \\ \beta \beta' \gamma \gamma'}} A^{[1]s_1}_{\alpha_L \beta} A^{[2]s_2}_{\beta \gamma} P_{\gamma \alpha_R} A^{[1]s_1 *}_{\alpha'_L \beta'} A^{[2]s_2 *}_{\beta' \gamma'} P^*_{\gamma' \alpha'_R} = \sum_{\gamma} P_{\gamma \alpha_R} P^*_{\gamma \alpha'_R} = (P^\dagger P)_{\alpha'_R \alpha_R},$$

where $P := \Lambda^{[n]}_R (\Lambda^{[n-1]})^{-1}$ and the orthogonality relations for the A matrices (4.4) were used.

In order to fulfill the left-orthogonality condition, the unit cell must thus be regauged. To obtain the appropriate gauge, we first find the dominant left eigenmatrix V of $\mathcal{T}^A$ with

$$\sum_{\alpha_L \alpha'_L} V_{\alpha'_L \alpha_L} \mathcal{T}^A_{(\alpha_L \alpha'_L)(\alpha_R \alpha'_R)} = \eta V_{\alpha'_R \alpha_R}. \tag{4.47}$$

This matrix is hermitian due to the form of the transfer matrix and can therefore be decomposed into $V = X^\dagger X$ (e.g. by means of an eigenvalue decomposition). If we now insert the identity $X^{-1} X$ after each unit cell, we can use $\tilde{M}^{s_1 s_2} = X A^{[1]s_1} A^{[2]s_2} P X^{-1}$ as the new unit cell, by which we achieve

$$\sum_{\alpha_L \alpha'_L} \delta_{\alpha_L \alpha'_L} \tilde{\mathcal{T}}^A_{(\alpha_L \alpha'_L)(\alpha_R \alpha'_R)} = \sum_{\substack{\beta \beta' \\ \gamma \gamma'}} \underbrace{\sum_{\alpha_L \alpha'_L} \delta_{\alpha_L \alpha'_L} X_{\alpha_L \beta} X^*_{\alpha'_L \beta'}}_{=V_{\beta' \beta}} \mathcal{T}^A_{(\beta \beta')(\gamma \gamma')} X^{-1}_{\gamma \alpha_R} X^{-1*}_{\gamma' \alpha'_R}$$

$$= \eta \sum_{\gamma \gamma'} V_{\gamma' \gamma} X^{-1}_{\gamma \alpha_R} X^{-1*}_{\gamma' \alpha'_R} = \eta \delta_{\alpha_R \alpha'_R},$$

where we used $V = X^\dagger X$ and (4.47). Hence, the new unit cell is left-orthogonal (which also implies normalization of the state) if we multiply its components by $1/\sqrt{\eta}$.

The procedure for right-orthogonalizing the iMPS is analogous. Starting with a unit cell $Q B^{[1]} B^{[2]}$, we find the dominant right eigenmatrix of the transfer matrix and decompose it into $Y Y^\dagger$. A right-orthogonal unit cell can then be constructed as $Y^{-1} Q B^{[1]} B^{[2]} Y / \sqrt{\eta}$.

Once orthogonalized, the unit cell matrices can be decomposed into new matrices $A^{[A]}$, $A^{[B]}$ and $B^{[A]}$, $B^{[B]}$, respectively, with standard methods.[1]

For the evaluation of expectation values, a mixed-canonical form is required (see Section 4.10.3). If we apply both transformations, the central part of the iDMRG prediction (4.43) can be written as

$$\dots \underbrace{X A^{[n]} A^{[n+1]} \Lambda^{[n]}_R \left(\Lambda^{[n-1]}\right)^{-1} X^{-1}}_{=A^{[A]} A^{[B]}} X \Lambda^{[n-1]} Y \underbrace{Y^{-1} \left(\Lambda^{[n-1]}\right)^{-1} \Lambda^{[n]}_L B^{[n+1]} B^{[n]} Y}_{=B^{[A]} B^{[B]}} \dots$$

We can thus choose $\Lambda = X \Lambda^{[n-1]} Y$ and if a diagonal Λ is desired, this can be achieved by singular-value decomposing it and absorbing U and $V^\dagger$ into the A and B matrices (which does not change their orthogonality properties).

---

[1] Note that for a left-orthogonal matrix, the SVD $M \to U(\Lambda V^\dagger)$ yields two left-orthogonal matrices, and for a right-orthogonal matrix, $(U \Lambda)$ and $V^\dagger$ are both right-orthogonal.

4.10.3. Expectation Values of Local Observables

In the mixed-canonical form of an iMPS, the measurement of local observables is simple: Assuming that the operator acts on one of the two sites directly to the right of Λ (which it can always be chosen to do because of the translational invariance of the state), the network collapses from both sides due to the orthogonality relations, only leaving the unit cell where the operator acts. An example thereof is shown in Figure 4.24.
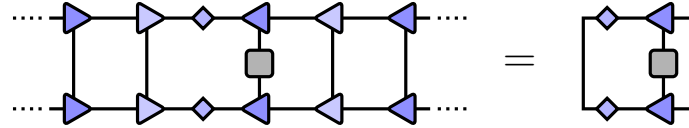

Figure 4.24. Graphical representation of the expectation value $\langle\psi|\hat{O}|\psi\rangle$ of a local operator $\hat{O}$ in a thermodynamic limit state represented by a mixed-canonical iMPS with a unit cell comprising two sites.

An iMPS resulting from two-site iDMRG has two sites in the unit cell. Even if the Hamiltonian is translationally invariant (with respect to one site), the matrices for the two sites can be different due to the bias of DMRG towards states with low entanglement [13, 66] (see also Section 4.7). The iMPS does then not represent the true ground state and measurements of observables other than the energy may be wrong. For many observables, however, this effect can be (at least partly) compensated by averaging over the two sites in the unit cell, i.e. measuring $\langle\psi|\hat{O}_1|\psi\rangle + \langle\psi|\hat{O}_2|\psi\rangle$ for a one-site operator, $\langle\psi|\hat{O}_{12}|\psi\rangle + \langle\psi|\hat{O}_{21}|\psi\rangle$ for a two-site operator (Figure 4.25) and so on.
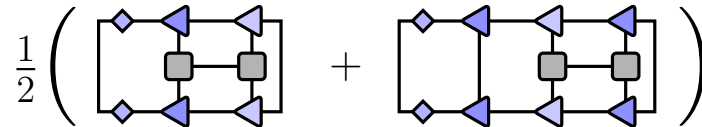
Figure 4.25. Measurement of the expectation value $\langle\psi|\hat{O}_{j,j+1}|\psi\rangle$ of a two-site observable $\hat{O}_{j,j+1}$ by averaging over both sites in the unit cell of a mixed-canonical iMPS.

As a simplified example, consider the measurement of the z-component of spin in an antiferromagnet with the true ground state $(|\dots \uparrow\downarrow\uparrow\downarrow \dots\rangle + |\dots \downarrow\uparrow\downarrow\uparrow \dots\rangle)/\sqrt{2}$, which has $\langle\hat{S}^z\rangle = 0$ at each site. If iDMRG finds the state $|\dots \uparrow\downarrow\uparrow\downarrow \dots\rangle$ instead, one would measure $\pm\frac{1}{2}$ at every other site, respectively. Averaging over two neighboring sites then again gives the correct result 0, because

$$(\langle\dots \uparrow\downarrow\uparrow_j\downarrow \dots| + \langle\dots \downarrow\uparrow\downarrow_j\uparrow \dots|)\hat{S}^z_j(|\dots \uparrow\downarrow\uparrow_j\downarrow \dots\rangle + |\dots \downarrow\uparrow\downarrow_j\uparrow \dots\rangle) = \langle\uparrow_j|\hat{S}^z_j|\uparrow_j\rangle + \langle\downarrow_j|\hat{S}^z_j|\downarrow_j\rangle,$$

where the other two terms vanish due to the orthogonality of the other sites $i \neq j$. The same is true for all other operators acting on a finite number of sites. Most models have more complicated ground states, but for those with antiferromagnetic behavior such as the XXZ model, Hubbard model or T-V model (with spin replaced by occupation number), they have a form similar to the one above and the discussion remains valid.

4.11. Transverse Contraction

In Section 4.8.2, time evolution was performed by approximating the time evolution operator for a small time step τ with an MPO and repeatedly applying it to the initial MPS. The following measurement of an observable in the time evolved state can be thought of as the contraction of a tensor network as shown in Figure 4.26 on the left for a local observable. Up to here, networks like this were contracted from bottom to top (and, implicitly, at the same time from top to bottom) by applying the time evolution operators to the MPS to obtain an approximation of $|\psi(t)\rangle$ and finally evaluating $\langle\psi(t)|\hat{O}|\psi(t)\rangle$ by means of another contraction.

However, there are many other possible ways to contract the network in Figure 4.26. One of them is the *transverse contraction* proposed by Bañuls et al. [15]. Formally, the leftmost and rightmost columns of the tensor network are MPS and the other columns are MPOs, having the bond indices of the original MPS and MPOs as "physical" indices and vice versa. To avoid confusion, we will refer to the bond indices of the transverse MPO and MPS (the vertical indices in Figure 4.26) as *transverse bond indices* and to the local indices of the transverse MPS (horizontal in Figure 4.26) as *transverse local indices*.

Due to the formal MPO-MPS structure, we can use the same methods to contract the network in the spatial direction instead of the time direction, i.e. from left to right and from right to left, by subsequently applying the MPO-columns to the MPS-columns on the left and right until only the central column containing the observable is left between two MPS (Figure 4.26 right).
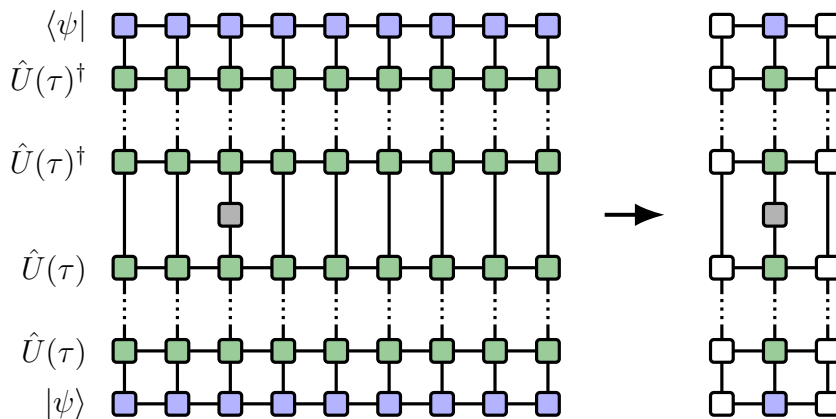
Figure 4.26. Full tensor network representing the expectation value $\langle\psi(t)|\hat{O}_3|\psi(t)\rangle$. The MPS representing the initial state is drawn in blue, the MPO representing the time evolution operator $\hat{U}(\tau)$ in green and the gray tensor is the operator $\hat{O}_3$ corresponding to the observable to be measured. Contracting the network on the left from both sides in spatial direction leads to the network on the right.

After each contraction step, the resulting transverse MPS must be truncated to keep its transverse bond dimension within reasonable limits. We know that the required bond dimension to store a state in an MPS with a certain accuracy depends on the bipartite entanglement of the state at the respective bond. Hence, the transverse bond dimension

required in the transverse MPS during a transverse contraction depends on the bipartite entanglement in time direction at the respective time step.

Whether or not the transverse contraction is more efficient than conventional time evolution methods depends on the details of the network. A clear benefit of the transverse approach is, that it provides a way to compute expectation values directly in the thermodynamic limit.

4.11.1. Infinite Systems and the Transfer Matrix

If both the Hamiltonian and the initial state are translationally invariant, which is usually the case in an infinite system, then so are the corresponding MPS and MPO (see Section 4.10). In this case, the tensor network representing the expectation value of an observable at a certain point in time consists of the central column, containing the operator corresponding to the observable to be measured, and infinitely many identical columns to the left and right of it. This structure is indicated in Figure 4.27 on the left. The columns of tensors appearing here are the so-called *transfer matrices* of the time-evolved state [15],

$$\mathcal{T}_{\{\alpha_i,\alpha_i'\}\{\beta_i,\beta_i'\}} = \sum_{\{s_i\},\{s_i'\}} A^{s_0'*}_{\alpha_0'\beta_0'}(W_1)^{s_1's_0'*}_{\alpha_1'\beta_1'} \dots (W_n)^{s_ns_{n-1}'*}_{\alpha_n'\beta_n'}(W_n)^{s_ns_{n-1}}_{\alpha_n\beta_n} \dots (W_1)^{s_1s_0}_{\alpha_1\beta_1} A^{s_0}_{\alpha_0\beta_0} \quad (4.48)$$

where A^s are the matrices representing the translationally invariant initial state and $W_j^{ss'}$ is the MPO representation of the time evolution operator evolving by one time step τ from time $(j-1)\tau$ to $j\tau$. The index labels s_i do not refer to different sites here, but to the different time steps. Note that the concept of a transfer matrix (albeit without time evolution) was already introduced in (4.45). If we denote the central column with the observable by $\mathcal{T}_O$,

$$(\mathcal{T}_O)_{\{\alpha_i,\alpha_i'\}\{\beta_i,\beta_i'\}} = \sum_{\{s_i\},\{s_i'\}} A^{s_0'*}_{\alpha_0'\beta_0'}(W_1)^{s_1's_0'*}_{\alpha_1'\beta_1'} \dots (W_n)^{s_n's_{n-1}'*}_{\alpha_n'\beta_n'} \langle s_n'|\hat{O}|s_n\rangle \times$$

$$\times (W_n)^{s_ns_{n-1}}_{\alpha_n\beta_n} \dots (W_1)^{s_1s_0}_{\alpha_1\beta_1} A^{s_0}_{\alpha_0\beta_0},$$

the time-dependent expectation value can be written as [15, 76]

$$\langle\psi(t)|\hat{O}|\psi(t)\rangle = \lim_{n\to\infty} \text{tr}(\mathcal{T}^n\mathcal{T}_O\mathcal{T}^n).$$

Note that instead of the usual edge vectors we simply use the trace (corresponding to periodic boundary conditions), which does not make a difference in the thermodynamic limit. To ensure the correct normalization we must actually calculate

$$\langle\hat{O}(t)\rangle = \frac{\langle\psi(t)|\hat{O}|\psi(t)\rangle}{\langle\psi(t)|\psi(t)\rangle} = \lim_{n\to\infty} \frac{\text{tr}(\mathcal{T}^n\mathcal{T}_O\mathcal{T}^n)}{\text{tr}(\mathcal{T}^{2n+1})}, \quad (4.49)$$

where the denominator corresponds to the same network as the numerator without the observable.

If the dominant eigenvalue λ of $\mathcal{T}$ is non-degenerate (according to [76] the generic case), then in the thermodynamic limit $n\to\infty$, the operators $\mathcal{T}^n$ can be replaced by $\lambda^n|R\rangle\langle L|$.

Here $|R\rangle$ and $\langle L|$ are the right and left eigenvectors corresponding to the dominant eigenvalue λ (which are in general distinct because the transfer matrix is not hermitian). The sought-for expectation value (4.49) becomes [15]

$$\langle \hat{O}(t) \rangle = \frac{\langle L | \mathcal{T}_O | R \rangle}{\langle L | \mathcal{T} | R \rangle}. \tag{4.50}$$

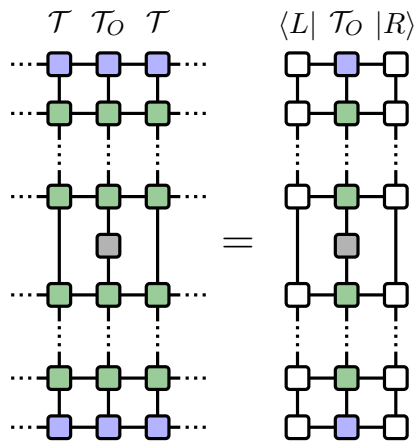A more rigorous derivation of this result is given in Appendix E and the graphical representation is shown in Figure 4.27.

Figure 4.27. Full tensor network representing the expectation value $\langle \psi(t) | \hat{O}_j | \psi(t) \rangle$ in the thermodynamic limit, where the initial state is given as a translationally invariant MPS (blue). The green tensors form the (also translationally invariant) MPO representing the time evolution operator $\hat{U}(\tau)$ and the gray tensor is the operator $\hat{O}_j$ corresponding to the observable to be measured. In this case the network can be reduced to a contraction of two transverse MPS and a transverse MPO (right).

So far, we only considered states and MPOs which are translationally invariant in the sense that the matrices are identical at every site. However, all results derived above can be easily generalized to unit cells larger than one site by using a transfer matrix comprising more than one column of tensors (see Figure 4.28). We must then find the eigenvectors of the product of all columns, e.g. $\langle L | \mathcal{T}_1 \mathcal{T}_2 = \lambda \langle L |$ and likewise for $|R\rangle$ for two sites in the unit cell. Of course, in this case it can make a difference at which of the sites in the unit cell the local observable is measured. If the larger unit cell does not have a physical origin, but results from the algorithms used to determine the initial state and time evolution MPO, this is undesirable, and we may have to average the observable over all sites in the unit cell to reduce this effect and obtain meaningful results (see also Section 4.10.3). For the case of invariance under translation by two sites, which is relevant when using an initial state obtained with two-site iDMRG or an MPO built from Trotter gates, this is discussed in more detail below (Section 4.11.3).

The generalization to multiple-site observables and correlation functions is equally simple. Instead of a single modified transfer matrix $\mathcal{T}_O$ we then have multiple columns $\mathcal{T}_{O1}, \mathcal{T}_{O2}, \ldots$ in the center of the network (see Figure 4.29 left and middle). In the same way we can treat initial states which are translationally invariant except at a finite number of sites in the center of the infinite chain, such as a ground state with a local excitation (see Figure 4.29 right). Whenever the initial state is modified, the same modification must be included in the network representing the denominator $\langle L | \mathcal{T} | R \rangle$ to ensure correct normalization. Similar networks also arise from two-point time-dependent correlation functions, which were calculated with the transverse method in [16].
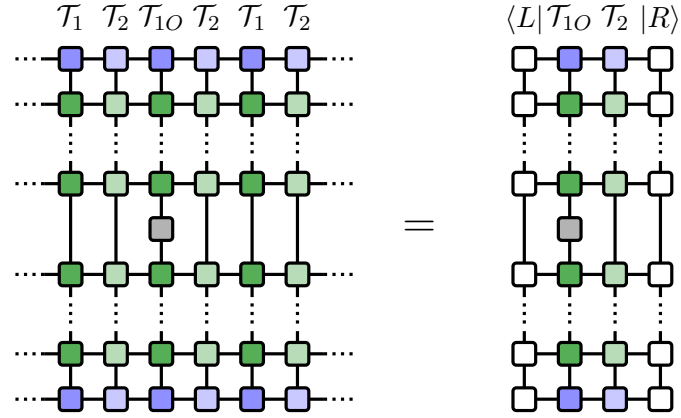
Figure 4.28. Tensor network representing the expectation value $\langle\psi(t)|\hat{O}_j|\psi(t)\rangle$ in the thermodynamic limit, where the initial state is given as a translationally invariant MPS with two sites per unit cell (indicated by the different shades of blue) and the time-evolution operator $\hat{U}(\tau)$ as an MPO (green) with the same translational invariance. Here the operator $\hat{O}_j$ (gray) acts on the first site in the unit cell.
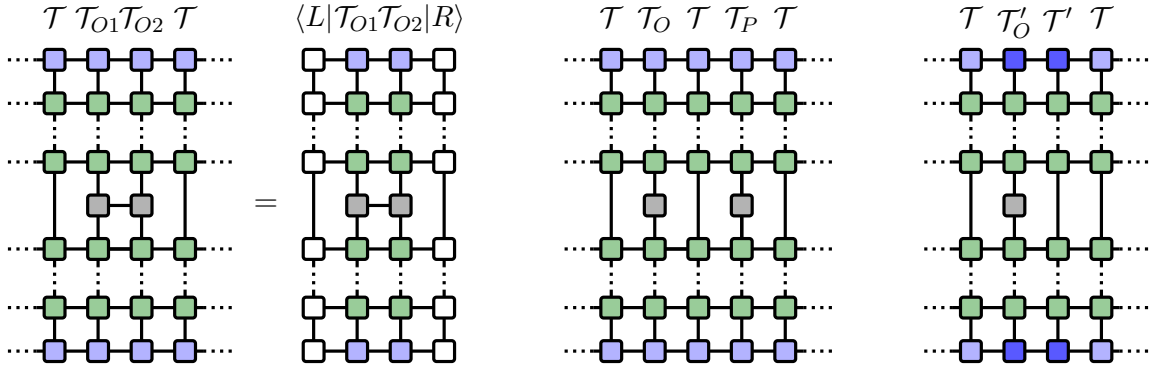

Figure 4.29. Examples for the tensor networks representing the expectation value of a multiple-site observable (here $\langle\hat{O}_{i,i+1}(t)\rangle$, left), a correlation function (here $\langle\hat{O}_i(t)\hat{P}_{i+2}(t)\rangle$, middle) and the expectation value of a local observable with a modified initial state (right) in the thermodynamic limit. The last case also includes two-time correlation functions $\langle\hat{O}_i(0)\hat{P}_j(t)\rangle$. All networks can be reduced to a contraction of two transverse MPS and several transverse MPOs as explicitly shown for the leftmost one. To obtain the correct expectation value, every network must be divided by the value represented by the same network without the gray operators.

4.11.2. Computation of Eigenvectors

The key task in the transverse contraction of the infinite network is to find the left and right eigenvectors corresponding to the dominant eigenvalue of the transfer matrix $\mathcal{T}$. Bañuls et al. [15] proposed the power method, which consists of repeated application of $\mathcal{T}$ (given as an MPO) to an initial vector $|v\rangle$ (given as an MPS) and normalization of the result after each step. If the zip-up algorithm (see Section 4.6.1) is used for computing the MPS-MPO product $\mathcal{T}|v\rangle$, each iteration requires $L_{\mathcal{T}} - 1$ SVDs for a transfer matrix consisting of $L_{\mathcal{T}}$ tensors (for n time steps $L_{\mathcal{T}} = 2n + 2$). Each of these SVDs involves $\mathcal{O}(D^3\chi^3 d)$ floating-point operations, where D is the transverse local dimension (which is the bond dimension of the time evolution MPO) and d the transverse bond dimension of the transfer matrix (which is the original physical dimension). Therefore, the overall scaling of this algorithm is $L_{\mathcal{T}} D^3 \chi^3 d$ per iteration.

In practice, the truncation to a fixed transverse bond dimension during the zip-up algorithm may prevent the algorithm from properly converging, because regions in Hilbert space which cannot be represented with the restricted transverse bond dimension cannot be reached.

As pointed out in [10], due to the MPO-MPS structure of the problem we can also use a modification of DMRG to find the dominant eigenvectors. Conventional DMRG was introduced for the task of finding the smallest eigenvalue of a hermitian operator, whereas here we need to find the largest (in magnitude) eigenvalue of a non-hermitian MPO. Therefore, the Lanczos (or Davidson) algorithm used to find the smallest eigenvalue of the effective Hamiltonian must be replaced by a large sparse eigensolver for non-hermitian matrices, e.g. the Arnoldi algorithm [80], and it must be targeted at the largest eigenvalue instead of the smallest. To obtain the right (left) eigenvector of the transfer matrix, the right (left) eigenvalue problem of the *effective transfer matrix* defined in analogy to (4.28) must be solved to locally update the current transverse MPS.

Such a DMRG-like procedure for finding the dominant eigenvectors of the transfer matrix has been used with imaginary time evolution to calculate thermodynamic properties of infinite systems at finite temperature [81, 82] and is known in this context as *transfer-matrix DMRG*. We will adopt this name and abbreviate it as TM-DMRG.

Throughout the present thesis, a two-site version of TM-DMRG is used, because for ordinary DMRG calculations the two-site version is known to get stuck in local minima less likely (see Section 4.7 for details on single-site and two-site DMRG). During each sweep, $2(L_{\mathcal{T}} - 1)$ eigenvalue problems have to be solved and the corresponding matrices are of dimension $D^2\chi^2$, where D is the transverse local dimension (which is the bond dimension of the time-evolution MPO) and χ is the transverse bond dimension (which in practice is limited to values below the maximum transverse bond dimension). The Arnoldi eigensolver uses $\mathcal{O}(m^2 n)$ operations for an n-by-n matrix and m iterations [83, sec. 6.2]. For the cases discussed here, a few iterations (~ 10) are sufficient even for very large matrices and thus the Arnoldi algorithm requires $\mathcal{O}(D^2\chi^2)$ floating-point operations. After solving the local eigenvalue problem, the two-site matrix ($D\chi \times D\chi$) must be split by an SVD to recover the MPS form, which gives an additional $\mathcal{O}(D^3\chi^3)$ operations. Hence, the overall cost of one TM-DMRG sweep is $\mathcal{O}(L_{\mathcal{T}} D^3\chi^3)$ operations.

At the first and last transverse site, the transverse local dimension equals the bond dimension of the initial state, which in case of highly entangled states (such as the ground states of Heisenberg and Hubbard models) is typically much larger than the bond dimension of the time-evolution MPO. However, this does usually not pose a problem, because unlike at the bulk sites these indices are not combined with transverse bond incides when reshaping the MPS tensors into matrices (e.g. for an SVD).

Both TM-DMRG and the power method need an initial guess and fail if the overlap of this initial vector with the dominant eigenvector is too small. For large transfer matrices (i.e. many time steps), this becomes likely when using random matrices for the initial MPS and, unlike for ordinary DMRG, it is not clear which kinds of initial states are physically meaningful and expected to have a high overlap with the eigenvector. This problem can be solved by starting with a small transfer matrix (e.g. the one without any time evolution) and inserting the time steps one at a time in an infinite-system DMRG-like fashion (see Section 4.7).

The MPS representing the initial state as well as the MPO used for time evolution have a gauge degree of freedom (see Section 4.3). Although measurable quantities do not depend on the gauge, it may certainly have an influence on the eigenvectors of the transfer matrix and therefore on the success and accuracy of the numerical calculation. This will be investigated in detail in Section 6.1.2 when we apply the transverse contraction method to the propagation of a single particle in a lattice.

4.11.3. Measurement of Observables

Once an approximation for the eigenvalues $\langle L|$ and $|R\rangle$ has been calculated, the expectation value $\langle\psi(t)|\hat{O}|\psi(t)\rangle$ can be obtained by contracting the remaining network in Figure 4.27 on the right. This is simply the matrix element of an MPO between two MPS, which is a standard task when working with MPS and is best evaluated by contracting row after row. The normalization $\langle L|R\rangle$ is also straightforward to calculate, as it corresponds to the overlap of two MPS.

For more complicated expectation values or correlation functions as in Figure 4.29, a contraction of the full remaining network rapidly becomes too costly and we must return to approximate methods for MPS-MPO products, e.g. the zip-up algorithm, and apply the columns to $\langle L|$ or $|R\rangle$ one after another. This, of course, involves truncation and therefore introduces an additional source of error.

The network depicted in Figure 4.27 only allows the calculation of the expectation value at the final time t. However, usually one is interested in the entire evolution of the observable from time 0 to t. Instead of repeating the whole algorithm (including the computationally expensive calculation of the eigenvectors) at each grid point $t_j = j\tau$ of the time series, we can make use of the fact that $\hat{U}(t_j + \tau, t_j)^\dagger \hat{U}(t_j + \tau, t_j) = \hat{\mathbb{1}}$ (which may be only approximately true for the respective approximation of $\hat{U}$) and obtain the expectation value at earlier times by simply shifting the tensor corresponding to the observable past the time evolution operators. The resulting network (see Figure 4.30) is

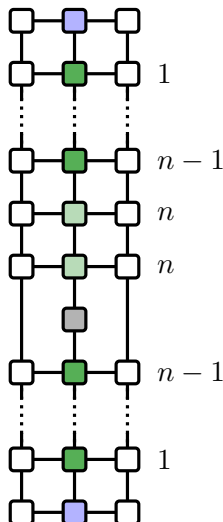**Figure 4.30.** Tensor network representing the expectation value $\langle\psi(t-\tau)|\hat{O}_j|\psi(t-\tau)\rangle$ in the thermodynamic limit, using the eigenvectors for the time $t = n\tau$. The labels on the right side denote the number of the respective time step. Since the two light green MPO tensors belong to $\hat{U}$ and $\hat{U}^\dagger$ for the same time step, the state is (at least approximately) evolved from $t-\tau$ to t and back *after* applying the gray operator.

then an approximation for the expectation value

$$\langle\psi(t_j)|\hat{U}(t, t_j)^\dagger\hat{U}(t, t_j)\hat{O}|\psi(t_j)\rangle = \langle\psi(t_j)|\hat{O}|\psi(t_j)\rangle.$$

A drawback of this method is that if the bond dimension during the eigenvector search is chosen too small for the final time, then one obtains wrong results for *all* times, although the bond dimension might have been sufficient for the network corresponding to a smaller total time.

Figure 4.31. Graphical representation of the expectation value of a two-site operator $\langle\psi(t)|\hat{O}_{j,j+1}|\psi(t)\rangle$ in the thermodynamic limit, where the initial state is given as a translationally invariant MPS with two sites per unit cell (indicated by the different shades of blue) and the time-evolution operator $\hat{U}(\tau)$ as an MPO (green) with the same translational invariance. The expectation value is averaged over both sites in the unit cell to cancel undesired even-odd effects.

If the initial state or the time-evolution MPO are invariant under translations by two sites only, then the transfer matrix consists of two columns (Figure 4.28). In this case, it may be necessary to average over the expectation values at both sites to suppress unwanted even-odd effects (see Section 4.10.3). This is shown in Figure 4.31 for an operator acting

on two adjacent sites. Note that, whenever the operator extends into the next unit cell, a full unit cell with both columns must be added to account for the translational invariance of the network. This additional unit cell also appears in the denominator of (4.50), giving an extra factor of the eigenvalue λ for the proper normalization.

4.11.4. Folding

For simple models, it has been observed [15, 16] that, due to the entanglement structure in the transverse eigenvectors, longer times can be reached by combining the tensors corresponding to the same time step into one tensor with squared dimensions. Graphically this corresponds to *folding* the network as shown in Figure 4.32.
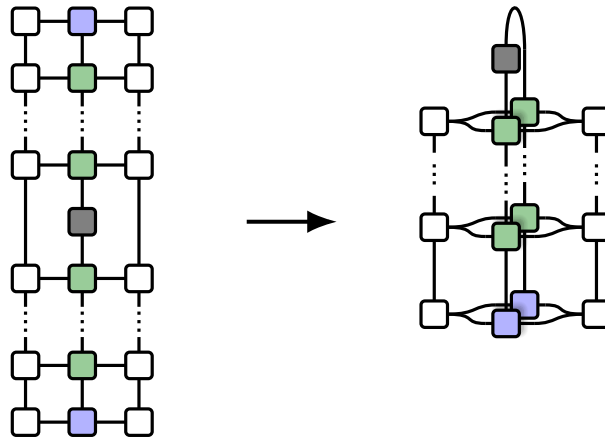
Figure 4.32. Folding method. Left: Final network resulting from the transverse contraction method in the thermodynamic limit, consisting of the transfer matrix containing the operator between the left and right eigenvectors (white) of the pure transfer matrix. Right: For the folding algorithm, tensors corresponding to the same time step are combined into a single one before calculating the eigenvectors.

Müller-Hermes et al. [16] investigated the entanglement in the transverse eigenvectors by means of a toy model that mimics freely propagating excitations, showing that for certain cases where conventional MPS-based time evolution algorithms fail (in the sense that they produce linearly growing entanglement) the folding algorithm still works.

The folding procedure reduces the number of tensors in the transfer matrix (i.e. of transverse "sites") for n time steps from $L_\mathcal{T} = 2n + 2$ to $n + 1$, but the transverse local dimensions as well as the transverse bond dimensions of the transfer matrix are squared due to the combination of indices. Since the number of floating-point operations required for the eigenvector search is at least $\mathcal{O}(L_\mathcal{T} D^3 \chi^3)$ for the ordinary transverse contraction (see Section 4.11.2), it becomes $\mathcal{O}(L_\mathcal{T} D^6 \chi^3)$ for the folded transfer matrix. Here, D is the transverse local dimension, i.e. the bond dimension of the original time-evolution MPO, and χ is the transverse bond dimension chosen for the eigenvector search. When comparing the computational costs, it must be taken into account that the length of the transfer matrix $L_\mathcal{T}$ is halved by the folding process.

For a comparable computational effort, the bond dimension in the folded case must thus

be lower. The above considerations suggest a factor of $D/\sqrt[3]{2}$, but this is only true if we assume the same dimension at each transverse bond and if we do not exploit the conservation of quantum numbers. Despite this lower bond dimension, we do not necessarily incur a loss of accuracy because of the reduced entanglement expected in the folded case.

5. Response of the T-V Model to Electromagnetic Pulses

In the following, we will investigate the time evolution of spinless fermions exposed to an electromagnetic pulse. Throughout this chapter, the models under consideration are simple or extended T-V models with $V = 6\,T$ at half filling. The general Hamiltonian reads

$$
\hat{H} = \sum_{i=1}^{L-1} \left(-T c_i^\dagger c_{i+1} - T^* c_{i+1}^\dagger c_i + V \left(\hat{n}_i - \tfrac{1}{2} \right) \left(\hat{n}_{i+1} - \tfrac{1}{2} \right) \right)
$$
$$
+ \sum_{i=1}^{L-2} \left(-T_2 c_i^\dagger c_{i+2} - T_2^* c_{i+2}^\dagger c_i + V_2 \left(\hat{n}_i - \tfrac{1}{2} \right) \left(\hat{n}_{i+2} - \tfrac{1}{2} \right) \right), \tag{5.1}
$$

where the hopping integral is denoted by a capital T to avoid confusion with time. We will refer to the case $T_2 = V_2 = 0$ as the *simple T-V model*.

First, various spectral functions are calculated with MPS-based techniques in Section 5.1 to support the interpretation of the dynamics of the system. Then we will use the TEBD algorithm (see Section 4.8.1) to simulate the time evolution of the system during and after an electromagnetic pulse in Section 5.2. In order to look for impact ionization (see Section 3.5), we compute the expectation values of the nearest-neighbor occupancy in the time-evolved states. Since in the present case, TEBD is limited to small systems for reasons explained in Section 5.2.1, we will use $L = 20$ throughout the chapter.

All MPS-related numerical calculations for this thesis were done in C++ with the ITensor library [84]. Many routines such as Davidson and Arnoldi eigensolvers or DMRG are already included in the library. Besides, a framework for conserved quantum numbers (see Section 4.9) is implemented in the library and used whenever possible.

5.1. Spectral Functions of the Extended T-V Model

MPS-based time evolution can also be used for the calculation of time-dependent correlation functions and spectral functions. In this section, the single-particle density of states as well as spectral functions for some relevant observables of the T-V model are calculated. The system shall be described by the particle-hole symmetric Hamiltonian with open boundary conditions (5.1) and half filling is assumed.

We find the single-particle density of states following (2.29), (2.31) and (2.36) by time-

evolving the states $|i_-\rangle := c_i |\psi_0\rangle$ and $|i_+\rangle := c_i^\dagger |\psi_0\rangle$ with TEBD and calculating

$$
D(\omega) = -\frac{1}{\pi} \sum_{i=1}^{L} \text{Im} \int_0^{t_{\max}} e^{i\omega t - \eta t^2} \langle \{c_i(t), c_i^\dagger\} \rangle \, dt
$$

$$
= -\frac{1}{\pi} \sum_{i=1}^{L} \text{Im} \int_0^{t_{\max}} e^{i\omega t - \eta t^2} \left(e^{iE_0 t} \langle \psi_0 | c_i \, e^{-i\hat{H}t} \, c_i^\dagger | \psi_0 \rangle + e^{-iE_0 t} \langle \psi_0 | c_i^\dagger \, e^{i\hat{H}t} \, c_i | \psi_0 \rangle \right) dt
$$

$$
= -\frac{1}{\pi} \sum_{i=1}^{L} \text{Im} \int_0^{t_{\max}} e^{i\omega t - \eta t^2} \left(e^{iE_0 t} \langle i_+ | i_+(t) \rangle + e^{-iE_0 t} \langle i_-(t) | i_- \rangle \right) dt \,, \tag{5.2}
$$

where $|\psi_0\rangle$ is the ground state and the small parameter $\eta > 0$ defines a window function for finite time evolutions, leading to a Gaussian broadening of the peaks in the spectrum. Each term of the sum can be considered the local density of states at the respective site,

$$
D_i(\omega) = -\frac{1}{\pi} \text{Im} \int_0^{t_{\max}} e^{i\omega t - \eta t^2} \left(e^{iE_0 t} \langle i_+ | i_+(t) \rangle + e^{-iE_0 t} \langle i_-(t) | i_- \rangle \right) dt \,. \tag{5.3}
$$

Since the main purpose of these results is to provide additional information on the systems considered later in Section 5.2, we use the same parameters (20 sites, $V = 6\,T$) here. The ground state at half filling $|\psi_0\rangle$ is obtained from a DMRG calculation. Since the excitation gap of the model (i.e. the energy difference between ground state and first excited state) vanishes exponentially in the thermodynamic limit [47], in large systems DMRG tends to get stuck in a linear combination of the ground state and first excited state with lower entanglement. To avoid this, we perform two separate calculations with small alternating chemical potentials of opposite sign added to the Hamiltonian,

$$
\hat{H}^\pm = \hat{H} \pm \varepsilon \sum_{i=1}^{L} (-1)^i \hat{n}_i.
$$

Using the average of the resulting states as the initial state for a few additional DMRG sweeps increases the chances that the calculated state converges to the true particle-hole symmetric ground state. We checked this by measuring the particle density at each site, which should be 0.5 in the ground state, and in all cases the deviations from 0.5 were small (less than 1 %).[1]

The time evolution is performed with a second-order Trotter decomposition and a time step of $\tau = 0.02\,T^{-1}$ up to a total time $t_{\max} = 40\,T^{-1}$. For the window parameter the value $\eta = 0.01\,T^2$ is chosen, corresponding to a broadening of $\sigma \approx 0.14\,T$ in frequency space.

In Figure 5.1, we show the global density of states (5.2) per unit volume and the local density of states (5.3) averaged over the two central sites, for several values of the next-nearest neighbor parameters T_2 and V_2. Corresponding functions for the simple T-V

---

[1]Except for cases with next-nearest neighbor hopping $T_2 \neq 0$. In these cases, neither the Hamiltonian nor the ground state is particle-hole symmetric and the quality of the ground state cannot be checked in this way.

model with different values of V have been calculated by Jeckelmann for larger systems with dynamical DMRG [85] and show a good agreement with functions obtained with the program used in this thesis.

For the system with 20 sites considered here, there are large differences between the local density of states in the center and the global DOS. These differences must vanish in the thermodynamic limit and therefore the results indicate that there are substantial finite-size effects for $L = 20$. In particular, in the cases without next-nearest neighbor Coulomb interaction the peaks at low frequencies seem to be a consequence of the finite size. Since they do not appear in the local density of states at all, this contribution must be due to sites closer to the edges of the system.

(a) $T_2 = V_2 = 0$

(b) $T_2 = 0, V_2/T = 1$

(c) $T_2/T = 0.4, V_2 = 0$

(d) $T_2/T = 0.4, V_2/T = 1$
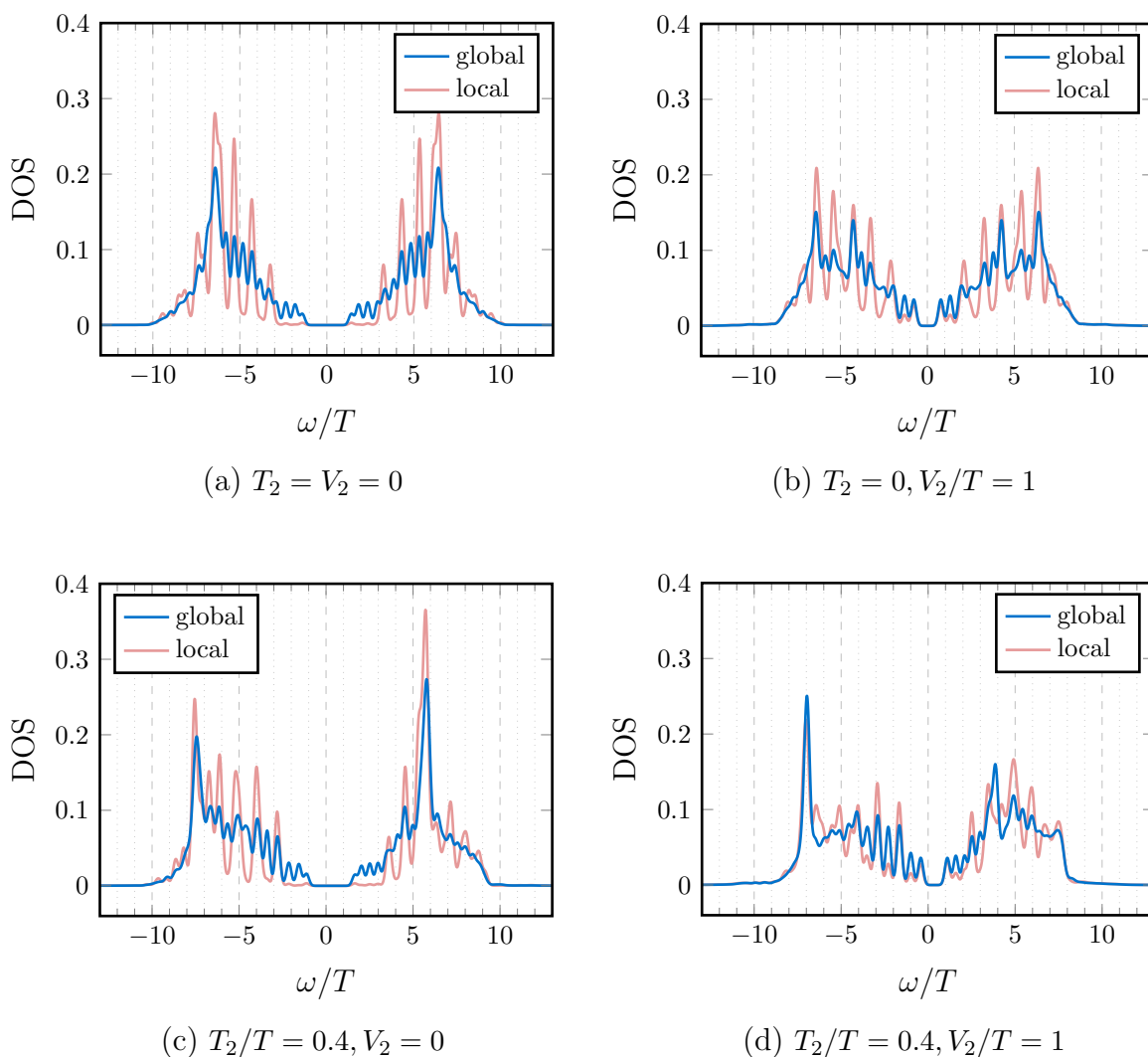
Figure 5.1. Global density of states per unit volume (average of the local DOS over all sites) and local density of states (averaged over the two central sites) of the simple and extended 1D T-V model with 20 sites, open boundary conditions and $V = 6\,T$ for several parameters T_2 and V_2.

(a) density $\hat{n}_i = c_i^\dagger c_i$

(b) nearest-neighbor occupation $\hat{\mathcal{N}}_i = \hat{n}_i \hat{n}_{i+1}$

(c) hopping $\hat{t}_i = c_i^\dagger c_{i+1} + c_{i+1}^\dagger c_i$

(d) current $\hat{j}_i = \mathrm{i}(c_{i+1}^\dagger c_i - c_i^\dagger c_{i+1})$
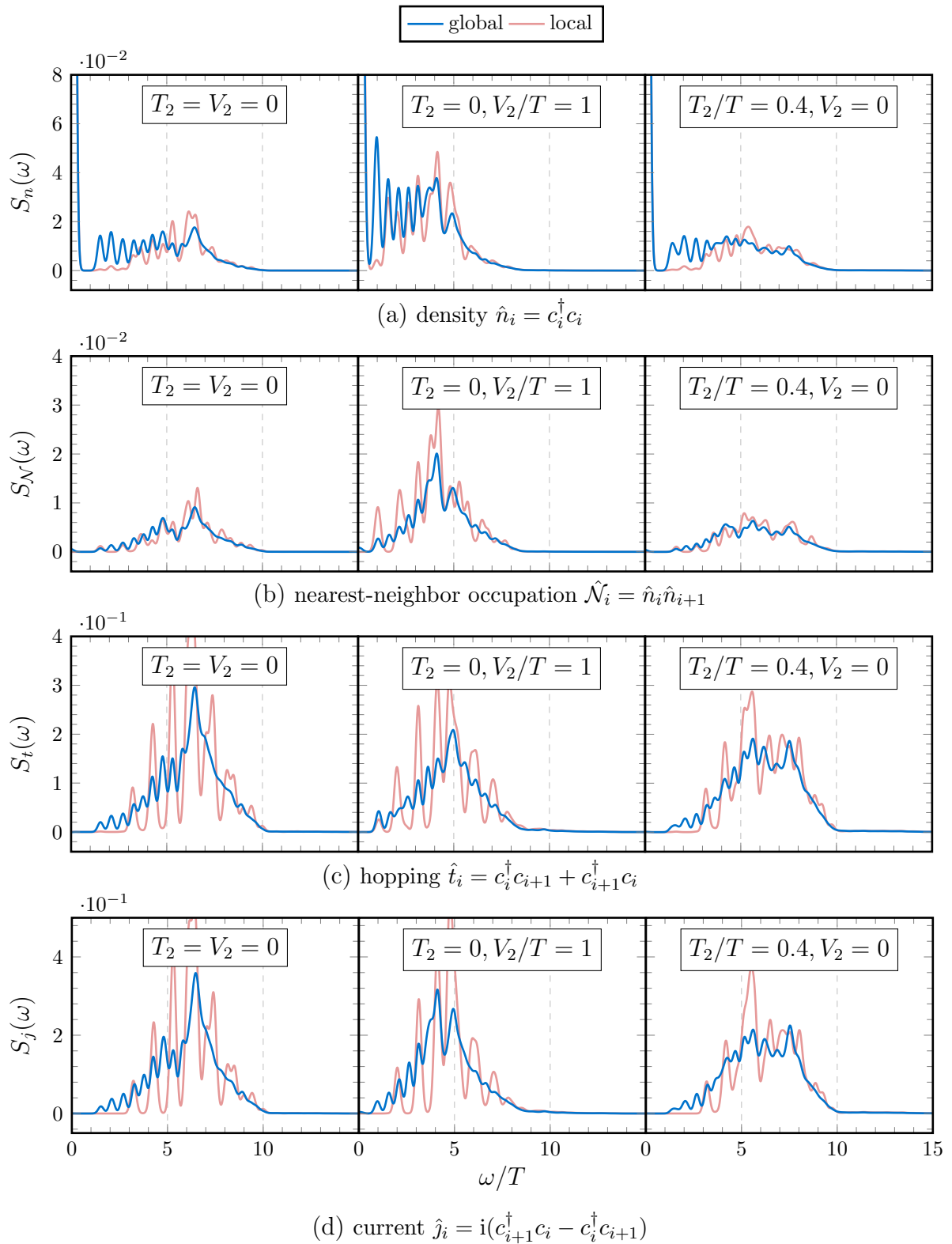
Figure 5.2. Various spectral functions (global per unit volume and local at the center of the chain) of the 1D simple and extended T-V model with 20 sites and $V = 6\,T$. Observables are defined in subcaptions.

Concerning next-nearest neighbor Coulomb interactions, the plots also show that these lead to a smaller band gap, particularly in the local density of states. This is an expected result, because the next-nearest neighbor repulsion in a certain sense counteracts the nearest-neighbor repulsion that causes the band gap. While the nearest-neighbor repulsion increases the energy of states where neighboring sites are occupied and therefore favors Néel-like states with alternating occupation, the next-nearest neighbor repulsion penalizes exactly these states.

Figure 5.1(c) and (d) confirm that the next-nearest neighbor hopping breaks the particle-hole symmetry of the system, leading to a non-symmetric density of states. The width of the bands and the band gap, however, is not significantly changed by the next-nearest neighbor hopping.

With the same method as described above, we can compute the spectral functions for several observables of interest. For a local hermitian operator $\hat{A}_i$, the global spectral function is given by

$$S_A(\omega) := \sum_i S_{A_i A_i}(\omega) = -\frac{1}{\pi} \sum_i \text{Im} \int_0^{t_{\max}} e^{i\omega t - \eta t^2} \langle [\hat{A}_i(t), \hat{A}_i] \rangle \, dt \ ,$$

where the sum runs over the entire lattice. Such functions for various observables are plotted in Figure 5.2 for the simple and extended T-V model with $V = 6\,T$, $V_2 \in \{0, T\}$ and $T_2 \in \{0, 0.4\,T\}$, where again the parameters $t_{\max} = 40$ and $\eta = 0.01$ were chosen. Due to the hermiticity of the operators, the functions are symmetric in ω and therefore only plotted for $\omega > 0$. The local spectral functions $S_{A_i A_i}(\omega)$ are averaged over the two central sites for one-site observables and taken at the central bond for two-site observables. Because of the equivalence of the T-V model and the XXZ model (see Section 3.2.1), the density-density spectral function of the T-V model is equal to the spin-spin spectral function (also known as *longitudinal dynamical structure factor*) of the XXZ model, the leading (two-spinon) contribution of which has been calculated in momentum space with the Bethe ansatz by Caux et al. [86] for the gapless regime (corresponding to $V < 2$) and by Castillo [87] for the gapped regime $V > 2$.

According to (2.33), these spectral functions are related to the possible excitations of the system by the respective operator $\hat{A}$. Like for the density of states, the peaks at low frequencies are not present in the local functions at the center for many cases, indicating that these correspond to finite-size effects.

For cases with next-nearest neighbor hopping, the spectral functions for the next-nearest neighbor hopping and current are also relevant. They are shown in Figure 5.3, where the local spectral functions are averaged over the two terms including the central bond. Since they are about one order of magnitude smaller than the spectral functions for the corresponding nearest-neighbor observables, we expect the next-nearest neighbor processes to play a minor role, but the next-nearest neighbor spectral functions are non-zero up to much higher frequencies, allowing higher-energy excitations.
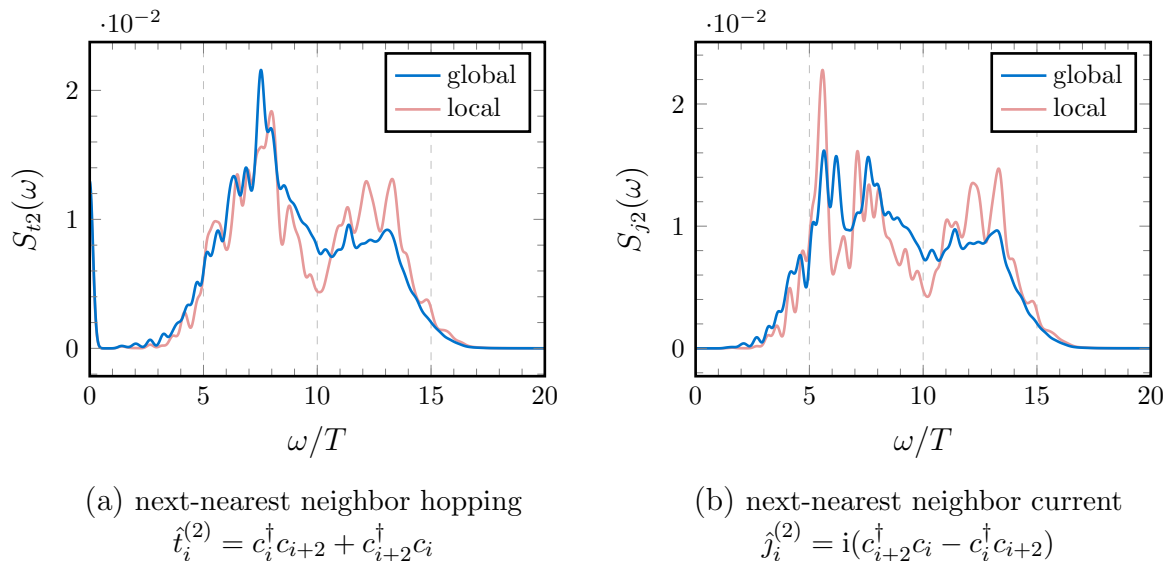
(a) next-nearest neighbor hopping
$$\hat{t}_i^{(2)} = c_i^\dagger c_{i+2} + c_{i+2}^\dagger c_i$$

(b) next-nearest neighbor current
$$\hat{j}_i^{(2)} = \mathrm{i}(c_{i+2}^\dagger c_i - c_i^\dagger c_{i+2})$$

Figure 5.3. *Next*-nearest neighbor hopping (left) and *next*-nearest neighbor current (right) spectral functions of the 1D extended T-V model with 20 sites, open boundary conditions, $V = 6\,T$, $T_2 = 0.4\,T$ and $V_2 = 0$.

5.2. Time Evolution of the Nearest-Neighbor Occupancy

We will now investigate the nearest-neighbor occupancy in the simple and extended T-V model after it is exposed to an electromagnetic pulse. Initially, the system shall be in its ground state, which is obtained from a DMRG calculation (see Section 4.7).

To simulate the incidence of electromagnetic radiation, the Hamiltonian is modified according to the Peierls substitution (see Section 2.2)

$$T \to T\,\mathrm{e}^{-\mathrm{i}A(t)}, \quad T_2 \to T_2\,\mathrm{e}^{-2\mathrm{i}A(t)}$$

during the time evolution. This corresponds to a spatially homogeneous electric field $E(t) = -\partial A/\partial t$ and therefore contains the assumption that the wavelength of the radiation is much larger than the system under consideration. For the vector potential, we use a single cosine with a Gaussian envelope,

$$A(t) = -A_0 \exp\left(-\frac{(t - t_0)^2}{2\sigma^2}\right) \cos(\Omega(t - t_0)). \tag{5.4}$$

The finite length in the time domain leads to a broadening in the frequency domain, which is given by $1/\sigma$. All results in this section are produced with pulses of width $\sigma = 3\,T^{-1}$ centered at $t_0 = 13\,T^{-1}$, an example of which is shown in Figure 5.4.

It is now interesting to relate the units of the amplitude to typical values of real light sources (e.g. for sunlight). The unit of electromagnetic vector potential used here corresponds to $\hbar/ed$ in SI units, where e is the elementary charge and d the lattice spacing. For $d = 1\,\text{Å}$ this gives a unit of approximately $10^{-5}\,\text{V}\,\text{s}\,\text{m}^{-1}$ for the vector potential. The time-averaged intensity of a plane, monochromatic electromagnetic wave is given in terms
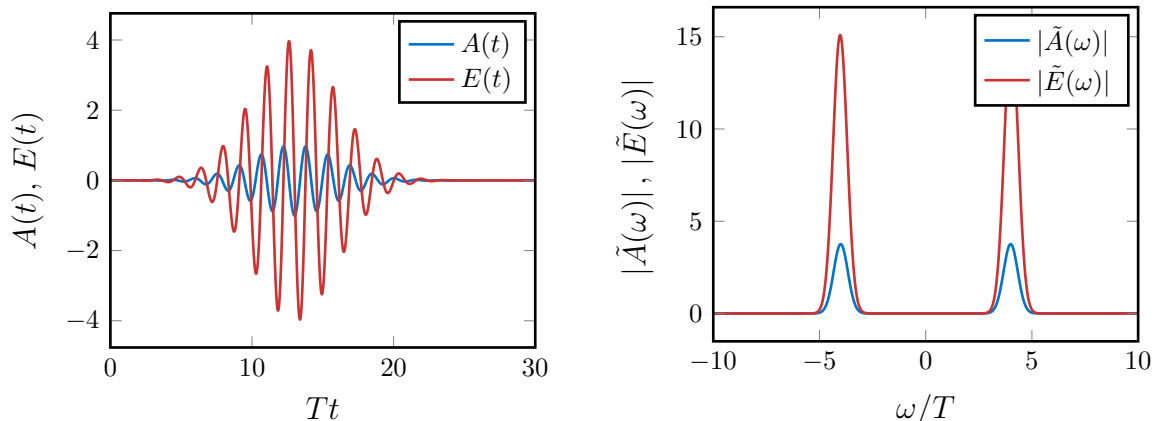
Figure 5.4.   Left: Vector potential A and electric field $E = -\partial A/\partial t$ of an electromagnetic pulse of width $\sigma = 3\,T^{-1}$ centered at $t_0 = 13\,T^{-1}$ with frequency $\Omega = 4\,T$. Right: Absolute value of the Fourier transforms of the vector potential and the electric field.

of the amplitude of the electric field $E_0 = A_0\Omega$ by $I = c\varepsilon_0 E_0^2/2$. With a frequency of 10^{15} Hz (corresponding to an energy of $\sim 1\,\text{eV}$), the unit of the vector potential (i.e. $A_0 = 1$) leads to an intensity $I \approx 10^{15}\,\text{W}\,\text{m}^{-2}$. However, the pulse has a duration of only $\sim 10^{-14}\,\text{s}$.

For sunlight, the intensity over the whole spectrum without attenuation in the atmosphere would be approximately $1360\,\text{W}\,\text{m}^{-2}$ [88]. Thus, with the amplitudes used in the present thesis to observe impact ionization (see Sections 5.2.2-5.2.5), the intensity is many orders of magnitude higher than that of sunlight on earth. With much smaller amplitudes, however, at unchanged numerical accuracy the observed effects would not lead to significant changes of the observables.

The time evolution is done with the TEBD algorithm, using a second-order Suzuki-Trotter decomposition of the time evolution operator (see Section 4.8.1). Actually, due to the Peierls substitution the Hamiltonian becomes explicitly time-dependent and the time evolution operator does not have the simple form $\exp(-i\hat{H}\tau)$. However, if the time step τ is chosen sufficiently small, such that the Hamiltonian is approximately constant during one time step, we can approximate the time evolution operator by

$$\hat{U}(t + \tau, t) \approx \exp\left(-i\hat{H}(t)\tau\right). \tag{5.5}$$

Specifically for a pulse as described above, the requirement for the time step is $\Omega\tau \ll 1$.

For the investigation of phenomena in the T-V model, which are similar to impact ionization in the Hubbard model, we study the long-term behavior of the nearest-neighbor occupancy

$$\mathcal{N} = \sum_{i=1}^{L-1} \langle (\hat{n}_i - \tfrac{1}{2})(\hat{n}_{i+1} - \tfrac{1}{2}) \rangle \tag{5.6}$$

after the pulse. In the simple T-V model, this observable is proportional to the total potential energy of the system.

5.2.1. Verification and Limits of TEBD

To ensure correctness and convergence of the results obtained from TEBD, they are compared to a full diagonalization calculation[1] for a small system (see Figure 5.5). Note that the larger time steps here do not only increase the Trotter error, but also the error due to the discretization (5.5) of the time evolution operator during the pulse (which affects both methods used). We see in Figure 5.5 that the TEBD results converge towards those from the full diagonalization with decreasing time step and discarded weight as expected. Although the time step $\tau = 0.01\,T^{-1}$ provides better results, for the further calculations we stick with $\tau = 0.02\,T^{-1}$, where the error is still reasonably small with the benefit of a considerably reduced computation time. For the maximum discarded weight, we will use 10^{-10}.
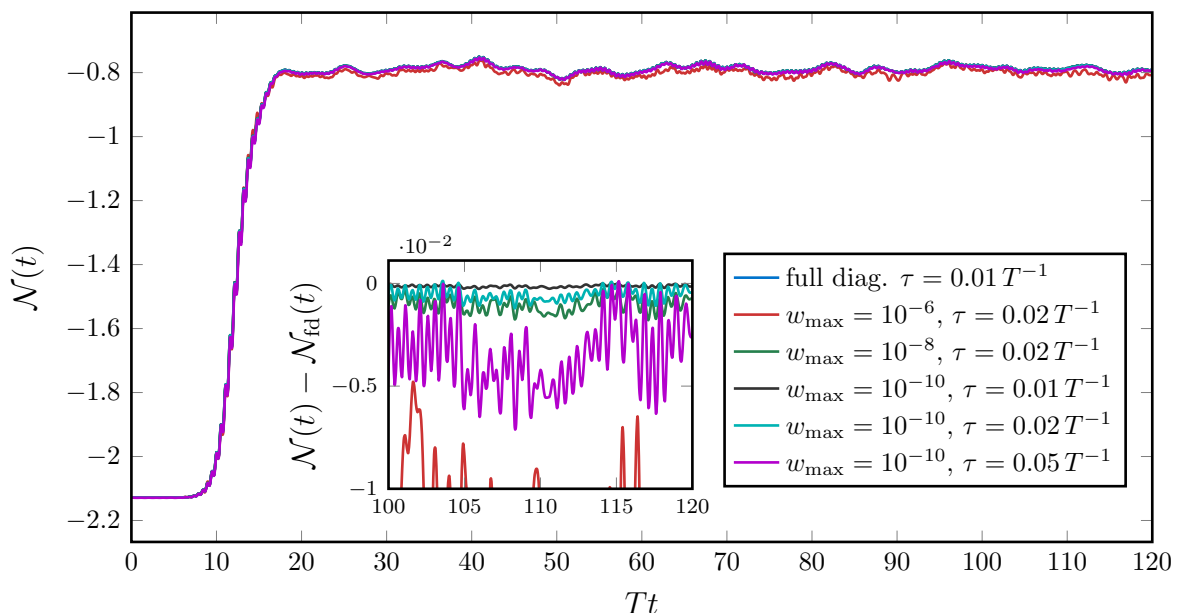
Figure 5.5. Comparison of the time dependent nearest-neighbor occupancy in the 1D extended T-V model with 12 sites calculated with TEBD and full diagonalization. Inset: deviation of the TEBD calculations from the full diagonalization results. The parameters are $V = 6$, $V_2 = T$, $T_2 = 0.4\,T$, $\Omega = 6\,T$ and $A_0 = 0.8$.

The success of MPS results from the fact that ground states of one-dimensional gapped systems typically live in a rather small portion of the full Hilbert space [34]. This is, however, not true for arbitrary excited states such as the state of the system during and after the pulse. In fact, we observe an enormous growth of entanglement during the pulse, which strongly limits the time scales accessible through MPS-based algorithms such as TEBD for large systems. In Figure 5.6, the bond dimension on the central bond required to keep the discarded weight below 10^{-10} is shown along with the entanglement across this bond for one case.

---

[1]Full diagonalization refers to exact diagonalization of the full Hamiltonian matrix H in the basis $|s_1 \ldots s_L\rangle$ to obtain the ground state and the exact time evolution matrix $\exp(-\mathrm{i}H\tau)$.
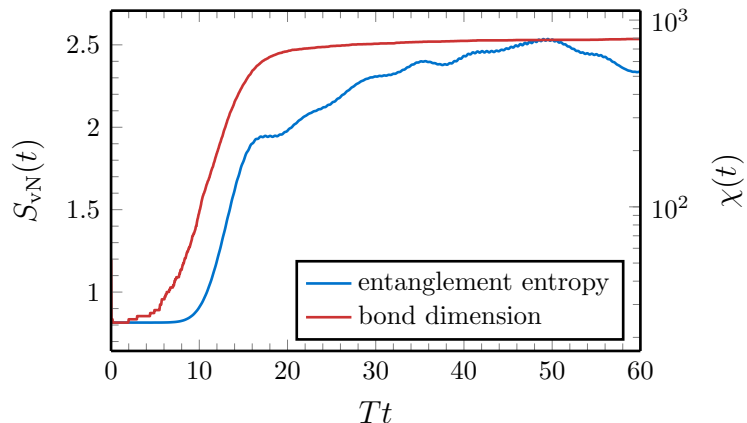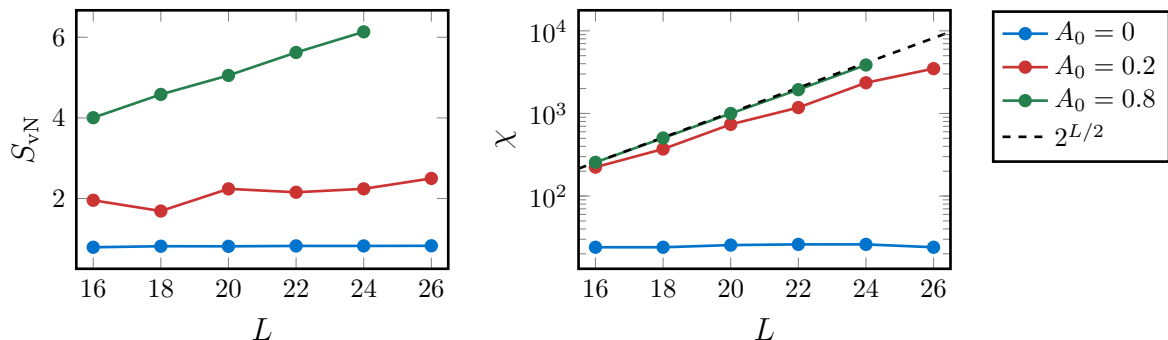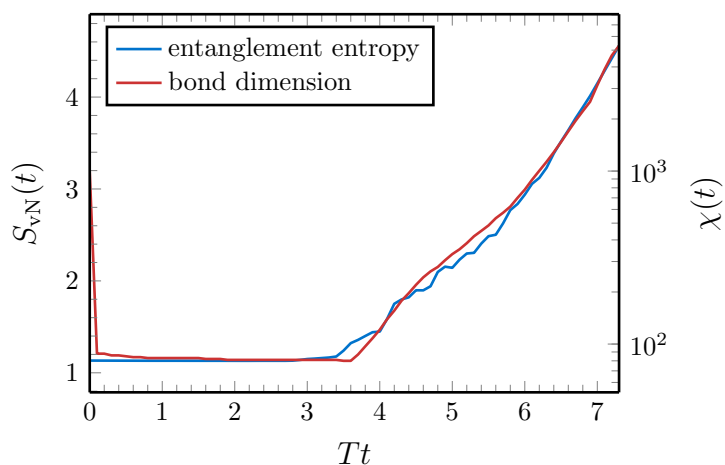
Figure 5.6. Von Neumann entanglement entropy across the central bond and corresponding bond dimension required to keep the discarded weight below 10^{-10} (logarithmic) in a 1D simple T-V model with 20 sites and $V = 6\,T^{-1}$ exposed to an electromagnetic pulse with frequency $\Omega = 6\,T$ and amplitude $A_0 = 0.2$.

Concerning the entanglement scaling with the system size, for ground states the growth is bounded by the area law (see Section 2.5.1), meaning that the entanglement entropy remains approximately constant in one dimension. In the excited states after the pulse, however, we observe a linear growth, which leads to an exponential scaling of the required bond dimension with the system size (see Figure 5.7).

Figure 5.7. Von Neumann entanglement entropy across the central bond (left) and corresponding bond dimension to keep the discarded weight below 10^{-10} (right, logarithmic) in a 1D simple T-V model with $V = 6\,T$ after an electromagnetic pulse with frequency $\Omega = 6\,T$ and various amplitudes A_0 as a function of the system size L. Despite being averaged over $Tt \in [25, 30]$ the entanglement entropy must be treated with caution due to its long-term oscillating behavior, which Figure 5.6 gives a hint of. The dashed line in the right plot marks the bond dimension $2^{L/2}$ required to represent the full Hilbert space by an MPS.

For high pulse amplitudes, the right plot in Figure 5.7 shows that we need to represent almost the full Hilbert space with the MPS, which completely eliminates the advantages of MPS and the time evolution methods coming with them over exact methods. In fact, the same system sizes would probably be accessible with the exact diagonalization methods used in [6], because the full[1] Hilbert space of a 12-site Hubbard model has the same size

---

[1] Full in the sense that no conservation laws are exploited. Otherwise there is an advantage on the side

as that of a 24-site T-V model.

Since $L = 20$ is the largest system size accessible with reasonable bond dimensions of ~ 1000 even for high field amplitudes, we restricted the system size to this value in the present thesis.

For the more physically relevant case of the Hubbard model, TEBD already fails at a system size of $L = 14$ (in the sense that it requires bond dimensions above the capabilities of a standard computer), which is why the discussion within this thesis is restricted to the simpler T-V model. Figure 5.8 shows the entanglement and the required bond dimension to keep the discarded weight below 10^{-7} for the extended Hubbard model with next-nearest neighbor hopping, exposed to an electromagnetic pulse.

Figure 5.8. Von Neumann entanglement entropy across the central bond and corresponding bond dimension required to keep the discarded weight below 10^{-7} (logarithmic) in a 1D extended Hubbard model ($U = 7\,T$, $T_2 = 0.83\,T$) with 14 sites exposed to an electromagnetic pulse with $\Omega = 10\,T$, $A_0 = 1$, $t_0 = 5\,T^{-1}$ and $\sigma = T^{-1}$.

5.2.2. Simple T-V Model ($T_2 = V_2 = 0$)

In Figure 5.9, the nearest-neighbor occupancy for the simple T-V model is plotted for various pulse frequencies. The oscillations occurring at certain frequencies are not a finite size effect, as they have a similar amplitude and period in different system sizes such as $L = 12$. They seem to be a consequence of the pulse, and their frequency (during as well as after the pulse) is about twice the frequency of the pulse. This was also observed by Maislinger and Evertz for the Hubbard model [6] and is plausible because due to the mirror symmetry of the system, the direction of the field cannot have an influence on the response of a global observable and thus the response can only depend on $A(t)^2$, which has the double frequency.

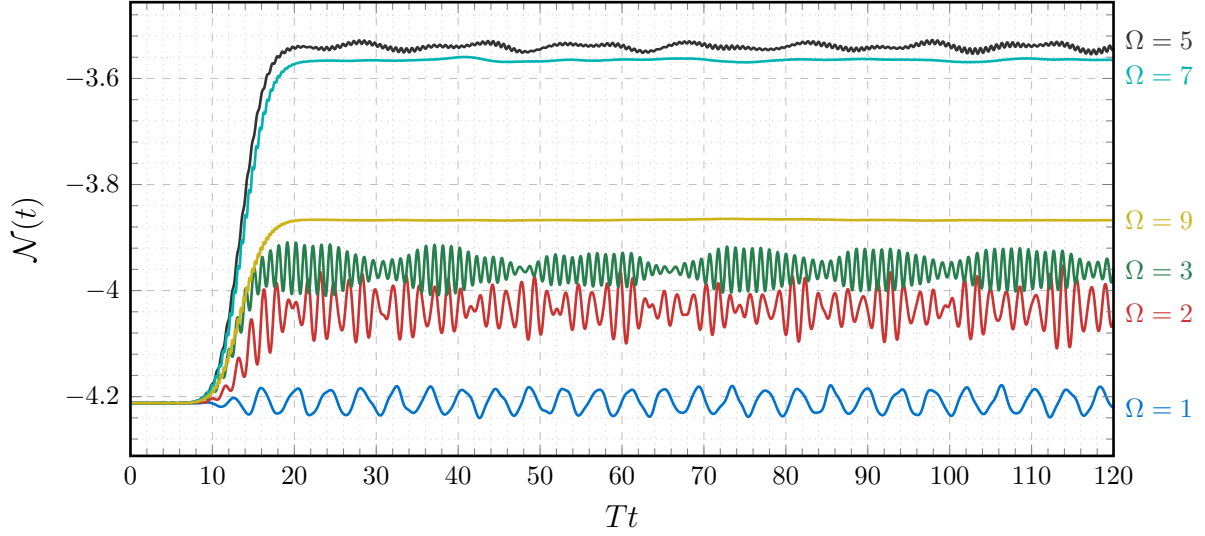of the Hubbard model, because it conserves particle number *and* spin.

Figure 5.9. Nearest-neighbor occupancy in the 1D simple T-V model with 20 sites and $V = 6\,T$ exposed to electromagnetic pulses with various frequencies Ω (in units of T) and amplitude $A_0 = 0.2$.

Relation of the Response to Spectral Functions

In Figure 5.10, the total absorbed energy during the pulse and the change of nearest-neighbor occupancy due to the pulse are plotted as a function of frequency for the simple T-V model and the cases with next-nearest neighbor hopping and next-nearest neighbor Coulomb interaction, respectively. After the pulse, the system is not in a stationary state anymore and thus the nearest-neighbor occupancy is not constant (see Figure 5.9). Its temporal average, however, seems to be approximately constant and therefore the value for $\Delta\mathcal{N}$ in Figure 5.10 is obtained by averaging over a certain time range after the pulse.
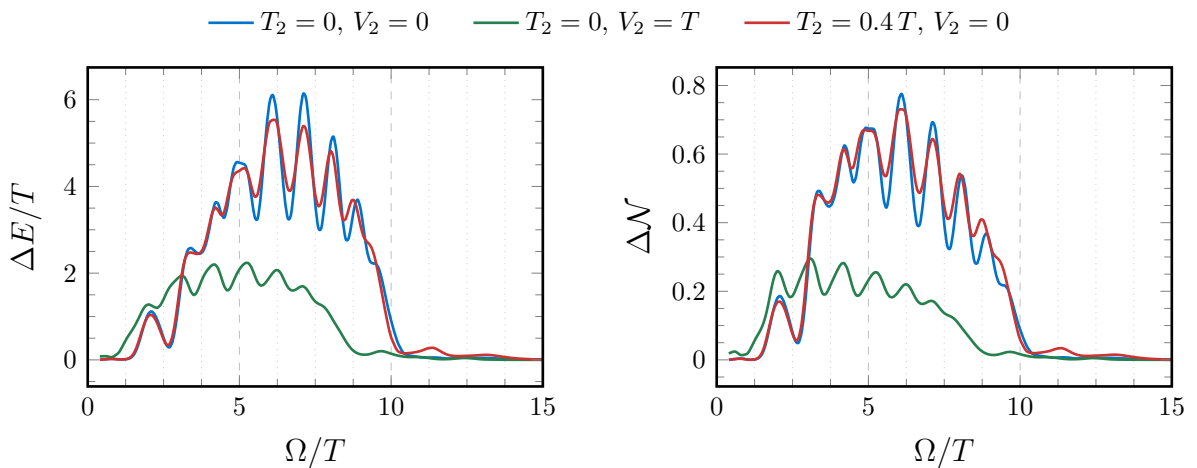
Figure 5.10. Change of energy (left) and of nearest-neighbor occupancy (right) due to a pulse with amplitude $A_0 = 0.2$ and frequency Ω in the extended T-V model with 20 sites and $V = 6\,T$. The nearest-neighbor occupancy after the pulse was averaged over the time range $[t_0 + 3\sigma, t_0 + 3\sigma + 9\,T^{-1}]$ with $t_0 = 13\,T^{-1}$ and $\sigma = 3\,T^{-1}$ to filter out oscillations.

Surprisingly, the absorbed energy as a function of the pulse frequency in Figure 5.10 exhibits strong oscillations. To clarify their origin, the calculations for the simple T-V model were repeated with different system sizes ($L = 12$ and $L = 16$). The results are compared in Figure 5.11 together with their Fourier transforms, which show the time scales corresponding to the oscillations in the frequency domain. Since the time scale seems to increase linearly with the system size L and the relative amplitude of the oscillations decreases with growing L, we can conclude that the oscillations are due to the finite size of the system.
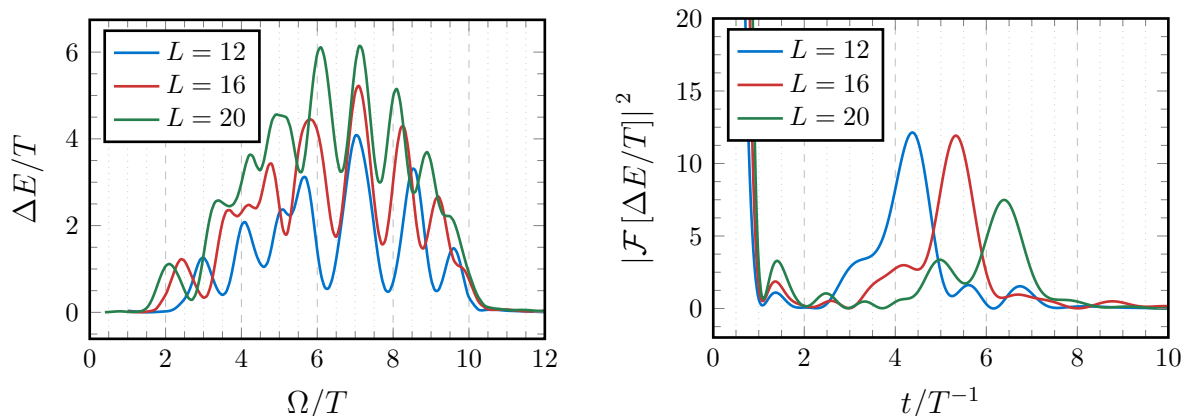
Figure 5.11. System-size dependence of the energy absorbed during a pulse with amplitude $A_0 = 0.2$ in the simple T-V model with $V = 6\,T$. Left: Change of total energy for several system sizes as a function of the pulse frequency Ω. Right: Fourier transforms of the curves on the left, showing the relevant time scales.

The different magnitude of the response with respect to the frequency, which is visible in Figure 5.9 and Figure 5.10, can be related to the allowed excitations in various spectral functions of the system.

Excitation processes in the Hubbard model seem to be well explainable by a single particle picture [6], but this appears not to be the case for the processes under consideration in the T-V model. The DOS of the extended T-V model for several parameters is shown in Figure 5.1. Since the whole system is exposed to the electromagnetic field, all sites contribute to the response and the relevant functions are the global densities of states. In a single-particle picture, we would expect that any frequency which corresponds to a transition compatible with the DOS would lead to a response of the system (e.g. a significant amount of energy absorbed, see Figure 5.10). According to the density of states, excitations with frequencies up to almost $20\,T^{-1}$ would be possible (a little lower with $V_2 > 0$), while the lowest-energy excitation across the band gap has an energy slightly above $2\,T$ in the cases without next-nearest neighbor Coulomb interaction (and also less with $V_2 > 0$). Figure 5.10 already shows a response below the size of the band gap, but this could be a consequence of the finite width of the pulse in frequency space ($\sigma_\omega = \frac{1}{3}\,T$). However, there is no response at the higher frequencies allowed by the DOS and the maximum response is found at $\Omega \approx 7\,T^{-1}$, while the DOS would suggest about twice this value. Thus, the single-particle picture fails in explaining the frequency dependence of the response.

This can be understood by the following considerations: Let a Hubbard system be in a Néel-like state $\uparrow\downarrow\uparrow\downarrow$. Adding a particle then leads to one doubly-occupied site, e.g. $\uparrow\uparrow\downarrow$ $\uparrow\downarrow$. In the T-V model, however, adding a particle to a state with alternating occupation $1\,0\,1\,0$ leads to a state like $1\,1\,1\,0$, which contains *two* pairs of occupied neighbors, i.e. two elementary excitations. Thus, unlike for the Hubbard model, the single-particle spectrum of the T-V model cannot be expected to explain excitations of the system due to the electromagnetic pulse.

Instead, we should consider the spectral functions appropriate for the response to the actual excitation, at least in linear response. Since the electromagnetic field couples to the hopping terms $\hat{t}_i = c_i^\dagger c_{i+1} + c_{i+1}^\dagger c_i$ and to the current $\hat{j}_i = \mathrm{i}(c_{i+1}^\dagger c_i - c_i^\dagger c_{i+1})$ via the real and imaginary parts of the Peierls phase,

$$\begin{aligned}
\mathrm{e}^{-\mathrm{i}A(t)}\, c_i^\dagger c_{i+1} + h.c. &= \cos\big(A(t)\big)(c_i^\dagger c_{i+1} + h.c.) - \mathrm{i}\sin\big(A(t)\big)(c_i^\dagger c_{i+1} - h.c.)\\
&= \cos\big(A(t)\big)\hat{t}_i + \sin\big(A(t)\big)\hat{j}_i,
\end{aligned} \tag{5.7}$$

the spectral functions of interest are the ones of these two observables (see Figure 5.2). Again, the global spectral functions are relevant because of the global pulse.

In the case $T_2 = V_2 = 0$, both spectral functions have small peaks in the range $\omega \in [1\,T, 3\,T]$ and a maximum between $\omega = 6\,T$ and $\omega = 7\,T$ with edges falling off to both sides. These features approximately coincide with the shape of the absorbed energy as a function of pulse frequency for the same case in Figure 5.10. For frequencies below $\omega \approx T$ and above $\omega \approx 10.5\,T$, the spectral functions are zero, which is also true for the response in terms of absorbed energy or change of nearest-neighbor occupancy. Thus, the current-current and hopping-hopping spectral functions succeed much better in explaining the frequency-dependence of the response of the system.

No Impact Ionization

As a measure for the change of the nearest-neighbor occupancy after the pulse we calculate its average directly after the pulse and a certain time Δt later, where both values are averaged over a time span of $20\,T^{-1}$ to filter out the high-frequency oscillations that are present in some cases (e.g. in Figure 5.9 at $\Omega = 3\,T$):

$$\Delta\bar{\mathcal{N}}(\Delta t) = \frac{1}{20\,T^{-1}} \int\limits_{t_1+\Delta t}^{t_2+\Delta t} \mathcal{N}(t)\,\mathrm{d}t - \frac{1}{20\,T^{-1}} \int\limits_{t_1}^{t_2} \mathcal{N}(t)\,\mathrm{d}t \tag{5.8}$$

with $t_1 := t_0 + 4\sigma$ and $t_2 := t_0 + 4\sigma + 20\,T^{-1}$, where $\sigma = 3\,T^{-1}$ is the width of the pulse centered around $t_0 = 13\,T^{-1}$.

The quantity (5.8) is displayed as a function of the pulse frequency in Figure 5.12. There is apparently no significant long-term change in the nearest-neighbor occupancy in the simple T-V model that would indicate impact ionization.
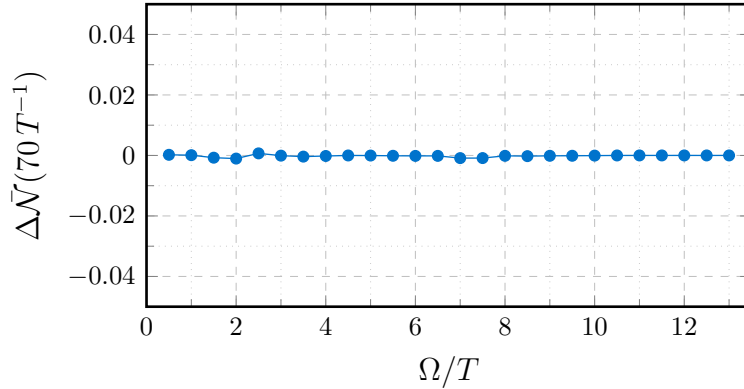
Figure 5.12. Change of the nearest-neighbor occupancy in the 1D T-V model with 20 sites and $V = 6\,T$ during a time span of $70\,T^{-1}$ after an electromagnetic pulse with frequency Ω and amplitude $A_0 = 0.2$.

5.2.3. Next-Nearest Neighbor Coulomb Interaction ($V_2 \neq 0$)

Now we consider the effects of a next-nearest neighbor Coulomb interaction. The spectral functions for this case (see Figure 5.2, middle column) are all shifted towards lower energies compared to those with $V_2 = 0$. This is also true for the energy absorption spectrum in Figure 5.10 and again the frequency range and the maximum of the energy absorption coincide with those of the global hopping-hopping and current-current spectral functions.

Figure 5.13 shows the time evolution of the nearest-neighbor occupancy for several pulse frequencies as well as the change of the nearest-neighbor occupancy after the pulse as a function of the pulse frequency. In this case, too, the average nearest-neighbor occupancy remains constant after the pulse.
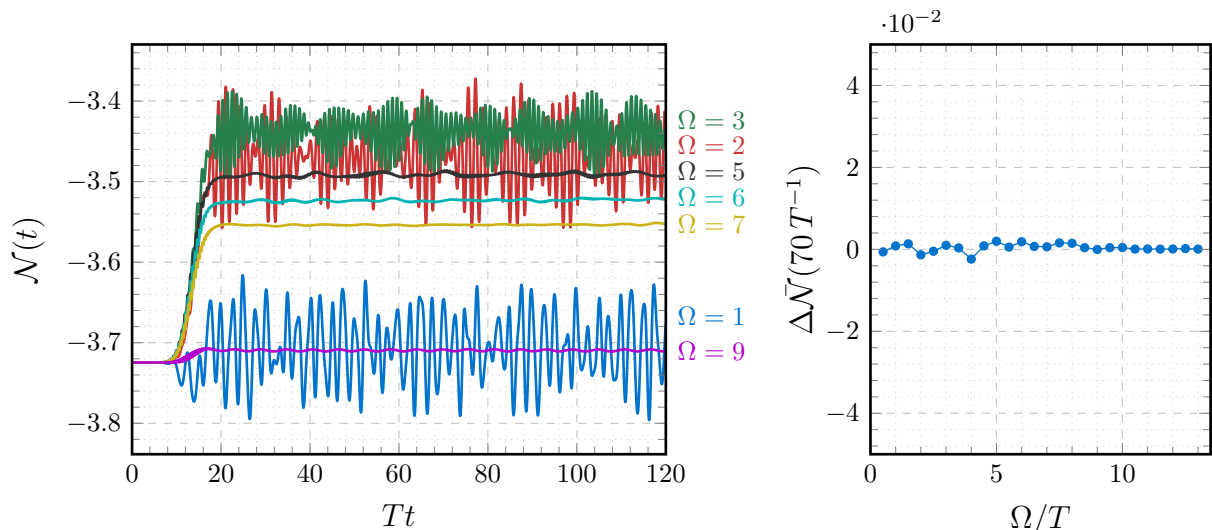
Figure 5.13. Left: Time dependent nearest-neighbor occupancy in the 1D extended T-V model with 20 sites, $V = 6\,T$ and $V_2 = T$, exposed to electromagnetic pulses with various frequencies Ω (in units of T) and amplitude $A_0 = 0.2$. Right: Change of the average nearest-neighbor occupancy after the pulse.

With non-zero V_2, next-nearest neighbor occupations can also raise the potential energy and could therefore contribute to impact ionization. To get a complete picture, all three contributions to the total energy for the case $V_2 = T$ for one frequency are visualized in Figure 5.14. One can see that the distribution between kinetic and potential energy stays approximately the same for all times after the pulse and we have found no frequency where this is otherwise.
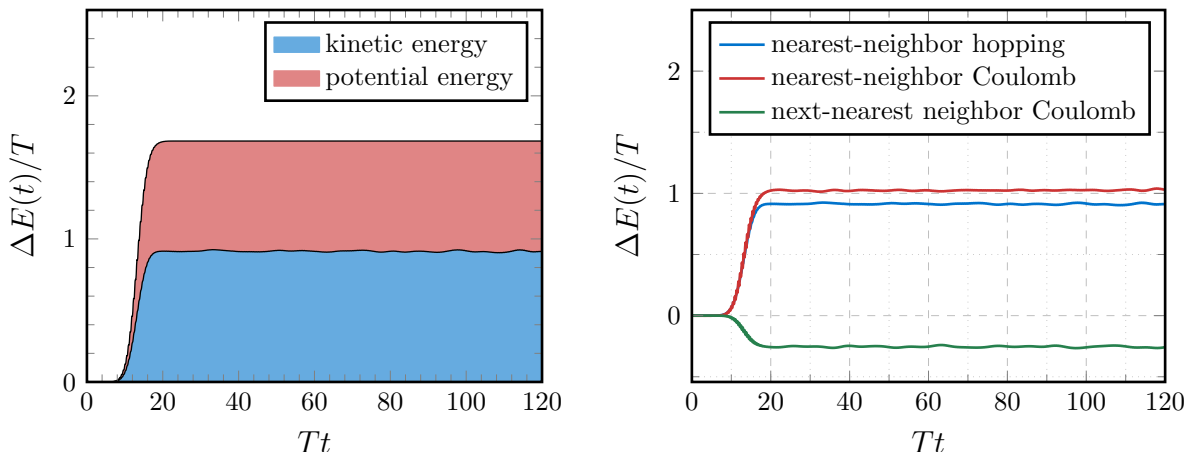

Figure 5.14. Distribution of the total energy change among the single terms of the Hamiltonian for the extended 1D T-V model with 20 sites, $V = 6\,T$ and $V_2 = T$, exposed to an electromagnetic pulse with frequency $\Omega = 7\,T$ and amplitude $A_0 = 0.2$.

Thus, we can conclude that also with next-nearest neighbor Coulomb interactions, impact ionization does not happen in the T-V model, although the model is then no longer integrable [7]. This shows that the occurrence of impact ionization is *not* simply a matter of non-integrability of the model as suggested by previous results (see Section 3.5).

5.2.4. Next-Nearest Neighbor Hopping ($T_2 \neq 0$): Impact Ionization

For the extended model with $T_2 \neq 0$, the global hopping and current spectral functions in Figure 5.2 (right column) differ from those with $T_2 = 0$ primarily at the frequencies in the middle of the range, which is also true for the energy absorption in Figure 5.10. Apart from that, the most apparent difference in the energy absorption with and without the next-nearest neighbor hopping is the finite absorption at frequencies above $\Omega \approx 11\,T$, which only occurs with $T_2 > 0$. This cannot be explained with the hopping-hopping and current-current spectral functions, but with $T_2 \neq 0$ the external field additionally couples to the next-nearest neighbor hopping and current via the Peierls substitution of T_2. Therefore, we must also take into account the spectral functions for these observables (see Figure 5.3), which are non-zero up to higher frequencies of $\Omega \approx 16\,T$ (albeit rather small compared to the nearest-neighbor spectral functions in Figure 5.2(c) and (d)) and thus can indeed explain the response in Figure 5.10 at the high frequencies.

Hence, as for all investigated cases, the response of the system (in terms of absorbed energy, see Figure 5.10) is consistent with the possible excitations given by the hopping-hopping and current-current spectral functions (see Figure 5.2(c) and (d)) and those for

the corresponding next-nearest neighbor observables (see Figure 5.3).

Figure 5.15 shows the time-dependence of the nearest-neighbor occupancy $\mathcal{N}$ and its change after the pulse. One can clearly see in the time evolution that for certain frequencies ($\Omega = 7\,T$, $\Omega = 9\,T$), $\mathcal{N}$ continues to grow after the end of the pulse at $t \approx 20\,T^{-1}$. The right plot in Figure 5.15 confirms this observation and shows that the effect only occurs for high frequencies $\Omega \gtrsim 6\,T$, whereas at lower frequencies the nearest-neighbor occupancy decreases after the pulse. Qualitatively, the frequency-dependence of the nearest-neighbor occupancy matches the result obtained by Maislinger and Evertz for the two-dimensional Hubbard model [6].
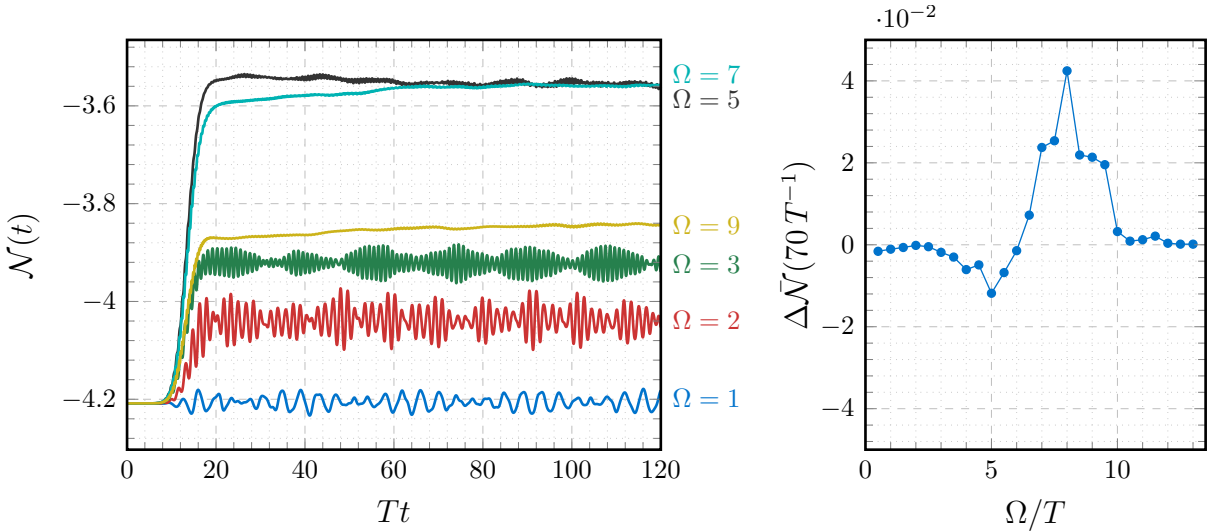
Figure 5.15. Left: Time dependent nearest-neighbor occupancy in the 1D extended T-V model with 20 sites, $V = 6\,T$ and $T_2 = 0.4\,T$, exposed to electromagnetic pulses with various frequencies Ω (in units of T) and amplitude $A_0 = 0.2$. Right: Change of the average nearest-neighbor occupancy after the pulse.

A possible explanation for the long-term changes in the nearest-neighbor occupancy after the pulse is depicted in Figure 5.16: High-energy excitations with $\omega > 2\omega_1$ can decay into two lower energy excitations, while two low-energy excitations with $\omega < \omega_2/2$ can combine into one higher-energy excitation (here ω_1 and ω_2 are the boundaries of the support of the spectral function). These processes are similar to impact ionization (see Section 3.5) and its inverse process (Auger recombination), to which the similar behavior in the two-dimensional Hubbard model was attributed by Maislinger and Evertz [6]. Regarding the excitations as quasiparticles we can imagine these processes as sketched in Figure 5.16.

Looking towards real materials, it is important to note that the time scale observed here for impact ionization is shorter than typical time scales of electron-phonon scattering: For a band gap[1] of $1\,\mathrm{eV}$, the time unit T^{-1} corresponds to approximately $1\,\mathrm{fs}$, meaning that impact ionization happens on a time scale of $10 - 100\,\mathrm{fs}$. On the other hand, typical time scales for electron-phonon relaxation processes are $0.1 - 1\,\mathrm{ps}$ [3].

The observation that next-nearest neighbor interactions are necessary for impact ionization is consistent with the results of Kauch et al. [5], who performed calculations for

---

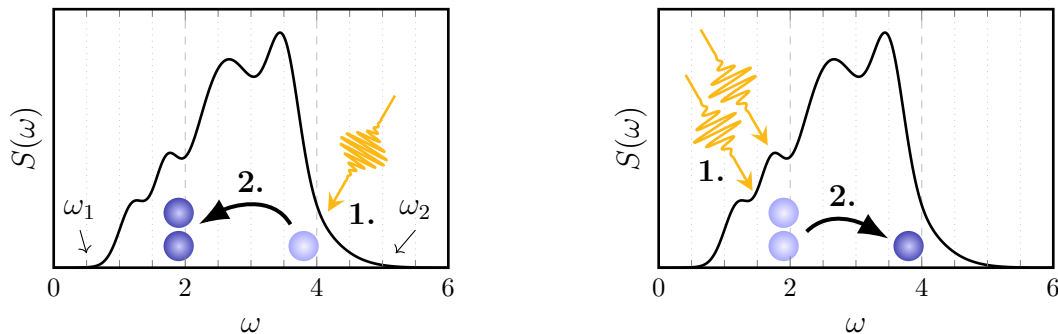[1]The band gap has a width of approximately $2\,T$, see Figure 5.1.

Figure 5.16. Schematic illustration of impact ionization (left) and Auger recombination (right) of arbitrary excitations (shown here as blue quasipartices) corresponding to a spectrum $S(\omega)$. Left: First a photon excites a high-energy quasiparticle (1). Since the number of quasiparticles is not conserved, this high-energy quasiparticle can lower its energy upon creation of a second one (2). Right: The same process can take place in the other direction, where two low-energy quasiparticles are excited by photons (1) and combine into a single one with higher energy (2).

the Hubbard model in various geometries and found that impact ionization occurs in all except the linear chain. Since next-nearest neighbor interactions in a one-dimensional chain are equivalent to a zig-zag chain (i.e. two coupled chains, somewhat similar to the 2-by-6 system treated in [5]), the same seems to be true for the T-V model.

It is, however, interesting that next-nearest neighbor *hopping* appears to be necessary for impact ionization, as we did not observe it with next-nearest neighbor Coulomb interaction in Section 5.2.3. Hence, the hopping geometry seems to be crucial for impact ionization. This was also noticed by Kauch et al. [5] who found that next-nearest neighbor hopping enhances impact ionization in the two-dimensional geometries they considered. In one dimension, we have seen that the next-nearest neighbor hopping enables impact ionization in the first place.

To check whether fermionic anticommutation relations are necessary for impact ionization to occur, the calculation for a case with impact ionization is repeated for hard-core bosons. That is, we use the same Hamiltonian (5.1) but the fermionic operators c and $c^\dagger$ are replaced by annihilation and creation operators b and $b^\dagger$ with *bosonic* commutation relations. However, these operators are still assumed to obey the Pauli principle, i.e. $b^2 = (b^\dagger)^2 = 0$. This hard-core boson model is only different from the fermionic T-V model with next-nearest neighbor hopping $T_2 \neq 0$ and it is equivalent to a spin-1/2 XXZ model with nearest and next-nearest neighbor interactions.

In Figure 5.17, results for $T_2 = 0.4\,T$ and $\Omega = 8\,T$ are presented for the hard-core boson and fermion models. The data show that impact ionization is not restricted to fermions, but also happens for hard-core bosons under the same circumstances.

5.2.5. Both Next-Nearest Neighbor Couplings ($T_2 \neq 0, V_2 \neq 0$)

For the case with next-nearest neighbor hopping *and* Coulomb interaction, the nearest-neighbor occupancy as a function of time and its long-term change after the pulse as a
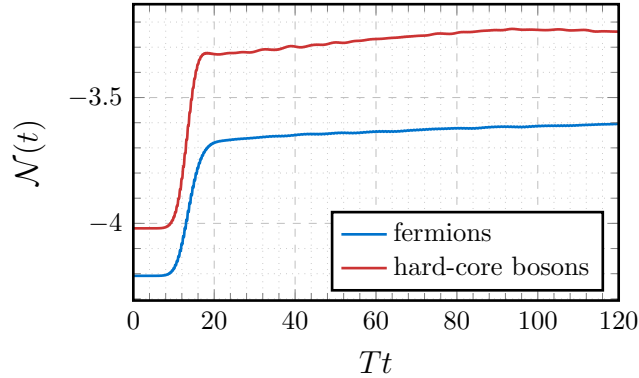
Figure 5.17. Time dependent nearest-neighbor occupancy in the 1D fermionic and hard-core bosonic extended T-V models with 20 sites, $V = 6\,T$ and $T_2 = 0.4\,T$ exposed to an electromagnetic pulse with frequency $\Omega = 8\,T$ and amplitude $A_0 = 0.2$, centered around $t_0 = 13\,T^{-1}$ with width $\sigma = 3\,T^{-1}$.

function of pulse frequency are plotted in Figure 5.18. Impact ionization and Auger recombination both still happen like in the case with $T_2 \neq 0$ and $V_2 = 0$, but the additionally switched on next-nearest neighbor Coulomb interaction seems to favor the latter. While the decrease of the nearest-neighbor occupancy in the lower frequency range (i.e. Auger recombination) is stronger than in the case with $V_2 = 0$ (see Figure 5.15), the increase for higher frequencies corresponding to impact ionization is very small compared to the $V_2 = 0$ case.
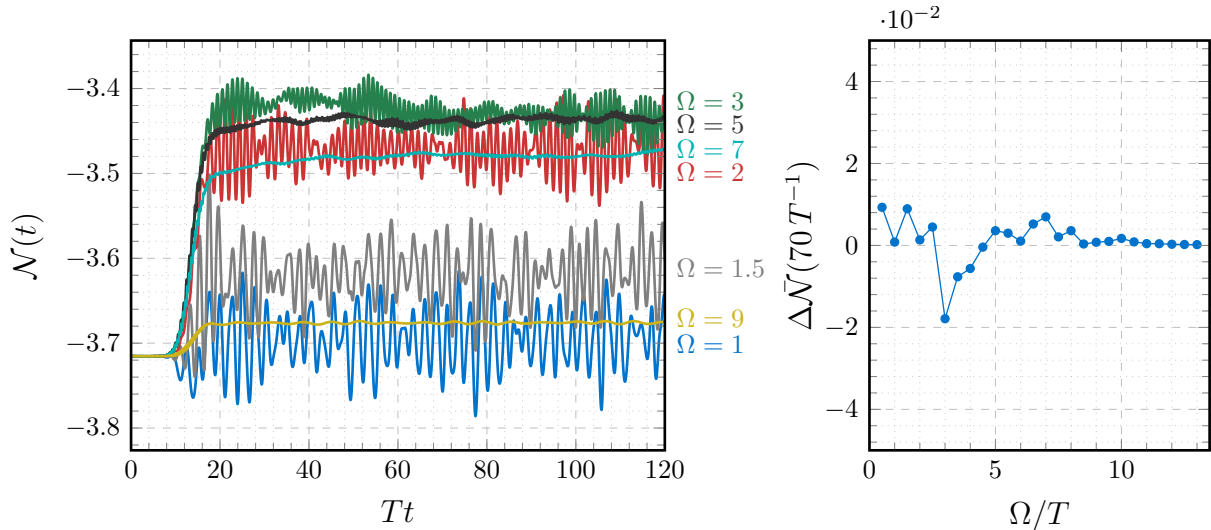

Figure 5.18. Left: Time dependent nearest-neighbor occupancy in the 1D extended T-V model with 20 sites, $V = 6\,T$, $V_2 = T$ and $T_2 = 0.4\,T$, exposed to electromagnetic pulses with various frequencies Ω (in units of T) and amplitude $A_0 = 0.2$. Right: Change of the average nearest-neighbor occupancy after the pulse.

For some of the lower frequencies, the oscillations of the nearest-neighbor occupancy do not have the same short periodicity as in Figure 5.15 (e.g. for $\Omega = 3\,T$), which makes the averaging procedure to obtain $\Delta\bar{\mathcal{N}}$ less reliable and in combination with the high amplitude of the oscillations at low frequencies causes the high values at some frequencies

below $3\,T$ in Figure 5.18 (see gray line for $\Omega = 1.5\,T$).

The frequency ranges in which impact ionization and Auger recombination happen are at lower frequencies than with $V_2 = 0$ (see Figure 5.15) in accordance with the spectral functions shown in Figure 5.2 for the case $T_2 = 0$, $V_2 = T$. Here $T_2 \neq 0$, but comparison of the first and third column in Figure 5.2 shows that T_2 seems not to change the frequency range where the spectral functions are non-zero, while a positive V_2 shifts the range towards $\omega = 0$.

5.3. Multi-Photon Absorption

In Figure 5.19, the energy absorption during the pulse and the change of nearest-neighbor occupancy after the pulse are plotted as a function of the pulse frequency for various pulse amplitudes for the case $T_2 = 0.4\,T$, $V_2 = 0$. Since, according to (2.34), in the linear response regime the absorbed energy depends on the square of the amplitude of the perturbation, the energy differences are scaled by the squared amplitude in Figure 5.19.[1] For the lower amplitudes, the scaled energy absorption is almost exactly the same, suggesting that these amplitudes are in the linear regime. For the highest amplitude $A_0 = 0.8$, however, the response already seems to be highly nonlinear as the absorbed energy is not proportional to the squared amplitude anymore.
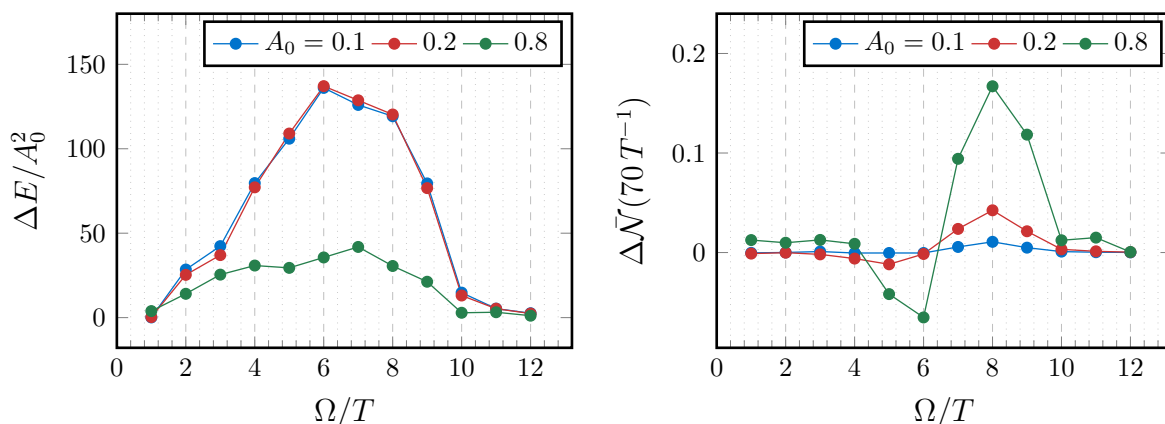

Figure 5.19. Change of energy due to the pulse (left) and change of nearest-neighbor occupancy after the pulse (right) in the extended T-V model with 20 sites, $V = 6\,T$ and $T_2 = 0.4\,T$ as a function of frequency Ω, for various amplitudes A_0 of the pulse.

At the highest intensity of the pulse, the response in terms of energy scaled by the squared amplitude (as plotted in Figure 5.19) is much smaller than with lower pulse intensities (suggesting some kind of saturation behavior) for most frequencies. However, in the low-frequency range this difference is smaller than for higher frequencies and for $\Omega = 1\,T$ the scaled (!) absorbed energy is even higher for $A_0 = 0.8$ than for the lower amplitudes. This is due to the absorption of multiple photons either at once (multiphoton absorption) or

---

[1]In the Hamiltonian, the perturbation appears as a factor $\mathrm{e}^{-\mathrm{i}A}$, but the leading order is still linear because $\mathrm{e}^{-\mathrm{i}A} = 1 - \mathrm{i}A + \mathcal{O}(A^2)$.

one after another. The former is a nonlinear process, which can lead to absorption even at photon frequencies below the linear absorption spectrum [89, 90].

Both kinds of processes lead to a contribution of eigenstates with energies (relative to the ground state), which are approximately integer multiples of the incident frequency, to the state of the system after the pulse. Hence, they are visible in the eigenstate spectrum (see Section 2.6) of the excited system, which can be calculated numerically with the already implemented methods according to (2.46) and (2.50), as peaks at $E_0 + n\Omega$. In Figure 5.20 and Figure 5.21, the eigenstate (Loschmidt) spectra of systems with and without next-nearest neighbor hopping, exposed to pulses with different amplitudes and frequencies, are shown.
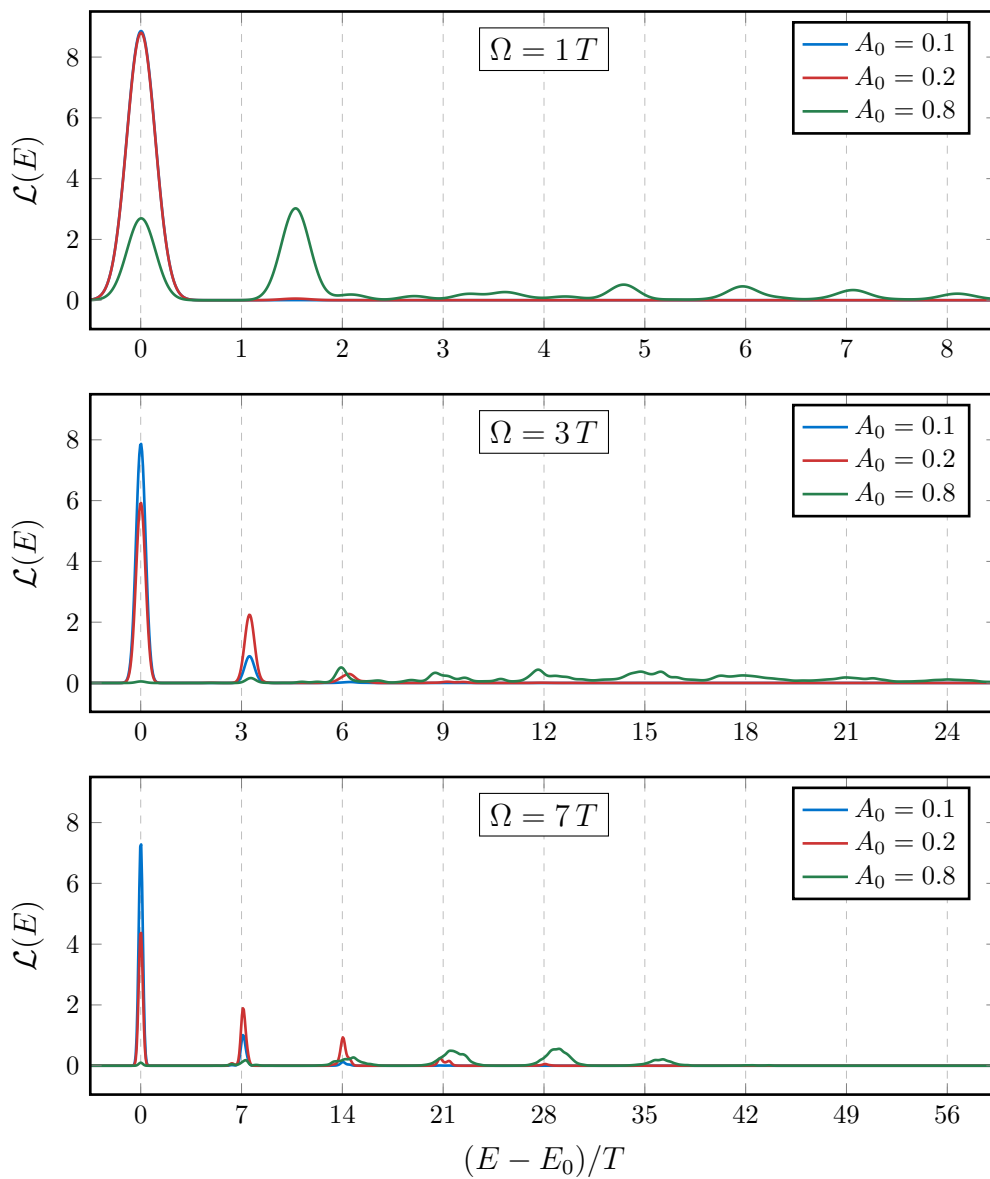

Figure 5.20. Loschmidt eigenstate spectra of the 1D simple T-V model ($T_2 = V_2 = 0$) with 20 sites and $V = 6\,T$ after a pulse with various frequencies Ω and several amplitudes A_0.

The spectra for both cases look almost exactly the same. It is clearly visible that the fraction of states with energies around $E_0 + n\Omega$ increases with larger intensity, which corresponds to the absorption of n photons. In particular, multiphoton absorption with $n > 1$ is not present at all at the lowest intensity $A_0 = 0.1$ and only very weak at $A_0 = 0.2$. While for $A_0 = 0.2$ only the two-photon process occurs, the highest intensity shown in the plot, $A_0 = 0.8$, also shows indications of absorption of more than two photons.
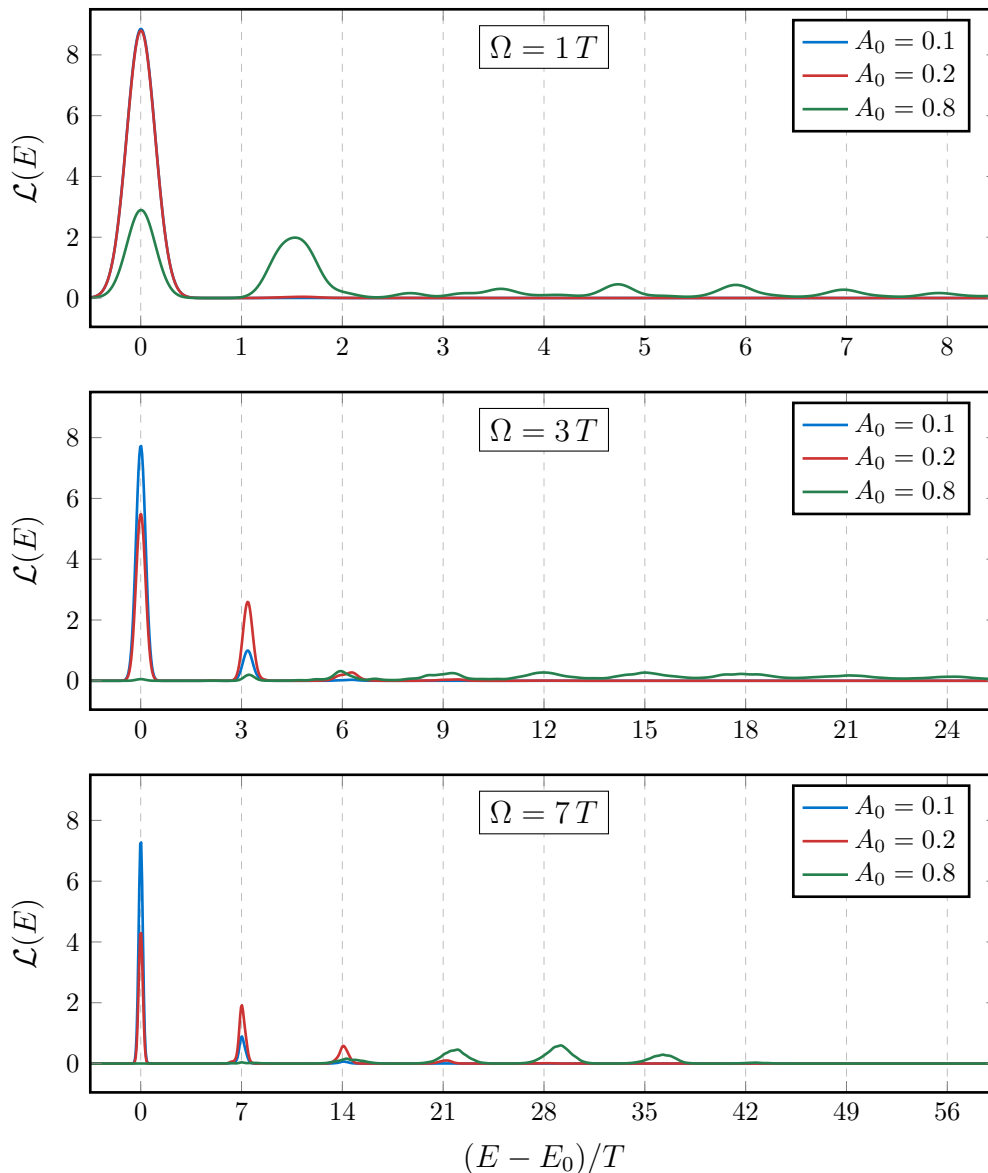

Figure 5.21. Loschmidt eigenstate spectra of the 1D extended T-V model with 20 sites, $V = 6\,T$ and $T_2 = 0.4\,T$ after a pulse with various frequencies Ω and several amplitudes A_0.

At $\Omega = T$, absorption of a single photon is not possible, yet energy is absorbed during the pulse according to Figure 5.19. The first plot in Figure 5.21 provides an explanation for this: No states are occupied at $E_0 + \Omega$, which is consistent with the expectation that no absorption occurs at the frequency Ω. However, with a sufficiently high intensity, two photons can be absorbed at once, which is indicated by the peak a little below $E_0 + 2\Omega$ in Figure 5.21 at the top. We might expect the peak to be exactly at $E_0 + 2\Omega$, but the

finite width of the pulse in the frequency domain (see Figure 5.4) in combination with the possible excitations of the system can lead to this deviation. In the present case, for instance, it is possible that the absorption of two photons with $\Omega = 0.8\,T$ has a higher probability than with $\Omega = 1\,T$.

The peaks at very high energies in the second and third plots, on the other hand, must be caused by subsequent absorption of multiple photons, because no photons with frequencies above approximately $15\,T$ are absorbed by the system (see Figure 5.10). At intermediate frequencies (in the range where energy is absorbed, see Figure 5.19) both processes can occur and contribute to the respective response in the Loschmidt spectra.

5.4. Summary

First, the density of states and various spectral functions were calculated for the extended T-V model with 20 sites by applying of TEBD for the computation of time-dependent correlations. The spectral functions show at which photon energies excitations of the system are possible and therefore absorption can be expected.

To search for signs of impact ionization, the ground state of the extended T-V model with 20 sites and several parameter sets was calculated with DMRG and then time-evolved with TEBD. During the time evolution, the system was exposed to electromagnetic waves modeled by means of the Peierls substitution. Since this electromagnetic pulse leads to linear growth of entanglement in the state and therefore exponential growth of the required bond dimensions, it was found that the TEBD algorithm is restricted to either short time scales or small systems, justifying the choice of only 20 lattice sites. The entanglement also depends on the amplitude of the pulse.

The dependence of the response of the system on the frequency of the electromagnetic field (i.e. the photon energy) was examined and compared to the current-current and hopping-hopping spectral functions, because the field couples to the current and hopping operators via the Peierls substitution. A good agreement concerning the frequency ranges and the location of the maxima was found.

As a measure for impact ionization, the long-term change of the nearest-neighbor occupancy after the pulse is used. In most cases, the nearest-neighbor occupancy grows during the pulse, showing that pairs of occupied neighboring sites are created by the incident photons. However, impact ionization, namely further growth after the end of the pulse, is only observed with next-nearest neighbor hopping $T_2 \neq 0$. The fact that impact ionization does not occur in all cases with next-nearest neighbor Coulomb interaction contradicts the idea that integrability alone is the reason for the absence of impact ionization in one-dimensional models.

Both impact ionization and Auger recombination are present with next-nearest neighbor hopping and both processes occur in certain frequency ranges that are compatible with the picture of high-energy excitations decaying into multiple lower-energy excitations. However, unlike in the Hubbard model, the energy ranges do not correspond to the spectra of single-particle excitations. Hopping-hopping and current-current spectral functions succeed much better in explaining the behavior of the system.

A repulsive next-nearest neighbor Coulomb interaction $V_2 > 0$ in addition to the next-nearest neighbor hopping appears to favor Auger recombination while suppressing impact ionization.

For comparison, the calculation was repeated with hard-core bosons instead of fermions for one case, showing that impact ionization also occurs for the bosons.

At high amplitudes of the pulse, evidence for multi-photon absorption was found. Eigenstate spectra of the state after the pulse were calculated, where these processes are visible.

6. Time-Evolution of the T-V Model with Transverse Contraction

In this chapter, the time evolution of the T-V model will be repeated with the transverse contraction approach in the thermodynamic limit, which was introduced in Section 4.11. To test the algorithm and reveal potential problems and difficulties, it is first applied to the simple case of an empty T-V model where a single particle is added at one site at time 0 (Section 6.1). Then, in Section 6.2, we study the applicability of the transverse method for the long-term measurement of the nearest-neighbor occupancy after an electromagnetic pulse (which was done in Section 5.2 for small systems).

Like in Chapter 5, all calculations are done with C++ programs using the ITensor library [84]. The conservation of the total particle number is exploited as explained in Section 4.9 with the framework included in the library.

6.1. Propagation of a Single Particle

As a first check of the transverse approach, we simulate the propagation of a single particle localized at a certain site 0 in an otherwise empty system in the thermodynamic limit. The system shall be described by the T-V Hamiltonian (see Section 3.2)

$$\hat{H} = \sum_{i=-\infty}^{\infty} \left(-T c_i^\dagger c_{i+1} - T^* c_{i+1}^\dagger c_i + V \left(\hat{n}_i - \tfrac{1}{2} \right) \left(\hat{n}_{i+1} - \tfrac{1}{2} \right) \right). \tag{6.1}$$

For only one particle in the system, the T-V model is equivalent to the tight-binding model and the time evolution can be calculated analytically in this subspace (see Appendix D).

6.1.1. The Transfer Matrix

Even though we want to simulate the dynamics of one particle, the initial state used for the transfer matrix is the one with no particles in the system. The reason for this is, that the transfer matrix describes the translationally invariant parts of the system to the left and right of the central region in which the particle is added and the measurements are done. The creation operator for the particle as well as all measurement operators must then be incorporated in the central, non-translationally invariant part of the system that is only used for the final measurement step (see Figure 6.1).

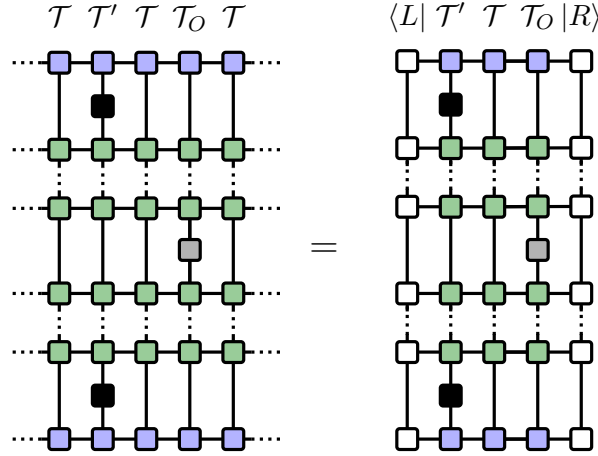$\mathcal{T}$ $\mathcal{T}'$ $\mathcal{T}$ $\mathcal{T}_O$ $\mathcal{T}$ $\langle L|\,\mathcal{T}'\,\,\mathcal{T}\,\,\mathcal{T}_O\,|R\rangle$

Figure 6.1. Network representing the expectation value of the particle density $\hat{n}$ on site 2 at time t after a particle was added on site 0 at time 0 in the thermodynamic limit. The translationally invariant initial state is given by the blue MPS, the green MPO is an approximation of the translationally invariant time evolution operator, the black tensors correspond to $c^\dagger$ (and c in the upper part, if read from bottom to top) and the gray ones to $\hat{n}$. In the actual calculations in this section, the MPO is invariant under translation by two sites only and the measurement is more complicated, see Section 6.1.3.

The empty system in the thermodynamic limit is described by the product state

$$|\psi\rangle = \bigotimes_{i=-\infty}^{\infty} |0\rangle_i$$

with the trivial iMPS representation $A^0 = 1$, $A^1 = 0$.

For the time evolution MPO, we use decomposed second-order Trotter gates or the second-order W^I-approximation, which are both described in Section 4.8.2. A comparison of the two methods with regard to the accuracy of the results is given in Section 6.2.3. Both second-order approximations require two different MPOs for one time step. In the present case, the Hamiltonian is time-independent and thus the MPOs are the same for each time step.

In order to read off the W^I-approximation (see Section 4.8.2), the Hamiltonian of the T-V model (6.1) must be written as an MPO. Since the anticommutation relations of fermionic operators on different sites can not be encoded in the corresponding matrices easily, we use the Jordan-Wigner transformation (3.8) (see Section 3.2.1) to transform to hard-core bosonic operators $b^\dagger$ and b which commute on different sites. In terms of these operators, the kinetic terms become

$$-Tc_i^\dagger c_{i+1} - T^* c_{i+1}^\dagger c_i = -Tb_i^\dagger b_{i+1} - T^* b_{i+1}^\dagger b_i = -Tb_i^\dagger b_{i+1} - T^* b_i b_{i+1}^\dagger$$

and the potential terms do not change, because $\hat{n}_i = c_i^\dagger c_i = b_i^\dagger b_i$.

The Hamiltonian for L sites can now be represented as an MPO $\hat{\mathcal{W}}^{[1]} \otimes \ldots \otimes \hat{\mathcal{W}}^{[L]}$ with

the operator-valued matrices

$$
\hat{\mathcal{W}}^{[i]} = \begin{pmatrix} \hat{\mathbb{1}}_i & V(\hat{n}_i - \frac{1}{2}) & -T^* b_i & -T b_i^\dagger & 0 \\ 0 & 0 & 0 & 0 & \hat{n}_i - \frac{1}{2} \\ 0 & 0 & 0 & 0 & b_i^\dagger \\ 0 & 0 & 0 & 0 & b_i \\ 0 & 0 & 0 & 0 & \hat{\mathbb{1}}_i \end{pmatrix} \quad \text{for } i = 2, \ldots, L-1. \tag{6.2}
$$

In the case of a finite system, it is easy to verify that with the edge vectors $\hat{\mathcal{W}}^{[1]} = (\hat{\mathbb{1}}\ 0\ 0\ 0\ 0)$ and $\hat{\mathcal{W}}^{[L]} = (0\ 0\ 0\ 0\ \hat{\mathbb{1}})^T$, one retrieves the T-V Hamiltonian (3.7). In the thermodynamic limit, the edge tensors are irrelevant and we simply use (6.2) on every site. According to (4.37), the W$^{\mathrm{I}}$ time-evolution MPO for this MPO-representation of the Hamiltonian is given by

$$
\hat{W}_{\mathrm{TV}}^{\mathrm{I}[i]}(\tau) = \begin{pmatrix} \hat{\mathbb{1}}_i & \sqrt{-\mathrm{i}\tau} V(\hat{n}_i - \frac{1}{2}) & -\sqrt{-\mathrm{i}\tau} T^* b_i & -\sqrt{-\mathrm{i}\tau} T b_i^\dagger \\ \sqrt{-\mathrm{i}\tau}(\hat{n}_i - \frac{1}{2}) & 0 & 0 & 0 \\ \sqrt{-\mathrm{i}\tau} b_i^\dagger & 0 & 0 & 0 \\ \sqrt{-\mathrm{i}\tau} b_i & 0 & 0 & 0 \end{pmatrix}. \tag{6.3}
$$

Note that for the second-order approximation, two MPOs of the form (6.3) with complex time steps $\frac{1 \pm \mathrm{i}}{2}\tau$ are used (see Section 4.8.2).

Like all MPOs, the representation (6.3) is not unique, but has a gauge degree of freedom. Consequences of the gauge on the algorithm are discussed in Section 6.1.2.

Finally, the transfer matrix is constructed from the initial state MPS and the time evolution MPOs as described in Section 4.11. If the MPO tensors are obtained by decomposing Trotter gates, the resulting MPO has a unit cell with two possibly distinct matrices for adjacent sites. Although here it should not make a difference which one is used, we will still build a transfer matrix with two columns (as in Figure 4.28), allowing us to reuse the code for ground states calculated with two-site iDMRG as initial states.

The transfer matrix is shown in Figure 6.2. Both columns consist of the trivial tensor representing an empty site (blue) and the MPO tensors. For the second-order Trotter approximation, we use the tensors $W^{[A]}$ (left column) and $W^{[B]}$ (right column) as defined in Section 4.8.2, where in the second-order case two sets $W^{[A1]}$, $W^{[B1]}$ and $W^{[A2]}$, $W^{[B2]}$ are applied alternatingly. If the W$^{\mathrm{I}}$-approximation is used, then $W^{[A]}$ and $W^{[B]}$ are both replaced by W^{I} from (6.3), and for the second-order approximation we obtain two tensors with complex time steps (see Section 4.8.2), which are again applied alternatingly. The upper half of the network in Figure 6.2 is simply the conjugate of the lower half.

For finding the dominant eigenvectors, the TM-DMRG method introduced in Section 4.11.2 is used. Since we need the eigenvectors of the full transfer matrix $\mathcal{T} = \mathcal{T}_1 \mathcal{T}_2$, we must modify the algorithm to consider both columns. This is equivalent to a generalization of DMRG (see Section 4.7) to an operator represented by two MPOs, which is in fact straightforward. If we define the effective Hamiltonian instead of (4.28) as

$$
H^{\mathrm{eff}}_{(\alpha_{j-1}\alpha_j s_j)(\alpha'_{j-1}\alpha'_j s'_j)} = \sum_{\substack{\beta_{j-1}\beta'_{j-1} \\ \beta_j \beta'_j s''_j}} L_{\alpha_{j-1}\beta_{j-1}\beta'_{j-1}\alpha'_{j-1}} W^{1[j]s_j s''_j}_{\beta_{j-1}\beta_j} W^{2[j]s''_j s'_j}_{\beta'_{j-1}\beta'_j} R_{\alpha_j \beta_j \beta'_j \alpha'_j}, \tag{6.4}
$$

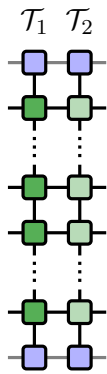$\mathcal{T}_1$ $\mathcal{T}_2$

Figure 6.2. Transfer matrix for an empty T-V model, time evolved with an MPO (green) with two sites in the unit cell. The gray lines indicate dummy indices with dimension 1, because the initial state is a product state.

with accordingly modified L and R, then (4.29) remains valid for the case with two MPOs given by the tensors $W^{1[j]}$ and $W^{2[j]}$, respectively. Remember, however, that in TM-DMRG, (4.29) has to be solved for the *largest* eigenvalue with a non-hermitian eigensolver. The left and right eigenvector are calculated separately, where, as explained in Section 4.11.2, the left or right eigenvectors of the effective transfer matrix have to be found in the course of the local optimization.

For the present case, very few TM-DMRG sweeps (about 5) are sufficient for convergence in the eigenvalues up to 14 digits (with a maximum discarded weight of 10^{-12}).

6.1.2. Overlap of Eigenvectors

The crucial part of the transverse approach is the computation of the left and right eigenvectors $\langle L|$ and $|R\rangle$ of the transfer matrix corresponding to the dominant eigenvalue. If they are normalized separately, i.e. $\langle L|L\rangle = \langle R|R\rangle = 1$, then their overlap $\langle L|R\rangle$ will be smaller than 1, because left and right eigenvectors are not the same for a general, non-hermitian operator (see also Appendix E). Since this overlap is the denominator in (4.50), very small values can cause numerical problems when calculating expectation values.

Gauge Dependence of the Overlap

For the time evolution of the empty system from the previous section, the overlap is shown as a function of total time for various time steps with an asymmetric gauge of the MPO in Figure 6.3. By asymmetric gauge we mean that the Trotter gates are decomposed into $(U\Lambda)V^\dagger$ as in Figure 4.21 and the W^I-matrices are formed as in (6.3) except that the full factor $-\mathrm{i}\tau$ is assigned to the entries in the first row (to obtain a "maximally asymmetric" form for comparison purposes). For both methods, the second-order versions are used, leading to two different MPOs for each time step (see Section 4.8.2). In all cases, the eigenvectors are found with the TM-DMRG algorithm (see Section 4.11).

The overlap seems to decrease exponentially with the number of time steps regardless of the size of the time step (i.e. not with the total time). Already for short times (below $t = 5\,T^{-1}$ for small time steps), the overlap becomes too small to be representable with a double precision floating-point number.[1]

---

[1] The double precision floating-point format can represent numbers as small as $2^{-1022} \approx 2 \cdot 10^{-308}$ or a
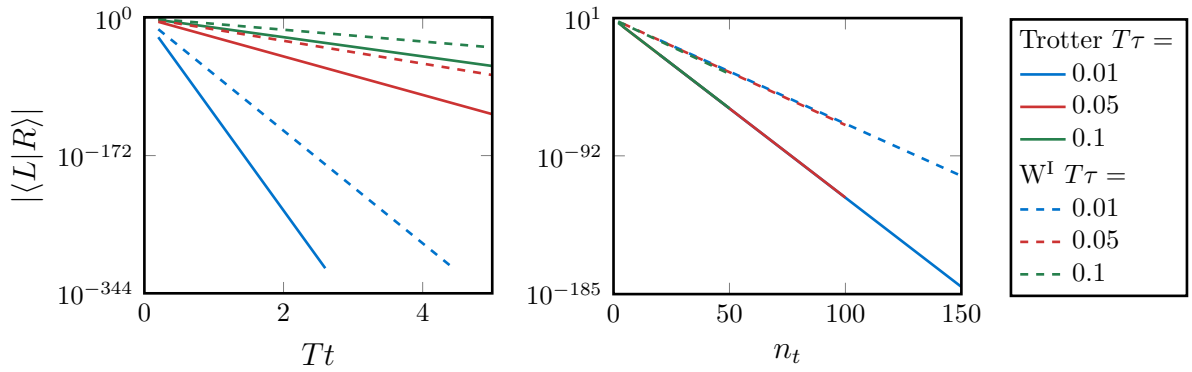
Figure 6.3. Overlap of the left and right eigenvectors of the transfer matrix for the time evolution of an empty T-V model with various time steps τ, where the transfer matrix is built from *asymmetric* MPO matrices. The MPOs are obtained from second-order Trotter or W^I approximations. Left: Overlap (logarithmic) as a function of total time t. Right: Overlap (logarithmic) as a function of the number of time steps n_t. In the right plot, for both methods all curves are on top of each other.

A major improvement of this scaling can be achieved by using a more symmetric gauge of the time-evolution MPO (see Section 4.3 for details on gauge transformations). For the W^I-approximation, instead of (6.3) we can equivalently use the matrices

$$
\hat{W}_{\text{TV}}^{\text{I}[i]}(\tau) = \begin{pmatrix} \hat{\mathbb{1}}_i & \sqrt{-\mathrm{i}\tau V}(\hat{n}_i - \tfrac{1}{2}) & \sqrt{\mathrm{i}\tau T^*}b_i & \sqrt{\mathrm{i}\tau T}b_i^\dagger \\ \sqrt{-\mathrm{i}\tau V}(\hat{n}_i - \tfrac{1}{2}) & 0 & 0 & 0 \\ \sqrt{\mathrm{i}\tau T^*}b_i^\dagger & 0 & 0 & 0 \\ \sqrt{\mathrm{i}\tau T}b_i & 0 & 0 & 0 \end{pmatrix} \tag{6.5}
$$

and when forming an MPO from Trotter gates, we can symmetrically distribute the singular values to the left and right, i.e. decompose the gates into $(U\sqrt{\Lambda})(\sqrt{\Lambda}V^\dagger)$ instead of simply pushing the singular values into the matrix to their left (see Section 4.8.2, Figures 4.21 and 4.22).

Figure 6.4 shows the overlap for this "symmetric" gauge (we will call it that although the matrices are not really symmetric). Although the overlap still decreases exponentially with time, the slope is much smaller than with the asymmetric gauge and the values are far from reaching the representability limits of a computer. The small values could still cause numerical instability, but this seems not to be the case as the results obtained with symmetrically gauged MPO matrices compare well with exact results (see next section). Besides, the overlap now depends on the total time and not the number of time steps, indicating a physical origin.

Apart from avoiding extremely small overlaps, a further advantage of the symmetric MPO gauge is that the entanglement between the transverse sites in the left and right eigenvectors is approximately the same, leading to similar transverse bond dimensions. When using an asymmetric gauge, the required transverse bond dimension χ is larger in one of the eigenvectors and smaller in the other, which is inconvenient because the

---

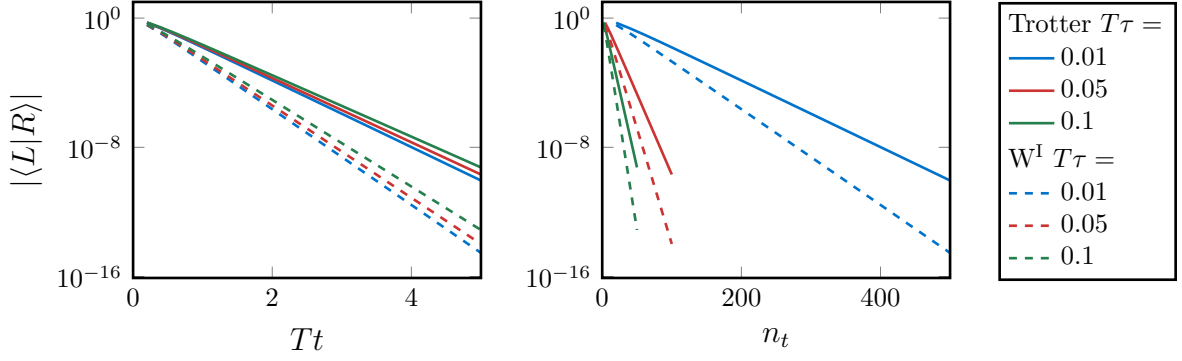few orders of magnitude smaller ($\approx 5 \cdot 10^{-324}$) at the cost of significant digits [91].

Figure 6.4. Overlap of the left and right eigenvectors of the transfer matrix for the time evolution of an empty T-V model with various time steps τ, where the transfer matrix is built from *symmetrically gauged* MPO matrices. The MPOs are obtained from second order Trotter or W^I approximations. Left: Overlap (logarithmic) as a function of total time t. Right: Overlap (logarithmic) as a function of the number of time steps n_t.

TM-DMRG algorithm used to find the eigenvectors scales as χ^3. For these reasons, symmetrically gauged MPOs are used for all further calculations, including Section 6.2.

The overlap is also influenced by the gauge of the MPS representing the initial state, but this only contributes a constant factor which does not play a big role compared to the large number of time-evolution MPOs. All results in this thesis were obtained using right-canonical iMPS for the initial state. Still, the overlap could be further increased by using a symmetric gauge for the MPS instead of a left- or right-orthogonal one. Similar to the MPOs, this can be achieved by using $\sqrt{\Lambda^{[i-1]}}\Gamma^{[i]}\sqrt{\Lambda^{[i]}}$ with Λ and Γ from the canonical form (see Sections 4.3 and 4.10.2).

Biorthonormalization of the Eigenvectors

Bañuls et al. used a biorthonormalization procedure to solve the problem of small overlaps (M. C. Bañuls, private communication, September 2020). Let $L^{[i]}$ and $R^{[i]}$ denote the tensors of the transverse MPS $\langle L|$ and $|R\rangle$, respectively (Figure 4.27, white tensors), which are numbered from bottom to top. Starting at the bottom ($i = 1$) we go through the transverse MPS and at each transverse site form the matrix

$$M^{[i]}_{\alpha_i\beta_i} = \sum_{r_i\alpha_{i-1}} L^{[i]r_i}_{\alpha_{i-1}\alpha_i} R^{[i]r_i}_{\alpha_{i-1}\beta_i},$$

which is shown graphically in Figure 6.5 in the leftmost diagram. For the first transverse site, α_0 is a dummy index with dimension 1. The matrix $M^{[i]}$ is then SV-decomposed into $U\Lambda V^\dagger$ (see Figure 6.5) and the matrices are transformed according to

$$L^{[i]l_i}_{\alpha_{i-1}\alpha_i} \rightarrow \sum_{\alpha_i} L^{[i]l_i}_{\alpha_{i-1}\alpha_i} U^\dagger_{\alpha_i\gamma}\sqrt{\Lambda_\gamma^{-1}}, \qquad L^{[i+1]l_{i+1}}_{\alpha_i\alpha_{i+1}} \rightarrow \frac{1}{\|\sqrt{\Lambda}\|}\sum_{\alpha_i}\sqrt{\Lambda_\gamma} U_{\gamma\alpha_i} L^{[i+1]l_{i+1}}_{\alpha_i\alpha_{i+1}},$$

$$R^{[i]r_i}_{\beta_{i-1}\beta_i} \rightarrow \sum_{\beta_i} R^{[i]r_i}_{\beta_{i-1}\beta_i} V_{\beta_i\gamma}\sqrt{\Lambda_\gamma^{-1}}, \qquad R^{[i+1]r_{i+1}}_{\beta_i\beta_{i+1}} \rightarrow \frac{1}{\|\sqrt{\Lambda}\|}\sum_{\beta_i}\sqrt{\Lambda_\gamma} V^\dagger_{\gamma\beta_i} R^{[i+1]r_{i+1}}_{\beta_i\beta_{i+1}}. \quad (6.6)$$

Apart from the normalization factor $1/\|\sqrt{\Lambda}\|$ that keeps the new matrices within reasonable orders of magnitude, this is (seemingly, see below) a gauge transformation that leaves the transverse MPS unchanged and leads to a biorthonormality relation as shown in Figure 6.5 on the right. After the transformation is carried out for all transverse sites $(i = 1, \ldots, L_{\mathcal{T}})$, the network representing the overlap $\langle L | R \rangle$ collapses due to this relation and the overlap is given by the contraction of the last two tensors, which can be set to 1 by appropriate scaling of the tensors.
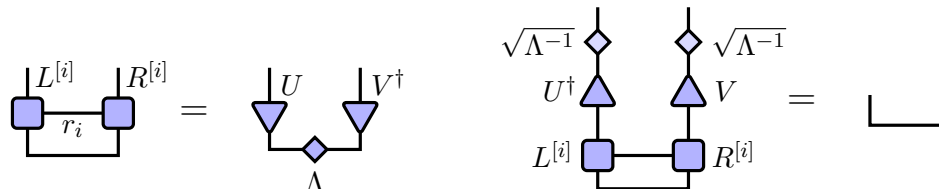
Figure 6.5. Biorthonormalization of the left and right eigenvector to ensure $\langle L | R \rangle = 1$. An SVD of the diagram on the left is used to regauge both transverse MPS according to the right diagrams. The next tensors in both MPS must be multiplied by $\sqrt{\Lambda} U$ and $\sqrt{\Lambda} V^{\dagger}$, respectively.

However, for the cases where the biorthonormalization procedure was tried in the present thesis, it failed for the following reason: During the contraction over the transverse local index r_i in Figure 6.5 on the left, non-zero contributions for a particular value of r_i in one tensor may be deleted by a zero matrix for that value of r_i in the other tensor (e.g. $L^{[i]2} \neq 0$ but $R^{[i]2} = 0$). Then it may happen that in the matrix which is SV-decomposed, subspaces are missing (in the sense that they are in the null space) that were present in $L^{[i]}$ or $R^{[i]}$. Singular values corresponding to these subspaces will be zero and this means that the transformation (6.6) does in fact not leave the MPS unchanged, because $U^{\dagger} \sqrt{\Lambda^{-1}} \sqrt{\Lambda} U = \mathbb{1}$ is only true outside the mentioned subspaces (Λ^{-1} is to be understood as a pseudoinverse with zeros where singular values are below a certain threshold). How exactly this issue emerges is investigated in more detail in terms of a specific example in Appendix F.

Besides, all measures taken to increase the overlap *after* the eigenvector search algorithm have the drawback that they potentially scale up errors in the eigenvector. Imagine the extremal case that the error of one of the eigenvectors is exactly parallel to the other eigenvector,

$$|\delta R\rangle := |\tilde{R}\rangle - |R\rangle = \big\| |\delta R\rangle \big\| \, |L\rangle \,,$$

where $|\tilde{R}\rangle$ is the approximation and $|R\rangle$ is the exact eigenvector. If we assume for simplicity that $\langle L|$ is exactly known, then the error in the overlap is

$$\langle L | \delta R \rangle = \big\| |\delta R\rangle \big\|.$$

We have seen that the overlap can easily become as low as 10^{-16} even for short time evolutions (see Figure 6.4), which for this example would mean that a rather low error of $\big\| |\delta R\rangle \big\| = 10^{-16}$ in the eigenvector corresponds to an error of $100\,\%$ in the overlap. If the component of $|R\rangle$ which is parallel to $|L\rangle$ is now scaled up by any means (which is necessary to increase the overlap), then so is the error. In most cases, of course, the error will be far from parallel to the other eigenvector, but for very small overlaps such

problems are likely to occur. They could be overcome by searching both eigenvectors simultaneously and enforcing the biorthonormality *during* whatever algorithm is used to solve the eigenvalue problem.

In this thesis, the biorthonormalization will not be used due to the problem of deleted subspaces and because the small overlap appears not to entail numerical problems.

6.1.3. Measurement and Results

For the discussion of the measurement of the particle density at various sites, we define the following transverse operators (Figure 6.6):

- $\mathcal{T}_1$ and $\mathcal{T}_2$ are the columns of the transfer matrix (see also Figure 6.2),

- $\mathcal{T}_1'$ and $\mathcal{T}_2'$ are the columns of the transfer matrix with $c^\dagger$ applied to the initial state at the respective site,

- $\mathcal{T}_{1O}$ and $\mathcal{T}_{2O}$ are the columns of the transfer matrix including the observable to be measured,

- $\mathcal{T}_{1O}'$ and $\mathcal{T}_{2O}'$ are the columns of the transfer matrix with $c^\dagger$ applied to the initial state, including the observable to be measured.
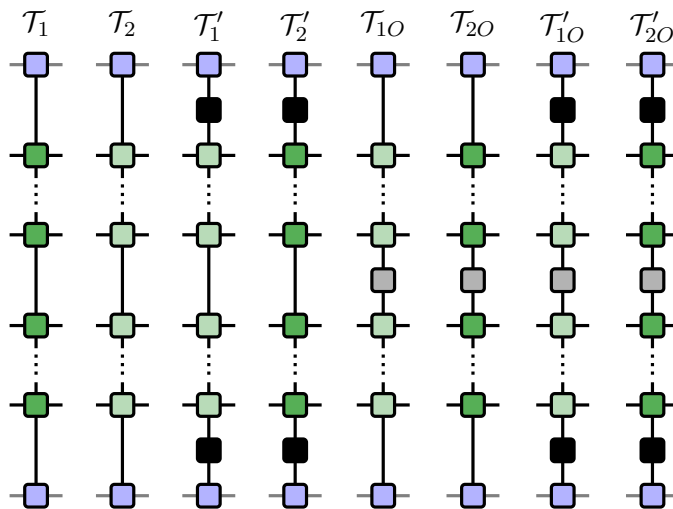

Figure 6.6. Transverse operators for the measurement of the particle density in the T-V model in the thermodynamic limit at various sites with transverse contraction, after a single particle was added to the otherwise empty system. The black tensors represent $c^\dagger$ (or c in the upper part if read from bottom to top) and the gray tensors represent the particle number operator $\hat{n}$. The gray lines indicate dummy indices with dimension 1 connecting the tensors of the initial product state.

The expectation value of the particle density at any site after a particle was added at site 0 can be expressed in terms of these operators and the eigenvectors $\langle L|$ and $|R\rangle$ by generalizing (4.50). In the network representing the denominator, which is always the same as the numerator without the measurement operator, the eigenvalue equations $\mathcal{T}_1\mathcal{T}_2|R\rangle = \lambda|R\rangle$ and $\langle L|\mathcal{T}_1\mathcal{T}_2 = \lambda\langle L|$ can be used. As in the case of multiple-site operators

Table 6.1. Expressions for the expectation value of the particle density $\hat{n}_j$ at various sites j at time t after a particle was added to an empty T-V model at site 0 with transverse contraction. A unit cell comprising two sites is assumed and the expectation values are averaged over both sites.

site j	$\langle \hat{n}_j(t) \rangle$
0	$\dfrac{1}{2}\left(\dfrac{\langle L|\mathcal{T}_{1O}'\mathcal{T}_2|R\rangle}{\langle L|\mathcal{T}_1'\mathcal{T}_2|R\rangle} + \dfrac{\langle L|\mathcal{T}_1\mathcal{T}_{2O}'|R\rangle}{\langle L|\mathcal{T}_1\mathcal{T}_2'|R\rangle} \right)$
1	$\dfrac{1}{2}\left(\dfrac{\langle L|\mathcal{T}_1'\mathcal{T}_{2O}|R\rangle}{\langle L|\mathcal{T}_1'\mathcal{T}_2|R\rangle} + \dfrac{\langle L|\mathcal{T}_1\mathcal{T}_2'\mathcal{T}_{1O}\mathcal{T}_2|R\rangle}{\lambda\,\langle L|\mathcal{T}_1\mathcal{T}_2'|R\rangle} \right)$
2	$\dfrac{1}{2}\left(\dfrac{\langle L|\mathcal{T}_1'\mathcal{T}_2\mathcal{T}_{1O}\mathcal{T}_2|R\rangle}{\lambda\,\langle L|\mathcal{T}_1'\mathcal{T}_2|R\rangle} + \dfrac{\langle L|\mathcal{T}_1\mathcal{T}_2'\mathcal{T}_1\mathcal{T}_{2O}|R\rangle}{\lambda\,\langle L|\mathcal{T}_1\mathcal{T}_2'|R\rangle} \right)$
3	$\dfrac{1}{2}\left(\dfrac{\langle L|\mathcal{T}_1'\mathcal{T}_2\mathcal{T}_1\mathcal{T}_{2O}|R\rangle}{\lambda\,\langle L|\mathcal{T}_1'\mathcal{T}_2|R\rangle} + \dfrac{\langle L|\mathcal{T}_1\mathcal{T}_2'\mathcal{T}_1\mathcal{T}_2\mathcal{T}_{1O}\mathcal{T}_2|R\rangle}{\lambda^2\,\langle L|\mathcal{T}_1\mathcal{T}_2'|R\rangle} \right)$
-1	$\dfrac{1}{2}\left(\dfrac{\langle L|\mathcal{T}_1\mathcal{T}_{2O}\mathcal{T}_1'\mathcal{T}_2|R\rangle}{\langle L|\mathcal{T}_1'\mathcal{T}_2|R\rangle} + \dfrac{\langle L|\mathcal{T}_{1O}\mathcal{T}_2'|R\rangle}{\langle L|\mathcal{T}_1\mathcal{T}_2'|R\rangle} \right)$
-2	$\dfrac{1}{2}\left(\dfrac{\langle L|\mathcal{T}_{1O}\mathcal{T}_2\mathcal{T}_1'\mathcal{T}_2|R\rangle}{\lambda\,\langle L|\mathcal{T}_1'\mathcal{T}_2|R\rangle} + \dfrac{\langle L|\mathcal{T}_1\mathcal{T}_{2O}\mathcal{T}_1\mathcal{T}_2'|R\rangle}{\lambda\,\langle L|\mathcal{T}_1\mathcal{T}_2'|R\rangle} \right)$

discussed in Section 4.11.3, the network must always contain an integer number of unit cells (because $\langle L|$ and $|R\rangle$ are the eigenvectors of the full unit cell). Expressions for the sites in the vicinity of site 0, already including the average over both sites in the unit cell (see Section 4.11.3) are given in Table 6.1.

For $c^\dagger$ acting on a particular site in the unit cell, the denominator is always the same apart from additional factors λ and therefore must be calculated only once. The networks containing two transverse operators (e.g. the denominators) can be contracted exactly from bottom to top, but with more operators this operation becomes inefficient and we contract the networks from the left and right instead, applying each column to $\langle L|$ or $|R\rangle$ with the zip-up algorithm (see Section 4.6.1) until only the column with the observable is left. Note that it is important to keep this column explicitly in order to measure expectation values at different times as explained in Section 4.11.3 (see e.g. Figure 4.30).

When measuring at sites to the right or left of site 0, already contracted parts of the network can be stored after each step and reused for the next site. As a specific example, consider the measurement of the particle density at sites $1, 2, \ldots$ with $c^\dagger$ acting on the left site in the unit cell (left terms in Table 6.1). For site 1, we compute $\langle L|\mathcal{T}_1' =: \langle L^{(1)}|$ with the zip-up algorithm and obtain the expectation value by contracting $\langle L^{(1)}|\mathcal{T}_{2O}|R\rangle$. Then we apply $\mathcal{T}_2$ to the previously calculated $\langle L^{(1)}|$ giving $\langle L^{(2)}| := \langle L|\mathcal{T}_1'\mathcal{T}_2$ and evaluate $\langle L^{(2)}|\mathcal{T}_{1O}\mathcal{T}_2|R\rangle$ for the expectation value at site 2. If, additionally, $\mathcal{T}_2|R\rangle$ is computed once in advance, we can reduce all numerators of the expectation values at the sites to the right of site 0 (which for the moment is chosen to be the left site in the unit cell) to simple MPS-MPO-MPS contractions. For the left sites $-1, -2, \ldots$ and the cases where the particle is added at the right site of the unit cell (i.e. the right terms in Table 6.1), we proceed analogously.
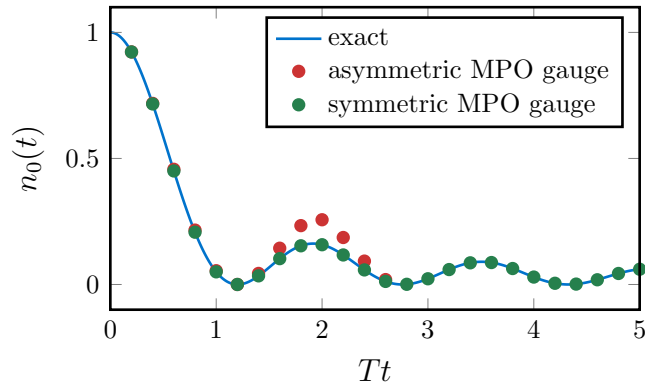
Figure 6.7. Comparison of the results with symmetrically and asymmetrically gauged time-evolution MPOs. The plot shows the particle density at a site in an infinite, empty T-V model after a single particle is inserted at this site. All time evolutions have been done with a second-order Trotter decomposition with a time step of $\tau = 0.01\,T^{-1}$ up to the time where the corresponding marker is placed. As a reference, the exact solution (D.3) is shown along with the numerical results. The points for the asymmetric gauge stop at $t = 2.6\,T^{-1}$ because for larger times, the overlap is too small to be represented by a floating-point number.

In Section 6.1.2, we observed extremely small overlaps of the eigenvectors $\langle L|R\rangle$ in the case of an asymmetric gauge of the time-evolution MPO. To confirm that this can lead to inaccurate results, we show the particle density at site 0 for symmetric and asymmetric MPO gauges in Figure 6.7. Indeed, the result obtained with asymmetrically gauged MPOs deviates strongly from the exact result starting approximately at time $t = 1.5\,T^{-1}$, where the overlap is of the order of 10^{-180} (see Figure 6.3). The discarded weight during TM-DMRG is kept below 10^{-12} in both cases.
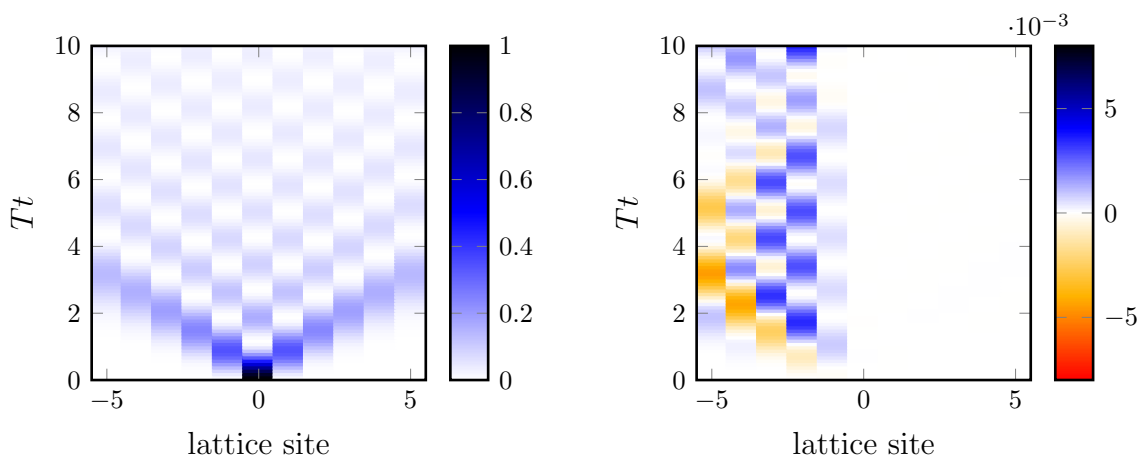

Figure 6.8. Single particle propagation with transverse contraction. Left: Particle density n in the infinite T-V model after a single particle was added at site 0. Right: Absolute error $n - n^{(\mathrm{ex})}$ with respect to the exact solution obtained from (D.3). At the sites $0 - 5$, the errors are of the order of 10^{-5}.

Figure 6.8 shows the results for the time-dependent particle density at the sites around site 0 and the error compared to the exact solution (D.3). The time evolution MPO for this

simulation was obtained from a second-order Trotter decomposition with a time step of $\tau = 0.02\, T^{-1}$ (for a comparison of the accuracy of the Trotter and W^{I} approximations see Section 6.2). During the computation of the eigenvectors with TM-DMRG, the transverse bond dimension was set such that the discarded weight stays below $w_{\max} = 10^{-12}$, leading to $\chi_{\max} = 196$ in the left eigenvector and $\chi_{\max} = 209$ in the right one. For the final measurement process the maximum transverse bond dimension was set to $\chi_{\max} = 600$.

The deviation from the exact solution (Figure 6.8 right) is much larger for the sites left of the central site 0. A closer examination of the discarded weights at each step of the measurement process shows that the main sources of this error are the computation of $\mathcal{T}_1'(\mathcal{T}_2\,|R\rangle)$ and the repeated applications of $\mathcal{T}_1$ and $\mathcal{T}_2$ to this product with the zip-up algorithm (see Table 6.1). Apparently, these steps need much higher transverse bond dimensions than the other similar contractions (e.g. for the right part). In Figure 6.9, the error at the site -2 is plotted for different transverse bond dimensions during the final contraction of the remaining network, which indeed shows that the results converge with increasing transverse bond dimension during the final contraction.
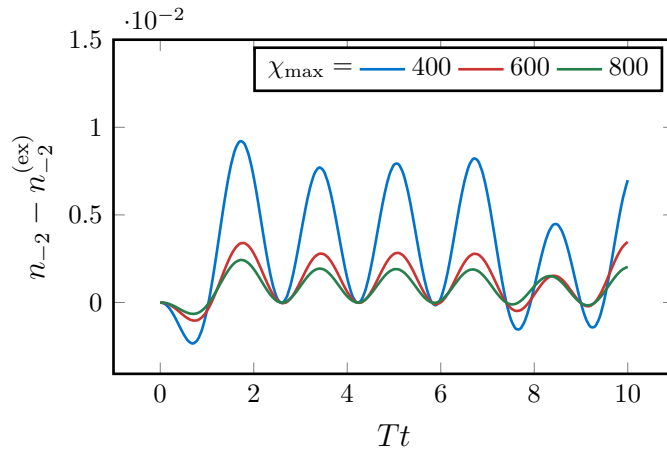

Figure 6.9. Absolute error of the simulated particle density at the site -2 after a particle was added to an empty infinite system at site 0. The simulation was done with the same eigenvectors but various bond dimensions $\chi_{\max}$ during the final contraction.

6.1.4. Folding

We repeated the calculation of the particle density at site 0 (where the particle is inserted at time 0) with the transfer matrix folded as described in Section 4.11.4. The results as well as the deviation from the exact solution are shown for various bond dimensions in Figure 6.10.

Without folding (see previous section, Figure 6.8), the transverse bond dimension required to keep the discarded weight below 10^{-12} was approximately 200. Since the bond dimension of an MPO formed from Trotter gates in the present case is 4 (see Section 4.8.2), according to the considerations in Section 4.11.4 the transverse bond dimension should be divided by $4/\sqrt[3]{2} \approx 3.2$ when using the folded transfer matrix to obtain a similar number of floating-point operations during the eigenvector search. However, this is based on the
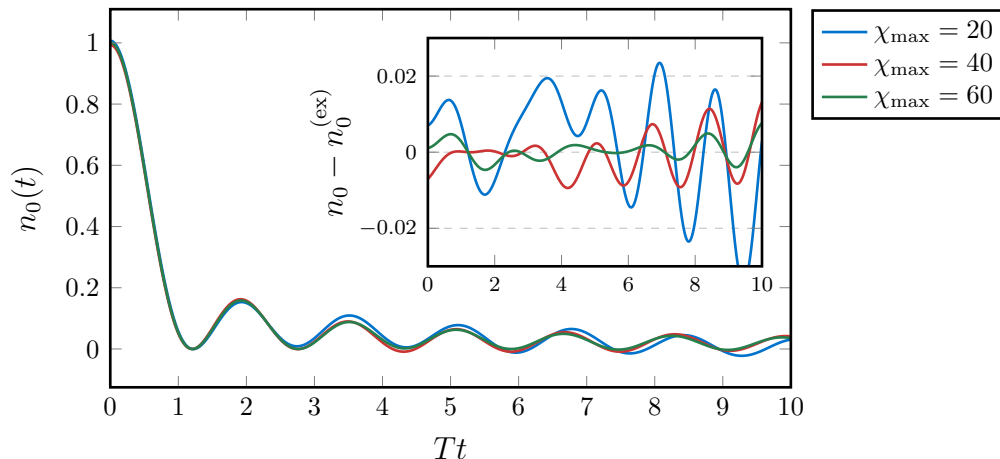
Figure 6.10. Single particle propagation with folding: Particle density at some site in the infinite, empty T-V model after a particle was added at that site, calculated with the transverse folding method with several transverse bond dimensions χ_{max} during TM-DMRG. The time evolution MPO is created from a second-order Trotter approximation with time step $\tau = 0.02\,T^{-1}$. Inset: Deviation from the exact result obtained from (D.3).

assumption that the matrix dimension is the same at each transverse bond, which is in general not the case if the matrices are truncated up to a certain discarded weight. Besides, the influence of the quantum number sectors was not taken into account in Section 4.11.4, although this can dramatically change the computational effort because the χ^3 scaling then only applies to each block separately. If the block sizes change due to the folding, the scaling may thus also change.

For the present case, we observe that the folding algorithm with a transverse bond dimension of 60 already requires considerably more CPU resources (by a factor of almost 10) than the transverse contraction without folding with the settings used in Section 6.1.3 ($\chi \approx 200$). Yet, the error of the folding algorithm with $\chi = 60$ is of the order of 10^{-2}, while the error at site 0 in the previous section without folding (see Figure 6.8) is of the order of 10^{-5}.

Thus, for the problem of a single particle in a T-V model, the folding method as implemented here seems not to provide any advantage over the simple transverse contraction without folding. However, a significant speedup of the folding method (also compared to the ordinary transverse contraction) could probably be achieved by using single-site TM-DMRG instead of the two-site version. This is discussed in more detail in Section s 6.2.5 and 6.2.6. It is possible that the folding method then gives similarly accurate (or even better) results than the transverse approach without folding at equal computational effort.

6.2. Nearest-Neighbor Occupancy with Pulse

Now the transverse contraction method is applied to the measurement of the nearest-neighbor occupancy during and after an electromagnetic pulse, i.e. to the problem treated

in Section 5.2.

The model under consideration is the T-V model with $V = 6\,T$ at half filling, described by the Hamiltonian (6.1). Like in Section 5.2, a global pulse with the shape (5.4) is applied to the system by means of the Peierls substitution (see Section 2.2). In the present section we use a pulse centered at $t_0 = 3\,T^{-1}$ with width $\sigma = 1\,T^{-1}$ and frequency $\Omega = 3\,T$. How exactly the pulse is taken into account is described in Section 6.2.1.

First, the ground state of the model is calculated with iDMRG (see Section 4.10.1). We use the two-site version of the algorithm and perform 300 steps (such that the final system size is 600 sites). For the iDMRG algorithm, we need the Hamiltonian of the T-V model represented as an MPO, which was already given in (6.2). A comparison of various bond dimension limits during iDMRG will be made in Section 6.2.3.

The ground state obtained from the iDMRG calculation is then cast into right-canonical form and normalized as described in Section 4.10.2. It is not important for the transverse contraction method whether the initial state has special orthogonality properties, but the orthogonalization must be done anyway to normalize the state and it allows measurements of local observables, which can be useful to check for convergence of observables other than the energy.

6.2.1. Incorporation of the Global Quench

For the time evolution including the pulse, the Peierls substitution must be employed while setting up the transfer matrix. As in Section 5.2, we neglect the resulting explicit time dependence of the Hamiltonian during a single time step and use a time evolution operator according to (5.5) for each step. For both, second-order Trotter gates and the second-order W^{I}-approximation, the rest is straightforward: Either the time evolution operator for each time step is decomposed into Trotter gates, from which the MPO is formed by SVD (see Section 4.8.2 and Section 6.1.2), or the W^{I}-matrices are built as in (6.5), where in both cases the modified hopping integrals T from the Peierls substitution (2.24) are used. In all cases we choose a symmetric gauge for the MPOs (see Section 6.1.2, page 96). As already described in Section 6.1, the second-order approximations require two different MPOs for one time step. In the spirit of (5.5), we use $\hat{H}(t)$ at the beginning of the full time step for both half steps.

Apart from the time-dependent Hamiltonian and the non-trivial initial state, the transfer matrix is built exactly as in Section 6.1.1. Here, the unit cell consisting of two sites is necessary in any case, because the ground state is obtained from two-site iDMRG and therefore consists of two distinct matrices for adjacent sites. In principle, there is an additional freedom in choosing which of the two tensors in the MPO unit cell is applied to which site in the MPS unit cell. However, when using the W^{I}-approximation, all MPO tensors are equal and in the case of Trotter gates this corresponds to choosing whether the even or odd gates are applied first, which is an arbitrary choice anyway and does not have any consequences within the accuracy of the approximation.

6.2.2. Measurement

The measurement of the nearest-neighbor occupancy per site in the thermodynamic limit

$$\frac{\mathcal{N}}{L} = \left\langle (\hat{n}_i - \tfrac{1}{2})(\hat{n}_{i+1} - \tfrac{1}{2}) \right\rangle \tag{6.7}$$

is done exactly as shown in Figure 4.31, where the operators both correspond to the occupation number operator $\hat{n}_i$ for the respective site. While the network containing only one unit cell, $\langle L | \mathcal{T}_{1O} \mathcal{T}_{2O} | R \rangle$, is contracted exactly from bottom to top, the larger network $\langle L | \mathcal{T}_1 \mathcal{T}_{2O} \mathcal{T}_{1O} \mathcal{T}_2 | R \rangle$ is contracted approximately in steps: First the leftmost and rightmost transfer matrix columns are applied to $\langle L |$ and $| R \rangle$ with the zip-up algorithm (see Section 4.6.1), yielding new transverse MPS $\langle L' |$ and $| R' \rangle$, and then the remaining network $\langle L' | \mathcal{T}_{2O} \mathcal{T}_{1O} | R' \rangle$ is evaluated exactly.

As explained in Section 4.11.3, expectation values at earlier times are measured with the same eigenvectors by shifting the observables $\hat{n}_i$ in time direction in the network.

6.2.3. Influence of Various Settings on the Results

Comparison of MPO Approximations

Figure 6.11 shows results for various combinations of time step and MPO type (second-order Trotter decomposition or second-order W^I-approximation). For comparison, the figure also contains the nearest-neighbor occupancy in the center of a large system obtained from TEBD. The TEBD results are converged in system size towards the thermodynamic limit as well as with respect to the time step and maximum discarded weight (up to the precision relevant for the following figures).

Concerning the accuracy of the results, the Trotter decomposition clearly outperforms the W^I-approximation at equal time steps τ and since for the T-V model with local dimension $d = 2$, the MPO formed from Trotter gates has the same bond dimension as the W^I-MPO (leading to similar computational effort), in the calculations following, we will always use the second-order Trotter approximation (unless explicitly mentioned otherwise). Note, furthermore, that the W^I-approximation does not preserve the unitarity of the time evolution operator (see Section 4.8.2, page 55) and therefore an additional error arises from the forward and backward evolution to evaluate earlier time steps (see Section 4.11.3).

If one wants to incorporate longer-range interactions, the W^I-approximation is still interesting despite the advantages of MPOs formed from Trotter gates. Concerning Trotter gates, next-nearest neighbor terms require either a much larger number of gates (when using swap gates), leading to a larger number of MPOs, or three-site gates, which lead to a squared bond dimension of the MPO (because there are two bonds between adjacent sites after the gates have been decomposed). With the W^I-approximation, the required bond dimension increases by 1 when the range of an interaction is increased by one lattice site [10, p. 61]. For the extended T-V model with next-nearest neighbor hopping and density interaction, the MPOs from Trotter gates would thus have a bond dimension of $4^2 = 16$ compared to $4 + 3 = 7$ for the W^I-MPO.
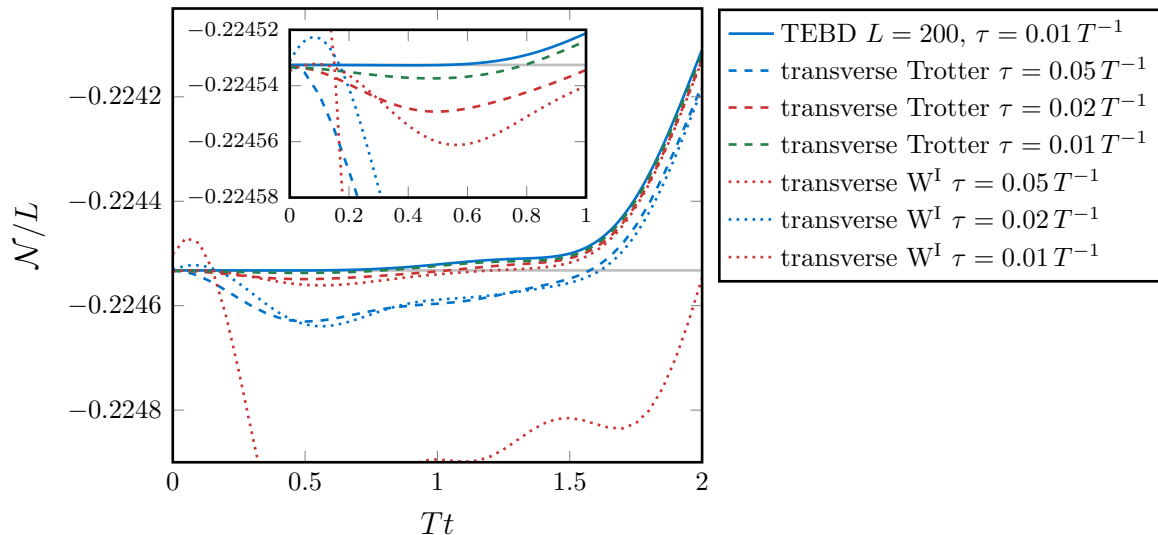
Figure 6.11. Nearest-neighbor occupancy per site in the T-V model during a pulse with amplitude $A_0 = 0.2$, calculated with TEBD at the center of a large system and with transverse contraction for an infinite system. All approximations of the time evolution operator are accurate up to second order in the time step τ. The gray line shows the exact result for the ground state double occupancy as obtained from (3.13). Inset: Zoom into the range $T\tau = [0, 1]$ showing a smaller section of the y-axis. The CPU times are approximately equal for the Trotter and W^I-approximations ($\sim 10\,000\,\text{s}$ for $\tau = 0.05\,T^{-1}$, $\sim 17\,000\,\text{s}$ for $\tau = 0.02\,T^{-1}$ and $\sim 30\,000\,\text{s}$ for $\tau = 0.01\,T^{-1}$).

Although there is still a visible difference between the results for time steps $\tau = 0.02\,T^{-1}$ and $0.01\,T^{-1}$ in Figure 6.11, the former is used for the further simulations, because a large number of time steps is computationally expensive with the transverse contraction method and the loss in accuracy seems acceptable.

Comparison of Algorithms for the Eigenvector Search

In the first papers dealing with the transverse contraction approach [15, 16], the authors proposed the power method for finding the eigenvectors $\langle L|$ and $|R\rangle$ by repeated application of the transfer matrix to an arbitrary initial MPS. In Figure 6.12, results obtained with this method are compared for several transverse bond dimensions during the application of the transfer matrix. Each data point corresponds to a separate calculation of the eigenvectors for the respective number of time steps.

Even for high bond dimensions, we observe significant errors already at short times, while the TM-DMRG method (see Section 4.11.2) requires bond dimensions of less than 100 to reach discarded weights below 10^{-12} at these times. TM-DMRG converges after very few sweeps (approximately 10 sweeps for convergence up to 10 digits in the eigenvalue at the present time scales) and for the power method 30 iterations seem a good choice to attain convergence in all cases. Concerning the computational effort, already for $\chi_{\max} = 100$ the power method with 30 iterations required more CPU time than TM-DMRG with 20 sweeps (and a maximum discarded weight $w_{\max} = 10^{-12}$, leading to transverse bond dimensions of about 100) for the same total time. Thus, we can conclude that the power method is not suitable for the present problem.
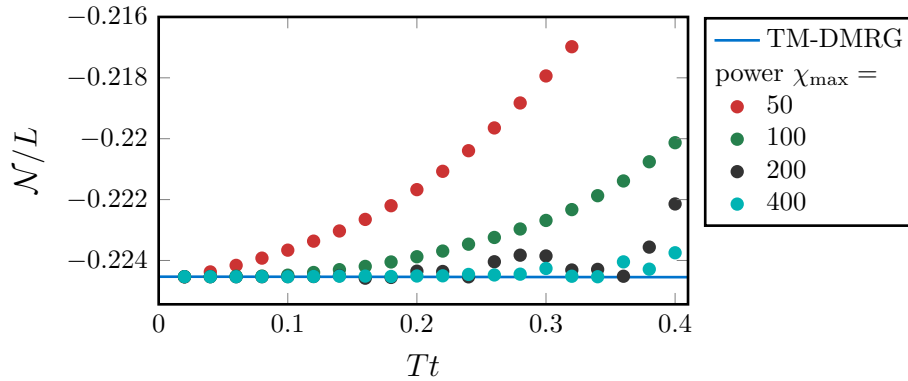
Figure 6.12. Comparison of TM-DMRG with 20 sweeps and the power method with 30 iterations for the T-V model exposed to an electromagnetic pulse: Nearest-neighbor occupancy per site during a pulse with amplitude $A_0 = 0.2$, calculated with transverse contraction using the power method with various transverse bond dimensions χ_{max}. As a reference, the result obtained with TM-DMRG is also shown. All calculations were done with a second-order Trotter approximation of the time evolution operator with time step $\tau = 0.02\,T^{-1}$. The change in time of the TM-DMRG result is not visible due to the scale of the y-axis.

Accuracy of the Ground State

Apart from the truncation during the search for the dominant eigenvectors, the ground state is another potential source of error. In Figure 6.13, the time evolution of the nearest-neighbor occupancy with a second-order Trotter decomposition and a time step $\tau = 0.02\,T^{-1}$ is shown for different bond dimensions χ_g during the ground state search with iDMRG. A matrix dimension of $\chi_g = 20$ already gives very good results.
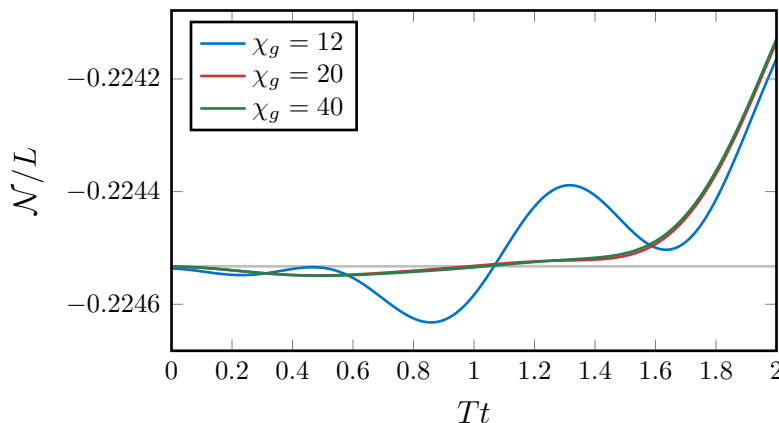

Figure 6.13. Nearest-neighbor occupancy per site in the infinite T-V model during a pulse with amplitude $A_0 = 0.2$, calculated with transverse contraction using ground states with various bond dimensions χ_g. All calculations were done with a second-order Trotter time evolution with time step $\tau = 0.02\,T^{-1}$. The gray line shows the exact result for the ground state double occupancy as obtained from (3.13).

6.2.4. Limits of Time Evolution by Transverse Contraction

Now the question arises how far we can go with the time evolution. Since truncation errors with the transverse contraction method manifest themselves throughout all time steps (unlike in conventional algorithms like TEBD where the errors accumulate towards later times), the quality of a longer time evolution can be assessed by comparing it with a shorter one in their common time range. With a transverse bond dimension of $\chi_{\max} = 400$ for the eigenvector search with TM-DMRG, it turns out that significant deviations start to occur when evolving to times of about $5\,T^{-1}$ (see Figure 6.14), where the discarded weight grows to about 10^{-9} (for the shorter times shown the maximum transverse bond dimension was not reached with $w_{\max} = 10^{-12}$). Although at $t_{\max} = 6\,T^{-1}$ (discarded weight $w \approx 5 \cdot 10^{-8}$) the quantitative deviations are already large, the qualitative behavior of the true solution is still captured.
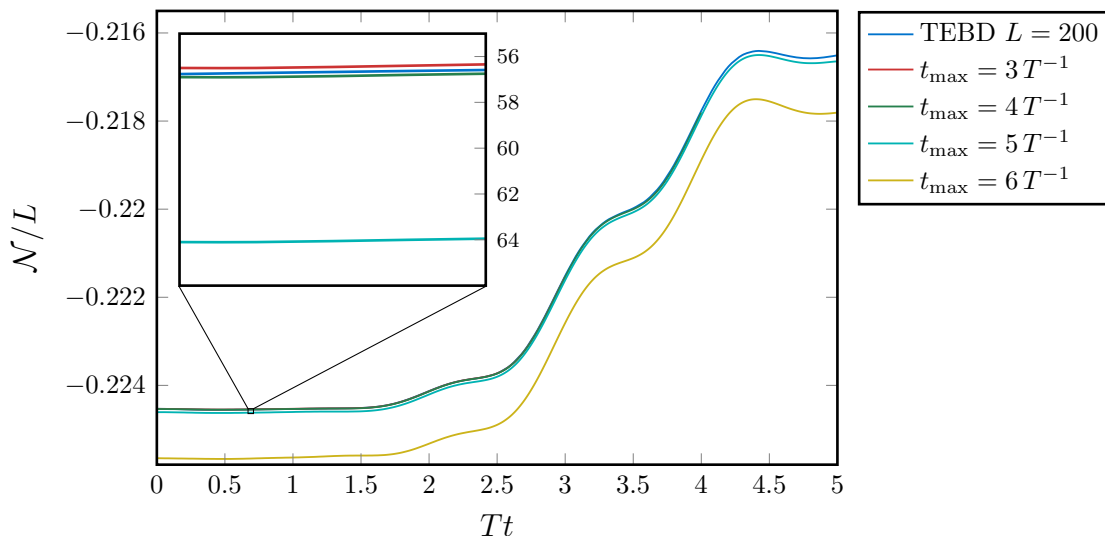

Figure 6.14. Nearest-neighbor occupancy per site in the infinite T-V model with $V = 6$ during a pulse with amplitude $A_0 = 0.2$, calculated with transverse contraction for several total times $t_{\max}$. All calculations were done with a second-order Trotter time evolution with time step $\tau = 0.02\,T^{-1}$ and a maximum transverse bond dimension of $\chi_{\max} = 400$ during TM-DMRG. For comparison, the nearest-neighbor occupancy in the center of a system with 200 sites, obtained from a TEBD calculation using a second-order Trotter decomposition and a time step of $\tau = 0.01\,T^{-1}$, is also shown. The y-axis in the inset is labeled with the additional digits after the value given on the main y-axis.

On the time scales reachable with the transverse contraction method, the phenomena discussed in Section 5.2 and in particular impact ionization cannot be observed. Therefore, the transverse approach is not suitable for the investigation of such processes. TEBD on large systems (e.g. $L = 200$ as used here for comparison) reaches similar times before the bond dimensions become too large (see also Section 6.2.5, page 112).

6.2.5. Entanglement in Eigenvectors

In conventional MPS-based algorithms, the bipartite entanglement across the bonds of the system determines the bond dimensions required to accurately store the state in an MPS and is therefore crucial for the success of the method. When using the transverse approach, the entanglement across transverse bonds (in time direction) plays the same role, which makes it a valuable information for assessing the applicability of the method. Therefore, in this section we investigate various influences on the entanglement in the eigenvectors of the transfer matrix.

The entanglement in the right eigenvector for the different approximations of the time evolution operator (second-order Trotter decomposition, second-order W^I approximation) and various time steps is plotted in Figure 6.15. Since the entanglement appears to be symmetric, only the first half (i.e. the "forward-time" part) of the eigenvector is shown. Due to the symmetric gauge of both the MPO and the ground state, the entanglement is approximately equal in both eigenvectors and it is sufficient to consider the right one. Obviously, neither the time step nor the type of the time evolution MPO has a significant influence on the entanglement in the eigenvectors.
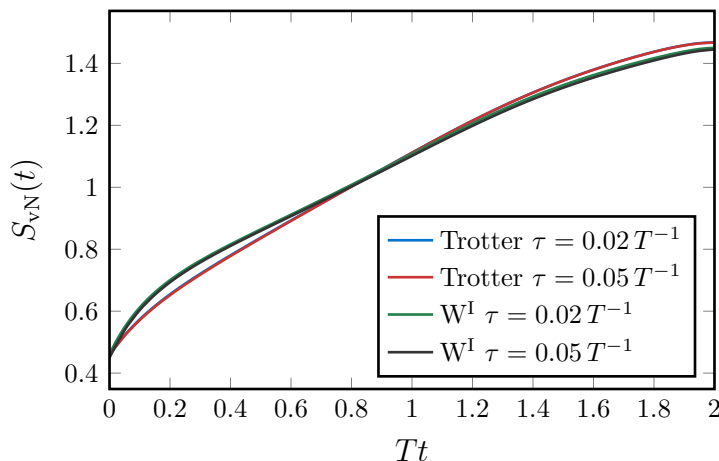

Figure 6.15. Von Neumann entanglement entropy across the forward-time bonds in the right eigenvector of the transfer matrix for a time evolution up to $t_{\max} = 2\,T^{-1}$ with different second-order approximations of the time-evolution operator and different time steps. The pulse with an amplitude $A_0 = 0.2$ is centered around $t_0 = 3\,T^{-1}$ with width $\sigma = T^{-1}$ and therefore has little influence in this range. In all calculations, the discarded weight during TM-DMRG was kept below 10^{-12} by adjusting the transverse bond dimensions. The green and black curves as well as the blue and red ones are on top of each other.

Figure 6.16 again shows the entanglement in the first half of the right eigenvector, but for various total times. We see a linear dependence of the maximum entanglement on the total time. When using TEBD, the entanglement also grows approximately linearly with time during the pulse and the right plot in Figure 6.16 shows that for the parameters used here, the scaling of the entanglement with time is considerably better for TEBD than for transverse contraction.

Müller-Hermes et al. [16] used a simple toy model to understand the entanglement structure in the network, which also led to linear scaling of the entanglement with time.

Although the insights gained from the toy model are probably not fully applicable to the much more complex model used here, the linear scaling is reproduced and the fact that the entanglement depends on the total time but not on the time step at least confirms that the entanglement in time direction has a physical meaning and is not merely a result of the numerics.
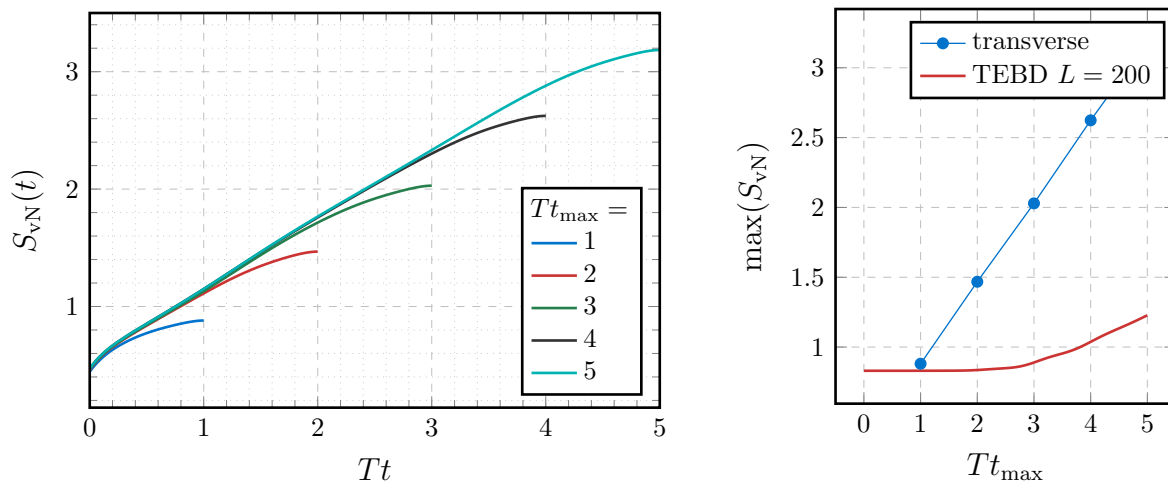

Figure 6.16. Left: Von Neumann entanglement entropy across the forward-time bonds in the right eigenvector of the transfer matrix for time evolutions up to several total times $t_{\max}$ with a second-order Trotter approximation of the time-evolution operator and a time step of $\tau = 0.02 \, T^{-1}$. The system is exposed to a pulse with an amplitude $A_0 = 0.2$ centered around $t_0 = 3 \, T^{-1}$ with width $\sigma = T^{-1}$. The discarded weight during TM-DMRG was kept below 10^{-12} for all calculations except for $t_{\max} = 5 \, T^{-1}$, where it reached about 10^{-9} with a transverse bond dimension of 400. Right: Maximum of the entanglement entropy plotted against the total time, compared to the maximum entanglement during a TEBD simulation with 200 sites and the same parameters.

Next, we investigate the dependence of the entanglement on the intensity of the pulse. Figure 6.17 shows the entanglement in the first half of the right eigenvector for various pulse intensities. Although the time evolution extends to times beyond the maximum of the pulse at $t_0 = 3 \, T^{-1}$, namely $t_{\max} = 4 \, T^{-1}$, the entanglement hardly changes with the amplitude of the pulse. Even in the case $A_0 = 0$, which corresponds to a simple time evolution of the ground state with the unperturbed Hamiltonian, the entanglement stays the same. Hence, the main source of entanglement in the transverse eigenvectors appears to be the time evolution by itself, regardless of the particular Hamiltonian. This is fundamentally different from traditional MPS time evolution methods such as TEBD, where the perturbation by the pulse is the only source of entanglement growth and without it the entanglement would stay the same for all times (see Figure 6.16).

This means that the superior scaling of the entanglement in TEBD compared to transverse contraction, which was observed in Figure 6.16 (right) for the case $A_0 = 0.2$, does not necessarily apply to cases with higher pulse amplitudes. In Figure 6.18, the maximum entanglement in the transverse eigenvectors for various total times is compared to the maximum entanglement during a TEBD calculation (like in Figure 6.16 on the right) for a pulse amplitude of $A_0 = 0.8$. In this case the scaling of the entanglement with total

time is similar for both methods and it can be assumed that for even higher amplitudes, the transverse approach outperforms TEBD concerning the entanglement.

Apart from the entanglement determining the required transverse bond dimension, of course, an additional dependence of the CPU time and memory on the total time arises from the fact that the number of tensors in the transfer matrix (and thus the number of transverse "sites" for TM-DMRG) is proportional to the number of time steps. Concerning the CPU time, however, this is also true for a conventional time evolution method such as TEBD.
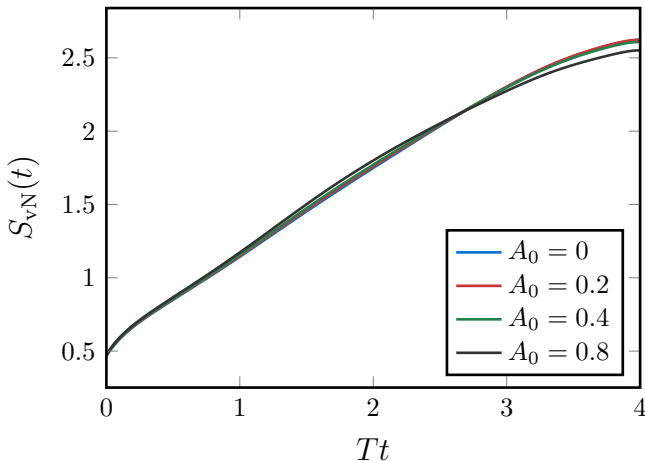
Figure 6.17. Von Neumann entanglement entropy across the forward-time bonds in the right eigenvector of the transfer matrix for a time evolution up to $t_{\mathrm{max}} = 4\, T^{-1}$ with several pulse amplitudes A_0. In all cases, the discarded weight during TM-DMRG was of the order of 10^{-12} with a maximum transverse bond dimension of 400.
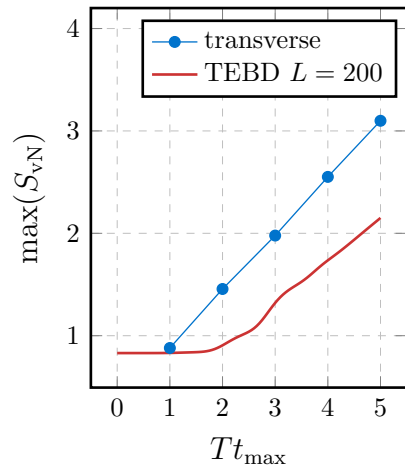
Figure 6.18. Maximum entanglement entropy for the pulse amplitude $A_0 = 0.8$, plotted against the total time, compared to the maximum entanglement in a TEBD simulation with 200 sites and the same parameters.

With TEBD, the reachable time depends on the amplitude of the pulse because of the strong influence of the amplitude on the entanglement (see Figures 6.16 and 6.18). However, due to the exponential growth of bond dimensions, the time evolution is limited to short times even for low amplitudes and the limit for the TEBD calculations with 200 sites is similar to that of the transverse method. At $t = 5\, T^{-1}$, the bond dimension required to keep the discarded weight below 10^{-9} in TEBD was approximately 300 with $A_0 = 0.2$ (Figure 6.16) and 400 for $A_0 = 0.8$ (Figure 6.18). These values are still manageable, but already large and we can assume that the exponential growth will let the bond dimensions become too large at times shortly after $5\, T^{-1}$.

When comparing the entanglement during the TEBD calculations here to that obtained with TEBD on a small system in Section 5.2, the different area under the pulse envelope due to the different width σ must be taken into account. A width of $\sigma = T^{-1}$ here instead of $\sigma = 3\, T^{-1}$ in Section 5.2 means that only $\frac{1}{3}$ of the energy is absorbed at the same amplitude, which can influence the entanglement generated by the pulse.

A possibility to extend the time that can be reached with the transverse approach would

be to use single-site TM-DMRG instead of the two-site version, i.e. update one matrix at a time instead of two as described in Section 4.11.2. This would decrease the dimension of the effective transfer matrix (which is fed into the eigensolver) by a factor of the transverse local dimension D (which is the bond dimension of the time evolution MPO) and the SVDs to split the optimized two-site matrix would not be required. However, in the case of ordinary DMRG, the single-site algorithm gets stuck in local minima more easily (see Section 4.7) and this could also be the case for TM-DMRG. Besides, since the transverse bond dimensions grow exponentially with time, this would increase the reachable time only by a small amount.

6.2.6. Folding

If the network is folded before the computation of the eigenvectors (see Section 4.11.4), lower transverse bond dimensions must be chosen for the same computational effort due to the higher transverse local dimension. A transverse bond dimension of $\chi_{\max} = 60$ already leads to much longer CPU times (by a factor of ~ 2.5) than $\chi_{\max} = 400$ in the calculations without folding in the previous section. In Figure 6.19, we show the nearest-neighbor occupancy calculated with a folded network for several total times with the transverse bond dimensions $\chi_{\max} = 60$ and 80 during TM-DMRG, compared to the results obtained without folding for $t_{\max} = 4\,T^{-1}$.
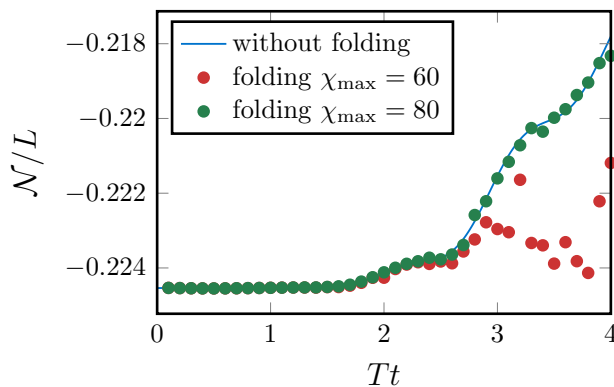

Figure 6.19. Nearest-neighbor occupancy per site in the infinite T-V model during a pulse with amplitude $A_0 = 0.2$, calculated with the transverse *folding* method for various total times (only the expectation value at the last time step is shown for each total time), compared to transverse contraction without folding (with maximum transverse bond dimension $\chi_{\max} = 400$). All calculations were done with a second-order Trotter time evolution with time step $\tau = 0.02\,T^{-1}$. The measured CPU times are $\sim 600\,000\,\text{s}$ for $\chi_{\max} = 60$ and $\sim 800\,000\,\text{s}$ for $\chi_{\max} = 80$.

Already for $\chi_{\max} = 80$, the results are reasonably accurate up to times $t = 4\,T^{-1}$, though visible deviations from the (apparently accurate, see Section 6.2.3) results without folding start to occur at $t \approx 2.5\,T^{-1}$. However, despite the much lower transverse bond dimension, the calculations with folding required considerably higher CPU times. This can be partly explained by the squared dimension of the transverse local Hilbert space due to the folding, but that only accounts for a factor $4/\sqrt[3]{2} \approx 3.2$ in the transverse bond dimension (see Section 4.11.4), i.e. we would expect to observe similar CPU times for $\chi_{\max} = 80$ with

folding as for $\chi_{\max} = 400$ without folding. That this is not the case was already observed and discussed for the single particle in Section 6.1.4.

The deviation could be partly due to differences in the entanglement structure in the transverse eigenvectors. Indeed, the entanglement seems to be more evenly distributed among the individual bonds in the folded transverse chain (Figure 6.20, left) than without folding (Figure 6.16, left). This leads to relatively high transverse bond dimensions throughout the MPS-represented eigenvectors of the folded transfer matrix, whereas without folding the entanglement concentrates at the center of the chain, allowing lower dimensions at transverse bonds closer to the edges.
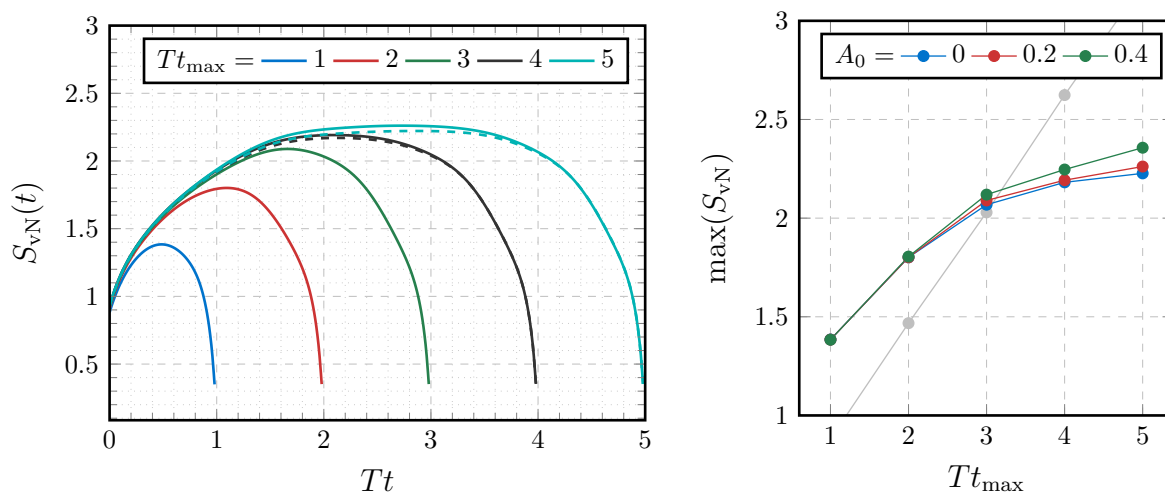

Figure 6.20. Left: Von Neumann entanglement entropy in the right eigenvector of the folded transfer matrix for time evolutions up to several total times $t_{\max}$ with a second-order Trotter approximation of the time-evolution operator and a time step of $\tau = 0.02\,T^{-1}$. The system is exposed to a pulse with an amplitude $A_0 = 0.2$ centered around $t_0 = 3\,T^{-1}$ with width $\sigma = T^{-1}$. In all calculations, the maximum transverse bond dimension during TM-DMRG was set to $\chi_{\max} = 80$, except for the two dashed curves showing the corresponding results for $\chi_{\max} = 60$. Right: Maximum of the entanglement entropy (with $\chi_{\max} = 80$) plotted against the total time for several pulse amplitudes A_0. For comparison, the maximum entanglement for the same parameters and $A_0 = 0.2$ without folding is shown in gray.

All curves in the left plot in Figure 6.20 (except for the dashed ones) were obtained with a maximum transverse bond dimension of 80. The dashed curves correspond to a maximum transverse bond dimension of 60, showing that at $t_{\max} = 4\,T^{-1}$ (and therefore certainly also for shorter times) the results are sufficiently converged in the bond dimension. The results for $t_{\max} = 5\,T^{-1}$ must still be treated with caution, because as there is still a significant difference in the maximum entanglement entropy between $\chi_{\max} = 60$ and 80, this calculation might not be fully converged.

The right plot in Figure 6.20 shows that the entanglement scaling with the total time appears to be considerably improved by folding the network. Even though it must be assumed that the points for $t_{\max} = 5\,T^{-1}$ are inaccurate, it is safe to say that the entanglement entropy does *not* scale linearly with $t_{\max}$. The data suggest a logarithmic scaling, which would lead to a polynomial (in the best case linear) scaling of the required transverse bond dimensions with time.

Due to the squared matrix dimensions after folding and the different entanglement distribution mentioned above, the transverse method without folding may be superior concerning CPU time even in cases where the maximum entanglement is higher than in the case with folding. But nevertheless, the additional folding step allows us to overcome the linear scaling of entanglement with total time and thus brings longer time scales within reach. The same improved scaling of the entanglement as compared to the transverse contraction without folding was also observed for the transverse-field Ising model and the XY model by Müller-Hermes et al. [16].

But despite the improved scaling, the transverse contraction method with folding does not reach longer time scales than without folding (see Section 6.2.4) for the present problem with the available computational resources and therefore it is not capable of producing reliable results on the time scales relevant for impact ionization.

Especially with folding, replacing two-site TM-DMRG with the single-site algorithm as suggested above could bring a crucial speedup, provided that single-site TM-DMRG converges properly. Due to the squared dimensions, a particularly large amount of computational time would be saved and this may considerably extend the reachable time because there is no exponential scaling of the transverse bond dimensions with time in this case.

6.3. Summary

As a first test for the transverse contraction method, the propagation of a single particle in an empty system described by the T-V model was simulated. A good agreement of the results with exact calculations was achieved.

It was observed that in the growing Hilbert space of transverse "sites" (actually time steps), the overlap of the left and right eigenvectors of the transfer matrix decreases exponentially with time and can become very small, leading to numerical problems. This overlap strongly depends on the gauge of the time-evolution MPO, where gauges with more symmetric matrices appear to be superior. A biorthonormalization procedure used in earlier works to avoid these problems has been abandoned due to issues with canceling subspaces, which might be alleviated with different initial states in future work.

Folding the network did not improve the results with a comparable computational effort in this case.

The transverse contraction method was then applied to the time-evolution of an infinite, translationally invariant T-V model at half filling, exposed to an electromagnetic pulse modeled with the Peierls substitution (i.e. the problem treated in Chapter 5). The ground state was calculated with iDMRG and the time-evolution MPO was obtained from a second-order Trotter decomposition or the second-order W^I-approximation. After computing the left and right eigenvectors of the transfer matrix with TM-DMRG or the power method, the nearest-neighbor occupancy in the thermodynamic limit was measured.

A comparison of the different methods for the single steps of the algorithm showed that the time-evolution MPO formed from Trotter gates outperforms the W^I-approximation in terms of accuracy at similar CPU time and that TM-DMRG for finding the eigenvectors leads to accurate results for much longer times than the power method, which shows significant deviations already at very short times even with large transverse bond dimensions.

Using the second-order Trotter approximation for the time-evolution MPO and TM-DMRG for the eigenvector search, accurate results were obtained up to times around $t = 5\,T^{-1}$ with an already relatively high maximum transverse bond dimension of 400. Due to linear growth of the entanglement in the transverse eigenvectors with time, much longer timescales are beyond reach. Similar time scales were achieved with TEBD on a large system with 200 sites. Unlike in TEBD, however, the entanglement in the transverse approach depends only very weakly on the amplitude of the electromagnetic pulse.

With the additional folding step, the scaling of the entanglement with time is improved and looks logarithmic instead of linear. This leads to a polynomial scaling of the required transverse bond dimensions with time, which in principle allows longer time scales to be simulated. In the present case, however, no improvement was possible by folding the network, because the short times that were also reachable without folding already exhausted the available computational resources.

A possible improvement of the performance of the transverse contraction method (particularly with folding) compared to the implementation in the present thesis could be to use single-site TM-DMRG instead of the two-site algorithm.

7. Conclusion

In the extended T-V model of spinless fermions, impact ionization occurs in one dimension if the hopping integral for next-nearest neighbors is non-zero and this is also the case for hard-core bosons. On the other hand, there is no impact ionization in the non-integrable case with next-nearest neighbor Coulomb interaction but without next-nearest neighbor hopping. The geometry of the hopping parameters thus seems to play an important role in connection with impact ionization, which is consistent with previous results, while neither integrability nor fermionic behavior are a decisive factor of whether or not this phenomenon occurs.

The frequency dependence of impact ionization and Auger recombination is consistent with the idea of decaying and combining excitations, but unlike in the Hubbard model comparison with the single-particle density of states shows that the relevant excitations are not of single-particle type.

These insights may prove helpful for further theoretical research on the topic of impact ionization in strongly correlated materials.

Concerning the methods used for time-evolution with matrix product states, TEBD for large systems and transverse contraction in the thermodynamic limit are both restricted to short times for the problems considered in this thesis. In both cases the reason is linear growth of the relevant entanglement entropy with time, but while in TEBD this entanglement growth is entirely due to the pulse, with transverse contraction it also occurs without any perturbation of the system.

When working with the transverse contraction method, many potential sources of error arise and must be taken into account to assess the validity of the results. Already when setting up the transfer matrix, there can be errors in the initial state (e.g. from DMRG if it is a ground state) and in the time-evolution MPO (e.g. the Trotter error or the error of the W^I-approximation). The method used to obtain the eigenvectors of the transfer matrix will also have a certain error and a small overlap of the left and right eigenvectors can lead to numerical problems. Finally, the contraction of the network, which is left after replacing the translationally invariant parts with the eigenvectors, in general needs to be done approximately and also contributes an error.

With an additional folding step, the linear scaling of entanglement with time in the transverse contraction method can be overcome. Therefore, folding potentially allows longer time scales to be reached. Testing this with sufficient computational resources could be the subject of future research.

Appendix

A. Evaluation of $\nabla\varphi_j$ for the Peierls Substitution

In order to calculate the gradient of

$$\varphi_j(\boldsymbol{r}, t) := \int\limits_{\boldsymbol{R}_j}^{\boldsymbol{r}} \boldsymbol{A}(\boldsymbol{r}', t) \cdot \mathrm{d}\boldsymbol{r}',$$

which appears in Section 2.2, it is expedient to rewrite it in the parameter form

$$\varphi_j(\boldsymbol{r}, t) = \int\limits_0^1 \boldsymbol{A}\big(\boldsymbol{R}_j + \lambda(\boldsymbol{r} - \boldsymbol{R}_j), t\big) \cdot (\boldsymbol{r} - \boldsymbol{R}_j) \, \mathrm{d}\lambda \,.$$

The gradient can be exchanged with the integral, and using Einstein's summation convention we obtain

$$\nabla\varphi_j(\boldsymbol{r}, t) = \int\limits_0^1 \boldsymbol{e}_l \frac{\partial}{\partial x_l} A_m (x_m - (\boldsymbol{R}_j)_m) \, \mathrm{d}\lambda = \boldsymbol{e}_l \int\limits_0^1 \left(\frac{\partial A_m}{\partial x_l}(x_m - (\boldsymbol{R}_j)_m) + A_m \delta_{lm} \right) \mathrm{d}\lambda \,.$$

According to the chain rule, $\partial A_m/\partial x_l = \lambda\, \partial A_m/\partial \rho_l^{(j)}$ with $\boldsymbol{\rho}^{(j)} := \boldsymbol{R}_j + \lambda(\boldsymbol{r} - \boldsymbol{R}_j)$, and integrating the second term by parts yields

$$\nabla\varphi_j(\boldsymbol{r}, t) = \boldsymbol{e}_l \int\limits_0^1 \lambda \frac{\partial A_m}{\partial \rho_l^{(j)}}(x_m - (\boldsymbol{R}_j)_m) \, \mathrm{d}\lambda + \boldsymbol{A}\big(\boldsymbol{R}_j + \lambda(\boldsymbol{r} - \boldsymbol{R}_j), t\big)\lambda\big|_0^1 - \int\limits_0^1 \lambda \frac{\partial \boldsymbol{A}}{\partial \lambda} \, \mathrm{d}\lambda$$

$$= \boldsymbol{A}(\boldsymbol{r}, t) + \boldsymbol{e}_l \int\limits_0^1 \lambda \left(\frac{\partial A_m}{\partial \rho_l^{(j)}}(x_m - (\boldsymbol{R}_j)_m) - \frac{\partial A_l}{\partial \rho_m^{(j)}} \frac{\partial \rho_m^{(j)}}{\partial \lambda} \right) \mathrm{d}\lambda$$

$$= \boldsymbol{A}(\boldsymbol{r}, t) + \boldsymbol{e}_l \int\limits_0^1 \lambda \left(\frac{\partial A_m}{\partial \rho_l^{(j)}} - \frac{\partial A_l}{\partial \rho_m^{(j)}} \right)(x_m - (\boldsymbol{R}_j)_m) \, \mathrm{d}\lambda$$

$$= \boldsymbol{A}(\boldsymbol{r}, t) + \boldsymbol{e}_l \int\limits_0^1 \lambda \frac{\partial A_p}{\partial \rho_q^{(j)}}(\delta_{mp}\delta_{lq} - \delta_{lp}\delta_{mq})(x_m - (\boldsymbol{R}_j)_m) \, \mathrm{d}\lambda$$

$$= \boldsymbol{A}(\boldsymbol{r}, t) + \boldsymbol{e}_l \int\limits_0^1 \varepsilon_{mlk}\varepsilon_{pqk} \lambda \frac{\partial A_p}{\partial \rho_q^{(j)}}(x_m - (\boldsymbol{R}_j)_m) \, \mathrm{d}\lambda \,,$$

where δ_{ij} is the Kronecker delta and ε_{ijk} the Levi-Civita symbol. Thus, as a final result we obtain

$$\boldsymbol{\nabla}\varphi_j = \boldsymbol{A}(\boldsymbol{r},t) + \int_0^1 \lambda(\boldsymbol{r} - \boldsymbol{R}_j) \times \boldsymbol{B}\big(\boldsymbol{R}_j + \lambda(\boldsymbol{r} - \boldsymbol{R}_j), t\big)\,\mathrm{d}\lambda\,, \qquad (\text{A.1})$$

where $\boldsymbol{B} = \boldsymbol{\nabla} \times \boldsymbol{A}$ is the magnetic field.

B. Particle-Hole Symmetry of the T-V Model

In Section 3.2, the T-V model is introduced. If T is real, and a bipartition AB of the lattice exists such that sites of sublattice A only have neighbors of sublattice B and vice versa, then its Hamiltonian

$$\hat{H}_{\text{TV}} = \sum_{\langle ij\rangle} \left(-T c_i^\dagger c_j - T^* c_j^\dagger c_i + V \left(\hat{n}_i - \tfrac{1}{2}\right)\left(\hat{n}_j - \tfrac{1}{2}\right)\right)$$

is symmetric under exchange of particles and holes ($c_i \leftrightarrow c_i^\dagger$).

Proof. First consider the hopping part

$$\hat{T}(\{c_i\},\{c_i^\dagger\}) = -T \sum_{\langle ij\rangle} \left(c_i^\dagger c_j + c_j^\dagger c_i \right)\,.$$

Exchanging c and $c^\dagger$ operators results in

$$\hat{T}(\{c_i^\dagger\},\{c_i\}) = -T \sum_{\langle ij\rangle} \left(c_i c_j^\dagger + c_j c_i^\dagger \right) = -T \sum_{\langle ij\rangle}(2\delta_{ij} - c_j^\dagger c_i - c_i^\dagger c_j)$$

$$= T \sum_{\langle ij\rangle} \left(c_j^\dagger c_i + c_i^\dagger c_j \right)\,.$$

In order to recover the sign, we must carry out a basis transformation that changes the sign of all operators on one of the sublattices, e.g. $c_i \to -c_i$ for all $i \in A$. Each product of nearest neighbors then undergoes a sign change and the original sign of the hopping term is restored.

The interaction part

$$\hat{V}(\{c_i\},\{c_i^\dagger\}) = V \sum_{\langle ij\rangle} \left(c_i^\dagger c_i - \frac{1}{2}\right)\left(c_j^\dagger c_j - \frac{1}{2}\right)$$

is not changed by the canonical transformation, because $(\pm c_i^\dagger)(\pm c_i) = c_i^\dagger c_i$. Exchanging creation and annihilation operators here leads to

$$\hat{V}(\{c_i^\dagger\},\{c_i\}) = V \sum_{\langle ij\rangle} \left(c_i c_i^\dagger - \frac{1}{2}\right)\left(c_j c_j^\dagger - \frac{1}{2}\right)$$

$$= V \sum_{\langle ij\rangle} \left(\frac{1}{2} - c_i^\dagger c_i\right)\left(\frac{1}{2} - c_j^\dagger c_j\right) = \hat{V}(\{c_i\},\{c_i^\dagger\})\,.$$

Thus, both parts of the Hamiltonian are unchanged by the exchange $c_i \leftrightarrow c_i^\dagger$. $\qquad\square$

C. Proof for Jordan-Wigner Transformation

In Section 3.2.1, the equivalence of the one-dimensional T-V and XXZ models is shown using the Jordan-Wigner transformation. Starting from creation and annihilation operators $b_j^\dagger, b_j$ with the commutation relations

$$[b_i, b_j] = 0, \quad [b_i^\dagger, b_j] = (2b_i^\dagger b_i - 1)\delta_{ij},$$

the Jordan-Wigner transformation consists in the introduction of new operators

$$c_j = \exp\left(i\pi \sum_{n=1}^{j-1} b_n^\dagger b_n\right) b_j =: \exp(i\hat{\varphi}_j) b_j.$$

Here it will be proved that these operators fulfill fermionic anticommutation rules.

The anticommutation relations for these new operators are

$$
\begin{aligned}
\{c_i, c_j\} &= \{\exp(i\hat{\varphi}_i) b_i, \exp(i\hat{\varphi}_j) b_j\} = b_i \exp\left(i(\hat{\varphi}_i + \hat{\varphi}_j)\right) b_j + b_j \exp\left(i(\hat{\varphi}_i + \hat{\varphi}_j)\right) b_i, \\
\{c_i^\dagger, c_j\} &= \{b_i^\dagger \exp(-i\hat{\varphi}_i), \exp(i\hat{\varphi}_j) b_j\} = b_i^\dagger \exp\left(i(\hat{\varphi}_i - \hat{\varphi}_j)\right) b_j + b_j \exp\left(i(\hat{\varphi}_i - \hat{\varphi}_j)\right) b_i^\dagger .
\end{aligned}
$$

For $i = j$, the first anticommutator vanishes trivially and in the second one the phases cancel, leaving

$$\{c_i^\dagger, c_i\} = b_i^\dagger b_i + b_i b_i^\dagger = 2b_i^\dagger b_i - [b_i^\dagger, b_i] = 1 .$$

Assuming $i > j$ (for the second anticommutator the case $i < j$ can be obtained by taking the hermitian conjugate), the expressions can be simplified to

$$\exp\left(i(\hat{\varphi}_i + \hat{\varphi}_j)\right) = \exp\left(2\pi i \sum_{n=1}^{j-1} b_n^\dagger b_n + i\pi \sum_{n=j}^{i-1} b_n^\dagger b_n\right) = \exp\left(i\pi \sum_{n=j}^{i-1} b_n^\dagger b_n\right) ,$$

$$\exp\left(i(\hat{\varphi}_i - \hat{\varphi}_j)\right) = \exp\left(i\pi \sum_{n=j}^{i-1} b_n^\dagger b_n\right) .$$

Since the operator b_j to the right of the exponential annihilates any fermion that possibly existed at site j and to the left of the exponential forces the site to be occupied (because otherwise b_j destroys the whole state), the value of $b_j^\dagger b_j$ in the sum is fixed. The rest of the sum commutes with b_i and b_j and the anticommutators become

$$\{c_i, c_j\} = \exp\left(i\pi \sum_{n=j+1}^{i-1} b_n^\dagger b_n\right) (b_i b_j - b_j b_i) = \exp\left(i\pi \sum_{n=j+1}^{i-1} b_n^\dagger b_n\right) [b_i, b_j] = 0,$$

$$\{c_i^\dagger, c_j\} = \exp\left(i\pi \sum_{n=j+1}^{i-1} b_n^\dagger b_n\right) (b_i^\dagger b_j - b_j b_i^\dagger) = \exp\left(i\pi \sum_{n=j+1}^{i-1} b_n^\dagger b_n\right) [b_i^\dagger, b_j] = 0 .$$

Thus, summing up the results we have

$$\{c_i, c_j\} = 0, \quad \{c_i^\dagger, c_j\} = \delta_{ij},$$

which are the anticommutation relations of fermionic creation and annihilation operators.

D. Exact Solution for a Single Particle in a T-V Model

For only one particle in the system, the T-V model is equivalent to the tight-binding model and in this case it can be solved exactly. The exact results are used for comparison with the numerical results in Section 6.1.3.

The space of all states containing one particle is obviously spanned by the states $c_i^\dagger \left|0\right\rangle$ or, by transforming to a plane-wave basis, also by the set

$$\left|k\right\rangle = \frac{1}{\sqrt{L}} \sum_{l=1}^{L} \mathrm{e}^{\mathrm{i}kl} c_l^\dagger \left|0\right\rangle, \tag{D.1}$$

where $k = 2\pi n/L$, $n \in \mathbb{N}$. These vectors are eigenvectors of $\hat{H}$ with eigenvalues

$$E(k) = -(L/4 - 1)V + 2T\cos(k). \tag{D.2}$$

Since the Hamiltonian conserves the particle number, a system prepared in an initial state with one particle will remain in the subspace with one particle for all times. Therefore, we can describe the time evolution of such a state with the projection of the time evolution operator onto the one-particle subspace. Replacing the sum over k with an integral for small Δk this projection reads

$$\hat{U}_1(t) = \frac{L}{2\pi} \int_{-\pi}^{\pi} \mathrm{e}^{-\mathrm{i}E(k)t} \left|k\right\rangle\!\left\langle k\right| \mathrm{d}k\,.$$

Inserting (D.1) and (D.2) and neglecting the constant part of the latter (which only yields a global phase), we obtain

$$\hat{U}_1(t) = \frac{L}{2\pi} \sum_{l,m=1}^{L} \int_{-\pi}^{\pi} \mathrm{e}^{\mathrm{i}2Tt\cos(k)} \mathrm{e}^{\mathrm{i}k(l-m)} \mathrm{d}k \left|l\right\rangle\!\left\langle m\right| = \sum_{l,m=1}^{L} \mathrm{i}^{l-m} J_{l-m}(2Tt) \left|l\right\rangle\!\left\langle m\right|,$$

where $J_n(x)$ denotes the Bessel functions of the first kind. Using this expression to calculate the occupation of a certain site b at a time t after a particle was placed on a site a results in

$$n_b(t) = \left\langle 0\right| c_a \hat{U}_1(t)^\dagger \hat{n}_b \hat{U}_1(t) c_a^\dagger \left|0\right\rangle = J_{b-a}(2Tt)^2. \tag{D.3}$$

This result is exact only in the thermodynamic limit when $\Delta k \to 0$ and hence the replacement of the sum over k with an integral becomes exact.

E. Expectation Values in the Thermodynamic Limit with Transverse Contraction

In terms of the transfer matrix of the time-evolved state $\mathcal{T}$, the expectation value of a local observable in the translationally invariant system is given by

$$\left\langle \hat{O}(t)\right\rangle = \frac{\left\langle \psi(t)\middle|\hat{O}\middle|\psi(t)\right\rangle}{\left\langle \psi(t)\middle|\psi(t)\right\rangle} = \lim_{n\to\infty} \frac{\mathrm{tr}(\mathcal{T}^n \mathcal{T}_O \mathcal{T}^n)}{\mathrm{tr}(\mathcal{T}^{2n+1})}, \tag{E.1}$$

as explained in Section 4.11.1. This expression can be simplified with the help of left and right eigenvectors of $\mathcal{T}$ as stated in Section 4.11.1 as well as in [15] and [16]. Here we give a more rigorous derivation of the result (4.50).

Since the Hilbert space on which $\mathcal{T}$ acts is finite-dimensional, we can regard $\mathcal{T}$ as a matrix, which must be square due to the translational invariance. Given the MPO, this matrix is obtained by simply combining all left and all right indices into a single one, respectively. If $\mathcal{T}$ is diagonalizable (which seems to be the case for the networks in this thesis), i.e. there are matrices S and Λ such that $\mathcal{T} = S\Lambda S^{-1}$, then it can be written in terms of its right and left eigenvectors $\boldsymbol{u}^{(i)}$ and $\boldsymbol{v}^{(i)T}$ as

$$\mathcal{T} = \sum_{i=1}^{D} \boldsymbol{u}^{(i)} \lambda_i \boldsymbol{v}^{(i)T}, \tag{E.2}$$

where D is the dimension of the Hilbert space defined by the indices of the MPO. This result can be easily extended to powers $\mathcal{T}^n$ by replacing λ_i with λ_i^n. The right eigenvectors $\boldsymbol{u}^{(i)}$ are the columns of S and the left eigenvectors $\boldsymbol{v}^{(i)T}$ are the rows of S^{-1} and since $S^{-1}S = \mathbb{1}$ they are *biorthonormal*:

$$\boldsymbol{v}^{(i)T} \boldsymbol{u}^{(j)} = \delta_{ij}. \tag{E.3}$$

However, both sets cannot be simultaneously normalized, because normalizing the $\boldsymbol{u}^{(i)}$ fixes the $\boldsymbol{v}^{(i)T}$ and vice versa due to the condition $S^{-1}S = \mathbb{1}$. Hence, if we choose the right eigenvectors $\boldsymbol{u}^{(i)}$ to be normalized, then the left eigenvectors will in general have a norm different from 1, $\boldsymbol{v}^{(i)} = \hat{\boldsymbol{v}}^{(i)} \|\boldsymbol{v}^{(i)}\|$. Using the biorthonormality condition $\boldsymbol{v}^{(i)T} \boldsymbol{u}^{(i)} = 1$, this norm can be expressed as $\|\boldsymbol{v}^{(i)}\| = 1/(\hat{\boldsymbol{v}}^{(i)T} \boldsymbol{u}^{(i)})$ and thus, the unnormalized left eigenvectors can be written in terms of the normalized vectors only:

$$\boldsymbol{v}^{(i)} = \frac{1}{\hat{\boldsymbol{v}}^{(i)T} \boldsymbol{u}^{(i)}} \, \hat{\boldsymbol{v}}^{(i)}. \tag{E.4}$$

The trace of an arbitrary matrix M can be evaluated in the biorthonormal bases of the eigenvectors as

$$\mathrm{tr}(M) = \mathrm{tr}\big(S^{-1}MS\big) = \sum_{ijk} S_{ij}^{-1} M_{jk} S_{ki} = \sum_i \boldsymbol{v}^{(i)T} M \boldsymbol{u}^{(i)}. \tag{E.5}$$

Inserting (E.2) and (E.5) into (E.1) yields

$$\langle \hat{O}(t) \rangle = \lim_{n\to\infty} \frac{\sum_{ijk} \boldsymbol{v}^{(i)T} \boldsymbol{u}^{(j)} \lambda_j^n \boldsymbol{v}^{(j)T} \mathcal{T}_O \boldsymbol{u}^{(k)} \lambda_j^n \boldsymbol{v}^{(k)T} \boldsymbol{u}^{(i)}}{\sum_{ij} \boldsymbol{v}^{(i)T} \boldsymbol{u}^{(j)} \lambda_j^{2n+1} \boldsymbol{v}^{(j)T} \boldsymbol{u}^{(i)}} = \lim_{n\to\infty} \frac{\sum_i \lambda_i^{2n} \boldsymbol{v}^{(i)T} \mathcal{T}_O \boldsymbol{u}^{(i)}}{\sum_i \lambda_i^{2n+1}}$$

where the biorthonormality condition (E.3) was used in the second step. Dividing the numerator and the denominator by the dominant eigenvalue λ yields

$$\langle \hat{O}(t) \rangle = \lim_{n\to\infty} \frac{\sum_i \left(\frac{\lambda_i}{\lambda}\right)^{2n} \boldsymbol{v}^{(i)T} \mathcal{T}_O \boldsymbol{u}^{(i)}}{\lambda \sum_i \left(\frac{\lambda_i}{\lambda}\right)^{2n+1}}.$$

Now all n-dependent expressions are null sequences except for the terms where $\lambda_i = \lambda$ and the limit can be evaluated. Here it is assumed that, as stated in Section 4.11, the dominant eigenvalue λ is non-degenerate. Denoting by $\boldsymbol{u}$ and $\boldsymbol{v}^T$ the right and left eigenvectors corresponding to the dominant eigenvalue λ we obtain

$$\langle \hat{O}(t) \rangle = \frac{\boldsymbol{v}^T \mathcal{T}_O \boldsymbol{u}}{\lambda}.$$

Using (E.4) and switching to Dirac notation with the *normalized* dominant eigenvectors $|R\rangle \leftrightarrow \boldsymbol{u}$ and $\langle L| \leftrightarrow \hat{\boldsymbol{v}}^T$ results in

$$\langle \hat{O}(t) \rangle = \frac{\langle L | \mathcal{T}_O | R \rangle}{\lambda \langle L | R \rangle} = \frac{\langle L | \mathcal{T}_O | R \rangle}{\langle L | \mathcal{T} | R \rangle}. \tag{E.6}$$

An important point of the above considerations is that, while $\boldsymbol{v}^{(i)T} \boldsymbol{u}^{(i)} = 1$ for the non-normalized vectors obtained from the matrices S and S^{-1}, the same is not true for the individually normalized eigenvectors denoted by $|R\rangle$ and $\langle L|$ in bra-ket notation, i.e. $\langle L | R \rangle \neq 1$.

F. Biorthonormalization for a Single Time Step

In order to understand why subspaces in the left and right eigenvectors of the transfer matrix may cancel each other during biorthonormalization (see Section 6.1.2), we consider the example of a single time step with a first-order approximation of the time-evolution MPO, where the initial state is the vacuum,

$$|\psi_0\rangle = \bigotimes_{i=-\infty}^{\infty} |0\rangle_i$$

and $V = 0$ (corresponding to a tight-binding model).

Case of W$^{\text{I}}$-Approximation

The tensors of the first-order W$^{\text{I}}$-MPO are the same as in (6.5) without the terms containing V and hence are given by (assuming real T)

$$\hat{W}(\tau) = \begin{pmatrix} \hat{\mathbb{1}} & \sqrt{\mathrm{i}T\tau}\, b & \sqrt{\mathrm{i}T\tau}\, b^{\dagger} \\ \sqrt{\mathrm{i}T\tau}\, b^{\dagger} & 0 & 0 \\ \sqrt{\mathrm{i}T\tau}\, b & 0 & 0 \end{pmatrix} \tag{F.1}$$

with hard-core bosonic operators b and $b^{\dagger}$.

The transfer matrix for one time step (Figure F.1) reads

$$\mathcal{T}_{(l_2 l_3)(r_2 r_3)} = \left[(\hat{W} \, |0\rangle)_{l_3 r_3} \right]^{\dagger} (\hat{W} \, |0\rangle)_{l_2 r_2}, \tag{F.2}$$
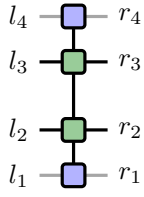
Figure F.1. Transfer matrix for one first-order W$^\text{I}$-time step and an initial product state of empty sites. The gray lines indicate dummy indices with dimension 1.

where l_i and r_i are the indices of the matrix (F.1) and the hermitian conjugation refers to each operator-valued entry of this matrix and does not involve any rearrangement of matrix elements. For the moment, the one-dimensional dummy indices l_1, l_4, r_1 and r_4 are not explicitly written. Applying $\hat{W}$ to $|0\rangle$ results in

$$\hat{W} |0\rangle = \begin{pmatrix} |0\rangle & 0 & \sqrt{iT\tau} \, |1\rangle \\ \sqrt{iT\tau} \, |1\rangle & 0 & 0 \\ 0 & 0 & 0 \end{pmatrix} \tag{F.3}$$

and thus, the elements of the transfer matrix, written in the matrix form (F.2), are

$$
\mathcal{T} =
\begin{array}{c}
 \\
l_2 l_3 \\
\begin{array}{c} 11 \\ 12 \\ 13 \\ 21 \\ 22 \\ 23 \\ 31 \\ 32 \\ 33 \end{array}
\end{array}
\begin{pmatrix}
1 & 0 & 0 & 0 & T\tau & 0 & 0 & 0 & 0 \\
0 & 0 & 0 & 0 & 0 & 0 & 0 & 0 & 0 \\
0 & 0 & 0 & T\tau & 0 & 0 & 0 & 0 & 0 \\
0 & 0 & 0 & 0 & 0 & 0 & 0 & 0 & 0 \\
0 & 0 & 0 & 0 & 0 & 0 & 0 & 0 & 0 \\
0 & 0 & 0 & 0 & 0 & 0 & 0 & 0 & 0 \\
0 & T\tau & 0 & 0 & 0 & 0 & 0 & 0 & 0 \\
0 & 0 & 0 & 0 & 0 & 0 & 0 & 0 & 0 \\
T\tau & 0 & 0 & 0 & 0 & 0 & 0 & 0 & 0
\end{pmatrix}
\begin{array}{c} \\ \\ \end{array}
\tag{F.4}
$$

$$
\begin{array}{ccccccccc}
11 & 12 & 13 & 21 & 22 & 23 & 31 & 32 & 33 \quad r_2 r_3
\end{array}
$$

The characteristic polynomial of $\mathcal{T}$ can be found by a few steps of Laplace expansion and it turns out that the matrix has only two eigenvalues: $\lambda_1 = 1$ and $\lambda_{2\ldots 9} = 0$ with multiplicity 8. We are interested in the dominant eigenvalue 1 and for the corresponding left and right eigenvectors we obtain

$$\boldsymbol{L} = \begin{pmatrix} 1 & 0 & 0 & T\tau & 0 & 0 & 0 & 0 & 0 \end{pmatrix},$$

$$\boldsymbol{R} = \begin{pmatrix} 1 & 0 & 0 & 0 & 0 & 0 & 0 & 0 & T\tau \end{pmatrix}^{\top}.$$

These vectors are now represented in the bases $(l_2 l_3)$ and $(r_2 r_3)$, respectively, because these are the left and right bases of $\mathcal{T}$. Reintroducing the dummy indices l_1, l_4, r_1 and r_4, the elements of $\boldsymbol{L}$ and $\boldsymbol{R}$ can be written as

$$L_{l_1 l_2 l_3 l_4} = \begin{cases} 1 & \text{if } l_1 = l_2 = l_3 = l_4 = 1 \\ T\tau & \text{if } l_1 = l_4 = 1 \text{ and } l_2 = l_3 = 2 \end{cases},$$

$$R_{r_1 r_2 r_3 r_4} = \begin{cases} 1 & \text{if } r_1 = r_2 = r_3 = r_4 = 1 \\ T\tau & \text{if } r_1 = r_4 = 1 \text{ and } r_2 = r_3 = 3 \end{cases}.$$

It is easy to check that they are represented by the MPS

$$L^{[1]l_1} = (1), \quad L^{[2]l_2} = \left\{ \begin{pmatrix} 1 & 0 \end{pmatrix}, \begin{pmatrix} 0 & 1 \end{pmatrix}, \begin{pmatrix} 0 & 0 \end{pmatrix} \right\},$$

$$L^{[3]l_3} = \left\{ \begin{pmatrix} 1 \\ 0 \end{pmatrix}, \begin{pmatrix} 0 \\ T\tau \end{pmatrix}, \begin{pmatrix} 0 \\ 0 \end{pmatrix} \right\}, \quad L^{[4]l_4} = (1) \tag{F.5}$$

and

$$R^{[1]r_1} = (1), \quad R^{[2]r_2} = \left\{ \begin{pmatrix} 1 & 0 \end{pmatrix}, \begin{pmatrix} 0 & 0 \end{pmatrix}, \begin{pmatrix} 0 & 1 \end{pmatrix} \right\},$$

$$R^{[3]r_3} = \left\{ \begin{pmatrix} 1 \\ 0 \end{pmatrix}, \begin{pmatrix} 0 \\ 0 \end{pmatrix}, \begin{pmatrix} 0 \\ T\tau \end{pmatrix} \right\}, \quad R^{[4]r_4} = (1), \tag{F.6}$$

where the sets of matrices in braces correspond to the different values of the indices l_i and r_i in ascending order.

One step of the biorthonormalization procedure described in Section 6.1.2 starts with contracting

$$\sum_{r_i \alpha_{i-1}} L^{[i]r_i}_{\alpha_{i-1}\alpha_i} R^{[i]r_i}_{\alpha_{i-1}\alpha'_i} = \sum_{r_i} L^{[i]r_i\top} R^{[i]r_i}.$$

Considering the example (F.5) and (F.6), the biorthonormalization step for the first transverse site is trivial and for the second one, the result of the contraction is

$$\sum_{r_2} L^{[2]r_2\top} R^{[2]r_2} = \begin{pmatrix} 1 & 0 \\ 0 & 0 \end{pmatrix}. \tag{F.7}$$

In this contracted tensor, the subspaces with $\alpha_i = 2$ and $\alpha'_i = 2$ are canceled. Singular-value decomposing it is trivial and gives

$$\begin{pmatrix} 1 & 0 \\ 0 & 0 \end{pmatrix} = U\Lambda V^\dagger = \begin{pmatrix} 1 \\ 0 \end{pmatrix} (1) \begin{pmatrix} 1 & 0 \end{pmatrix}.$$

The key step in the biorthonormalization algorithm is now the insertion of $U^\dagger \sqrt{\Lambda} \sqrt{\Lambda^{-1}} U$ between $L^{[2]}$ and $L^{[3]}$ and $V \sqrt{\Lambda} \sqrt{\Lambda^{-1}} V^\dagger$ between $R^{[2]}$ and $R^{[3]}$. However, due to the missing subspaces in (F.7), $U^\dagger U = \mathbb{1}$ and $VV^\dagger = \mathbb{1}$ is only true in the remaining $\alpha_i = \alpha'_i = 1$ subspace,

$$U^\dagger U = VV^\dagger = \begin{pmatrix} 1 & 0 \\ 0 & 0 \end{pmatrix} \neq \mathbb{1}. \tag{F.8}$$

Therefore, the transformation that is carried out does *not* leave the state represented by the MPS unchanged. In the specific example treated here, we would obtain

$$L^{[1]l_1} = (1), \quad L^{[2]l_2} = \{(1), (0), (0)\}, \quad L^{[3]l_3} = \{(1), (0), (0)\}, \quad L^{[4]l_4} = (1)$$

and

$$R^{[1]r_1} = (1), \quad R^{[2]r_2} = \{(1), (0), (0)\}, \quad R^{[3]r_3} = \{(1), (0), (0)\}, \quad R^{[4]r_4} = (1)$$

after the biorthonormalization, which are definitely not the same states as (F.5) and (F.6).

The reason for the cancellation during the contraction of $L^{[i]}$ and $R^{[i]}$ is that the left and right null spaces of the transfer matrix (F.4) correspond to different values of the indices l_i and r_i. Following the construction of $\mathcal{T}$, this can be traced back to the initial state: Since we chose the state $|0\rangle$ on every site, particles can be created but not annihilated. Therefore, the transfer matrix allows particles to hop *onto* the site it describes, but not *off*. This asymmetry first appears in (F.3) and finally causes the form of $\mathcal{T}$ with different left and right null spaces.

A possibility to avoid this for the problem considered here might be to work in a different basis where the state $|0\rangle$ becomes e.g. $(|0\rangle + |1\rangle)$ (like the x-basis for the spin state $|\downarrow\rangle$).

Case of Trotter Approximation

The first-order Trotter gates for the present model read

$$G_{(s_i s_{i+1})(s_i' s_{i+1}')} := \left(e^{-\mathrm{i}h_{i,i+1}\tau}\right)_{(s_i s_{i+1})(s_i' s_{i+1}')} = \begin{pmatrix} 1 & 0 & 0 & 0 \\ 0 & \cos(T\tau) & \mathrm{i}\sin(T\tau) & 0 \\ 0 & \mathrm{i}\sin(T\tau) & \cos(T\tau) & 0 \\ 0 & 0 & 0 & 1 \end{pmatrix}. \quad \text{(F.9)}$$

Reshaping them into $G_{(s_i s_i')(s_{i+1} s_{i+1}')}$ followed by an SVD gives unitary matrices $U_{(s_i s_i')\alpha}$ and $V^\dagger_{\alpha(s_{i+1} s_{i+1}')}$ as well as singular values λ_α. According to Section 4.8.2 (see in particular Figure 4.22), the two tensors forming the unit cell of the time-evolution MPO are

$$W^{[A]ss'}_{\alpha\beta} = \sum_{s''} U_{(s''s')\beta}\sqrt{\lambda_\beta}\sqrt{\lambda_\alpha}V^\dagger_{\alpha(ss'')}, \qquad W^{[B]ss'}_{\beta\alpha} = \sum_{s''} \sqrt{\lambda_\beta}V^\dagger_{\beta(s''s')}U_{(ss'')\alpha}\sqrt{\lambda_\alpha} .$$

The full transfer matrix now consists of two columns (see Figure F.2) and in the basis of the previous section with the W^{I}-approximation it is given by

$$\mathcal{T}_{(l_2 l_3)(r_2 r_3)} = \left[\sum_\beta (\hat{W}^{[A]}|0\rangle)_{l_3\beta} \otimes (\hat{W}^{[B]}|0\rangle)_{\beta r_3}\right]^\dagger \sum_\beta (\hat{W}^{[A]}|0\rangle)_{l_2\beta} \otimes (\hat{W}^{[B]}|0\rangle)_{\beta r_2}. \quad \text{(F.10)}$$
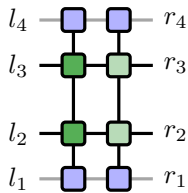

Figure F.2. Transfer matrix for one first-order Trotter time step and an initial product state of empty sites. The two columns contain the matrices $\hat{W}^{[A]}$ (dark green) and $\hat{W}^{[B]}$ (light green), respectively, and the gray lines indicate dummy indices with dimension 1.

Defining the short-hand notations

$$s := \sin(T\tau), \quad c := \cos(T\tau), \quad \sigma := \sin^2\left(\tfrac{1}{2}T\tau\right), \quad \kappa := \cos^2\left(\tfrac{1}{2}T\tau\right),$$

$$x := \frac{1}{2}s(1-c), \quad y := \frac{1}{2}s(1+c),$$

we obtain the matrix elements

$$
\mathcal{T} =
\begin{array}{c}
l_2 l_3 \\
\begin{array}{c}
11 \\ 12 \\ 13 \\ 14 \\ 21 \\ 22 \\ 23 \\ 24 \\ 31 \\ 32 \\ 33 \\ 34 \\ 41 \\ 42 \\ 43 \\ 44
\end{array}
\left(
\begin{array}{cccccccccccccccc}
\sigma^2 & -\tfrac{1}{2}s\sigma & 0 & 0 & -\tfrac{1}{2}s\sigma & \tfrac{1}{4}s^2 & 0 & 0 & 0 & 0 & x & 0 & 0 & 0 & 0 & 0 \\
-\tfrac{1}{2}s\sigma & \sigma\kappa & 0 & 0 & \tfrac{1}{4}s^2 & -\tfrac{1}{2}s\kappa & 0 & 0 & 0 & 0 & -\tfrac{1}{2}s^2 & 0 & 0 & 0 & 0 & 0 \\
0 & 0 & 0 & 0 & 0 & 0 & 0 & 0 & 0 & 0 & 0 & 0 & 0 & 0 & 0 & 0 \\
0 & 0 & 0 & 0 & 0 & 0 & 0 & 0 & 0 & 0 & 0 & 0 & 0 & 0 & 0 & 0 \\
-\tfrac{1}{2}s\sigma & \tfrac{1}{4}s^2 & 0 & 0 & \sigma\kappa & -\tfrac{1}{2}s\kappa & 0 & 0 & 0 & 0 & -\tfrac{1}{2}s^2 & 0 & 0 & 0 & 0 & 0 \\
\tfrac{1}{4}s^2 & -\tfrac{1}{2}s\kappa & 0 & 0 & -\tfrac{1}{2}s\kappa & \kappa^2 & 0 & 0 & 0 & 0 & y & 0 & 0 & 0 & 0 & 0 \\
0 & 0 & 0 & 0 & 0 & 0 & 0 & 0 & 0 & 0 & 0 & 0 & 0 & 0 & 0 & 0 \\
0 & 0 & 0 & 0 & 0 & 0 & 0 & 0 & 0 & 0 & 0 & 0 & 0 & 0 & 0 & 0 \\
0 & 0 & 0 & 0 & 0 & 0 & 0 & 0 & 0 & 0 & 0 & 0 & 0 & 0 & 0 & 0 \\
0 & 0 & 0 & 0 & 0 & 0 & 0 & 0 & 0 & 0 & 0 & 0 & 0 & 0 & 0 & 0 \\
0 & 0 & 0 & 0 & 0 & 0 & 0 & 0 & 0 & 0 & 0 & 0 & 0 & 0 & 0 & 0 \\
0 & 0 & 0 & 0 & 0 & 0 & 0 & 0 & 0 & 0 & 0 & 0 & 0 & 0 & 0 & 0 \\
0 & 0 & 0 & 0 & 0 & 0 & 0 & 0 & 0 & 0 & 0 & 0 & 0 & 0 & 0 & 0 \\
0 & 0 & 0 & 0 & 0 & 0 & 0 & 0 & 0 & 0 & 0 & 0 & 0 & 0 & 0 & 0 \\
0 & 0 & 0 & 0 & 0 & 0 & 0 & 0 & 0 & 0 & 0 & 0 & 0 & 0 & 0 & 0 \\
x & -\tfrac{1}{2}s^2 & 0 & 0 & -\tfrac{1}{2}s^2 & y & 0 & 0 & 0 & 0 & s^2 & 0 & 0 & 0 & 0 & 0
\end{array}
\right)
\\
\begin{array}{cccccccccccccccc}
11 & 12 & 13 & 14 & 21 & 22 & 23 & 24 & 31 & 32 & 33 & 34 & 41 & 42 & 43 & 44
\end{array}\ r_2 r_3
\end{array}
.
$$

Due to the larger size and larger number of non-zero elements, the eigenvectors of this matrix are not as easy to find as in the case of the W^I-MPO, but from the form of the matrix we can already see that the left and right null spaces are different in the present case, too. Thus, the same problem as above with the W^I-approximation will also occur when the MPO is built from Trotter gates.

Bibliography

[1] W. Shockley and H. J. Queisser. Detailed Balance Limit of Efficiency of p-n Junction Solar Cells. *Journal of Applied Physics* 32(3):510–519, 1961. DOI: 10.1063/1.1736034.

[2] E. Manousakis. Photovoltaic effect for narrow-gap Mott insulators. *Physical Review B* 82:125109, 2010. DOI: 10.1103/PhysRevB.82.125109.

[3] P. Werner, K. Held, and M. Eckstein. Role of impact ionization in the thermalization of photoexcited Mott insulators. *Physical Review B* 90(23), 2014. DOI: 10.1103/PhysRevB.90.235102. arXiv: 1408.3425.

[4] M. E. Sorantin, A. Dorda, K. Held, and E. Arrigoni. Impact ionization processes in the steady state of a driven Mott-insulating layer coupled to metallic leads. *Physical Review B* 97:115113, 2018. DOI: 10.1103/PhysRevB.97.115113. arXiv: 1708.05011.

[5] A. Kauch, P. Worm, P. Prauhart, M. Innerberger, C. Watzenböck, and K. Held. Enhancement of impact ionization in Hubbard clusters by disorder and next-nearest-neighbor hopping. Preprint, 2020. arXiv: 2007.16035 [cond-mat.str-el].

[6] F. Maislinger and H. G. Evertz. Impact ionization and multiple photon absorptions in the two-dimensional photoexcited Hubbard model. Preprint, 2020. arXiv: 2007.16201 [cond-mat.str-el].

[7] M. Szyniszewski and E. Burovski. The generalized t-V model in one dimension. *Journal of Physics: Conference Series* 592:012057, 2015. DOI: 10.1088/1742-6596/592/1/012057. arXiv: 1409.8344.

[8] F. C. Sabou, N. Bodington, and J. B. Marston. Rectification by Doped Mott-Insulator Junctions. *2012 Lester Eastman Conference on High Performance Devices (LEC)*:1–4, 2012. DOI: 10.1109/lec.2012.6410983. arXiv: 1208.1729.

[9] D. M. Kennes, A. de la Torre, A. Ron, D. Hsieh, and A. J. Millis. Floquet Engineering in Quantum Chains. *Physical Review Letters* 120(12):127601, 2018. DOI: 10.1103/PhysRevLett.120.127601. arXiv: 1801.06885.

[10] U. Schollwöck. The density-matrix renormalization group in the age of matrix product states. *Annals of Physics* 326(1):96–192, 2011. DOI: 10.1016/j.aop.2010.09.012. arXiv: 1008.3477.

[11] S. R. White. Density matrix formulation for quantum renormalization groups. *Physical Review Letters* 69:2863–2866, 1992. DOI: 10.1103/PhysRevLett.69.2863.

[12] S. Östlund and S. Rommer. Thermodynamic Limit of Density Matrix Renormalization. *Physical Review Letters* 75:3537–3540, 1995. DOI: 10.1103/PhysRevLett.75.3537. arXiv: cond-mat/9503107.

[13] J. Dukelsky, M. A. Martín-Delgado, T. Nishino, and G. Sierra. Equivalence of the variational matrix product method and the density matrix renormalization group applied to spin chains. *Europhysics Letters* 43(4):457–462, 1998. DOI: 10.1209/epl/i1998-00381-x.

[14] G. Vidal. Efficient Simulation of One-Dimensional Quantum Many-Body Systems. *Physical Review Letters* 93:040502, 2004. DOI: 10.1103/PhysRevLett.93.040502. arXiv: quant-ph/0310089.

[15] M. C. Bañuls, M. B. Hastings, F. Verstraete, and J. I. Cirac. Matrix Product States for Dynamical Simulation of Infinite Chains. *Physical Review Letters* 102(24):240603, 2009. DOI: 10.1103/PhysRevLett.102.240603. arXiv: 0904.1926.

[16] A. Müller-Hermes, J. I. Cirac, and M. C. Bañuls. Tensor network techniques for the computation of dynamical observables in one-dimensional quantum spin systems. *New Journal of Physics* 14(7): 075003, 2012. DOI: 10.1088/1367-2630/14/7/075003. arXiv: 1204.5080.

[17] W. Nolting and W. D. Brewer. *Fundamentals of Many-body Physics: Principles and Methods*. Springer Berlin Heidelberg, 2009.

[18] W. Nolting. *Theoretical Physics 7: Quantum Mechanics - Methods and Applications*. Springer International Publishing, 2017.

[19] S. Roman. *Advanced linear algebra*. 3rd ed. Graduate texts in mathematics 135. Springer New York, 2007.

[20] V. Fock. Konfigurationsraum und zweite Quantelung. *Zeitschrift für Physik* 75:622–647, 1932. DOI: 10.1007/BF01344458.

[21] B. Kendrick. Invariance of the geometrical phase under time-dependent unitary transformations. *Journal of Physics A: Mathematical and General* 25(4):885–897, 1992. DOI: 10.1088/0305-4470/25/4/025.

[22] F. Bloch. Über die Quantenmechanik der Elektronen in Kristallgittern. *Zeitschrift für Physik* 52: 555–600, 1929. DOI: 10.1007/BF01339455.

[23] G. H. Wannier. The Structure of Electronic Excitation Levels in Insulating Crystals. *Physical Review* 52:191–197, 1937. DOI: 10.1103/PhysRev.52.191.

[24] N. Marzari, A. A. Mostofi, J. R. Yates, I. Souza, and D. Vanderbilt. Maximally localized Wannier functions: Theory and applications. *Reviews of Modern Physics* 84(4):1419–1475, 2012. DOI: 10.1103/RevModPhys.84.1419. arXiv: 1112.5411.

[25] R. Peierls. Zur Theorie des Diamagnetismus von Leitungselektronen. *Zeitschrift für Physik* 80(11-12):763–791, 1933. DOI: 10.1007/BF01342591.

[26] J. M. Luttinger. The Effect of a Magnetic Field on Electrons in a Periodic Potential. *Physical Review* 84(4):814–817, 1951. DOI: 10.1103/PhysRev.84.814.

[27] W. Kohn. Theory of Bloch Electrons in a Magnetic Field: The Effective Hamiltonian. *Physical Review Letters* 115(6):1460–1478, 1959. DOI: 10.1103/PhysRev.115.1460.

[28] A. Alexandrov and H. Capellmann. Orbital diamagnetism of two-dimensional electrons. *Physical Review Letters* 66(3):365–368, 1991. DOI: 10.1103/PhysRevLett.66.365.

[29] D. A. McQuarrie. *Statistical Mechanics*. Harper & Row, 1975.

[30] R. A. Horn and C. R. Johnson. *Matrix Analysis*. 2nd ed. Cambridge University Press, 2013.

[31] L. N. Trefethen and D. Bau. *Numerical Linear Algebra*. Other Titles in Applied Mathematics 50. Society for Industrial and Applied Mathematics, 1997.

[32] M. A. Nielsen and I. L. Chuang. *Quantum Computation and Quantum Information*. Cambridge University Press, 2000.

[33] L. Mirsky. Symmetric gauge functions and unitarily invariant norms. *The Quarterly Journal of Mathematics* 11(1):50–59, 1960. DOI: 10.1093/qmath/11.1.50.

[34] J. Eisert, M. Cramer, and M. B. Plenio. Colloquium: Area laws for the entanglement entropy. *Reviews of Modern Physics* 82:277–306, 2010. DOI: 10.1103/RevModPhys.82.277. arXiv: 0808.3773.

[35] F. Verstraete and J. I. Cirac. Matrix product states represent ground states faithfully. *Physical Review B* 73:094423, 2006. DOI: 10.1103/PhysRevB.73.094423. arXiv: cond-mat/0505140.

[36] R. A. Jalabert and H. M. Pastawski. Environment-Independent Decoherence Rate in Classically Chaotic Systems. *Physical Review Letters* 86:2490–2493, 2001. DOI: 10.1103/PhysRevLett.86.2490. arXiv: cond-mat/0010094.

[37] T. Gorin, T. Prosen, T. H. Seligman, and M. Žnidarič. Dynamics of Loschmidt echoes and fidelity decay. *Physics Reports* 435(2):33–156, 2006. DOI: 10.1016/j.physrep.2006.09.003. arXiv: quant-ph/0607050.

[38] A. Silva. Statistics of the Work Done on a Quantum Critical System by Quenching a Control Parameter. *Physical Review Letters* 101:120603, 2008. DOI: 10.1103/PhysRevLett.101.120603. arXiv: 0806.4301.

[39]   C. Rylands and N. Andrei. Loschmidt amplitude and work distribution in quenches of the sine-Gordon model. *Physical Review B* 99:085133, 2019. DOI: 10.1103/PhysRevB.99.085133. arXiv: 1809.05582.

[40]   D. M. Kennes, C. Karrasch, and A. J. Millis. Loschmidt-amplitude wave function spectroscopy and the physics of dynamically driven phase transitions. *Physical Review B* 101:081106, 2020. DOI: 10.1103/PhysRevB.101.081106. arXiv: 1809.00733.

[41]   W. Heisenberg. Zur Theorie des Ferromagnetismus. *Zeitschrift für Physik* 49:619–636, 1928. DOI: 10.1007/BF01328601.

[42]   T. Giamarchi. *Quantum Physics in One Dimension*. International Series of Monographs on Physics. Clarendon Press, 2004.

[43]   H. Bethe. Zur Theorie der Metalle. *Zeitschrift für Physik* 71:205–226, 1931. DOI: 10.1007/BF01341708.

[44]   C. N. Yang and C. P. Yang. One-Dimensional Chain of Anisotropic Spin-Spin Interactions. I. Proof of Bethe's Hypothesis for Ground State in a Finite System. *Physical Review* 150:321–327, 1966. DOI: 10.1103/PhysRev.150.321.

[45]   C. N. Yang and C. P. Yang. One-Dimensional Chain of Anisotropic Spin-Spin Interactions. II. Properties of the Ground-State Energy Per Lattice Site for an Infinite System. *Physical Review* 150:327–339, 1966. DOI: 10.1103/PhysRev.150.327.

[46]   E. Lieb, T. Schultz, and D. Mattis. Two soluble models of an antiferromagnetic chain. *Annals of Physics* 16(3):407–4660, 1961. DOI: 10.1016/0003-4916(61)90115-4.

[47]   S. Grijalva, J. De Nardis, and V. Terras. Open XXZ chain and boundary modes at zero temperature. *SciPost Physics* 7(2), 2019. DOI: 10.21468/scipostphys.7.2.023. arXiv: 1901.10932.

[48]   B. Sutherland. *Beautiful Models: 70 Years of Exactly Solved Quantum Many-body Problems*. World Scientific, 2004.

[49]   P. Jordan and E. Wigner. Über das Paulische Äquivalenzverbot. *Zeitschrift für Physik* 47:631–651, 1928. DOI: 10.1007/BF01331938.

[50]   W. Rudin. *Principles of Mathematical Analysis*. 3rd ed. International series in pure and applied mathematics. McGraw-Hill, 1976.

[51]   J. Hubbard. Electron correlations in narrow energy bands. *Proceedings of the Royal Society of London. Series A. Mathematical and Physical Sciences* 276(1365):238–257, 1963. DOI: 10.1098/rspa.1963.0204.

[52]   J.-S. Caux and J. Mossel. Remarks on the notion of quantum integrability. *Journal of Statistical Mechanics: Theory and Experiment* 2011(02):P02023, 2011. DOI: 10.1088/1742-5468/2011/02/p02023. arXiv: 1012.3587.

[53]   M. Ganahl. *Dynamics of Strongly Correlated One-Dimensional Quantum Systems using Matrix Product States*. PhD thesis. Graz University of Technology, 2014.

[54]   T. D. Märk and G. H. Dunn. *Electron Impact Ionization*. Springer Vienna, 1985. DOI: 10.1007/978-3-7091-4028-4.

[55]   W. Shockley. Problems related to p-n junctions in silicon. *Czechoslovak Journal of Physics* 11:81–121, 1961. DOI: 10.1007/BF01688613.

[56]   P. T. Landsberg, H. Nussbaumer, and G. Willeke. Band-band impact ionization and solar cell efficiency. *Journal of Applied Physics* 74(2):1451–1452, 1993. DOI: 10.1063/1.354886.

[57]   M. Wolf, R. Brendel, J. H. Werner, and H. J. Queisser. Solar cell efficiency and carrier multiplication in $Si_{1-x}Ge_x$ alloys. *Journal of Applied Physics* 83(8):4213–4221, 1998. DOI: 10.1063/1.367177.

[58]   A. P. Kirk and M. V. Fischetti. Fundamental limitations of hot-carrier solar cells. *Physical Review B* 86:165206, 2012. DOI: 10.1103/PhysRevB.86.165206.

[59]   R. Penrose. Applications of negative dimensional tensors. In *Combinatorial Mathematics and its Applications*, edited by D. Welsh, pp. 221–244. Academic Press, New York, 1971.

[60] G. Vidal. Efficient Classical Simulation of Slightly Entangled Quantum Computations. *Physical Review Letters* 91(14):147902, 2003. DOI: 10.1103/PhysRevLett.91.147902. arXiv: quant-ph/0301063.

[61] E. M. Stoudenmire and S. R. White. Minimally entangled typical thermal state algorithms. *New Journal of Physics* 12(5):055026, 2010. DOI: 10.1088/1367-2630/12/5/055026. arXiv: 1002.1305.

[62] F. Verstraete, J. J. García-Ripoll, and J. I. Cirac. Matrix Product Density Operators: Simulation of Finite-Temperature and Dissipative Systems. *Physical Review Letters* 93:207204, 2004. DOI: 10.1103/PhysRevLett.93.207204. arXiv: cond-mat/0406426.

[63] I. P. McCulloch. From density-matrix renormalization group to matrix product states. *Journal of Statistical Mechanics: Theory and Experiment* 2007(10):P10014, 2007. DOI: 10.1088/1742-5468/2007/10/p10014. arXiv: cond-mat/0701428.

[64] C. Lanczos. An Iteration Method for the Solution of the Eigenvalue Problem of Linear Differential and Integral Operators. *Journal of Research of the National Bureau of Standards* 45(4):255–282, 1950. DOI: 10.6028/jres.045.026.

[65] E. R. Davidson. The iterative calculation of a few of the lowest eigenvalues and corresponding eigenvectors of large real-symmetric matrices. *Journal of Computational Physics* 17(1):87–94, 1975. DOI: 10.1016/0021-9991(75)90065-0.

[66] E. M. Stoudenmire and S. R. White. Studying Two-Dimensional Systems with the Density Matrix Renormalization Group. *Annual Review of Condensed Matter Physics* 3(1):111–128, 2012. DOI: 10.1146/annurev-conmatphys-020911-125018. arXiv: 1105.1374.

[67] A. J. Daley, C. Kollath, U. Schollwöck, and G. Vidal. Time-dependent density-matrix renormalization-group using adaptive effective Hilbert spaces. *Journal of Statistical Mechanics: Theory and Experiment* 2004(04):P04005, 2004. DOI: 10.1088/1742-5468/2004/04/p04005. arXiv: cond-mat/0403313.

[68] S. Paeckel, T. Köhler, A. Swoboda, S. R. Manmana, U. Schollwöck, and C. Hubig. Time-evolution methods for matrix-product states. *Annals of Physics* 411:167998, 2019. DOI: 10.1016/j.aop.2019.167998. arXiv: 1901.05824.

[69] N. Hatano and M. Suzuki. Finding Exponential Product Formulas of Higher Orders. In *Quantum Annealing and Other Optimization Methods*, edited by A. Das and B. K. Chakrabarti, pp. 37–68. Springer Berlin Heidelberg, 2005. DOI: 10.1007/11526216_2. arXiv: math-ph/0506007.

[70] D. Bauernfeind, M. Aichhorn, and H. G. Evertz. Comparison of MPS based real time evolution algorithms for Anderson Impurity Models. Preprint, 2019. arXiv: 1906.09077 [cond-mat.str-el].

[71] S. R. White and A. E. Feiguin. Real-Time Evolution Using the Density Matrix Renormalization Group. *Physical Review Letters* 93:076401, 2004. DOI: 10.1103/PhysRevLett.93.076401. arXiv: cond-mat/0403310.

[72] B. Pirvu, V. Murg, J. I. Cirac, and F. Verstraete. Matrix product operator representations. *New Journal of Physics* 12(2):025012, 2010. DOI: 10.1088/1367-2630/12/2/025012. arXiv: 0804.3976.

[73] M. P. Zaletel, R. S. K. Mong, C. Karrasch, J. E. Moore, and F. Pollmann. Time-evolving a matrix product state with long-ranged interactions. *Physical Review B* 91(16):165112, 2015. DOI: 10.1103/PhysRevB.91.165112. arXiv: 1407.1832.

[74] S. Keller and M. Reiher. Spin-adapted matrix product states and operators. *The Journal of Chemical Physics* 144(13):134101, 2016. DOI: 10.1063/1.4944921. arXiv: 1602.01145.

[75] D. Muth. Particle number conservation in quantum many-body simulations with matrix product operators. *Journal of Statistical Mechanics: Theory and Experiment* 2011(11):P11020, 2011. DOI: 10.1088/1742-5468/2011/11/p11020. arXiv: 1104.1611.

[76] D. Pérez-García, F. Verstraete, M. Wolf, and J. Cirac. Matrix product state representations. *Quantum Information and Computation* 7:401–430, 2007. DOI: 1854/LU-8589272. arXiv: quant-ph/0608197.

[77] G. Vidal. Classical Simulation of Infinite-Size Quantum Lattice Systems in One Spatial Dimension. *Physical Review Letters* 98:070201, 2007. DOI: 10.1103/PhysRevLett.98.070201. arXiv: cond-mat/0605597.

[78] I. P. McCulloch. Infinite size density matrix renormalization group, revisited. Preprint, 2008. arXiv: 0804.2509 [cond-mat.str-el].

[79] R. Orús and G. Vidal. Infinite time-evolving block decimation algorithm beyond unitary evolution. *Physical Review B* 78(15):155117, 2008. DOI: 10.1103/PhysRevB.78.155117. arXiv: 0711.3960.

[80] W. E. Arnoldi. The principle of minimized iterations in the solution of the matrix eigenvalue problem. *Quarterly of Applied Mathematics* 9:17–29, 1951. DOI: 10.1090/qam/42792.

[81] R. J. Bursill, T. Xiang, and G. A. Gehring. The density matrix renormalization group for a quantum spin chain at non-zero temperature. *Journal of Physics: Condensed Matter* 8(40):L583–L590, 1996. DOI: 10.1088/0953-8984/8/40/003. arXiv: cond-mat/9609001.

[82] X. Wang and T. Xiang. Transfer-matrix density-matrix renormalization-group theory for thermodynamics of one-dimensional quantum systems. *Physical Review B* 56:5061–5064, 1997. DOI: 10.1103/PhysRevB.56.5061.

[83] Y. Saad. *Numerical Methods for Large Eigenvalue Problems.* Algorithms and architectures for advanced scientific computing. Manchester University Press, 1992.

[84] *ITensor Library (version 2.1.1).* 2017. URL: https://itensor.org.

[85] E. Jeckelmann. Local density of states of the one-dimensional spinless fermion model. *Journal of Physics: Condensed Matter* 25(1):014002, 2012. DOI: 10.1088/0953-8984/25/1/014002. arXiv: 1111.6545.

[86] J.-S. Caux, R. Hagemans, and J. M. Maillet. Computation of dynamical correlation functions of Heisenberg chains: the gapless anisotropic regime. *Journal of Statistical Mechanics: Theory and Experiment* 2005(9):P09003–P09003, 2005. DOI: 10.1088/1742-5468/2005/09/P09003. arXiv: cond-mat/0506698.

[87] I. P. Castillo. The exact two-spinon longitudinal dynamical structure factor of the anisotropic XXZ model. Preprint, 2020. arXiv: 2005.10729 [cond-mat.str-el].

[88] G. Kopp and J. L. Lean. A new, lower value of total solar irradiance: Evidence and climate significance. *Geophysical Research Letters* 38(1):L01706, 2011. DOI: 10.1029/2010GL045777.

[89] M. Göppert-Mayer. Über Elementarakte mit zwei Quantensprüngen. *Annalen der Physik* 9:273–294, 1931. DOI: 10.1002/andp.19314010303.

[90] S. Carusotto, G. Fornaca, and E. Polacco. Two-Photon Absorption and Coherence. *Physical Review* 157:1207–1213, 1967. DOI: 10.1103/PhysRev.157.1207.

[91] IEEE Standard for Floating-Point Arithmetic. *IEEE Std 754-2019 (Revision of IEEE 754-2008)*: 1–84, 2019. DOI: 10.1109/IEEESTD.2019.8766229.